

SOIL-PIPE INTERACTION UNDER PLANE STRAIN CONDITIONS

A Dissertation

Presented to the Faculty of the Graduate School

of Cornell University

In Partial Fulfillment of the Requirements for the Degree of

Doctor of Philosophy

by

Jai Kyoung Jung

January 2011

© 2011 Jai Kyoung Jung

SOIL-PIPE INTERACTION UNDER PLANE STRAIN CONDITIONS

Jai Kyoung Jung, Ph. D.

Cornell University 2011

Permanent ground deformations associated with geohazards such as earthquakes, liquefaction and landslides can introduce substantial axial and bending strains on buried pipeline systems. Longitudinal and transverse bending strains depend on the force imposed on the pipeline by relative displacement between the pipeline and surrounding soil.

Analytical models used currently in design are based on p-y, t-x, and q-z for interaction relationships, and they require reliable p-y, q-z and oblique force-displacement relationships. Moreover, to advance the state-of-the-art for soil continuum models, it is necessary to develop better simulations of soil-pipeline interactions rather than rely on empirically based p-y and q-z relationships.

In this study, various modeling procedures are developed for simulating soil-pipeline interactions under lateral and vertical relative movement between soil and pipe as well as relative movement at oblique angles with respect to the pipeline for dry and partially saturated sand. Mohr-Coulomb (MC) strength parameters applied in FE analyses for both dry and partially saturated sand are developed from direct shear test data and from multiple linear regression. To represent strain softening, the model proposed by Anastasopoulos, et al. (2007) is used in this work to diminish both the friction and dilation angles to residual values. The MC parameters are applied in the

FE simulations to produce dimensionless force vs. dimensionless displacement plots. The results show excellent agreement with large-scale 2D experimental results in terms of pre-peak, peak, and post-peak for both dry and partially saturated soil.

The modeling process is expanded to investigate and characterize the maximum lateral force as a function of pipe depth. The analytical results from simulations of lateral, vertical, and oblique pipe movement for semi-infinite, plane strain soil conditions are summarized in dimensionless form. They are plotted on a polar coordinate graph from which the maximum force can be estimated for any size pipe at any depth in response to any orientation of relative movement between the pipe and soil for both dry and partially saturated sands.

BIOGRAPHICAL SKETCH

Jai was born in Seoul, capital of South Korea and raised in Chung-Ju, Chung-Chong Buk Do. After graduating from Han-Il High School, he attended Han-Yang University in Seoul. In 2002, he joined the Republic of Korea Army to serve an honorable duty for his country as KATUSA (Korean Augmentation to the United States Army). While serving in the military, he led a team of six American soldiers and received three Army Achievement medals and one Army Commendation medal, all awarded by the Department of the United States Army. In addition, during the fourth quarter of 2003, he was selected as the “Engineer Brigade KATUSA” for being the most outstanding soldier in brigade. After he finished his military service, he returned to Han-Yang University and graduated with a Bachelor of Science degree in Civil Engineering in August 2006. Jai came to Cornell University to pursue his doctoral degree in the School of Civil and Environmental Engineering at Cornell, under the guidance of Dr. T.D. O’Rourke, the person who influenced Jai the most.

To my family, and friends

ACKNOWLEDGMENTS

First and foremost, I must express the deepest thanks and gratitude to the chair of my Special Committee, Professor Thomas D. O'Rourke. His encouragement, guidance, support, patience, and knowledge were vital to my success as a graduate student at Cornell University. My first language is not English and it was Professor O'Rourke's guidance that prompted me to write thesis in 'English'. I appreciate the patience with which he guided me through long months of numerical analyses. I could not have accomplished this without him. I must also thank Professor Wilkins Aquino for guiding me to the numerical simulation, and for his encouragement and guidance in the early months of investigation. He was very helpful when modeling an initial input file for the simulation, and taught me a background of finite element analyses. I thank my other committee member, Professor Harry E. Stewart, for his guidance in my studies, and for the excellent courses I was able to take from him while at Cornell University. In this regard, I also thank Professors Fred H. Kulhawy, James Jenkins, Stephen D. DeGloria, and Alan Zehnder. I must mention Professor Christopher J. Earls for his great help, guidance and his kindness.

I was privileged to share an office with Dr. Xavier Perez during my years as a graduate student at Cornell. Xavier's support, help and ideas were a great lift throughout my time as a graduate student. We took courses together and looked as team members on many projects. I will never forget the time we went to Denver a geotechnical conference. I thank Dr. Nathaniel Olson and Jeremiah Jezerski for their friendship and support. In particular, Nathaniel's support for obtaining appropriate soil properties were critical for my simulation. In this regard, I also thank Dilan

Robert. His great help with establishing a FORTRAN subroutine was crucial in my own simulations. I also thank Dr. Kunyong Zhang, Wooyoung Jeong, Joonwoo Sohn, and especially Sojeong Moon for their support and the friendship we still share.

I also extend my gratitude to Dr. Michael Palmer, Paul Charles, Cameron Willkens, Tim Brock, and the staffs of the Harry E. Bovay Jr. Civil Infrastructure Laboratory Complex - Tim Bond, and Joe Chipalowsky for their endless support and help.

Financial support for my graduate tuition and stipend, the excellent facilities from the Cornell University and the Department of Civil and Environmental Engineering were vitally important for me.

Completing my degree would not have been possible without the love and support of my family. My parents, Kyoungsup Jung and Misun Jeong, brother Jai-Min Jung and his wife Jisu Moon, and grandparents Intaek Jung and Soonja Lee have provided love and financial support for which I am extremely grateful. I also thank my 9 month old niece, Hyun-Jin Jung, for being healthy and always knowing how to brighten my day.

TABLE OF CONTENTS

	<u>Page</u>
BIOGRAPHICAL SKETCH.....	iii
DEDICATION	iv
ACKNOWLEDGMENTS.....	v
TABLE OF CONTENTS	vii
LIST OF FIGURES	xiv
LIST OF TABLES	xxiv
LIST OF ABBREVIATIONS.....	xxvi
LIST OF SYMBOLS.....	xxvii
CHAPTER 1 INTRODUCTION	1
1.1 Background	1
1.2 Research Objectives	5
1.2.1 Plasticity and Strain Softening Model	5
1.2.2 Comparison of Finite Element and Experimental Results for Lateral Pipe Movement	6
1.2.3 Expansion of Lateral Soil-Pipe Interaction Model	6
1.2.4 Comparison of Finite Element and Experimental Results for Vertical Upward Pipe Movement	7
1.2.5 Simulations of Vertical Downward Pipe Movement	7
1.2.6 Simulations of Oblique Pipe Movement and Guidelines for Practice	8
1.3 Scope and Organization	9

CHAPTER 2	MOHR-COULOMB PLASTICITY, FLOW RULE, AND SOFTENING BEHAVIOR	11
2.1	Introduction	11
2.2	Mohr-Coulomb Yield Criterion	12
2.3	Flow Rule Associated with the Model	21
2.4	Strain Softening Behavior in the Model	25
CHAPTER 3	COMPARISON OF FINITE ELEMENT AND EXPERIMENTAL RESULTS FOR LATERAL PIPE MOVEMENT	33
3.1	Introduction	33
3.2	Pipe Force vs. Displacement Relationship	34
3.3	Dry Soil Strength Properties	36
3.3.1	Trautmann and O'Rourke Tests	36
3.3.2	Olson Tests	39
3.3.3	Turner Tests	41
3.3.4	Summary	41
3.4	Finite Element Analyses Model for Dry Sand	43
3.5	Comparison of FE Analyses and Measured Peak Forces	47
3.6	Young's Modulus for Lateral Pipe Movement	52
3.7	Strain Softening Behavior	60
3.8	Comparison of Force vs. Displacement Curves for Analytical and Test Results	63
3.9	Soil Strength Properties and Finite Element Analyses Model for Partially Saturated RMS Graded Sand	67
3.10	Comparison of Partially Saturated RMS Graded Soil Force vs. Displacement Curves for Analytical and Test Results	72

CHAPTER 4	LATERAL PIPE MOVEMENT IN SEMI-INFINITE SOIL AT	
	VARIABLE DEPTHS	78
4.1	Introduction	78
4.2	Finite Element Model	78
4.3	Comparison of Peak Forces for Semi-Infinite Soil and Experimental Simulations with Measured Peak Forces	82
4.4	Comparison of Semi-Infinite Numerical and Experimental Results for Maximum Force at Various Depths	87
4.5	Comparison of Force vs. Displacement Curves for Semi-Infinite Soil and Experimental Simulations with Measured Force vs. Displacement Curves	88
4.6	Comparison of Semi-Infinite Soil and Experimental Simulations with Measured Data for Partially Saturated RMS Graded Sand	94
4.7	Refinements in Soil Strength Modeling	97
	4.7.1 Depth Dependent Soil Strength Properties	97
	4.7.2 σ'_N Reference Stress	100
4.8	Relationship Between Maximum Lateral Force and Pipe Depth	104
	4.8.1 Model Geometry and Properties for Maximum Dimensionless Lateral Force and Dimensionless Depth	104
	4.8.2 Analytical Results of Lateral Maximum Dimensionless Force and Dimensionless Depth	106
	4.8.3 Analytical Results of Maximum Lateral Dimensionless Forces for Various Pipe Diameters	111
	4.8.4 Investigation of Maximum Dimensionless Lateral Force and Dimensionless Depth in Partially Saturated RMS Graded Sand	115

CHAPTER 5	VERTICAL UPWARD PIPE MOVEMENT	118
5.1	Introduction	118
5.2	Finite Element Model and Soil Strength Properties	118
5.3	Comparison of FE Analyses and Measured Peak Forces	121
5.4	Young's Modulus for Vertical Upward Pipe Movement	131
5.5	Comparison of Simulated and Measured Upward Force vs. Displacement Curves	134
5.6	Relationship Between Maximum Vertical Upward Force and Pipe Depth	138
5.7	Analytical Results of Maximum Vertical Upward Dimensionless Forces for Various Pipe Diameters	140
5.8	Analytical Results of Maximum Vertical Upward Force in Partially Saturated RMS Graded Sand	143
CHAPTER 6	VERTICAL DOWNWARD PIPE MOVEMENT	146
6.1	Introduction	146
6.2	Finite Element Model and Soil Strength Properties	146
6.3	Analytical Results of Maximum Vertical Downward Force in Dry Sand	147
6.4	Comparison Between Pipe Peak Force and the Bearing Capacity for Deep Foundations	151
6.4.1	Deep Foundation Bearing Capacity	151
6.4.2	Finite Element Model for Deep Foundations	154
6.5	Young's Modulus for Vertical Downward Pipe Movement	159
6.6	Analytical Results of Maximum Vertical Downward Force for Various Pipe Diameters	164
6.7	Analytical Results of Maximum Vertical Downward Force in	

Partially Saturated RMS Graded Sand	165
CHAPTER 7 OBLIQUE PIPE MOVEMENT AND GUIDELINES FOR PRACTICE	167
7.1 Introduction	167
7.2 Analytical Results for Maximum Oblique Force in Dry Sand	167
7.3 Peak Dimensionless Force Associated with Oblique Pipe Movement	169
7.4 Relationship Between Force and Pipe Movement Direction	172
7.4.1 Simplified Approach	172
7.4.2 Visualization of Maximum Dimensionless Force and Movement Direction	173
7.5 Relationship Between Young's Modulus and Pipe Movement Direction	180
7.6 Peak Dimensionless Force for Oblique and Vertical Downward Pipe Movement in Partially Saturated RMS Graded Sand	182
7.7 Force vs. Displacement Relationships for One Dimensional Modeling of Soil-Pipeline Interaction	183
7.7.1 Lateral Pipe Movement	188
7.7.2 Vertical Upward Pipe Movement	191
7.7.3 Vertical Downward Pipe Movement	193
7.7.4 Oblique Downward Pipe Movement	197
7.7.5 Oblique Upward Pipe Movement	200
CHAPTER 8 SUMMARY AND CONCLUSIONS	204
8.1 Introduction	204
8.2 Comparison of Finite Element and Experimental Results for Lateral Pipe Movement	204

8.3	Lateral Pipe Movement in Semi-Infinite Soil at Various Depths	206
8.4	Vertical Upward Pipe Movement	208
8.5	Vertical Downward Pipe Movement	209
8.6	Oblique Pipe Movement	210
8.7	Guidelines for Practice	211
8.8	Future Research Directions	212
APPENDIX A STRAIN-COMPATIBLE MODULUS		215
A.1	Introduction	215
A.2	Derivation of Secant Modulus Associated with Stress Levels	215
A.3	Relationship Between Secant Modulus and Mobilized Fraction of Soil Strength	218
A.4	Mobilized Soil Strength Fraction for Horizontal, Vertical Upward, and Vertical Downward Pipe Movement	222
APPENDIX B THEORETICAL BACKGROUND OF INFINITE ELEMENTS		224
B.1	Introduction	224
B.2	Theoretical Background of Infinite Element	224
APPENDIX C CONVENTIONAL BEARING CAPACITY CALCULATIONS		230
C.1	Introduction	230
C.2	Bearing Capacity for Deep Foundations	230
APPENDIX D DATABASE FOR LOAD TESTS ON DEEP		

FOUNDATIONS UNDER AXIAL COMPRESSION	235
D.1 Introduction	235
D.2 Case 1	237
D.3 Case 2	238
D.4 Case 3G1	239
D.5 Case 3G2	240
D.6 Case 4P1	241
D.7 Case 4P2	242
D.8 Case 4P3	243
D.9 Case 4P4	244
D.10 Case 4P5	245
D.11 Case 5	246
D.12 Case 6A	247
D.13 Case 6D	248
D.14 Case 7C1	249
D.15 Case 7C4	250
D.16 Summary	251
REFERENCES	253

LIST OF FIGURES

Figure No.		Page No.
2.1	Concept of Mohr Criterion	13
2.2	Simplest Form of the Mohr Failure Envelope	14
2.3	The Failure Loci for the Mohr-Coulomb Criterion in $\sigma_3 = 0$ Plane (After Chen and Han, 1987)	16
2.4	Angle, θ , Defined in Deviatoric Plane (After Chen and Han, 1987)	18
2.5	Mohr-Coulomb Criterion in Meridian Plane $\theta = 0^\circ$ (After Chen and Han, 1987)	19
2.6	Mohr-Coulomb Criterion in Deviatoric Plane	20
2.7	Mohr-Coulomb Criterion in Principal Stress Plane	20
2.8	The Smooth Triple Symmetric Ellipse Function (Menetrey and Willam, 1995)	22
2.9	Flow Potential Used in ABAQUS (ABAQUS, 2009)	25
2.10	Variation of Friction Angle and Dilation Angle (Anastasopoulos, 2007)	26
2.11	Typical Stress Ratio vs. Horizontal Displacement, and Vertical Displacement vs. Horizontal Displacement Curve (After Shibuya et al., 1997)	28

Figure No.		Page No.
2.12	Typical Direct Shear Test Box	29
2.13	Simple Shear Shape for a) Finite Element Mesh and b) Along the Shear Band (After Anastasopoulos, et al., 2007)	31
3.1	Typical Dimensionless Force-Displacement Curve for Lateral Pipe Movement	34
3.2	ψ_p vs. γ_{dry} for Dry CU Filter Sand at $\sigma'_N = 2.1$ kPa (Olson, 2009)	37
3.3	Plot of $\psi_p/\psi_{p/\sigma'_N Ref.}$ vs. σ'_N	38
3.4	ψ_p vs. γ_d for Dry RMS Graded Sand at $\sigma'_N = 2.1$ kPa (Olson, 2009)	40
3.5	Geometry of the Numerical Model for Lateral Pipe Movement	44
3.6	The Soil/Test Box and Soil/Pipe Interfaces	45
3.7	Geometry of the Test Box for Each Test	46
3.8	Comparison of the Measured and FE Analyses Peak Force	49
3.9	Plot of N_{qH} vs. H_c/D for Dry CU Filter Sand	50
3.10	Summary Plot of N_{qH} vs. H_c/D for All Dry FE Results	51
3.11	K_{70} Approach of Bilinear Model for Dimensionless Force-Displacement Curve	53

Figure No.		Page No.
3.12	Relationships between E_{70-H}/P_a and σ'_{vc}/P_a of CU Filter Sand	55
3.13	E_{70-H} Multiple Linear Regression for γ_d and σ'_{vc} .	58
3.14	Histogram of Equivalent E_{70-H} from Turner (2004) Tests and the Computed E_{70-H} from Multiple Linear Regression Analysis	59
3.15	Simulated Dimensionless Force vs. Displacement Curve for Turner Tests	59
3.16	Stress Ratio, d_y vs. d_x Plot in a DS Test of CU Filter Sand	62
3.17	Dimensionless Force vs. Displacement Curves of Medium CU Filter Sand	64
3.18	Dimensionless Force vs. Displacement Curves of Very Dense CU Filter Sand	65
3.19	Dimensionless Force vs. Displacement Curves of RMS Graded Sand	66
3.20	$\tan(\psi_p)_{p.sat}$ vs. σ_N for RMS Graded Sand at $\gamma_{dry} = 15.8 \text{ kN/m}^3$ ($\gamma_{total} = 16.5 \text{ kN/m}^3$) (Olson, 2009)	67
3.21	Plot of τ_p/σ_N vs. $(\psi_p)_{p.sat}$	69
3.22	Geometry of the Partially Saturated RMS Graded Sand Test (Olson, 2009)	70

Figure No.		Page No.
3.23	Dimensionless Force vs. Displacement Curves of Partially Saturated RMS Graded Sand Using E_{70-H}	74
3.24	Dimensionless Force vs. Displacement Curves of Partially Saturated RMS Graded Sand Using $E_{70-H \text{ sat}}$	75
3.25	Plot of N_{qH} vs. H_c/D for Partially Saturated RMS Graded Sand	76
4.1	Geometry for the Numerical Analysis of Each Test	79
4.2	Comparison of FE Semi-Infinite Soil N_{q-si} vs. Measured N_{q-m}	83
4.3	Comparison of FE Semi-Infinite Soil N_{q-si} vs. FE Experimental N_{q-e}	84
4.4	Displacement Pattern for Very Dense CU Filter Sand FE Semi-Infinite Soil and Experimental Simulation at $H_c/D = 5.5$	86
4.5	Comparison Plot of N_q vs. H_c/D for CU Filter Sand	87
4.6	Summary Plot of N_{qH} vs. H_c/D for Infinite Field Boundary Condition FEA and FE Simulation of the Large-Scale Tests	89
4.7	Dimensionless Force vs. Displacement Curves for Medium CU Filter Sand	91
4.8	Dimensionless Force vs. Displacement Curves for Dense CU Filter Sand	92

Figure No.		Page No.
4.9	Dimensionless Force vs. Displacement Curves for RMS Graded Sand	93
4.10	Dimensionless Force vs. Displacement Curves for Partially Saturated RMS Graded Sand	95
4.11	Plot of N_{qH} vs. H_c/D of Semi-Infinite Soil and Measured Data for Partially Saturated RMS Graded Sand	96
4.12	Geometry of Depth Dependent Soil Strength Properties Model	98
4.13	Dimensionless Force vs. Displacement Curve for Depth Dependent Model and Pipe Depth Dependent Model	99
4.14	Relationship Between σ'_N and Principal Stresses	100
4.15	σ'_N/σ'_{vc} Plot for $H_c/D = 5.5$ and 15 at the Peak	102
4.16	Dimensionless Force vs. Displacement Curve for σ'_N Model and σ'_{vc} Reference Stress Model	103
4.17	Summary Plot of N_{qH} vs. H_c/D for Lateral Pipe Movement	107
4.18	Displacement Pattern for Medium Sand at $H_c/D = 8$	109
4.19	Displacement Pattern for Medium Sand at $H_c/D = 11$	109
4.20	Displacement Pattern for Medium Sand at $H_c/D = 15$	110
4.21	Displacement Pattern for Medium Sand at $H_c/D = 100$	110

Figure No.		Page No.
4.22	Geometry of the Numerical Model for Various Pipe Diameters	111
4.23	Summary Plot of N_{qH} vs. H_c/D for Various Pipe Diameters	114
4.24	Lateral N_{qH} vs. H_c/D for Partially Saturated RMS Graded Sand	117
5.1	Geometry of the Finite Element Model for Upward Pipe Movement	119
5.2	Displacement Field Interpretive Diagram for Upward Pipe Movement (Trautmann and O'Rourke, 1983)	120
5.3	Force vs. Displacement Curve for Medium CU Filter Sand Vertical Upward Pipe Movement Test at $H_c/D = 1.5$	123
5.4	Displacement Field for Vertical Upward Pipe Movement Test in Medium Sand at $H_c/D = 1.5$ (Trautmann and O'Rourke, 1983)	123
5.5	Deformed Shape of FE Analysis for Vertical Upward Pipe Movement Test in Medium Sand at $H_c/D = 1.5$	124
5.6	Deformed Shape of FE Analysis for Vertical Upward Pipe Movement Test After Mesh Modification	125
5.7	Force vs. Displacement Curve for Vertical Upward Pipe Movement Test in Medium and Very Dense Sand Test at $H_c/D =$ 1.5 and $H_c/D = 4$	127

Figure No.		Page No.
5.8	Comparisons of Vertical Upward N_{qVU-m} and N_{qVU-e} in Medium and Very Dense CU Filter Sand Using the Regular FEA	128
5.9	Comparisons of N_{qVU-m} and N_{qVU-e} for the Modified Mesh Model	129
5.10	Plot of Vertical Upward Pipe Movement N_{qVU} vs. H_c/D	130
5.11	Relationships between E_{70-VU}/P_a and σ'_{vc}/P_a of Vertical Upward Pipe Movement Tests	132
5.12	E_{70-VU} Multiple Linear Regression for γ_d and σ'_{vc} for Vertical Upward Pipe Movement	134
5.13	Vertical Upward Movement Dimensionless Force vs. Displacement Curves for Medium CU Filter Sand	136
5.14	Vertical Upward Movement Dimensionless Force vs. Displacement Curves for Very Dense CU Filter Sand	137
5.15	Finite Element Model for Upward Pipe Movement in Dry RMS Graded Sand	138
5.16	Photo of N_{qVU} vs. H_c/D for Vertical Upward Pipe Movement	141
5.17	Geometry of the Vertical Upward Pipe Movement Numerical Model for Various Pipe Diameters Simulation	142
5.18	Summary Plot of N_{qVU} vs. H_c/D for Various Pipe Diameters	143
5.19	Vertical Upward N_{qVU} vs. H_c/D for Partially Saturated Sand	144

Figure No.		Page No.
6.1	Typical Load-Settlement Curve of Axial Compression Test on Foundation (After Akbas and Kulhawy, 2009)	148
6.2	Summary Plot of N_{qVD} vs. H_c/D for Vertical Downward Pipe Movement	150
6.3	Comparison of Q_{tc} and Q_{tc-fea}	152
6.4	FE Model for Deep Foundation	155
6.5	Detailed Boundary Conditions at A	156
6.6	Comparison of Q_{tc-c} and Q_{tc-d}	158
6.7	Contour of $(\sigma'_1 - \sigma'_3) / (\sigma'_1 - \sigma'_3)_f$ for Deep Foundation in Dense Sand at Maximum Load	160
6.8	Contour of $(\sigma'_1 - \sigma'_3) / (\sigma'_1 - \sigma'_3)_f$ for Vertical Downward Pipe in Dense Sand at Maximum Load	161
6.9	Typical Vertical Force vs. Settlement Results for a Pipe and Vertical Tip Resistance of a Frictionless Deep Foundation	163
6.10	Summary Plot of N_{qVD} vs. H_c/D for Various Pipe Diameters	164
6.11	Vertical Downward N_{qVD} vs. H_c/D for Partially Saturated RMS Graded Sand	165
7.1	Directions for Oblique Pipe Movement	168

Figure No.		Page No.
7.2	Summary Plot of N_{qOD} vs. H_c/D for Oblique Downward Pipe Movement	170
7.3	Summary Plot of N_{qOU} vs. H_c/D for Oblique Upward Pipe Movement	171
7.4	Comparison of N_{qOD-e} and N_{qOD-s}	174
7.5	Comparison of N_{qOU-e} and N_{qOU-s}	175
7.6	Visualization of N_q/N_{qH} for $H_c/D = 3.5 - 11$	177
7.7	Visualization of N_q/N_{qH} for $H_c/D = 15 - 100$	178
7.8	Comparison of N_q/N_{qH} of Medium and Very Dense Sand	179
7.9	Contour of $(\sigma'_1 - \sigma'_3) / (\sigma'_1 - \sigma'_3)_f$ for Dense Sand at Peak Pipe Force for Oblique Pipe Movement	181
7.10	Summary Plot of N_{qOD} vs. H_c/D of Oblique Downward Pipe Movement in Partially Saturated RMS Graded Sand	184
7.11	Summary Plot of N_{qOU} vs. H_c/D for Oblique Upward Pipe Movement in Partially Saturated RMS Graded Sand	185
7.12	Comparison of FE Analyses and Simplified Approach	186
7.13	Soil Load and Restraints (ASCE, 1984)	187
7.14	Y_{fH}/H_c vs. H_c/D Plots for Lateral Pipe Movement	189

Figure No.		Page No.
7.15	Force vs. Displacement Relationships for One Dimensional Modeling of Soil-Pipeline Interaction for Lateral Pipe Movement	190
7.16	Y_{fVU}/H_c vs. H_c/D Plots for Vertical Upward Pipe Movement	192
7.17	Force vs. Displacement Relationships for One Dimensional Modeling of Soil-Pipeline Interaction for Vertical Upward Pipe Movement	194
7.18	Y_{fVD}/H_c vs. H_c/D Plots for Vertical Downward Pipe Movement	195
7.19	Force vs. Displacement Relationships for One Dimensional Modeling of Soil-Pipeline Interaction for Vertical Downward Pipe Movement	196
7.20	Y_{fOD}/H_c vs. H_c/D Plots for Vertical Downward Pipe Movement	198
7.21	Force vs. Displacement Relationships for One Dimensional Modeling of Soil-Pipeline Interaction for Oblique Downward Pipe Movement	199
7.22	Y_{fOU}/H_c vs. H_c/D Plots for Vertical Downward Pipe Movement	201
7.23	Force vs. Displacement Relationships for One Dimensional Modeling of Soil-Pipeline Interaction for Oblique Downward Pipe Movement	202

LIST OF TABLES

Table No.		Page No.
3.1	Summary of the Input Parameters Used in Finite Element Analyses for Lateral Pipe Movement	42
3.2	Summary of Dry Sand Strength Parameters	43
3.3	Summary of E_{70-H} Used in Dry Lateral Pipe Movement Simulation	60
3.4	Summary of the Input Parameters Used in Finite Element Analyses of Partially Saturated RMS Graded Sand	72
3.5	Summary of $E_{70-H \text{ sat}}$ Used in Partially Saturated RMS Graded Sand Lateral Pipe Movement Simulation	73
4.1	Summary of the Input Parameters Used in Finite Element Analyses for Maximum Force and Pipe Depth	105
4.2	Summary of the Input Parameters Used in Finite Element Analyses for Various Pipe Diameters	113
4.3	Summary of the Input Parameters Used in Partially Saturated Sand Finite Element Analyses for Lateral Pipe Movement	116
5.1	Summary of the Input Parameters Used in Vertical Upward Pipe Movement Finite Element Analysis for CU Filter Sand	122

<u>Table No.</u>		<u>Page No.</u>
5.2	Summary of E_{70-VU} Used in Dry Vertical Upward Pipe Movement Simulations	133
5.3	Summary of E_{70-VU} for Vertical Upward Pipe Movement Simulations	140
6.1	Upper and Lower Bound $E_{\alpha-VD}$ for Select Case of Sand Density and H_c/D	157
7.1	Summary of Mobilized Soil Strength Fraction at Peak Pipe Force, α , and Various Pipe Movements	180

LIST OF ABBREVIATIONS

ASTM	American Society for Testing and Materials
BC	boundary condition
COV	coefficient of variation
CU	Cornell University
DS	direct shear
EX	experimental
FE	finite element
FEA	finite element analysis
FEM	finite element method
HDPE	high density polyethylene
Inf.	Infinite
MC	Mohr-Coulomb
MLR	multiple linear regression
NEES	George E. Brown, Jr. Network for Earthquake Engineering Simulation
OD	oblique downward
OU	oblique upward
PGD	permanent ground deformation
VD	vertical downward

LIST OF SYMBOLS

ARABIC SYMBOLS

A_s	area of side wall in contact with displaced soil
A_{tip}	area of the foundation tip
c	soil cohesion (y-intercept in plot of τ_p vs σ_N)
$c _0$	the initial cohesion yield stress
c_{ds}	c measured from DS test
c_{ps}	c in plane strain parameters
D	pipeline outside diameter
d	spatial distance measured from a “pole”
d_{50}	median grain size
d_H	horizontal displacement from direct shear test
d_{FE}	size of the element
d_v	vertical displacement of direct shear test
d_x	horizontal displacement of direct shear test
d_{xp}	horizontal displacements at yielding
d_{xy}	horizontal displacements at peak
d_{xf}	horizontal displacements at softening completion
DF_{L1}	dimensionless force at L_1
DD_{L1}	dimensionless displacement at L_1
DS	direct shear
E	Young’s modulus
E_α	strain compatible modulus
E_{70}	Equivalent Young’s modulus which was developed according to the K_{70} - procedure

E_{70-H}	Equivalent Young's modulus which was developed according to the K_{70} - procedure for horizontal pipe movement
E_{70-VU}	Equivalent Young's modulus which was developed according to the K_{70} - procedure for vertical upward pipe movement
$E_{CU \text{ medium}}$	Young's modulus of Cornell University filter medium sand
$E_{CU \text{ dense}}$	Young's modulus of Cornell University filter dense sand
E_i	initial tangent modulus
E_t	tangent modulus
E_{sat}	Young's modulus of partially saturated sand
E_{sec}	secant modulus
e	the eccentricity used in the smooth triple symmetric ellipse function
F	force
F'	lateral dimensionless force
F_C	strength in simple compression
F_f	resisting frictional force
F_{max}	maximum force
F_T	strength in simple tension
F_u	unknown function in the mapped ξ domain
G	the flow potential
H	height of soil sample in DS test
H_b	height of the shear band
H_{bt}	height from the pipe center to the interior box bottom
H_{bk}	closest distance from the center of the pipe to the test box wall
H_c	depth to center of pipeline
H_{mesh}	height of the mesh
i_u	ratio of N_q of lateral movement to N_q of vertical movement of pipe

I_1	the first invariants of the stress tensor
I_2	the second invariants of the stress tensor
I_3	the third invariants of the stress tensor
J_1	the first invariant of the stress deviator tensor
J_2	the second invariant of the stress deviator tensor
J_3	the third invariant of the stress deviator tensor
L_1	end of the initial linear range
K	a modulus number
K_0	initial horizontal stress ratio
K_1	spring constant
K_{L1}	slope of the force-displacement plot to the end of the linear range
L	length of the pipe
n	modulus exponent
N_i	shape function
N_q	maximum dimensionless force
N_q	bearing capacity factor
N_{q-e}	the maximum dimensionless lateral forces from the FE analyses for an experimental soil condition
N_{qH}	horizontal maximum dimensionless force
N_{q-m}	the maximum dimensionless lateral forces measured in the large-scale experiments
N_{qOD}	the maximum dimensionless oblique downward force
N_{qOD-s}	the maximum dimensionless oblique downward force given by simplified approach
N_{qOU}	the maximum dimensionless oblique upward force
N_{qOU-s}	the maximum dimensionless oblique upward force

	given by simplified approach
N_{q-si}	the maximum dimensionless lateral forces from the FE analyses for a semi-infinite soil medium
N_{qVD}	the maximum dimensionless vertical downward force
N_{qVU}	the maximum dimensionless vertical upward force
n	number of data points
P_a	atmospheric pressure
p	the equivalent pressure stress
Q_{L2}	applied load at the failure threshold
Q_{tc}	the maximum tip resistance
Q_{tc-c}	calculated maximum tip resistance
Q_{tc-d}	the maximum tip resistance from the FE analyses for deep foundation
Q_{tc-fea}	the peak forces from the FE analyses for vertical downward pipe movement
Q_{vd}	the peak vertical downward force exerted on a pipe
q	the Mises equivalent pressure stress
q	effective stress at H_c
q_{ult}	the maximum bearing capacity at the tip
$R_{mw}(\theta, e)$	the elliptic function used in ABAQUS model
R_f	failure ratio
r^2	coefficient of determination
$r(\theta, e)$	a smooth triple symmetric ellipse function in the deviatoric plane
S	stress level (percentage of failure stress)
s	the deviatoric stress
S_1, S_2, S_3	the principal values of the invariants of the stress deviator tensor
S_{ij}	the invariants of the stress deviator tensor

u_i	displacement component at point x_i
Y	lateral displacement of the pipe
Y'	lateral dimensionless displacement
Y'_f	lateral dimensionless displacement at maximum dimensionless force
Z	vertical upward displacement of the pipe
Z'	vertical upward dimensionless displacement
Z'_f	vertical upward dimensionless displacement at maximum dimensionless force

GREEK SYMBOLS

α_s	angle with respect to the horizontal of soil movement observed during the tests
α	an orientation of relative movement between pipe and soil with respect to horizontal direction
$d\mathcal{E}'_i$	the plastic strain increment
k	the yield stress in pure shear
γ^p	plastic shear strain
γ^p_f	plastic shear strain at which softening has been completed
γ^p_p	plastic shear strain at the peak
γ_d	soil dry unit weight
γ_{d-ds}	dry unit weight measured by density scoop
γ_{d-ng}	dry unit weight measured by nuclear gage
γ_{mesh}	shear strain calculated in the finite element mesh
γ_p	peak shear strain
γ_{total}	soil total unit weight

γ_y	yield shear strain
δ_{SI}	angle of interface shear resistance between the soil and sidewall
ε	the eccentricity that defines the rate at which the function approaches the asymptote
θ	the deviatoric polar angle
κ	modulus number
λ	ratio between γ_{mesh} and γ_b
μ	ratio of interface friction
ξ	mapped infinite element formulation
ξ_{qr}	rigidity factor
ξ_{qs}	shape factor
ξ_{qd}	depth factor
σ	stress
σ_3	the minor principal stress
σ'_N	normal stress
$\sigma'_{N \text{ Ref.}}$	reference normal stress
σ_{vc}	total vertical stress at the center of the pipe
σ'_{v0}	initial effective vertical stress in the soil
σ'_{vc}	effective vertical stress at the center of the pipe
τ	shear stress
ϕ_{crit}	critical state friction angle
ϕ_{ds}	direct shear friction angle
$\phi_{\text{ds-ld}}$	large displacement direct shear friction angle
$\phi_{\text{ds-p}}$	peak direct shear friction angle
$\phi_{\text{ps-p}}$	peak plane strain friction angle

Ψ_p	dilation angle
$(\Psi_p)_{p.sat}$	(Ψ_p) value for partially saturated RMS graded sand
$\Psi_{p/\sigma' N Ref.}$	Ψ_p value at the reference normal stress

SUFFIXES

'	superscript indicating effective stress parameters
-H	horizontal pipe movement
-OD	oblique downward pipe movement
-OU	oblique upward pipe movement
-VD	vertical downward pipe movement
-VU	vertical upward pipe movement
d	subscript indicating dry conditions
ds	subscript indicating direct shear stress parameters
ld	subscript indicating large displacement
p	subscript indicating value of a parameter at peak state in DS test
ps	subscript indicating plane strain stress parameters

CHAPTER 1

INTRODUCTION

1.1 Background

Research and engineering practice for the earthquake response of underground lifelines has focused on permanent and transient ground deformation (PGD and TGD) effects, with the recognition that PGD often causes the most serious local damage in buried lifeline networks (Hamada and O'Rourke, 1992; O'Rourke, 1998; O'Rourke, 2010). Permanent ground deformation effects not only apply to earthquakes, but also occur in response to floods, landslides, tunneling, deep excavations, and subsidence caused by dewatering or the withdrawal of minerals and fluids during mining and oil production. Such loading conditions are becoming increasingly more important as technologies are developed to cope with natural hazards, human threats, and construction in congested urban environments. Many previous studies (e.g. Trautmann and O'Rourke, 1983; ASCE Guidelines for the Seismic Design of Oil and Gas Pipeline Systems, 1984; O'Rourke, 1998; Pauline et al., 1998; Conte et al., 2002; Yargici, 2003; Anderson et al., 2004; Bird et al., 2004; Yeh et al. 2006; Giovanazi and Cubrinovski, 2007; O'Rourke and Bonneau, 2007; Ha et al., 2008; O'Rourke, M.J. et al., 2008 ; O'Rourke, T.D. et al., 2008; Ledezma and Bray, 2010, and Oliveira et al., 2010) have addressed PGD, including the effects of soil liquefaction, landslides, surface faulting, and tunneling and urban excavations on critical underground infrastructure.

Whereas simplified models for pipeline response to abrupt soil movement

(Kennedy et al., 1977; O'Rourke and Trautmann, 1981; O'Rourke and Liu, 1999; Netravali et al., 2000;) provide guidance for design, they have been replaced more generally in current practice by numerical simulations of the nonlinear and post-yield performance of pipelines (O'Rourke and Liu, 1999; Eiding et al., 2002; O'Rourke et al., 2008). For example, a hybrid model has been developed and successfully applied to model pipeline bends and elbows by representing the pipeline as a combination of beam and shell elements (Yoshishaki et al., 2001). Buckling and shell wrinkling modes of deformation have been incorporated directly in solid finite element simulations of pipeline response to earthquake-induced PGD (Tutuncu and O'Rourke, 2006; Mason et al., 2010). Both modeling methods have been validated through large-scale tests that simulate soil-structure interaction, which are essential for reliable model development and acceptance in practice (O'Rourke and Liu, 1999; O'Rourke, 2010).

Of key importance for more accurate models is the physical simulation of PGD effects on pipelines through large-scale testing. Such testing is essential to discover and refine 3-D mechanical behavior that has not been previously explored, validate complex numerical models, and characterize soil properties for accurate continuum modeling in the future. As pointed out by O'Rourke (2010), a significant trend in geotechnical engineering has been the implementation of large-scale testing facilities for soil-structure interaction, such as those at the Japanese National Research Institute for Earth Science and Disaster Prevention that have been used to characterize soil-pile interaction during liquefaction (Tokimatsu and Suzuki, 2004) and the large-scale split box experiments at the George E. Brown, Jr. Network for Earthquake Engineering Simulation (NEES) equipment site at Cornell University (e.g., Palmer et al., 2006; O'Rourke and Bonneau, 2007). The large-scale facilities allow for testing

in which field conditions can be simulated reliably under laboratory control.

Earthquake-induced PGD often involves large, irrecoverable soil distortion with geometric soil mass changes and large plastic pipeline deformation, involving both material and geometric nonlinearities (O'Rourke et al., 2004). Such behavior imposes significant demands on modeling. The current generation of modeling accounts for soil-pipeline interaction by means of force-displacement interactions in the lateral, vertical, and axial directions (ASCE, 1984; Honegger and Nyman, 2004; American Lifelines Alliance, 2005). This approach benefits from ease of application and its incorporation in available finite element (FE) codes (ASCE, 1984; ABAQUS, 2009), but suffers from the uncoupled representation of soil as a series of spring-slider reactions (Honegger and Nyman, 2004). Continuum models are now being developed for replicating soil-pipeline interaction in a realistic way (O'Rourke, 2010). Their development is critical for next generation capabilities to address the complexities of soil and pipe performance, consistent with full-scale experimental results (O'Rourke, 2010).

Of key importance in the response of underground lifelines to PGD is the adjacent soil reaction that develops as the pipe moves relative to the ground. As indicated by Trautmann and O'Rourke (1983), lateral, vertical, and oblique soil pressures associated with relative soil-pipe movement affect both the pipeline curvature and the normal stresses acting on the pipe to generate longitudinal friction. The soil reaction forces also affect pipeline ovaling. Large-scale tests on 400-mm-diameter high density polyethylene (HDPE) pipelines showed a 12% reduction of pipe diameter due to ovaling under abrupt ground movement (O'Rourke, 2010), indicating that loss of HDPE pipe cross-sectional area is likely to govern pipe failure for large

diameter-to-thickness ratios, D/t , under PGD effects.

Although industry guidelines provide procedures for characterizing the force-displacement relationships for vertical uplift, settlement, and lateral displacement of underground pipelines in soil (e.g., ASCE, 1983), a comprehensive means for characterizing the force-displacement relationship for relative pipe movement in any direction is not available. As already mentioned, continuum models are now being developed for modeling soil-pipeline interaction. Such models are able to account for the actual stresses and deformation in the soil, and thus provide the means of simulating underground pipeline behavior in a more reliable way than the one-dimensional finite element modeling with spring-slider elements that is often preformed in current practice (Nobahar et al., 2007; Xu et al., 2009)

The research described in this thesis was undertaken to improve the analysis of underground pipelines under the effects of PGD by simulating soil-pipeline interaction with continuum finite element models. The force-displacement relationship between soil and pipe under plane strain conditions is investigated with elasto-plastic constitutive laws and a Mohr-Coulomb (MC) yield criterion. The intention is to provide for the comprehensive characterization of force-displacement relationships associated with any size pipe at any depth in response to any orientation of relative movement between pipe and soil for both dry and partially saturated sands, ranging in density from medium to very dense. Moreover, the results of large-scale tests are used throughout to compare with numerical results to either validate the finite element models or generate improvements in the modeling process, resulting in more effective simulation techniques.

1.2 Research Objectives

The overall objective of this research is to simulate the force-displacement response of underground pipelines to relative soil displacement under plane strain conditions for dry and partially saturated sand. Various modeling procedures are developed for simulating soil-pipeline interaction under lateral and vertical relative movement between soil and pipe, as well as relative movement at oblique angles with respect to the pipeline. The ultimate goal of simulating soil-pipe interaction is to provide guidelines for characterizing the force-displacement response of underground pipe for any angle of soil movement with respect to the pipe.

To accomplish the overall goals, the research was conducted in several discrete stages, each with its own objectives and work plan, as discussed briefly under the subheadings that follow.

1.2.1. Plasticity and Strain Softening Model

For analytical purposes, an elasto-plastic constitutive model is used to represent soil behavior, for which the Mohr-Coulomb (MC) criterion defines the yield surface, with a softening relationship to simulate the post peak response of the soil. The theoretical background for the constitutive model and post peak stress-deformation relationships are described herein. The equations governing the MC criterion are presented, which involve a smooth triple symmetric ellipse for flow rule characterization. The softening model proposed by Anastasopoulos, et al. (2007) is used in this work. The model involves an equation to account for scale effects, which are evaluated by comparing force vs. displacement relationships for horizontal

movement of a pipe in soil using finite element meshes of different sizes.

1.2.2. Comparison of Finite Element and Experimental Results for Lateral Pipe Movement

To validate and qualify the soil-structure interaction modeling, full-scale laboratory test results are compared with the results of numerical simulations. Comparison of numerical and experimental results are made for the lateral force-displacement behavior of pipelines in dry and partially saturated sand with different unit weights under plane strain conditions. Because many experimental results are available for lateral pipe movement, this mode of deformation allows for a detailed assessment of the numerical modeling methods, including refinements to represent elastic as well as post-peak soil performance, under relatively large pipe displacements.

1.2.3. Expansion of Lateral Soil-Pipe Interaction Model

The modeling process is expanded to account for lateral soil-pipeline interaction within a semi-infinite soil medium. This modeling refinement allows for better simulation of pipeline performance in the field. The numerical modeling is performed with infinite elements that are attached within the finite element mesh to the boundaries of the regular elements. Peak forces and force-displacement relationships are compared for the experimental and infinite element simulations. In addition, the relationship between peak lateral force and pipe depth is investigated by plotting the numerical results in terms of dimensionless lateral force vs. dimensionless depth. It is shown that the dimensionless lateral force attains a maximum value at critical depth to pipe diameter ratio (H_c/D) of about 20 for both dry and partially

saturated sand at various sand densities.

1.2.4. Comparison of Finite Element and Experimental Results for Vertical Upward Pipe Movement

The soil and soil-structure interaction predicted by numerical models are compared with full-scale laboratory test results to validate the models for vertical upward pipe displacement in dry sand with different unit weights under plane strain conditions. Inconsistencies exist between the numerical and experimental results at shallow depth because the continuum elements cannot deform adequately into the void beneath the upward moving pipe. A modified simulation method is developed by which the finite element mesh is adjusted to remain level during upward pipe movement, thus accounting for the effects of soil movement from top to bottom of the pipe. Favorable agreements between numerical and experimental results are shown for this modified procedure. The relationship between peak upward force and pipe depth is evaluated for which the maximum dimensionless force occurs at H_c/D at approximately 30, which is similar to the H_c/D at maximum force for lateral movement.

1.2.5. Simulations of Vertical Downward Pipe Movement

The numerical model is modified to account for vertical downward soil-pipeline interaction within a semi-infinite soil medium. Because there are no large-scale experimental results for downward pipe movement, the numerical modeling procedures are evaluated with respect to full-scale field measurements of pile and drilled shaft load vs. settlement behavior. Downward movements of both pipe and

deep foundations in medium to very dense sand result in a strain hardening type behavior with a gradual increase in vertical load at high levels of settlement. Methods recommended for the interpretation of pile and drilled shaft load tests (Hirany and Kulhawy, 1998, 1989, 2002) are used to identify maximum elastic and failure threshold levels of load and settlement. The relationship between the vertical load levels so defined and pipe depth is investigated. The upper bound vertical load for downward pipe movement is shown to be lower by approximately 30 – 40 % of the bearing capacity load associated with deep foundation bearing surfaces for the same dimensions and soil conditions.

1.2.6. Simulations of Oblique Pipe Movement and Guidelines for Practice

To develop a comprehensive basis for evaluating force-displacement relationships for underground pipelines, the modeling process is expanded to account for oblique movement of the pipe. Numerical simulations are performed for pipe displacement, with both upward and downward movement components, at an angle of 45° with respect to the horizontal. With these additional simulations, maximum load and force-displacement relationships for lateral, vertical upward, vertical downward, and 45° oblique orientations are combined to produce guidance for modeling pipeline-soil interaction at any orientation for plane strain conditions. The analytical results are normalized with respect to maximum lateral force, and the normalized maximum forces are provided on 360° plots that can be used to predict maximum pipe loads for medium to very dense dry and partially saturated sand at various H_c/D . Guidance is also provided for choosing the appropriate elastic modulus for elasto-plastic modeling at any orientation, and for direct estimation of the force-displacement relationship at any depth and orientation for one-dimensional modeling of soil-pipeline interaction.

1.3 Scope and Organization

This thesis consists of eight chapters, the first of which provides introductory and background information, explains the research objectives, and describes the scope of the work. The second chapter provides the theoretical background for the elasto-plastic soil model used in the simulation of plane strain soil-pipeline interaction, including a description of the MC criterion, flow rule, and strain softening methodology. Chapter 3 compares finite element simulation results with the large-scale measurements of soil-pipeline lateral force vs. displacement relationships. This chapter also describes the methodology for obtaining Young's modulus from large-scale experiments for use in the elasto-plastic model. Chapter 4 provides a description of how the modeling process is expanded to evaluate lateral force-displacement relationships within a semi-infinite soil medium, and to investigate and characterize the maximum lateral force as a function of pipe depth. Chapter 5 covers the modeling of the vertical upward force-displacement behavior of buried pipe, and compares numerical and experimental results. Finite element results are presented for a semi-infinite soil medium to show maximum upward reaction force as a function of pipe depth. Chapter 6 addresses the modeling of the vertical downward force-displacement behavior of buried pipe, and compares the maximum reaction forces for downward pipe movement with the forces predicted by conventional bearing capacity formulations for deep foundations with the same bearing dimensions and soil properties. Chapter 7 presents the numerical results for force-displacement relationships of pipe subject to oblique relative displacement. The analytical results from simulations of lateral, vertical upward and downward, and oblique pipe movement for semi-infinite, plane strain soil conditions are summarized in dimensionless form. They are plotted in 360° diagrams from which the maximum

force can be estimated for any size pipe at any depth in response to any orientation of relative movement between pipe and soil for both dry and partially saturated sands, ranging in density from medium to very dense. Chapter 8 presents the conclusions, guidelines for practice, and recommendations for future research.

CHAPTER 2

MOHR-COULOMB PLASTICITY, FLOW RULE, AND SOFTENING BEHAVIOR

2.1 Introduction

Finite element analyses (FEA) with the software package ABAQUS 6.9 (2009) were performed to predict the pipe forces associated with relative soil movement and to compare the analytical peak forces with experimental results. Eight-node biquadratic plane strain quadrilateral reduced integration elements (element type CPE8R) were used to represent the soil. The elastic part of the soil behavior was assumed to be linear isotropic, and the plastic part of the soil behavior was modeled with the Mohr-Coulomb (MC) criterion. The MC yield criterion has been widely used for many geotechnical applications, and still plays major role in geotechnical studies and design calculations (Schweiger, 1994; Abbo and Sloan, 1995; Schweiger, 2008).

The softening model proposed by Anastasopoulos, et al. (2007) is used to represent the softening behavior of the soil. A FORTRAN subroutine was used ABAQUS 6.9 (2009) to apply the proposed softening model. In this chapter, the theoretical background of the MC yield criterion, flow rule associated with MC yield criterion, and the softening subroutine are described under the subheadings that follow.

2.2 Mohr-Coulomb Yield Criterion

The simulation of soil-pipeline interaction depends on the plasticity model for predicting the maximum stress state and peak load, mobilized in the soil. Many constitutive models (e.g., MC, Drucker-Prager, Modified Drucker-Prager/Cap, Cam-Clay) have been proposed to obtain a better representation of soil behavior. The choice of constitutive model depends on the type of analysis, material characteristics, and available experimental data. Due to its simplicity, an elasto-plastic representation of the soil in combination with an MC yield surface is frequently applied for soil-structure interaction analyses (e.g., Horn et al., 1994; Smith and Su, 1997; Bernat and Cambou, 1998; Mroueh and Shahrour, 1999; Ellis and Springman, 2001; Hu and Pu, 2003; Sun et al., 2006; Li et al., 2009), and many researchers have used the MC criterion to investigate soil stress and deformation under yield conditions (e.g. Massoudi and Mehrabadi, 2000; Chen and Martin, 2002; Mroueh and Shabrouh, 2003; Rha and Taciroglu, 2007; Wu and Thomson, 2007; Alsaleh and Shahrour, 2009; Pimentel, et al., 2009). Programs, such as ABAQUS (2009), are equipped with subroutines that can be applied directly for MC characterization.

The Mohr criterion was developed in early 1900, and can be considered as generalized version of the Tresca criterion (Chen and Han, 1987). The basic assumption of the Tresca and Mohr criteria is that the maximum shear stress controls failure. The difference between the two criteria is that the critical value of the shear stress at yield is constant for the Tresca criterion, whereas for the Mohr criterion, the shear stress, τ , is a function of the normal stress, σ_N , on the plane corresponding to the point of tangency between the Mohr circle of stress and the yield surface. This relationship can be represented as

$$|\tau| = f(\sigma) \quad (2.1)$$

where $f(\sigma)$ is a function that is determined by testing.

Figure 2.1 illustrates the Mohr yield criterion and physical representation of Eqn. 2.1. Equation 2.1 indicates that yield will occur if the radius of the largest Mohr circle is tangent to the failure envelope curve, $f(\sigma)$.

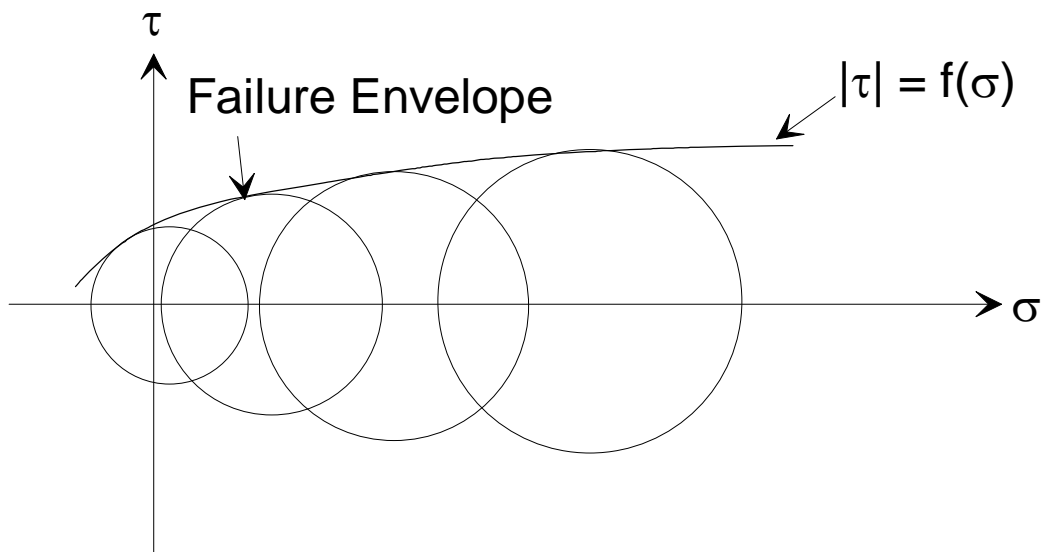


Figure 2.1 Concept of Mohr Criterion

An illustration of the simplest form of the Mohr failure envelope is shown in Fig. 2.2, wherein, the Mohr failure envelope is a straight line, known as Coulomb's equation, which is expressed as

$$|\tau| = c + \sigma \tan \phi \quad (2.2)$$

in which c is cohesion and ϕ is the friction angle of the material. Both c and ϕ are material constants and can be determined by experiment.

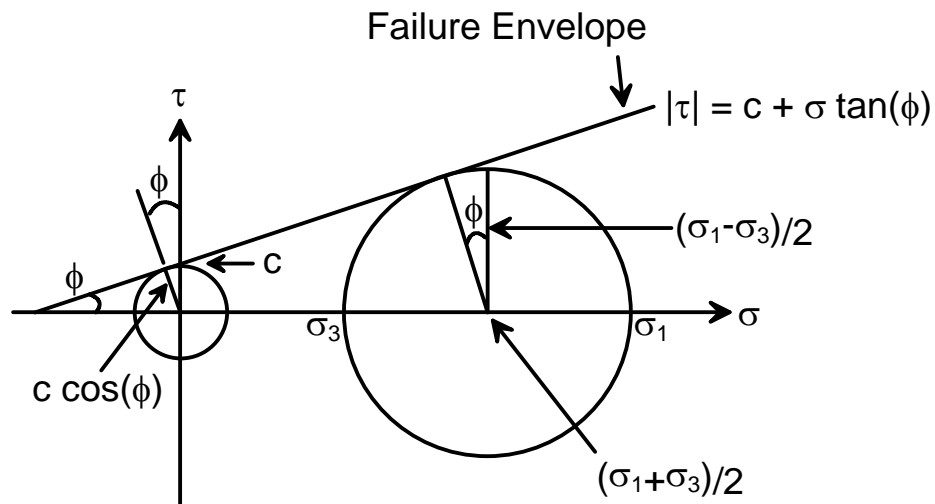


Figure 2.2 Simplest Form of the Mohr Failure Envelope

The Mohr yield criterion associated with Coulomb's equation is referred to as the MC criterion. In the case of non-frictional material ($\phi = 0$), cohesion equals the yield stress in pure shear, k , and Eqn. 2.2 becomes

$$|\tau| = k \quad (2.3)$$

which is known as the maximum-shear-stress criterion of Tresca.

With reference to Fig. 2.2, let σ_1 = major principal stress and σ_3 = minor principal stress ($\sigma_1 \geq \sigma_3$), then Eqn. 2.2 becomes

$$\frac{\sigma_1 - \sigma_3}{2} \cos \phi = c + \left(\frac{\sigma_1 + \sigma_3}{2} - \frac{\sigma_1 - \sigma_3}{2} \sin \phi \right) \tan \phi \quad (2.4)$$

and can be rewritten as

$$\sigma_1 \frac{1 - \sin \phi}{2c \cos \phi} - \sigma_3 \frac{1 + \sin \phi}{2c \cos \phi} = 1 \quad (2.5)$$

If we let

$$F_T = \frac{2c \cos \phi}{1 - \sin \phi} \quad (2.6)$$

and

$$F_C = \frac{2c \cos \phi}{1 + \sin \phi} \quad (2.7)$$

Eqn. 2.5 can be simplified as

$$\frac{\sigma_1}{F_T} - \frac{\sigma_3}{F_C} = 1 \quad (2.8)$$

where F_T is the strength in simple tension and F_C is the strength in simple compression.

Chen and Han (1987) introduced a parameter m , where

$$m = \frac{F_C}{F_T} = \frac{1 - \sin \phi}{1 + \sin \phi} \quad (2.9)$$

with which Eqn. 2.8 can be written in slope-intercept form as

$$m\sigma_1 - \sigma_3 = F_c \tag{2.10}$$

Figure 2.3 shows the failure loci for the MC criterion using Eq. 2.10 in the $\sigma_3 = 0$ plane. In the figure, σ_2 lies between σ_1 and σ_3 so that $\sigma_1 \geq \sigma_2 \geq \sigma_3$ is satisfied. When $\phi = 0$ ($m = 1$), the shape of failure locus is similar to the Tresca hexagon and the shape becomes an irregular hexagon as ϕ increases (m decreases).

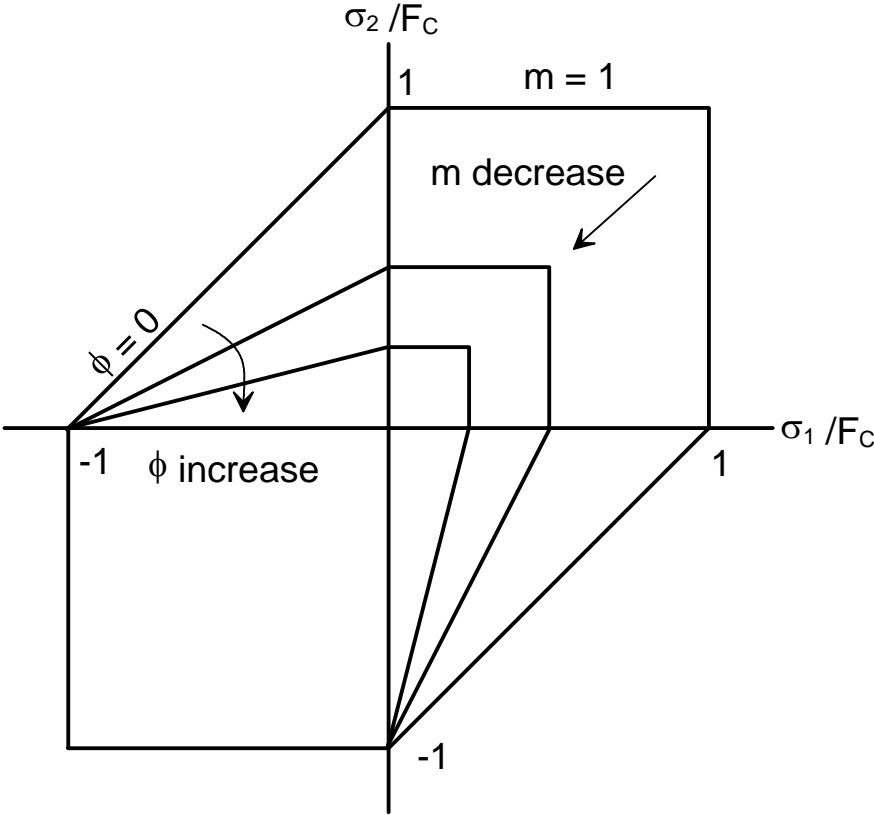


Figure 2.3 The Failure Loci for the Mohr-Coulomb Criterion in $\sigma_3 = 0$ Plane
(After Chen and Han, 1987)

For three-dimensional (3D) conditions, Eqn. 2.5 takes the form

$$f(I_1, J_2, \theta) = \frac{1}{3} I_1 \sin \phi + \sqrt{J_2} \sin\left(\theta + \frac{\pi}{3}\right) + \frac{\sqrt{J_2}}{\sqrt{3}} \cos\left(\theta + \frac{\pi}{3}\right) \sin \phi - c \cos \phi = 0 \quad (2.11)$$

where I_1 , I_2 , and I_3 are the invariants of the stress tensor, defined as

$$\begin{aligned} I_1 &= \sigma_{11} + \sigma_{22} + \sigma_{33} \\ I_2 &= \begin{vmatrix} \sigma_{22} & \sigma_{23} \\ \sigma_{32} & \sigma_{33} \end{vmatrix} + \begin{vmatrix} \sigma_{11} & \sigma_{13} \\ \sigma_{31} & \sigma_{33} \end{vmatrix} + \begin{vmatrix} \sigma_{11} & \sigma_{12} \\ \sigma_{21} & \sigma_{22} \end{vmatrix} \\ I_3 &= \begin{vmatrix} \sigma_{11} & \sigma_{12} & \sigma_{13} \\ \sigma_{21} & \sigma_{22} & \sigma_{23} \\ \sigma_{31} & \sigma_{32} & \sigma_{33} \end{vmatrix} \end{aligned} \quad (2.12)$$

and J_1 , J_2 , and J_3 are the second invariants of the stress deviator tensor defined as

$$\begin{aligned} J_1 &= 0 \\ J_2 &= \frac{1}{3} (I_1^2 - 3I_2) \\ J_3 &= \frac{1}{27} (2I_1^3 - 9I_1I_2 + 27I_3) \end{aligned} \quad (2.13)$$

The angle, θ , is shown in Fig. 2.4 and defined as

$$\cos \theta = \frac{\sqrt{3}}{2} \frac{s_1}{\sqrt{J_2}} \quad (2.14)$$

and s_1, s_2 , and s_3 are the principal values of the invariants of the stress deviator tensor S_{ij} .

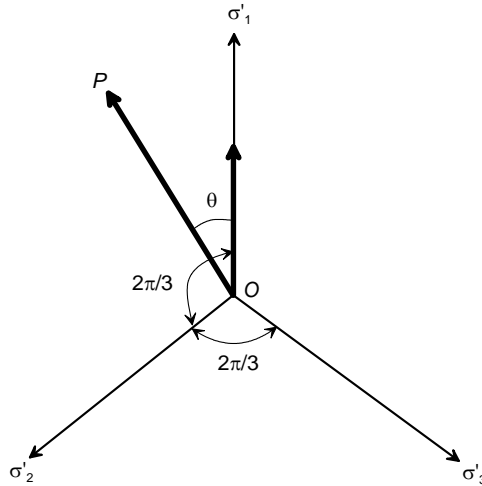


Figure 2.4 Angle, θ , Defined in Deviatoric Plane (After Chen and Han, 1987)

In the Fig. 2.4, the σ'_1, σ'_2 , and σ'_3 axes are the projections of the σ_1, σ_2 , and σ_3 axes on the deviatoric plane. OP is the projection of vector OP on the same plane, and P is an arbitrary state of stress at a given point with stress components σ_1, σ_2 , and σ_3 . Equation 2.11 can be rewritten in Haigh-Westergaard stress space as

$$f(\xi, \rho, \theta) = \sqrt{2}\xi \sin \phi + \sqrt{3} \sin\left(\theta + \frac{\pi}{3}\right) + \rho \cos\left(\theta + \frac{\pi}{3}\right) \sin \phi - \sqrt{6}c \cos \phi = 0 \quad (2.15)$$

in which ξ, ρ , and θ are the Haigh-Westergaard coordinates, defined as

$$\begin{aligned}
\xi &= \frac{\sigma_1 + \sigma_2 + \sigma_3}{\sqrt{3}} \\
\rho &= \sqrt{2J_2} \\
\cos \theta &= \frac{\sqrt{3}}{2} \frac{s_1}{\sqrt{J_2}}
\end{aligned}
\tag{2.16}$$

Equations 2.11 and 2.15 are satisfied only if $\sigma_1 \geq \sigma_2 \geq \sigma_3$ and $\frac{\pi}{3} \geq \theta \geq 0$.

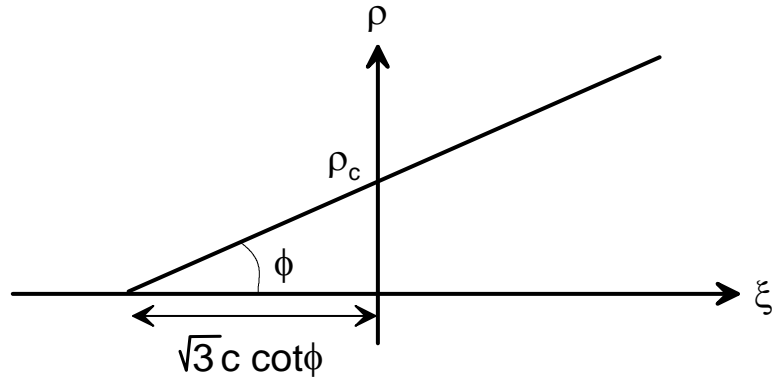


Figure 2.5 Mohr-Coulomb Criterion in Meridian Plane $\theta = 0^\circ$

(After Chen and Han, 1987)

Figure 2.5 shows the MC criterion in the meridian plane with $\theta = 0^\circ$. In the figure, compression is positive. If we use Eqn. 2.6, ρ_c can be expressed on the π plane as

$$\rho_c = \frac{2\sqrt{6}c \cos \phi}{3 - \sin \phi} = \frac{\sqrt{6}F_T(1 - \sin \phi)}{3 - \sin \phi}
\tag{2.17}$$

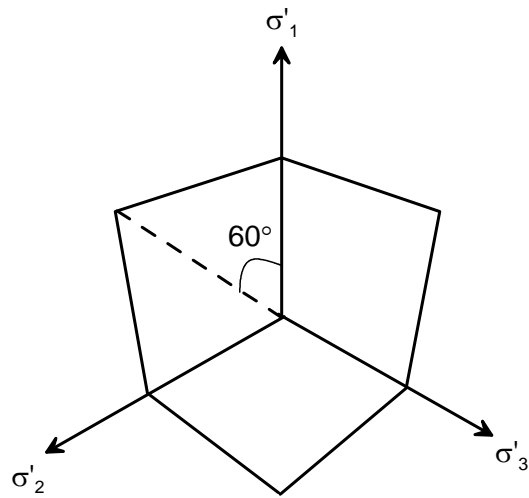


Figure 2.6 Mohr-Coulomb Criterion in Deviatoric Plane

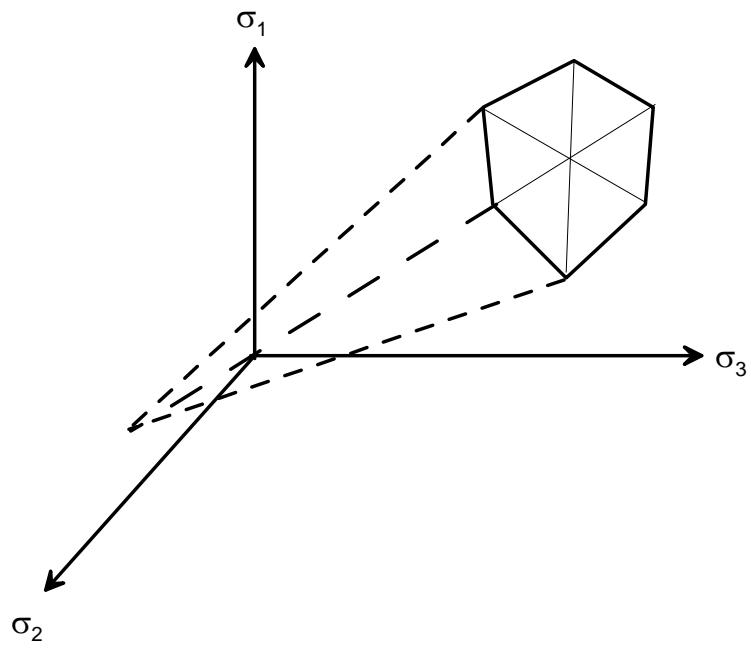


Figure 2.7 Mohr-Coulomb Criterion in Principal Stress Plane

Figure 2.6 and 2.7 show the MC criterion in the deviatoric, and principal stress plane, respectively. The irregular hexagon shown in Fig. 2.7 is formed at intersection of the $\sigma_3 = 0$ plane, as shown in Fig. 2.3. Since the MC criterion

possesses the shape of an irregular hexagon, it has vertices in the deviatoric plane, as shown in Fig. 2.6. Therefore, the model may be calibrated and extended. The constitutive model, which is used in numerical simulations for the current study is an elasto-plastic model. The elasto-plastic model has a yield function that includes isotropic cohesion hardening, softening, and has the MC form. The model also uses a flow potential G , which is a hyperbolic function in the meridian plane and a smooth elliptic function in the deviatoric plane (ABAQUS, 2009). Thus, the flow potential has no corners in the deviatoric plane. A detailed description of flow potential is discussed in the next section.

2.3 Flow Rule Associated with the Model

The flow rule is used to investigate the plastic strain increment, $d\varepsilon^p_i$, and is reviewed in this section. As explained in the previous section, the flow potential must be continuous in the deviatoric plane to provide a unique direction of plastic flow. Klisinski and Mroz (1988) and Menetrey and Willam (1995) proposed a smooth triple symmetric ellipse function, $r(\theta, e)$, based on the five-parameter model by Willam and Warnke (1974), which is expressed as

$$r(\theta, e) = \frac{4(1 - e^2)\cos^2 \theta + (2e - 1)^2}{2(1 - e^2)\cos \theta + (2e - 1)[4(1 - e^2)\cos^2 \theta + 5e^2 - 4e]^{0.5}} \quad (2.18)$$

The deviatoric eccentricity e describes the out-of-roundness of the deviatoric trace in terms of the ratio between the shear stress along the extension and compression meridian (Menetrey and Willam, 1995; ABAQUS, 2009). Along the θ

= 0 (extension meridians) and the $\theta = \frac{\pi}{3}$ (compression meridians), $r(\theta, e)$ has the following values:

$$\begin{aligned} r(\theta = 0, e) &= \frac{1}{e} \\ r\left(\theta = \frac{\pi}{3}, e\right) &= 1 \end{aligned} \tag{2.19}$$

Although $r(\theta, e)$ is defined between $\theta = 0$ and $\theta = \frac{\pi}{3}$, it can be extended to all directions ($2\pi \geq \theta \geq 0$) using the triple symmetry shown in Fig. 2.8.

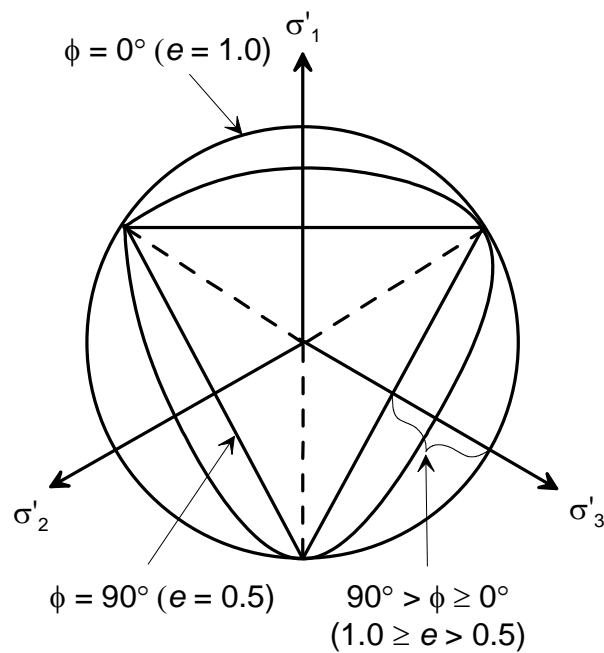


Figure 2.8 The Smooth Triple Symmetric Ellipse Function
(Menetrey and Willam, 1995)

The eccentricity is usually determined by Eqn. 2.20 such that the extension and the compression meridians exactly match.

$$e = \frac{3 - \sin \phi}{3 + \sin \phi} \quad (2.20)$$

Convexity and smoothness of the elliptic function does not hold when $\phi = 90^\circ$ ($e = 0.5$). The upper limit, $\phi = 0^\circ$ ($e = 1.0$) leads to $r(\theta, 1) = 1$, which represent a circle in Fig. 2.8, and the lower limit, $\phi = 90^\circ$ ($e = 0.5$) leads to $r(\theta, 0.5) = 2\cos\theta$, which represents a triangle in Fig. 2.8. The triangle shape violates the smoothness and the uniqueness of the gradients at the corners. To avoid the corners, ϕ must be defined between $90^\circ > \phi \geq 0^\circ$ ($1.0 \geq e > 0.5$).

The finite element analysis used in this study has the flow potential, G , and the form of a smooth triple symmetric ellipse function in the deviatoric plane given by Eqn. 2.18. In the meridional plane, G has the form of hyperbolic function, which is expressed as

$$G = \sqrt{[\varepsilon(c|_0)\tan\psi]^2 + (R_{mw}q)^2} - p \tan\psi \quad (2.21)$$

in which p is the equivalent pressure expressed as

$$p = -\frac{I_1}{3} \quad (2.22)$$

q is the von Mises equivalent stress expressed as

$$q = \sqrt{\frac{9}{2}(S_{ij}S_{ji})} \quad (2.23)$$

S is the deviatoric stress expressed as

$$S_{ij} = \sigma_{ij} + p\delta_{ij} \quad (2.24)$$

and $R_{mw}(\theta, e)$, is the elliptic function, expressed as

$$R_{mw}(\theta, e) = r(\theta, e) \frac{3 - \sin \phi}{6 \cos \phi} \quad (2.25)$$

In Eqn. 2.21, ψ is the dilation angle, $c|_0$ is the initial cohesion yield stress, and ε is the eccentricity that defines the rate at which the function approaches the asymptote.

Figure 2.9 shows a family of flow potentials chosen as a hyperbolic function in a meridional plane are used in ABAQUS. As mentioned above, G is continuous and smooth in both meridional and deviatoric planes, and thus, the flow direction is defined uniquely in those planes. The elliptic function, $R_{mw}(\theta, e)$, ensures that the flow potential matches the yield surface for triaxial compression and extension in the deviatoric plane.

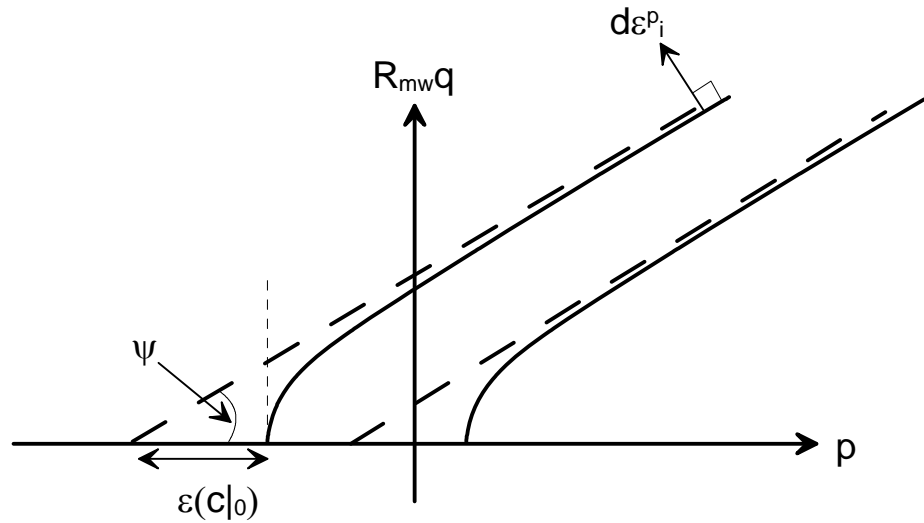


Figure 2.9 Flow Potential Used in ABAQUS (ABAQUS, 2009)

2.4 Strain Softening Behavior in the Model

Walters and Thomas (1982) performed experiments similar to those performed earlier by Horsefield (1977) to develop reverse fault rupture through cohesionless soil. These experiments were performed in a box with dimensions 100 cm x 10 cm x 10 cm in which upward displacement was generated by a rigid motor drive block. They showed that the ground rupture observed in the experiment could be replicated with FE analyses using a nonlinear incremental constitutive model, with a non-associated flow rule and strain softening behavior. This study showed that the experimental results could only be reproduced by a non-associated flow rule and strain softening behavior. Bray (1990) and Bray et al. (1994a, b) report on the use of numerical models, using an elasto-plastic constitutive model with MC yield criteria and strain softening behavior to develop recommendations to minimize the potentially adverse effects of earthquake fault rupture on dam stability and integrity. Potts et al. (1990, 1997) also used similar constitutive laws with strain softening behavior to model the failure of embankment dams.

To incorporate the strain softening behavior in the numerical analysis in this work, the model proposed by Anastasopoulos, et al. (2007) was used to diminish linearly the peak plane strain friction angle ϕ'_{ps-p} to a residual value at the critical state friction angle ϕ'_{crit} from the plastic strain at ϕ'_{ps-p} to the plastic strain at ϕ_{crit} . Similarly, the dilation angle ψ_p is diminished linearly to a residual value of 0 from the plastic strain at ϕ'_{ps-p} to the plastic strain at ϕ_{crit} . The reduction of ϕ'_{ps-p} and ψ_p are illustrated in Fig. 2.10. Equation for the strain dependent reduction of ϕ'_{ps-p} and ψ_p are given as

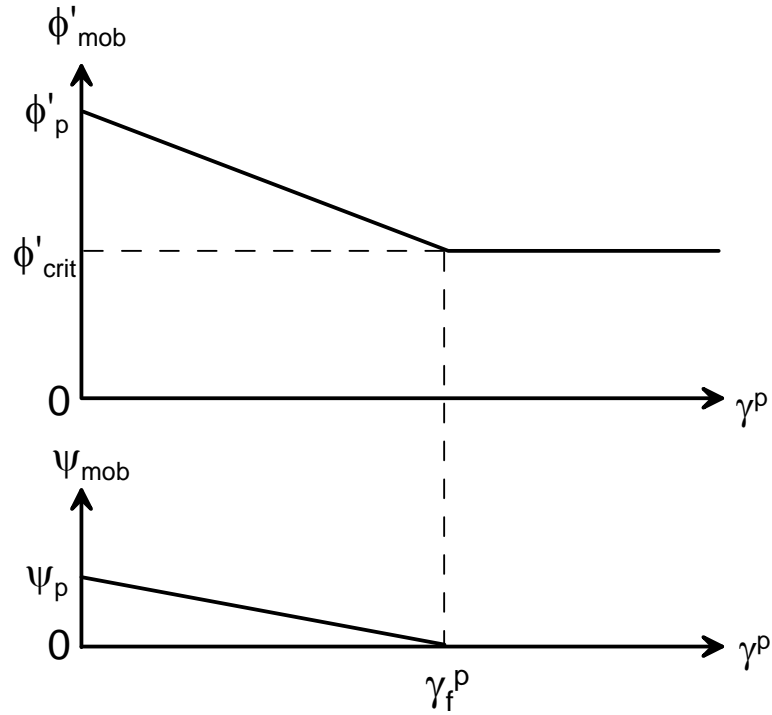


Figure 2.10 Variation of Friction Angle and Dilation Angle (Anastasopoulos, 2007)

$$\phi'_{mob} = \left[\phi'_{ps-p} - \left(\frac{\phi'_{ps-p} - \phi'_{crit}}{\gamma_f^p} \right) \gamma^p \right] \quad (\gamma_f^p \geq \gamma^p \geq 0) \quad (2.26)$$

$$\phi'_{mob} = \phi'_{crit} \quad (\gamma^p \geq \gamma_f^p)$$

$$\begin{aligned} \psi_{mob} &= \left[\psi_p - \frac{\psi_p}{\gamma_f^p} \gamma^p \right] & (\gamma_f^p \geq \gamma^p \geq 0) \\ \psi_{mob} &= 0 & (\gamma^p \geq \gamma_f^p) \end{aligned} \quad (2.27)$$

in which γ^p is plastic shear strain and γ_f^p is the plastic shear strain at which softening has been completed.

Figure 2.11 shows the ratio of shear to vertical stress, τ'/σ'_v , vs. horizontal displacement, d_x , as well as vertical displacement, d_v , vs. d_x from a direct shear (DS) test on Toyoura sand reported by Shibuya et al. (1997). Four distinct phases of soil behavior are identified: 1) quasielastic, 2) plastic, 3) softening, and 4) residual behavior. Jewell and Roth (1987) performed many DS tests and reported quasielastic soil behavior between points O and A, after which plastic behavior occurs. The displacement, d_{x-y} , corresponding to point A, is defined where d_v/d_x is minimum. The displacement, d_{x-p} , is defined at the maximum τ'/σ'_v . After the peak τ'/σ'_v , the soil shows softening behavior and develops a single horizontal shear band at the middle of the specimen (e.g., Jewell and Roth, 1987; Gerolymos et al., 2007). The softening behavior continues until d_v/d_x becomes approximately 0 at displacement, d_{x-f} . Although stress and strain may vary along the DS plane due to progressive failure (Terzaghi and Peck, 1948; Morgenstern and Tchalenko, 1967; Saada and Townsend, 1981; Budhu, 1984), a number of studies (e.g., Potts et al., 1987; Anastasopoulos, et al., 2007) show that progressive failure for the DS test is insignificant, allowing the interpretation of test results as simple shear (Anastasopoulos, et al., 2007).

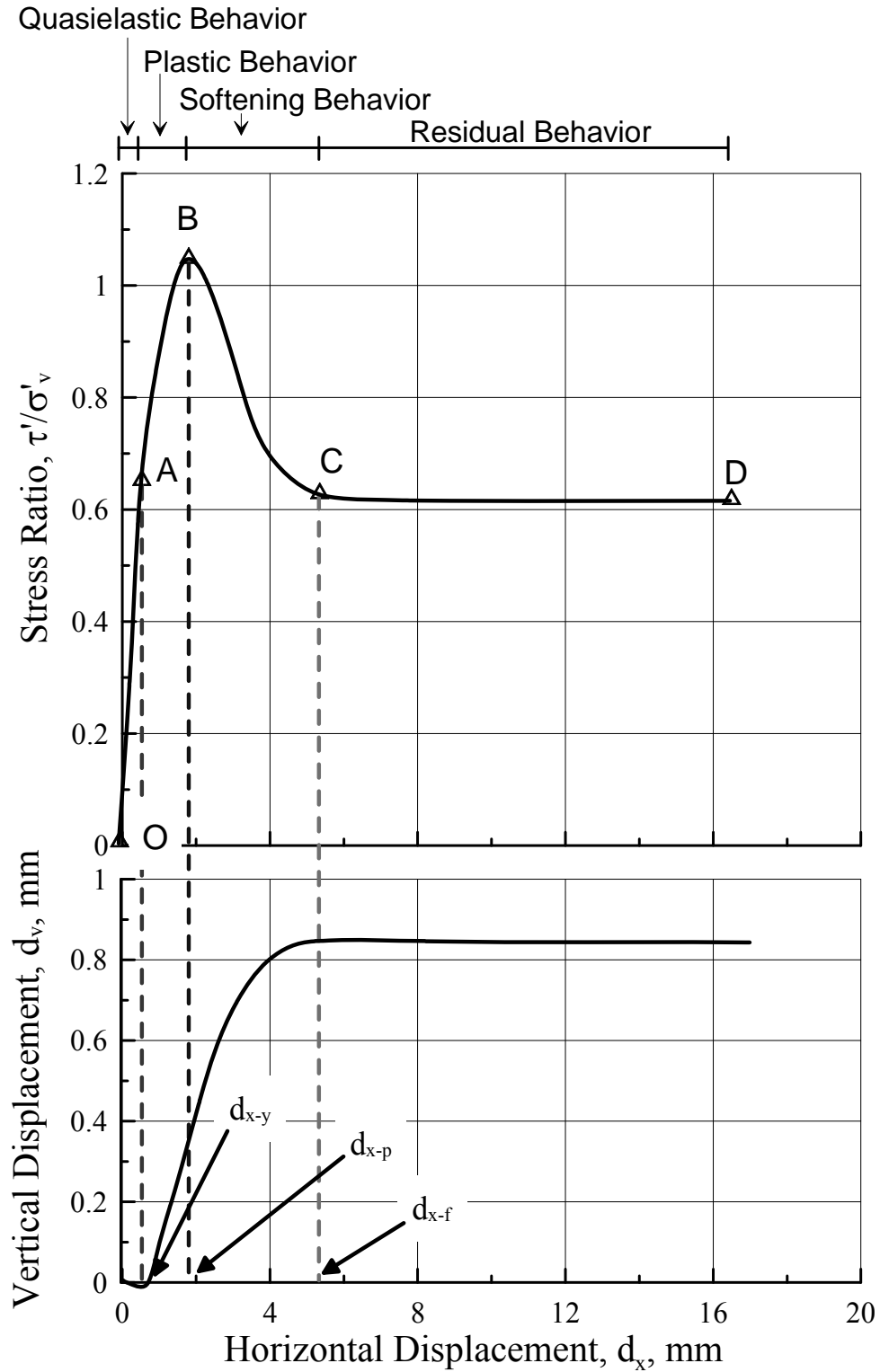


Figure 2.11 Typical Stress Ratio vs. Horizontal Displacement, and Vertical Displacement vs. Horizontal Displacement Curve (After Shibuya et al., 1997)

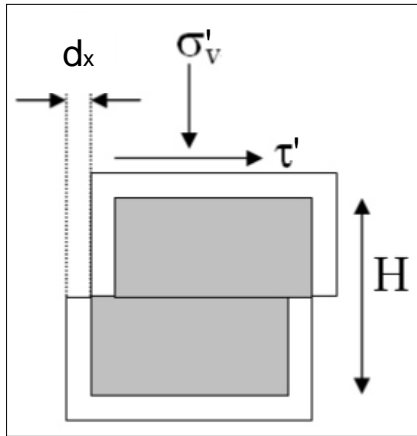


Figure 2.12 Typical Direct Shear Test Box

Figure 2.12 shows a schematic of the DS test. From the beginning of the test to the stage when the shear band is created, it is assumed that the shear strain is uniformly distributed throughout the test box. The yield shear strain, γ_y , is

$$\gamma_y = \frac{d_{x-y}}{H} \quad (2.28)$$

for which H is the height of soil sample in direct shear test, and d_{x-y} is shown in Fig. 2.11.

Similarly, the peak shear strain, γ_p , is

$$\gamma_p = \frac{d_{x-p}}{H} \quad (2.29)$$

for which d_{x-p} is shown in Fig. 2.11. Consequently, the plastic shear strain at γ_p^p can be expressed as

$$\gamma^p_p = \frac{d_{x-p} - d_{x-y}}{H} \quad (2.30)$$

After the peak, a shear band is formed and plastic shear deformation takes place within the shear band. The soil outside of the shear band is assumed to be in an elastic state (Shibuya, et al., 1997). The plastic shear strain at which full softening occurs, γ^p_f , can be expressed as

$$\gamma^p_f = \frac{d_{x-p} - d_{x-y}}{H} + \frac{d_{x-f} - d_{x-p}}{H_b} \quad (2.31)$$

where H_b is the height of the shear band. Several researchers (e.g., Roscoe, 1970; Vardoulakis and Graf, 1985; Muhlhaus and Vardoulakis, 1987; Bardet and Proubet, 1992; Huang, et al., 2002) reported H_b as $8 - 20 d_{50}$, where d_{50} is the median grain size.

The solutions from FE analyses associated with the strain softening process depend on the mesh size (Pietruszczak and Mroz, 1981; Arslan and Sture, 2008). The model proposed by Anastasopoulos, et al. (2007), provides a way to account for shear band formation through mesh size selection.

As shown in Fig. 2.13 a), the shear strain calculated in the finite element mesh, γ_{mesh} , can be expressed as

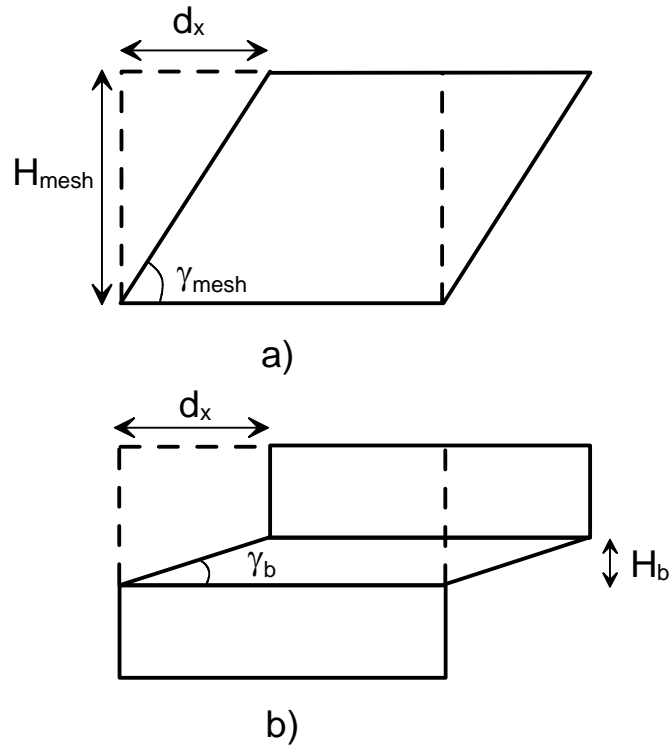


Figure 2.13 Simple Shear Shape for a) Finite Element Mesh and b) Along the Shear Band (After Anastasopoulos, et al., 2007)

$$\gamma_{\text{mesh}} = \frac{d_x}{H_{\text{mesh}}} \quad (2.32)$$

in which H_{mesh} is the height of the mesh that undergoes uniform shear deformation.

Equation 2.32 is valid until a shear band is formed. After the peak τ'/σ'_v , when the shear band forms, shear strain, γ_b , can be expressed as

$$\gamma_b = \frac{d_x}{H_b} \quad (2.33)$$

The ratio between γ_b and γ_{mesh} is defined as λ and can be expressed as

$$\lambda = \frac{\gamma_b}{\gamma_{mesh}} = \frac{d_x / H_b}{d_x / H_{mesh}} = \frac{H_{mesh}}{H_b} \quad (2.34)$$

Knowing that γ_y and γ_p are not influenced by scale effects, the γ_f^p compatible with the actual strain is obtained by dividing Eqn. 2.31 by λ .

$$\gamma_f^p = \frac{d_{x-p} - d_{x-y}}{H} + \frac{d_{x-f} - d_{x-p}}{H_b} \frac{H_b}{H_{mesh}} = \frac{d_{x-p} - d_{x-y}}{H} + \frac{d_{x-f} - d_{x-p}}{H_{mesh}} \quad (2.35)$$

Hence, γ_f^p depends on the size of the mesh where the shear band develops, H_{mesh} , and the width of the elements surrounding the pipe are chosen such that $H_{mesh} = H_b$. In this way, the mesh size is compatible with shear band formation, and shear distortion in the FE model is suitably accounted for, as indicated in Eqn. 2.35.

CHAPTER 3

COMPARISON OF FINITE ELEMENT AND EXPERIMENTAL RESULTS FOR LATERAL PIPE MOVEMENT

3.1 Introduction

A series of finite element (FE) analyses with ABAQUS 6.9 (2009) were performed to predict the peak force and to compare the measured peak forces with experimental results. Comparing the results of numerical simulations and actual experiments is necessary to validate the numerical model. The experimental database used for the comparisons is derived from full-scale, 2-D tests on pipe buried in dry and partially saturated sand. The experimental results were obtained at the Cornell University Large Scale Lifelines Testing Facility, which is part of the George E. Brown, Jr. Network for Earthquake Engineering Simulation (NEES) supported by the National Science Foundation (NSF), and with testing equipment that predated NEES. The full-scale tests and test results for dry sand are described by Trautmann and O'Rourke (1983), Trautmann (1983), Turner (2004), and Olson (2009), and the testing and test results for partially saturated sand are described by Olson (2009) and O'Rourke (2010). In this chapter, the procedures for estimating Young's modulus from the large-scale experimental data, peak lateral force from direct shear (DS) laboratory test data, and post peak softening characteristics from the DS data are described.

3.2 Pipe Force vs. Displacement Relationship

To facilitate the comparison of experimental and analytical results, both the measurements and numerical output are converted to dimensionless form. The dimensionless format also facilitates the application of the results to a variety of pipe diameter and depth conditions of practical interest. Figure 3.1 shows a typical dimensionless pipe force vs. displacement curve. Shown on the vertical axis is the

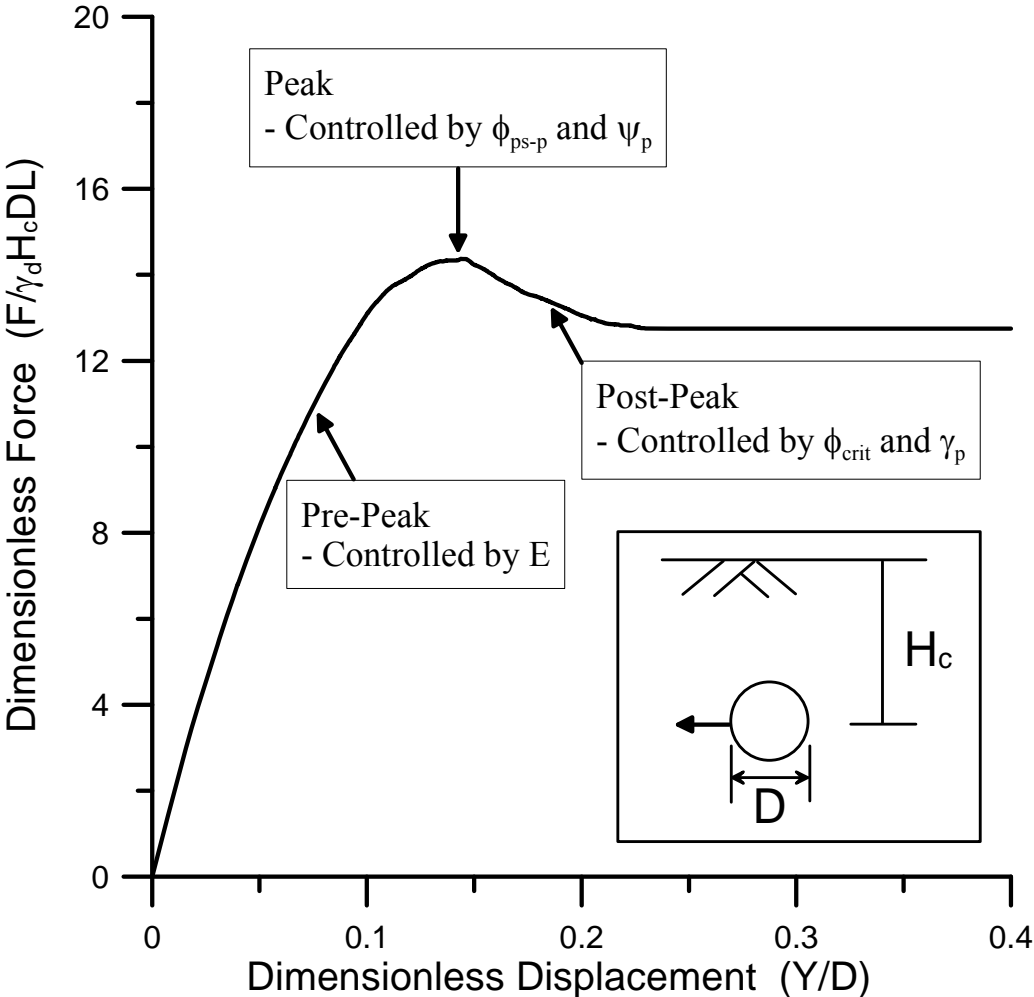


Figure 3.1 Typical Dimensionless Force-Displacement Curve for Lateral Pipe Movement

lateral force imposed on the pipe by relative lateral displacement in sand, which is expressed as $F' = F / (\gamma_d H_c D L)$, in which F is the measured lateral pipe force, γ_d is the dry unit weight of the sand, H_c is the depth from the top of the soil to the center of the pipe, D is the external diameter of the pipe, and L is the length of the pipe involved in the test. The horizontal axis is the dimensionless pipe displacement expressed as $Y' = Y/D$, in which Y is the measured lateral pipe movement.

As shown in Figure 3.1, the dimensionless force-displacement curve can be characterized by three major parts. The pre-peak, observed from the beginning of the curve to the peak force, is controlled by Young's modulus E . In this stage, the force continuously increases as the pipe moves laterally until it reaches a maximum. The peak force is controlled by the peak plane strain friction angle, ϕ'_{ps-p} . After the peak, the force decreases and converges to a residual force controlled by the critical friction angle, ϕ_{crit} , and plastic shear strain γ_p .

In this study, the peak forces from the experiments and analyses are compared first, since peak force is the most important factor when evaluating pipe response to lateral movement. Then the Young's modulus is evaluated by developing a relationship between modulus dry density of the sand, and effective vertical stress at the pipe centerline, σ'_{vc} , from full-scale experimental data. Finally, the DS test data are incorporated in strain softening model by applying a model proposed by Anastasopoulos, et al. (2007).

3.3 Dry Soil Strength Properties

Modeling soil-pipe interaction during lateral pipe movement within the ground requires that the soil strength properties of the sand be determined by appropriate laboratory tests. In this work, DS test results are converted to plane strain strength parameters and used in the Mohr-Coulomb (MC) model of the soil. The results of numerical analyses using the MC model are then compared with large-scale experimental results.

The large-scale tests were performed with different types of fluvio-glacial sand having similar, but not identical, grain size characteristics (Olson, 2009), referred to as CU filter sand and RMS graded sand. The DS test results and strength characterization for large-scale tests performed by Trautmann and O'Rourke (1983), Turner (2004), and Olson (2009) are described under the following subheadings.

3.3.1. Trautmann and O'Rourke Tests

Input parameters for CU filter sand strength were obtained from DS tests performed by Olson (2009). The results from 7 DS tests with $\gamma_d = 15.7 \text{ kN/m}^3 - 17.9 \text{ kN/m}^3$ are plotted in Fig. 3.10. The figure shows the relationship between ψ_p and γ_d at $\sigma'_{N \text{ Ref.}} = 2.1 \text{ kPa}$ as

$$\psi_{p / \sigma'_{N \text{ Ref.}}} = 8.66 \times \gamma_d - 134.56 \quad (3.1)$$

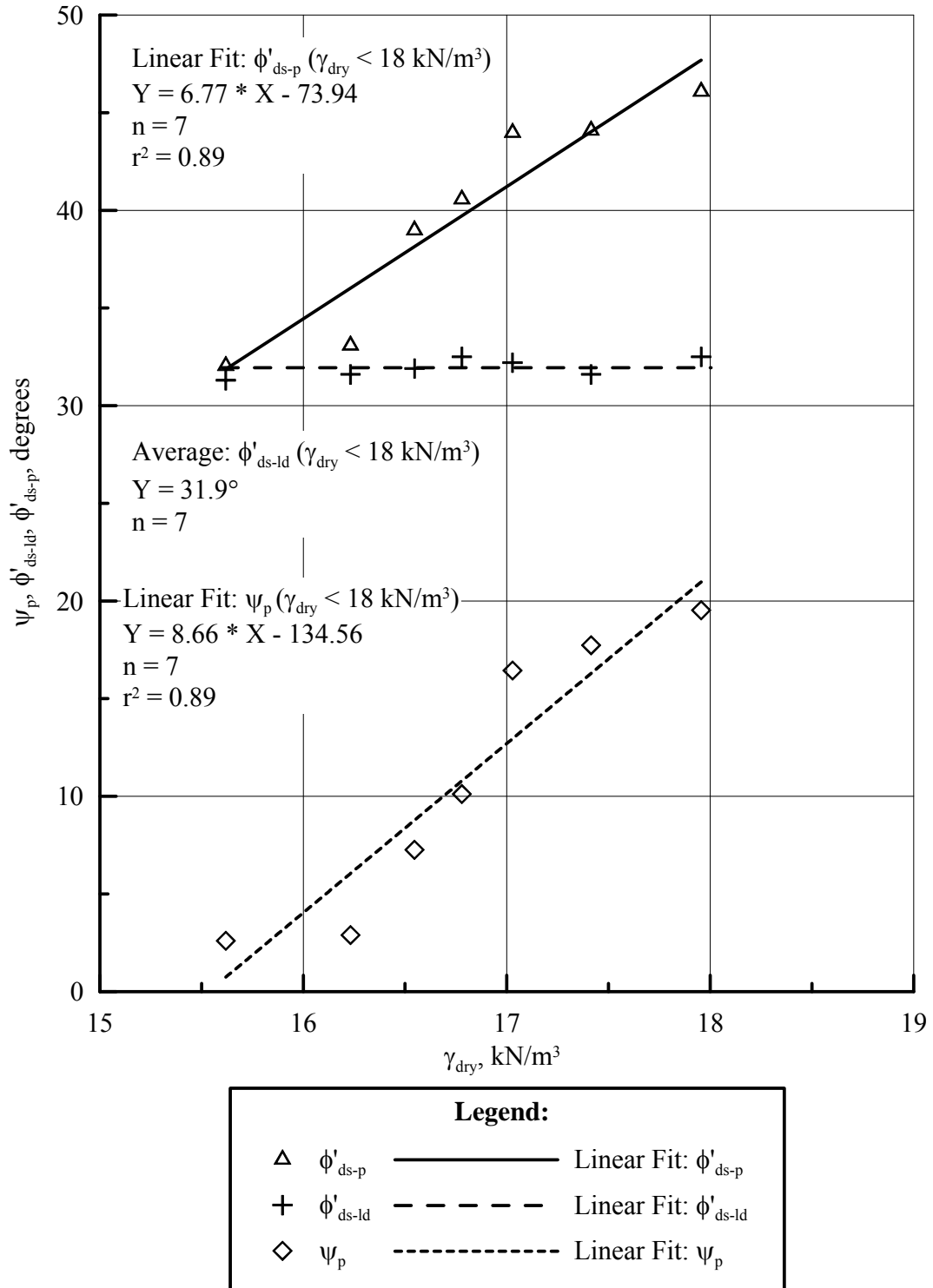


Figure 3.2 ψ_p vs. γ_{dry} for Dry CU Filter Sand at $\sigma'_N = 2.1 \text{ kPa}$ (Olson, 2009)

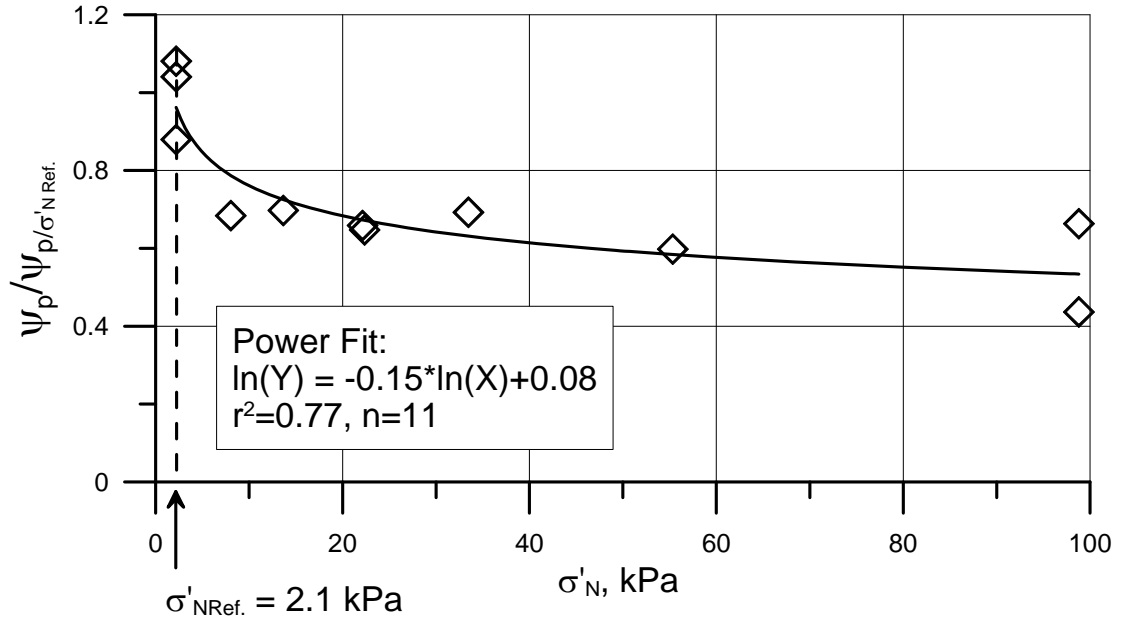


Figure 3.3 Plot of $\psi_p / \psi_{p/\sigma'_{N Ref.}}$ vs. σ'_N

Olson (2009) provided data for ψ_p vs. various σ'_N from DS tests. All ψ_p vs. σ'_N plots were digitized, and were converted to the normalized $\psi_p / \psi_{p/\sigma'_{N Ref.}}$ vs. σ'_N as shown in Fig. 3.3 to estimate ψ_p for variable σ'_N . The data for $\psi_p / \psi_{p/\sigma'_{N Ref.}}$ and σ'_N has $r^2 = 0.77$ and nonlinear regression equation for $\psi_p / \psi_{p/\sigma'_{N Ref.}}$ is

$$\frac{\psi_p}{\psi_{p/\sigma'_{N Ref.}}} = \exp(-0.15 \ln \sigma'_N + 0.08) \quad (3.2)$$

Lings and Dietz (2004) show the relationship between peak direct shear friction angle, ϕ'_{ds-p} , and ψ_p as

$$\tan \phi'_{ds-p} = \frac{\sin \phi'_{crit} + \sin \psi_p}{\cos \psi_p} \quad (3.3)$$

Olson (2009) reported ϕ'_{crit} for CU filter sand as 38.6° and RMS graded sand

as 40.8°. The calculated ϕ'_{ds-p} from Eqn. 3.3 is converted to the plane strain peak friction angle, ϕ'_{ps-p} , using the relationship first derived by Davis (1968) as

$$\sin \phi'_{ps-p} = \frac{\tan \phi'_{ds-p}}{\cos \psi_p + \sin \psi_p \times \tan \phi'_{ds-p}} \quad (3.4)$$

Equation 3.4 provides the ϕ'_{ps-p} at maximum obliquity ($\max \tau'/\sigma'_N$), which is required for the M-C model in ABAQUS.

Full scale tests by Trautmann and O'Rourke (1983) were performed for medium CU filter sand ($\gamma_d = 16.4 \text{ kN/m}^3$) and very dense CU filter sand ($\gamma_d = 17.7 \text{ kN/m}^3$). Using the Eqns 3.1 through 3.4, $\psi_p = 5.2^\circ - 6.2^\circ$, $\phi'_{ds-p} = 35.6^\circ - 36.4^\circ$, corresponding to $\phi'_{ps-p} = 42.6^\circ - 43.3^\circ$ for medium CU filter sand, and $\psi_p = 12.9^\circ - 15.4^\circ$, $\phi'_{ds-p} = 41.0^\circ - 42.7^\circ$, corresponding to $\phi'_{ps-p} = 48.1^\circ - 49.7^\circ$ for very dense CU filter sand, were obtained for $H_c/D = 3.5 - 11$.

3.3.2. Olson Tests

The input parameters for RMS graded sand were obtained from DS tests performed by Olson (2009). The results of 11 tests are plotted in Fig. 3.4, and the linear regression equation for ψ_p and γ_d at $\sigma'_{N \text{ Ref.}} = 2.1 \text{ kPa}$ is

$$\psi_{p/\sigma'_{N \text{ Ref.}}} = 6.99 \times \gamma_d - 109.48 \quad (3.5)$$

The γ_d measured by Olson (2009) was used with Eqn. 3.5 to obtain $\psi_p/\psi_{p/\sigma'_{N \text{ Ref.}}}$, and Eqns. 3.4 – 3.6 to obtain ψ_p , ϕ'_{ds-p} , and ϕ'_{ps-p} , respectively.

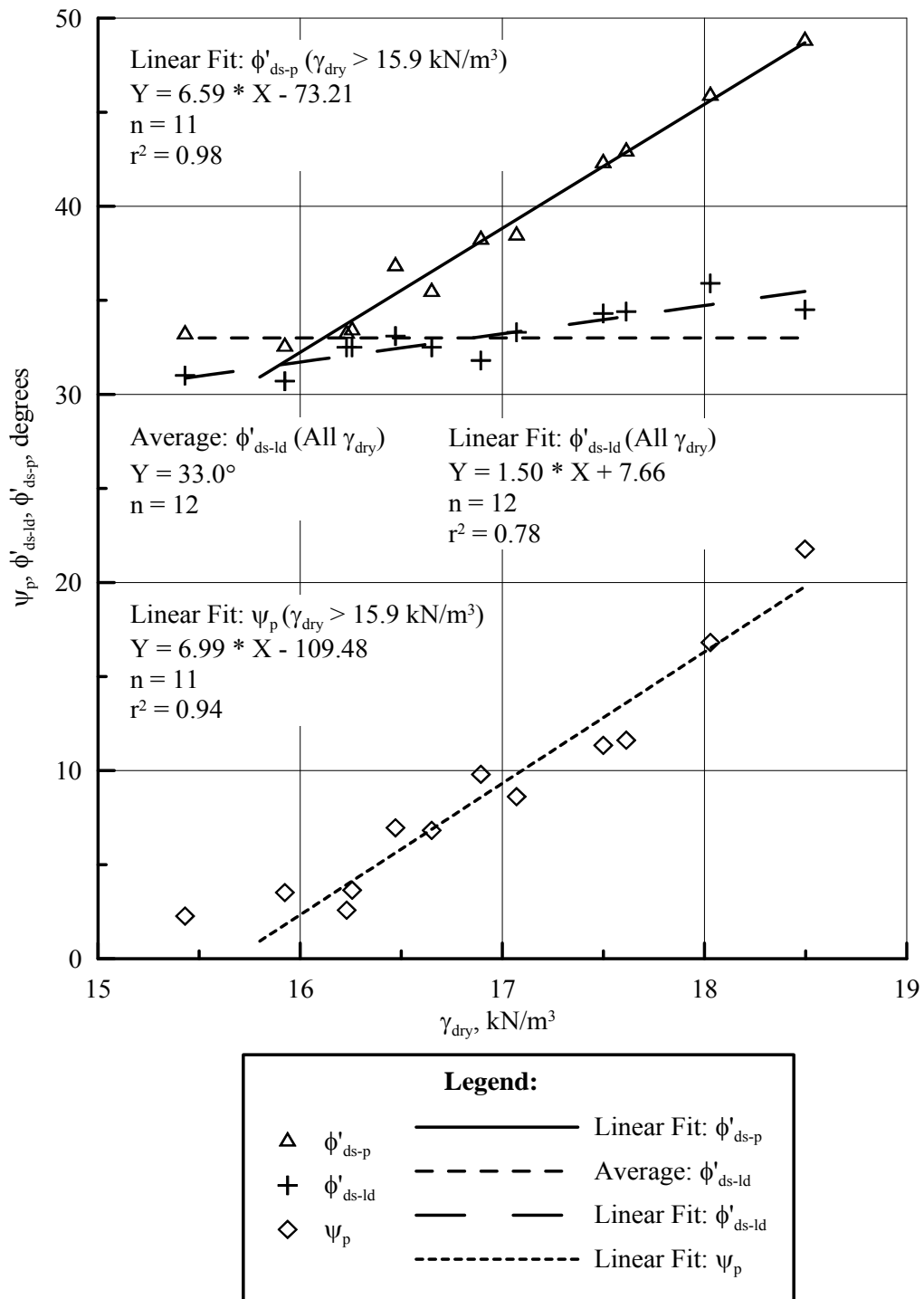


Figure 3.4 ψ_p vs. γ_d for Dry RMS Graded Sand at $\sigma'_N = 2.1 \text{ kPa}$ (Olson, 2009)

3.3.3. Turner Tests

Turner performed 6 large-scale 2D tests with dry RMS graded sand having $\gamma_d = 16.9 \text{ kN/m}^3 - 17.2 \text{ kN/m}^3$, as determined by density scoop measurements (Turner 2004). Olson (2009) compared the dry unit weights measured by the more accurate nuclear gage, γ_{d-ng} , with those measured by the density scoop, γ_{d-ds} , and developed a correction equation for the determination of γ_{d-ng} , using density scoop measurements as follows

$$\gamma_{d-ng} = 0.93 \times \gamma_{d-ds} + 0.95 \quad (3.6)$$

The density scoop measurements of γ_{d-ds} by Turner were corrected with Eqn. 3.6, and these values were used with Eqn. 3.5 to obtain ψ_p . Eqns. 3.2 and 3.3 were used to obtain ψ and ϕ'_{ds-p} , which were used in Eqn. 3.4 to calculate ϕ'_{ps-p} .

3.3.4. Summary

Table 3.1 summarizes key dimensions from the full-scale tests as well as soil properties, in terms of unit weight and strength parameters, that were used in the full-scale tests. These dimensions and soil properties were used in input parameters for the finite element analyses of 2-D lateral pipe movement, as described in the next section.

The tests reported by Trautmann and O'Rourke (1983), Olson (2009), and Turner (2004) were performed with dry sand characterized as medium, dense, and very dense. The soil strength properties associated with each density description are

Table 3.1 Summary of the Input Parameters Used in Finite Element Analyses for
Lateral Pipe Movement

Test No.	H_c/D	Diameter (mm)	Length (mm)	γ_d (kN/m ³)	ϕ'_{ds-p} (degrees)	Ψ_p (degrees)	ϕ'_{ps-p} (degrees)
T & O*26, 27, 29, 30	3.5	102	1200	16.4	36.4	6.2	43.3
T & O 46	5.5	102	1200	16.4	36.1	5.8	43.1
T & O 51	8	102	1200	16.4	35.9	5.5	42.8
T & O 48, 49	11	102	1200	16.4	35.7	5.2	42.6
T & O 23	3.5	102	1200	17.7	42.7	15.4	49.7
T & O 24	5.5	102	1200	17.7	42.0	14.4	49.0
T & O 25	8	102	1200	17.7	41.5	13.6	48.5
T & O 32	11	102	1200	17.7	41.0	12.9	48.1
Os 2D-1**	5.47	120	2440	16.9	38.4	7.6	46.3
Os 2D-2	5.29	124	2440	17.1	38.4	7.5	46.3
Os 2D-3	5.29	124	2440	17.2	38.4	7.5	46.3
Tn Test 2***	5.5	120	1210	17.1	38.4	7.5	46.3
Tn Test 3	5.5	120	1210	17.2	38.4	7.5	46.3
Tn Test 6	5.5	120	1210	16.9	38.4	7.6	46.3
Tn Test 7	5.5	120	1210	17.2	38.4	7.5	46.3
Tn Test 8	5.5	120	1210	17.2	38.4	7.5	46.3
Tn Test 9	5.5	120	1210	17.0	38.4	7.5	46.3

* T & O: Trautmann & O'Rourke (1983); ** Os: Olson (2009); *** Tn: Turner (2004)

summarized in Table 3.2. The full-scale test results associated with each density description are listed in the table. Average values of dry unit weight as well as friction and dilation angles are also given. The experimental range in the friction and dilation angle is approximately $\pm 1^\circ$ of the value in the table, and the range in dry unit weight is $\pm 0.15 \text{ kN/m}^3$ of the value in the table.

Table 3.2 Summary of Dry Sand Strength Parameters

Density Description	γ_d (kN/m^3)	ϕ'_{ds-p} (degrees)	ψ_p (degrees)	ϕ'_{ps-p} (degrees)	Full-scale Test Results
Medium	16.4	36.0	4.0	43.8	Trautmann and O'Rourke (1983)
Dense	17.1	38.5	7.7	46.4	Olson (2009), Turner (2004)
Very Dense	17.7	40.6	10.9	48.6	Trautmann and O'Rourke (1983)

3.4 Finite Element Analyses Model for Dry Sand

Each FE analyses mesh was developed to replicate the geometry and material properties of the soil, pipe, and experimental facilities in each test. Figure 3.5 shows the typical geometry of the numerical model, which is taken directly from the large-scale experimental test equipment. In the figure, H_{bt} is the height from the pipe center to the interior box bottom, H_{bk} is the closest distance from the center of the pipe to the test box wall, and H_c and D are as defined previously. The pipe was modeled as a rigid cylinder. In the simulations the exterior of the test box was fixed in all directions. The finite element mesh was composed of 8-node biquadratic, plane

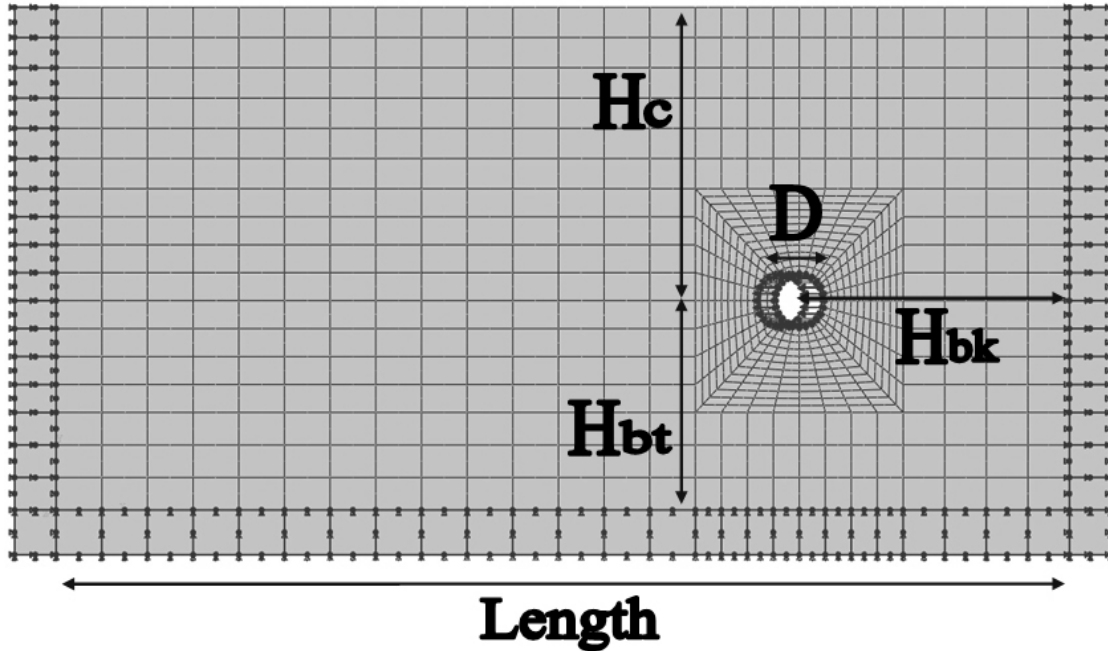


Figure 3.5 Geometry of the Numerical Model for Lateral Pipe Movement

strain, quadrilateral, reduced integration elements (element type CPE8R). A refined mesh was used within a distance of approximately two pipe diameters from the test pipe. The thickness of the elements within the refined mesh was taken as the shear band thickness observed by various researchers during DS tests (e.g., Roscoe, 1970; Vardoulakis and Graf, 1985; Muhlhaus and Vardoulakis, 1987; Bardet and Proubet, 1992; Huang, et al., 2002; Olson, 2009). Approximately 800 to 1000 elements were used in the meshes to simulate different experimental conditions.

A mesh convergence study was performed to select the appropriate mesh for analysis. Starting with a mesh containing 250 elements, analyses were performed with meshes of 380, 613, 814, and 1544 elements. The convergence study showed only a 0.1 % difference in peak pipe force as the mesh size was increased from approximately 814 to 1544 elements. Given the very small change in peak force for 1544 elements, a mesh size of 800 to 1000 elements was used to obtain good resolution of results and promote computational efficiency.

Geostatic loads were applied at the start of each simulation under $K_0 = 1$ conditions. Sensitivity analysis was performed with different K_0 values, and the results showed that the peak dimensionless force varies approximately 1 % while K_0 varies from 0.5 to 2. A Poisson's ratio, $\nu = 0.3$, was assumed for the sand. To promote numerical stability, all simulations were performed with a nominal cohesion $c' = 0.1 - 0.3$ kPa. Sensitivity analyses were performed with different c' values to show that the range of $c' = 0.1 - 0.3$ kPa had negligible effect on the results.

Figure 3.6 shows the soil/test box and soil/pipe interfaces. The interface friction angle between the soil and pipe (smooth steel) and vertical box wall (formica and glass) was taken as $0.6 \phi'_{ds-p}$ on the basis of laboratory tests performed by Trautmann and O'Rourke (1983) and Olson (2009). The interface friction angle between soil and the wooden base of the box was estimated as $0.8 \phi_{ds-p}$ (Kulhawy et al, 1983).

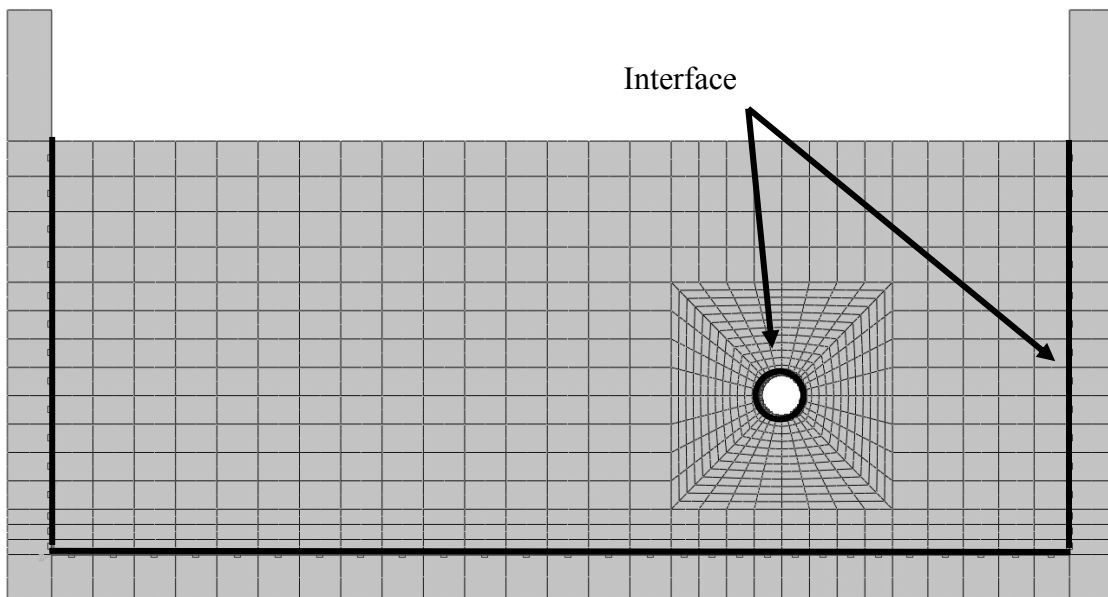


Figure 3.6 The Soil/Test Box and Soil/Pipe Interfaces

Figure 3.7 shows the geometry of the numerical model used for analyses of each series of tests referred to a) Trautmann and O'Rourke (1983), b) Olson 2D-1 (2009), c) Olson 2D-2 and 3 (2009), and d) Turner (2004). The test box used by Trautmann and O'Rourke had an inside length of 2.3 m, $H_{bt} = 0.35$ m, $H_{bk} = 0.65$ m, and H_c was varied to obtain different H_c/D . The test pipe had an outside diameter of 102 mm, a length of 1.2 m, a wall thickness of 6.4 mm, and is normal to the 2-D plane in Fig. 3.6. Olson performed tests with two different boxes each with an inner length of 2.44 m, $H_{bt} = 0.47$ m, $H_{bk} = 0.65$ m, pipe length = 2.44 m, and pipe wall thickness =

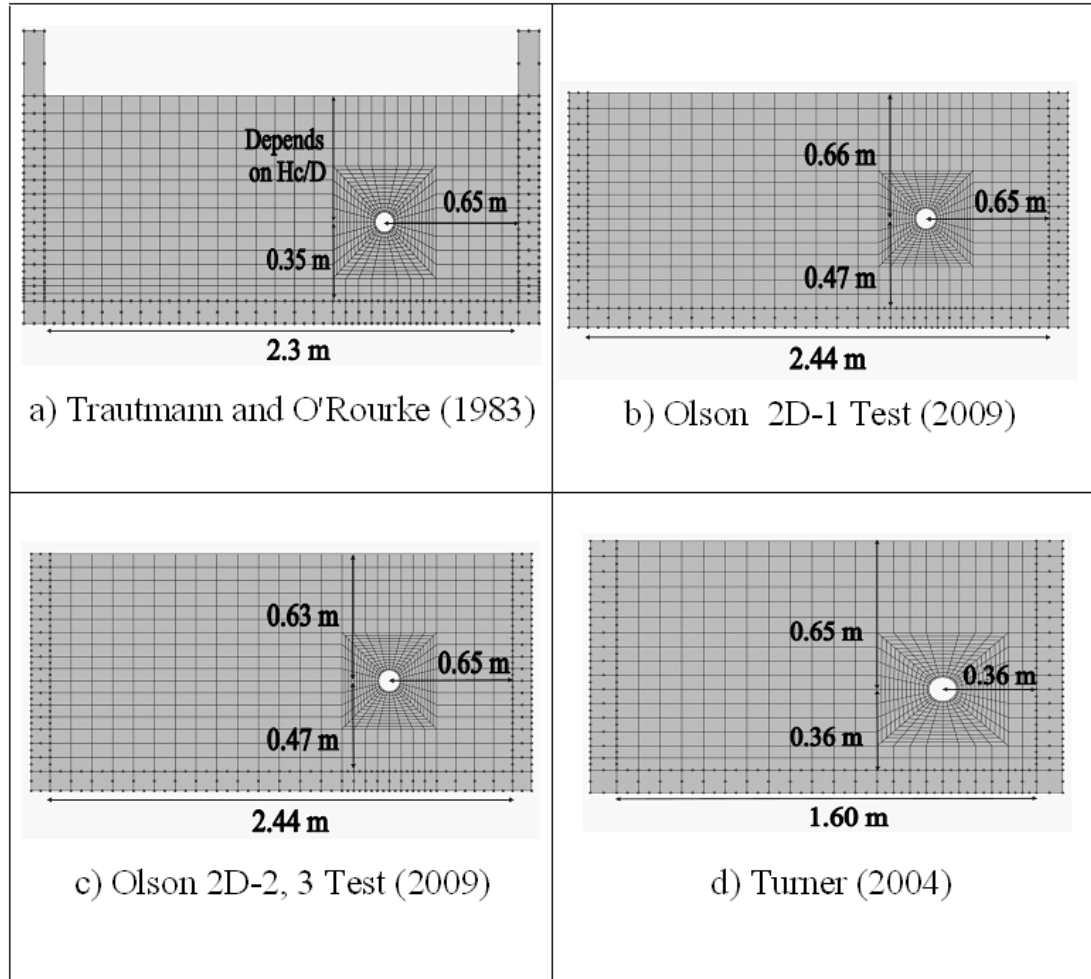


Figure 3.7 Geometry of the Test Box for Each Test

6.4 mm. For the 2D-1 test, $H_c = 0.66$ m and $D = 120$ mm. For the 2D-2 and 2D-3 tests, $H_c = 0.63$ m and $D = 124$ mm. For the Turner tests, the box had an inner length of 1.6 m, $H_{bt} = 0.36$ m, $H_{bk} = 0.36$ m, $H_c = 0.65$ m, $D = 0.119$ m, and pipe length = 1.21 m.

The peak angle of dilation, ψ_p was evaluated using Eqn. 3.2, where σ'_N is taken as σ'_{vc} , which is the vertical effective stress at the pipe centerline. With ψ_p estimated relative to σ'_{vc} , Eqns 3.3 and 3.4 were used to evaluate ϕ'_{ps-p} . Because ψ_p is explicitly related to $\sigma'_{vc} = \gamma H_c$, ϕ'_{ps-p} will decrease with depth for a given γ_d because of diminishing capacity for dilation as confining stress increases.

Characterizing ψ_p in terms of a single σ'_{vc} is a simplification that does not account for variable ψ_p and ϕ'_{ps-p} with depth or link ψ_p with the appropriate σ'_N at any given depth. As described in Chapter 4, FE simulations were run for layered soil conditions in which ψ_p and ϕ'_{ps-p} were varied with depth and σ'_N was estimated with greater accuracy. The results for simulations using a variable friction angle with depth and a more accurate assessment of σ'_N were compared with those using ψ_p and ϕ'_{ps-p} linked to a single σ'_{vc} at the pipe centerline. Because the comparisons show only 0.2 – 3.3 % difference in the results, the more simple and straightforward characterization of friction angle relative to the vertical effective stress at the pipe centerline was used in the production runs of the numerical simulations.

3.5 Comparison of FE Analyses and Measured Peak Forces

The experimental maximum forces for 2-D tests with CU filter sand and RMS graded sand were used as reported by Trautmann and O'Rourke (1983) and Olson

(2009) because these data were already corrected for side shear effects or steps had been taken experimentally to reduce the side shear forces. The experimental data obtained by Turner (2004), however, required correction for side wall friction effects, following the procedures used by Olson (2009) to produce a consistent data set for the 2-D tests with RMS graded sand.

The correction procedure used by Olson was based on tactile pressure sensor measurements of soil pressure on the test box sidewalls (Olson, 2009) and observations of soil movement patterns, resulting in the following relationship for the horizontal frictional resisting force, F_f , contributed by both sidewalls

$$F_f = 2K_0\sigma'_{vc} A_s \times \tan \delta_{SI} \cos \alpha_s \quad (3.7)$$

in which K_0 is the ratio of horizontal stress acting on the sidewalls to vertical effective stress at the pipe center, σ'_{vc} ; A_s = area of sidewall in contact with displaced soil; δ_{SI} = the angle of interface shear resistance between the soil and sidewall; and α_s = angle with respect to the horizontal of soil movement observed during the tests. Tactile pressure measurements by Olson show that on average throughout the test, $K_0 = 0.72$ is representative of the 2-D soil test pressures. The value of δ is determined by using $\delta/\phi'_{ds-p} = 0.6$, which was shown by Trautmann & O'Rourke (1983) and Olson (2009) to be representative of the glass and formica of the sidewalls. The DS soil friction angle, ϕ'_{ds-p} , is the appropriate strength parameter for failure on a rigid interface, and was used to estimate δ . Finally, F_f was subtracted from the lateral force measured by Turner. On average, the correction for side wall friction decreased the measured peak force between 3 to 5 %, so the change associated with this correction is relatively small.

Figure 3.8 shows the measured peak dimensionless force plotted with respect to the FE peak dimensionless forces. The preponderance of the measurements obtained by Trautmann and O'Rourke (1983), Turner (2004), and Olson (2009) show a clear peak load. For medium sand tests with no clear peak, the procedure used by Trautmann and O'Rourke (1983) was used to interpret the maximum load. With this procedure, the horizontal force vs. displacement data were fit to a hyperbolic curve, and the peak force was estimated as the asymptote of the hyperbolic fit, multiplied by a reduction factor, $R_f = 0.9$.

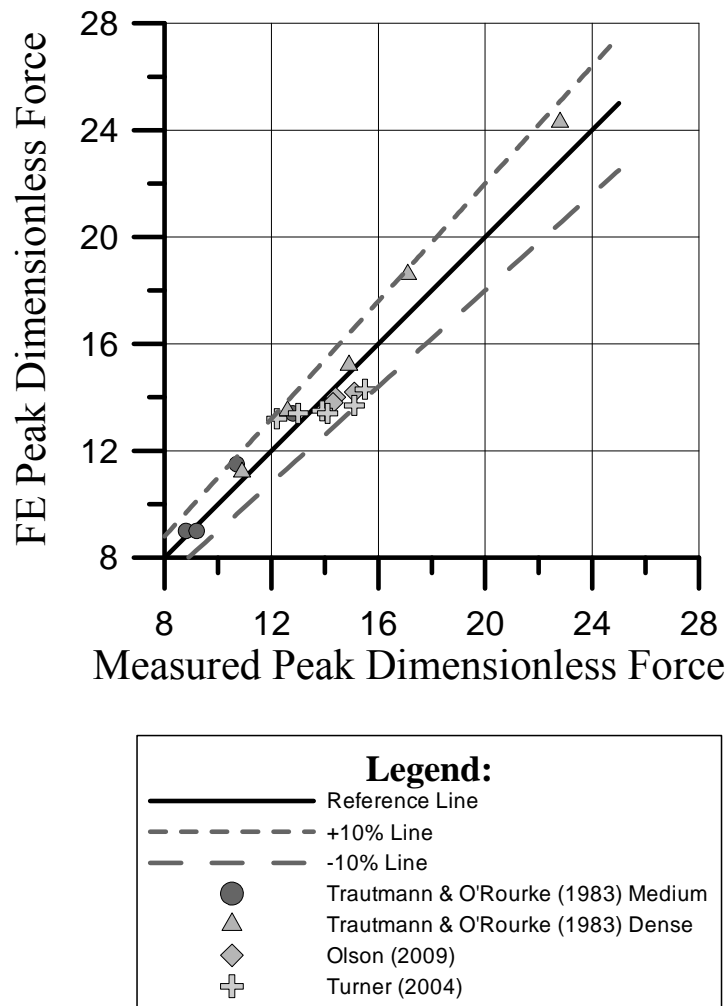


Figure 3.8 Comparison of the Measured and FE Analyses Peak Force

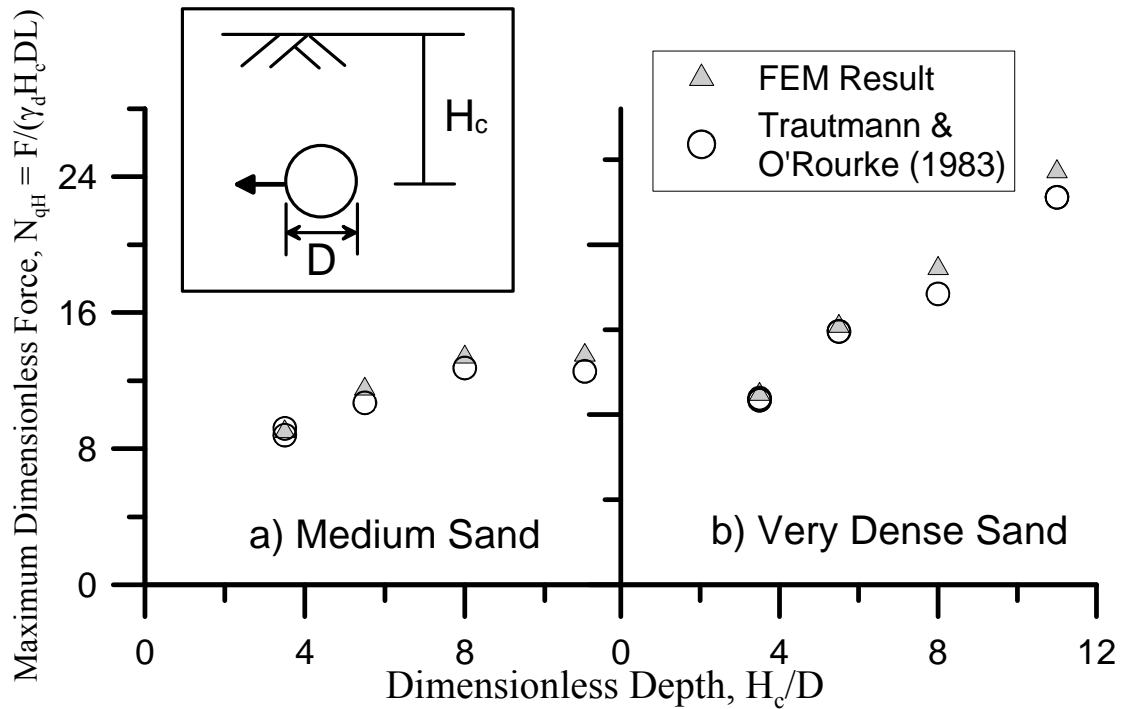


Figure 3.9 Plot of N_{qH} vs. H_c/D for Dry CU Filter Sand

All FE analyses peak forces are within $\pm 10\%$ of the measured maximum forces, and no FE analyses forces differ from the experimental data by more than 9.3%. The average difference between the FE analyses and measured force is 5.1%.

Figure 3.9 compares the FE analyses and 2-D test results of Trautmann and O'Rourke (1983), in which the dimensionless force, N_{qH} , is plotted as a function of the dimensionless depth. There is a favorable agreement among the data for all H_c/D . In general, the FE analyses results over predict the measured dimensionless peak force by 2 – 7%. Both the measured and FE analyses peak forces are relatively constant for medium sand at $H_c/D = 8$ and $H_c/D = 11$. Overall, the average difference between the FE analyses and measured force for dry CU filter sand is 4.5%.

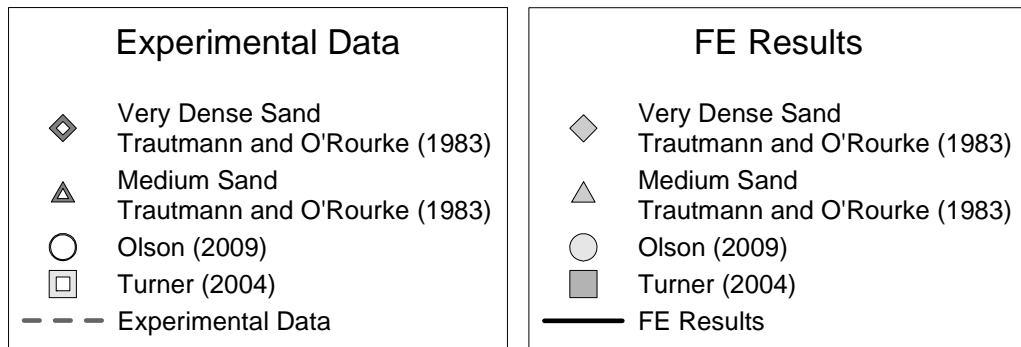
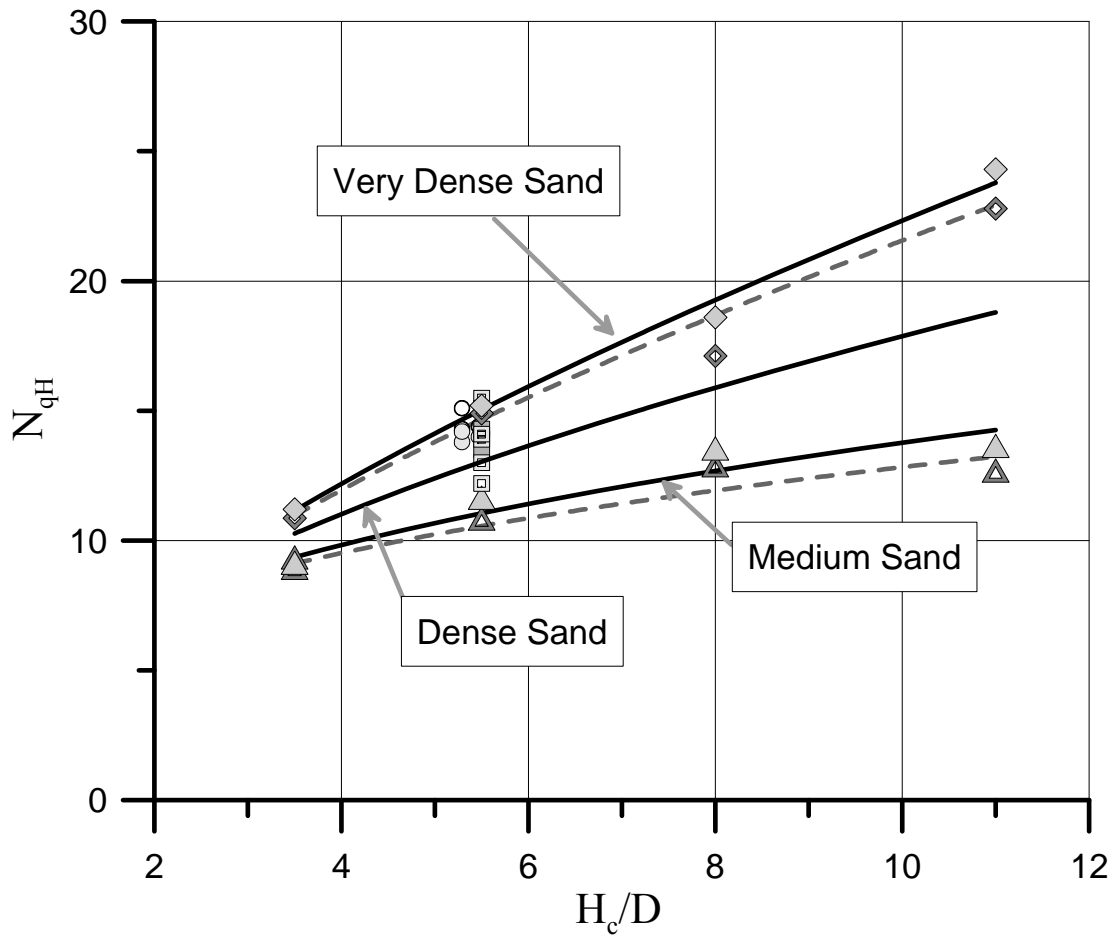


Figure 3.10 Summary Plot of N_{qH} vs. H_c/D for All Dry FE Results

Figure 3.10 summarizes N_{qH} vs. H_c/D for all dry sand tests with CU filter and RMS graded sand. Both the experimental data and numerical results for peak load are plotted for medium, dense, and very dense sand as characterized in Table 3.2. Nonlinear regression lines are plotted for the experimental data and numerical results pertaining to medium and very dense sand. Also plotted is the regression for dense sand numerical results. Experimental data for dense dry sand are available from Olson (2009) and Turner (2004) for $H_c/D = 5.5$ only. To produce a curve for dense sand, FE analyses were performed for $H_c/D = 3.5, 5.5, 8, 11$, and the regression line for those results is shown in the figure. The numerical results exceed measured peak forces by about 4.1 % for very dense sand, and 4.8 % for medium sand with $H_c/D \leq 11$.

3.6 Young's Modulus for Lateral Pipe Movement

The Mohr-Coulomb plasticity model in this work is based on representing the soil response as linear elastic until stresses in the soil are equal to and exceed the Mohr-Coulomb yield surface. Thus, an elastic modulus is required as one of the constituent soil properties. The model uses a constant elastic modulus to approximate the nonlinear stress-strain behavior of soil before yield, and thus provides a simplified “equivalent” representation of soil response to horizontal pipe movement.

To select the Young's modulus on the basis of an appropriate response, the method proposed by Thomas (1978) and used by Trautmann & O'Rourke (1983) was applied to the horizontal force vs. displacement response of the pipe as shown in Fig. 3.11. Thomas (1978) suggested that using an initial slope, K_{70} , from the origin through the point corresponding to 70 % peak force was generally adequate in 1-D numerical simulations of soil-structure interaction. In general, bisecting the

experimental pipe-displacement plot by a K_{70} -line results in approximately equal areas between K_{70} and the nonlinear data plot below and above the 70 % peak force value. The K_{70} -line thus tends to equalize the amount of over- and under-prediction associated with an initial linear slope simplification.

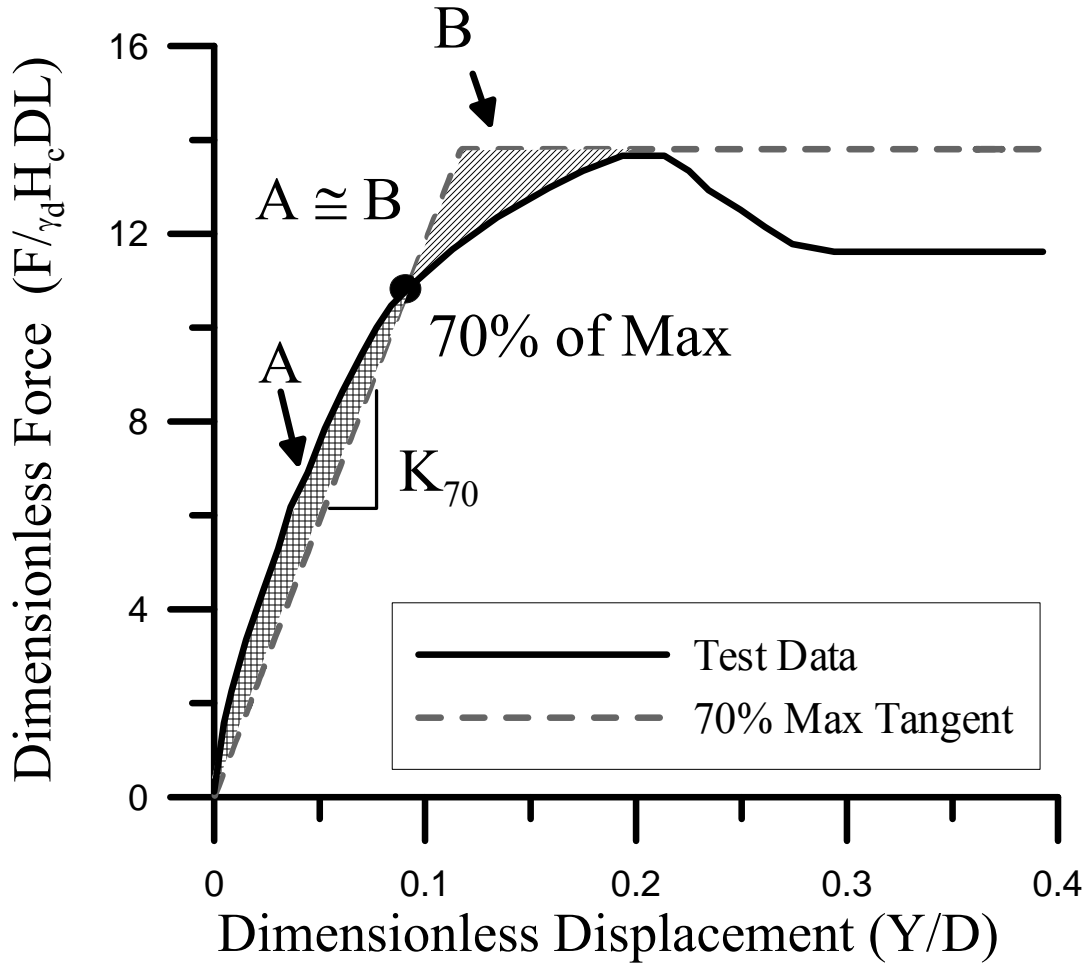


Figure 3.11 K_{70} Approach of Bilinear Model for Dimensionless Force-Displacement Curve

The equivalent modulus for lateral pipe movement, E_{70-H} , was determined by running FE simulations with different values of E and the same strength parameters for each experimental data set from Trautmann & O'Rourke (1983) and Olson (2009)

until the initial linear force displacement response coincided with K_{70} at 70 % of the peak force. The E-value corresponding to this condition was selected as E_{70-H} .

Janbu (1963) proposed a relationship between initial tangent modulus E_i , and confining pressure, σ'_3 , as

$$E_i = K \times p_a \times \left(\frac{\sigma'_3}{p_a} \right)^n \quad (3.8)$$

in which K = constant, σ'_3 = minor principal effective stress, and n = exponent determining the rate of variation of E_i with σ'_3 .

In Fig. 3.12 equations following the form of Eqn. 3.8 are fit to the Trautmann and O'Rourke (1983) test data for medium, dense, and very dense sand in which σ'_3 is expressed as the vertical effective stress at the center of the pipe, σ'_{vc} . The K and n -values are 59 and 0.6 for medium sand, and 181 and 0.6 for dense sand. These K and n -values are substantially smaller than the K and n -values for the initial tangent modulus, E_i , summarized by Duncan and Chang (1970) and Wong and Duncan (1974) for sand having similar γ_d and grain size characteristics. As explained in Appendix A, the moduli back-calculated from the large-scale test data represent strain-compatible moduli. They are consistent with the high levels of soil stress that coincide with the peak pipe force. Appendix A shows that the secant modulus associated with stress levels at a high percentage of yield is much smaller than the initial tangent modulus, and is consistent with the values depicted in Fig. 3.12.

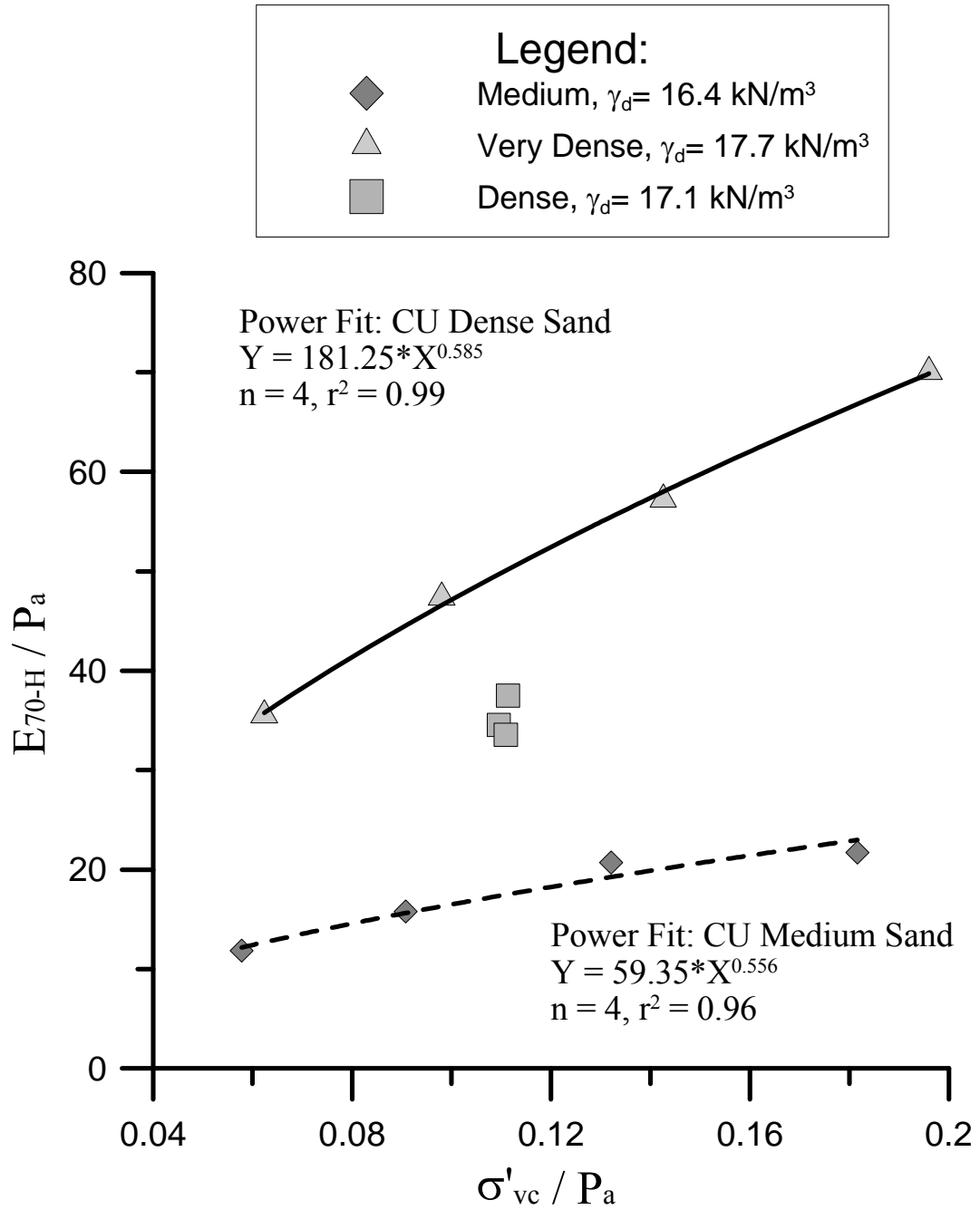


Figure 3.12 Relationships between E_{70-H}/P_a and σ'_{vc}/P_a of CU Filter Sand

The figure shows that E_{70-H} increases with increasing γ_d , for constant σ'_{vc} . Multiple linear regression (MLR) analyses were performed on E_{70-H} , σ'_{vc} , and γ_d to obtain an expression for these variables with highest statistical significance as

$$\log \frac{E_{70-H}}{P_a} = \log K + \alpha \log \frac{\gamma_d}{\gamma_w} + \beta \log \frac{\sigma'_{vc}}{P_a} \quad (3.9)$$

in which K , α , and β are constants, P_a is an atmospheric pressure, and γ_w is unit weight of water. The form of Eqn. 3.9 is similar to that obtained by Jeon and O'Rourke (2005) for correlations between earthquake damage and seismic parameters.

Using the data from the Trautmann and O'Rourke (1983) and Olson (2009), the MLR analyses provide the following

$$\log \frac{E_{70-H}}{P_a} = -0.264 + (10.42) \log \frac{\gamma_d}{\gamma_w} + (0.7787) \log \frac{\sigma'_{vc}}{P_a} \quad (3.10)$$

in which log is for base 10. For this equation $r^2 = 0.90$, indicating a high degree of statistical significance.

Equation 3.8 can be re-written in dimensionless form as

$$\frac{E_{70-H}}{P_a} = K \left[\frac{\gamma_d}{\gamma_w} \left(\frac{\sigma'_{vc}}{P_a} \right)^{\frac{\beta}{\alpha}} \right]^{\alpha} \quad (3.11)$$

in which $[(\gamma_d/\gamma_w)(\sigma'_{vc}/P_a)^{\beta/\alpha}]^{\alpha}$ is a scaled parameter combining dry unit weight and vertical effective stress. Using the experimental data, Eqn 3.10 is re-written as

$$\frac{E_{70-H}}{P_a} = 10^{-0.264} \left[\frac{\gamma_d}{\gamma_w} \left(\frac{\sigma'_{vc}}{P_a} \right)^{0.075} \right]^{10.42} \quad (3.12)$$

The experimental data and Eqn. 3.12 are plotted in Fig. 3.13. The equation provides a close fit to the data, and thus provides a dependable way of re-producing the data trends. To test the predictive capability of Eqn. 3.12, it is necessary to compare the modulus given by the equation with modulus and soil properties obtained by independent testing.

Data obtained by Turner (2004) for medium dense sand from 6 large-scale 2-D tests were used to determine E according to the K_{70} - procedure previously discussed. Figure 3.14 shows a histogram of the E_{70-H} -values and a probability density function for the data. Using the σ'_{vc} and average γ_d from the 6 Turner tests, Eqn. 3.12 is used to predict $E_{70-H} = 3300$ kPa, which is plotted in the figure. The predicted E is consistent with the experimentally determined values, and is within one standard deviation from the mean.

Figure 3.15 shows the dimensionless force vs. dimensionless displacement plot determined by numerical simulation using the predicted E_{70-H} and the peak strength data for RMS graded sand compared with the dimensionless force vs. dimensionless displacement data for the six 2-D tests in RMS graded sand by Turner (2004). The average dimensionless force vs. dimensionless displacement curve for Turner's data is also plotted in the figure. The numerical simulation of force vs. displacement bisects the average experimental data approximately $Y/D = 0.05$, and compare favorably in terms of peak force and post-peak behavior. The numerical

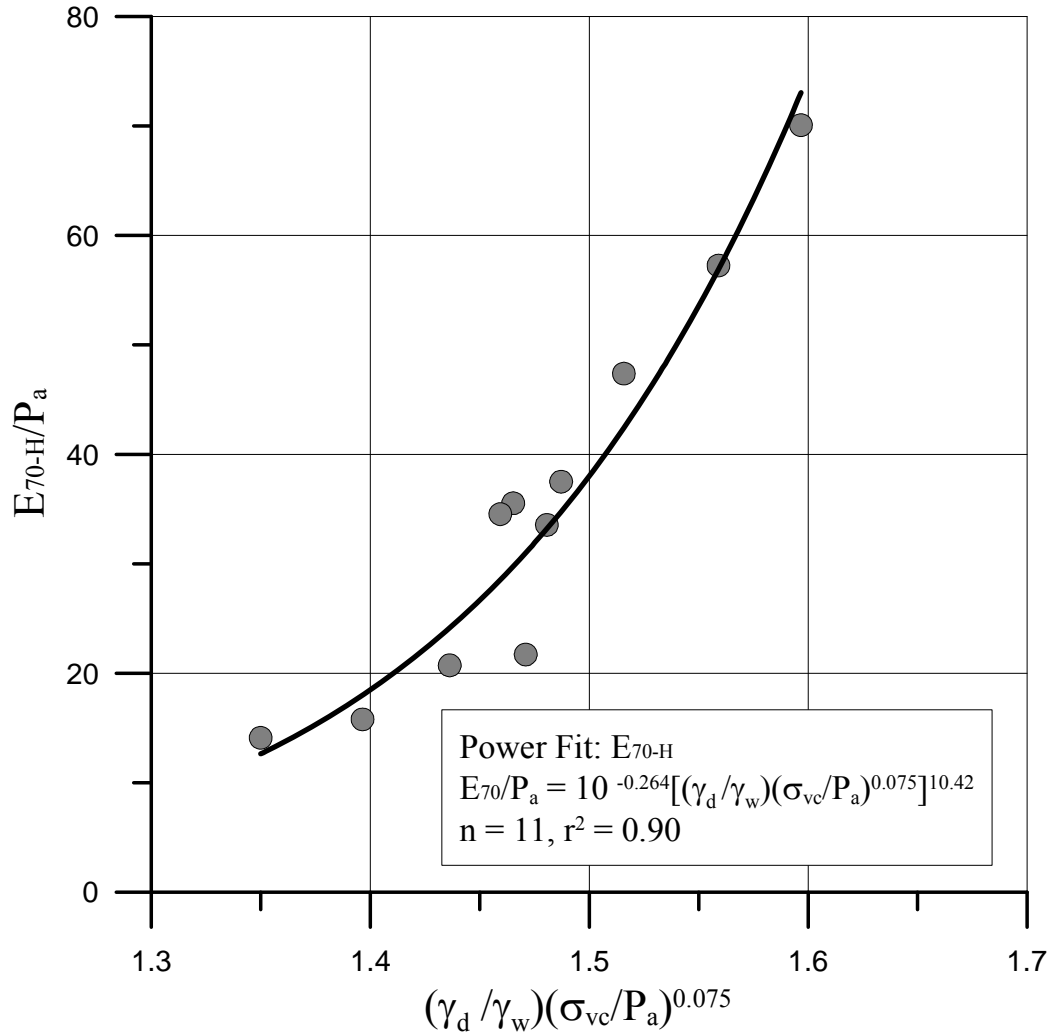


Figure 3.13 E_{70-H} Multiple Linear Regression for γ_d and σ'_{vc} .

simulation is somewhat stiffer within the equivalent elastic range, and over predicts the force by about 10 % at $Y/D = 0.1$. Overall, the predicted force-displacement behavior provides a favorable representation of the experimental trend, which are both consistent with the average test data and within 9 % of the measured peak load. The predicted behavior is higher than the measured response between $Y/D = 0.05$ and 0.15 , thus resulting in slightly conservative estimate of force in this range. Table 3.3 summarized E_{70-H} used in the lateral pipe movement simulation calculated from Eqn. 3.16.

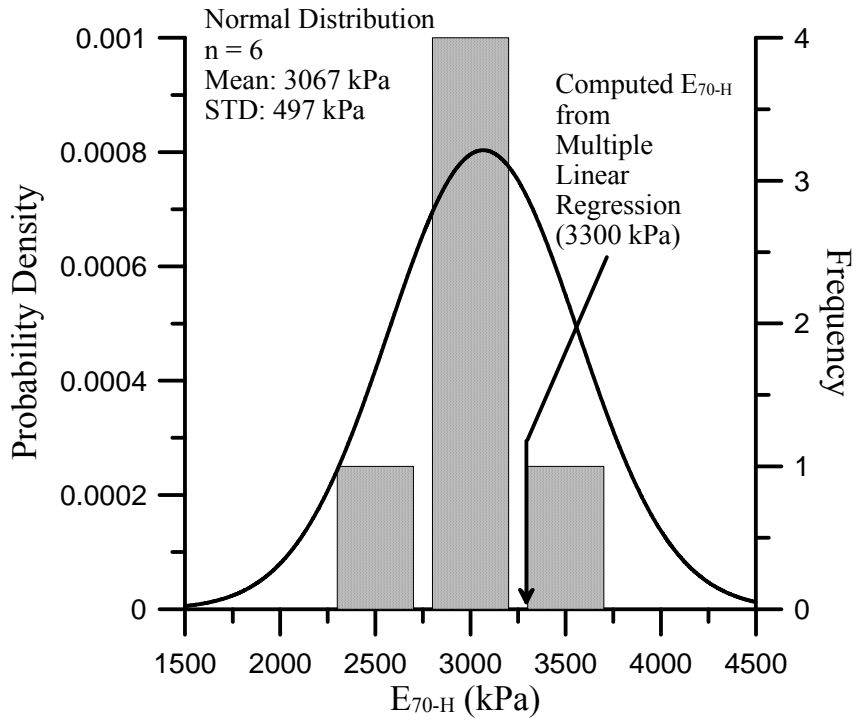


Figure 3.14 Histogram of Equivalent E_{70-H} from Turner (2004) Tests and the Computed E_{70-H} from Multiple Linear Regression Analysis

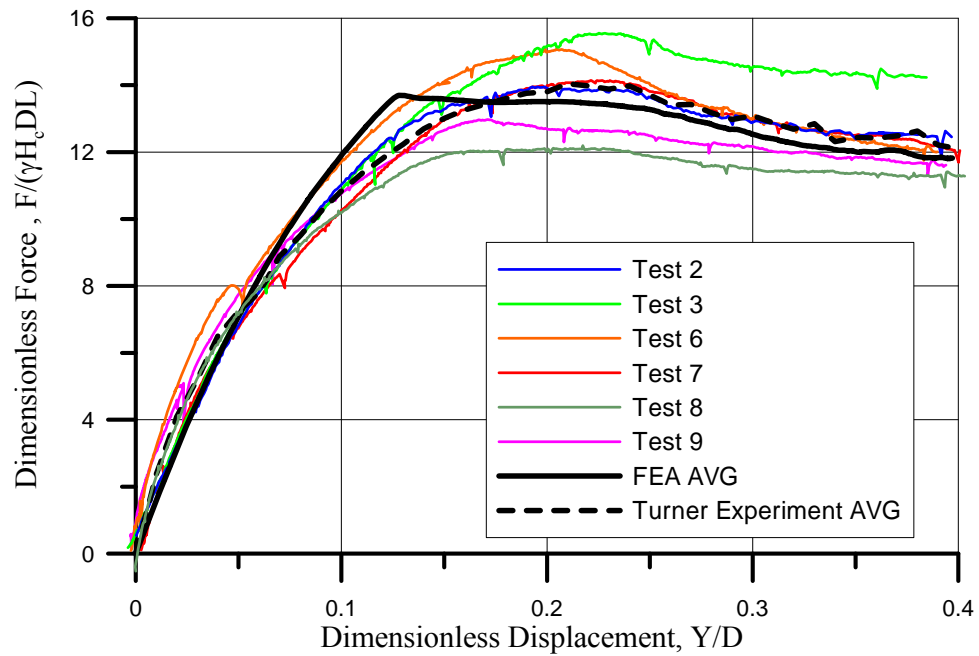


Figure 3.15 Simulated Dimensionless Force vs. Displacement Curve for Turner Tests

Table 3.3 Summary of E_{70-H} Used in Dry Lateral Pipe Movement Simulation

Test No.	H_c/D	E_{70-H} (kPa)	Test No.	H_c/D	E_{70-H} (kPa)
T & O* 26, 27, 29, 30	3.5	1300	Os 2D-2	5.29	3400
T & O 46	5.5	1800	Os 2D-3	5.29	3600
T & O 51	8	2400	Tn*** Test 2	5.5	3400
T & O 48, 49	11	3100	Tn Test 3	5.5	3400
T & O 23	3.5	3000	Tn Test 6	5.5	2800
T & O 24	5.5	4200	Tn Test 7	5.5	3300
T & O 25	8	5600	Tn Test 8	5.5	3400
T & O 32	11	7200	Tn Test 9	5.5	3100
Os** 2D-1	5.47	2800			

* T & O: Trautmann & O'Rourke (1983); ** Os: Olson (2009); *** Tn: Turner (2004)

3.7 Strain Softening Behavior

As discussed in Chapter 2, the Mohr-Coulomb model in ABAQUS is not able to reproduce strain softening behavior. To represent strain softening, the model proposed by Anastasopoulos, et al. (2007) was used to diminish linearly both ϕ'_{ps-p} and ψ_p to residual values at ϕ'_{crit} and 0, respectively, from the plastic strain at ϕ'_{ps-p} to the plastic strain at ϕ_{crit} , using the results of DS testing as

$$\gamma^p_f = \frac{d_{xp} - d_{xy}}{H} + \frac{d_{xf} - d_{xp}}{d_{FE}} \quad (3.13)$$

in which H = thickness of the DS specimen, d_{FE} = FE element size, and d_{xy} , d_{xp} , d_{xf} are

the horizontal displacements at yield, peak strength, and ϕ_{crit} at which full softening occurs.

A FORTRAN subroutine was prepared by Robert and Soga (2009) to apply the Anastasopoulos, et al. (2007) model in the Mohr-Coulomb model used by ABAQUS. This subroutine was applied in the 2-D FE simulations of soil-pipeline interaction.

To illustrate how DS test data are incorporated in the strain softening model, the stress ratio and vertical displacement for a typical DS test on RMS graded sand are plotted in Fig. 3.16 as a function of horizontal displacement. The values for the various parameters in Eqn. 3.13 are illustrated in the figure. The d_{FE} in the refined part of the finite element mesh was 12 mm. This thickness compares favorably with the shear band thickness as reported by several investigators (e.g., Roscoe, 1970; Vardoulakis and Graf, 1985; Muhlhaus and Vardoulakis, 1987; Bardet and Proubet, 1992; Huang, et al., 2002) as $8 - 20 d_{50}$, where d_{50} is the median grain size. For RMS graded sand, d_{50} was reported as 0.6 mm (Olson, 2009). Hence, the element size in the FE mesh is consistent with shear band dimensions associated with the DS tests. A value of $\gamma_f^p = 0.3$ is calculated from Eqn. 3.13.

Because $\phi'_{\text{ps-p}}$ is linearly decreased to ϕ'_{crit} , it is necessary to evaluate ϕ'_{crit} . Olson (2009) reported ϕ'_{crit} for CU filter sand and RMS graded sand as 38.6° and 40.8° , respectively. Olson's relationships for ψ_p as a function of γ_d (Olson, 2009), and the procedure explained in Section 3.3 were used to select the peak strength and dilation parameters.

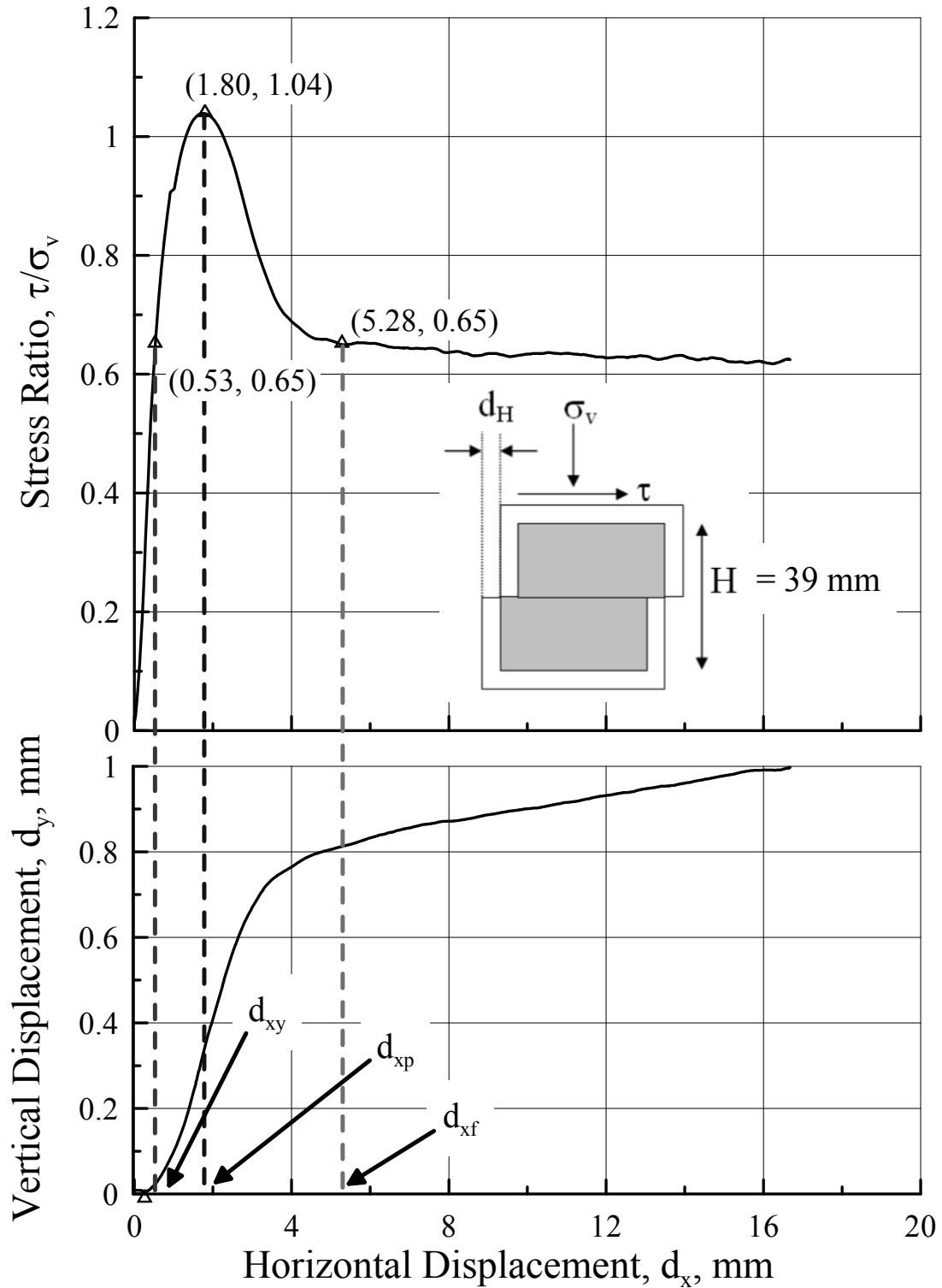


Figure 3.16 Stress Ratio, d_y vs. d_x Plot in a DS Test of CU Filter Sand

3.8 Comparison of Force vs. Displacement Curves for Analytical and Test Results

Comparisons between analytical and experimental force vs. displacement plots are provided in Fig 3.17 to 3.19 for medium and very dense CU filter sand (Trautmann and O'Rourke 1983) as well as RMS graded sand (Olson, 2009). The analytical force vs. displacement relationship is based on E_{70-H} as explained in Section 3.4.2. The lateral pipe forces are shown as dimensionless force $F' = F/(\gamma_d H_c DL)$, and lateral pipe displacements are shown as dimensionless displacement $Y' = Y/D$.

The numerical simulations for medium CU filter sand in Fig. 3.17 agree well with the test data for $H_c/D = 3.5$ and 8. Overall, the analytical results are consistent with the data trends for $H_c/D = 5.5$ and 11, but tend to over predict peak loads by 7 – 8 %.

The numerical simulations for very dense CU filter sand in Fig. 3.18 agree well with the experimental data for all H_c/D . The analytical peak forces are larger than the measured forces by about 2 – 7 %.

Figure 3.19 shows the dimensionless force vs. dimensionless displacement plot predicted by numerical simulation for RMS graded sand compared with the dimensionless force vs. dimensionless displacement data for the three 2-D tests in RMS sand by Olson (2009). The numerical simulation for RMS graded sand shows favorable agreement with the experimental data for all Olson dry sand tests. The numerical simulation compares favorably in terms of dimensionless force-displacement curve, except for pre-peak behavior where the experimental data tends to higher values than shown by the numerical simulation. The analytical peak forces are within 3 – 6 % of the experimental peak forces.

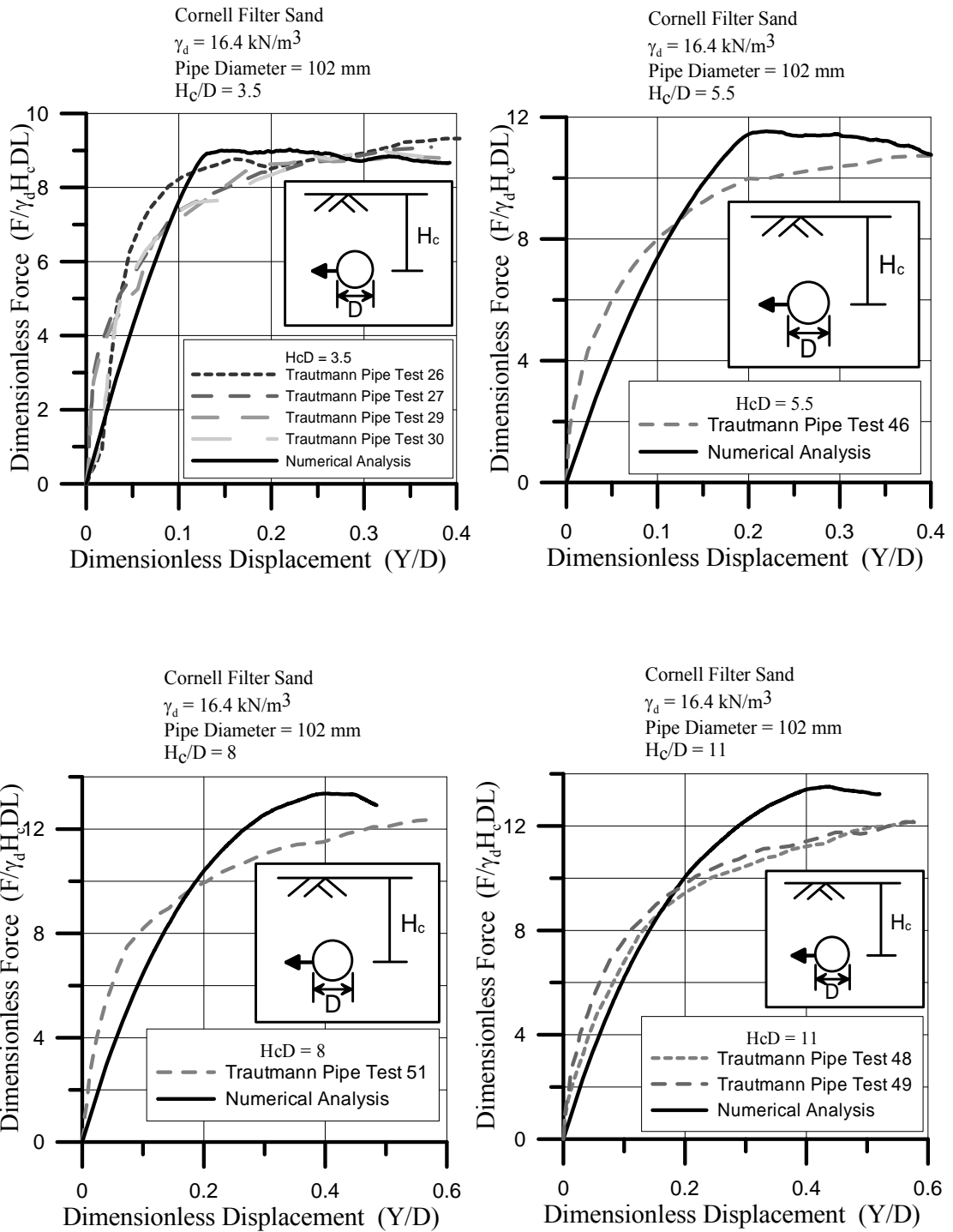


Figure 3.17 Dimensionless Force vs. Displacement Curves of Medium CU Filter Sand

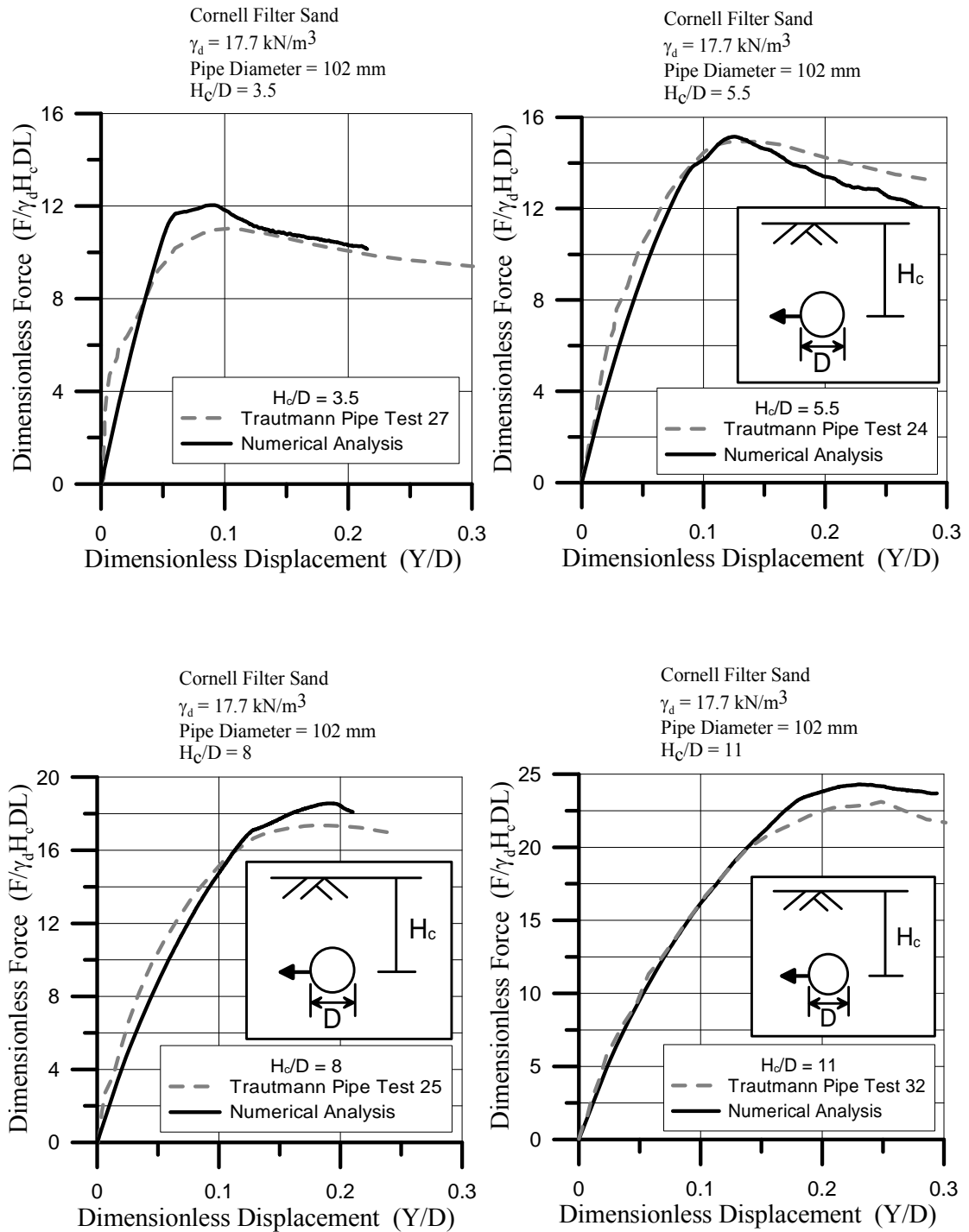


Figure 3.18 Dimensionless Force vs. Displacement Curves of Very Dense CU Filter Sand

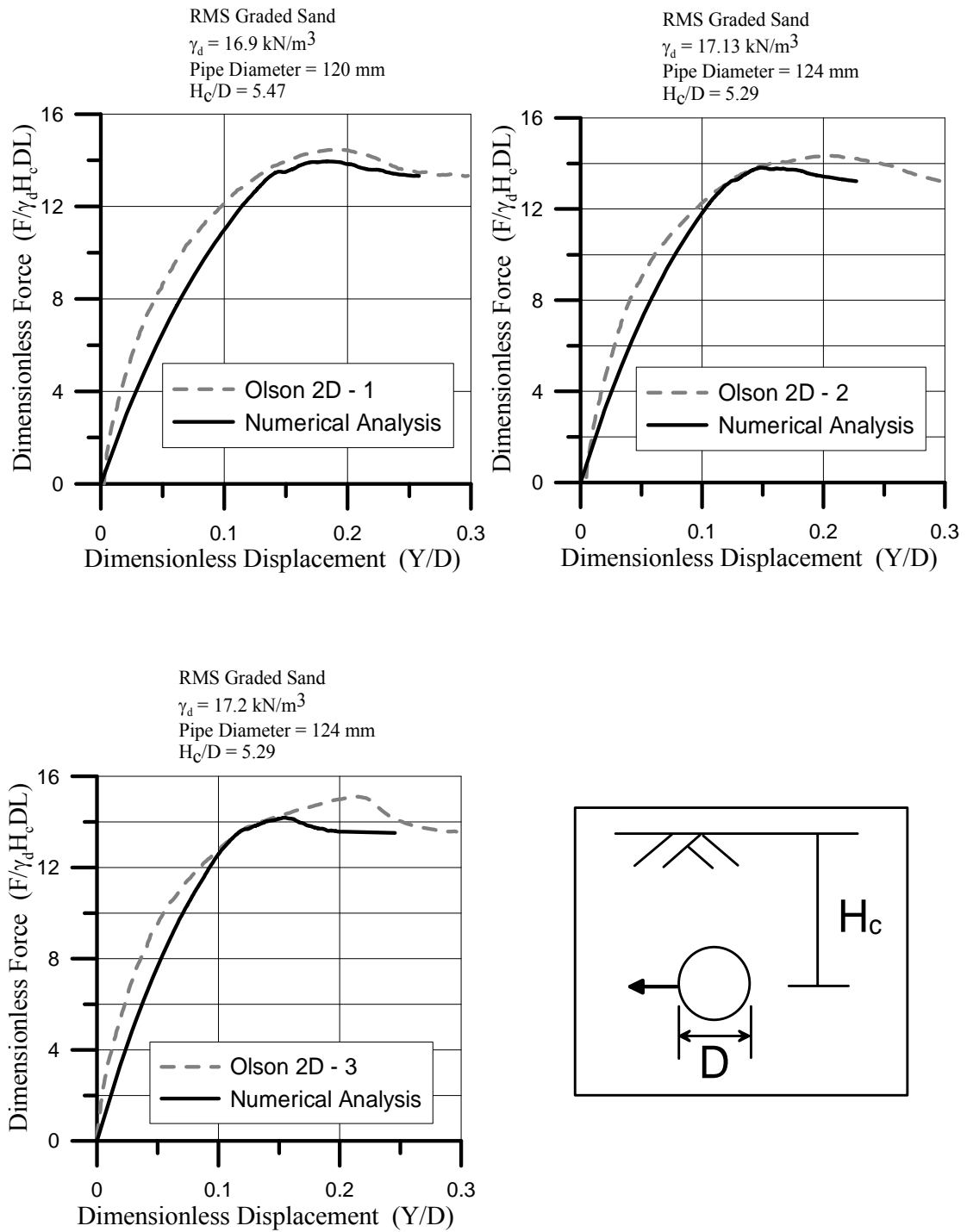


Figure 3.19 Dimensionless Force vs. Displacement Curves of RMS Graded Sand

3.9 Soil Strength Properties and Finite Element Analyses Model for Partially Saturated RMS Graded Sand

In the analyses for partially saturated RMS graded sand, the total unit weight of the sand γ_{total} , as well as ϕ_{ds-p} , and ϕ_{ps-p} were used in the analyses. Input parameters for partially saturated RMS graded sand strength were obtained from DS tests performed by Olson (2009). The results from 7 DS tests with water contents = 4 – 5 % and $\gamma_d = 15.8 \text{ kN/m}^3$ (approximately equal to $\gamma_{total} = 16.5 \text{ kN/m}^3$) are plotted in

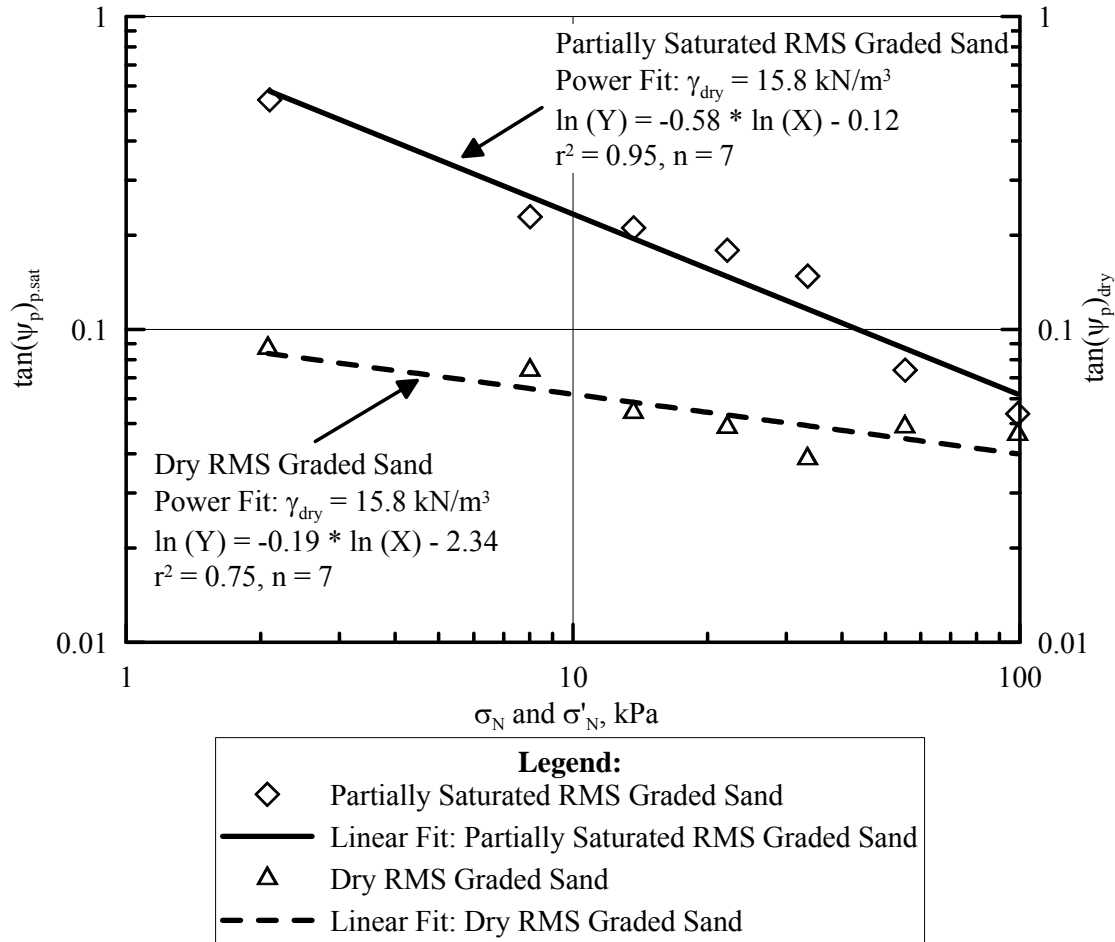


Figure 3.20 $\tan(\psi_p)_{p.sat}$ vs. σ_N for RMS Graded Sand at $\gamma_{dry} = 15.8 \text{ kN/m}^3$ ($\gamma_{total} = 16.5 \text{ kN/m}^3$) (Olson, 2009)

Fig. 3.20. The figure shows the relationship between $\tan(\psi_p)$ value for partially saturated RMS graded sand, $\tan(\psi_p)_{p.sat}$, and σ_N , which has $r^2 = 0.95$. The nonlinear regression equation for $\tan(\psi_p)_{p.sat}$ is

$$\tan(\psi_p)_{p.sat} = \exp\{-0.58 \ln(\sigma_N) - 0.12\} \quad (3.14)$$

Rowe (1962, 1969) proposed the flow rule to account for the cohesion introduced in partially saturated sand as

$$\tan \phi_{ds-p} + \frac{c_{ds}}{\sigma_N} = \sin(\phi_{crit}) + \tan(\psi_p)_{p.sat} \quad (3.15)$$

in which c_{ds} is soil cohesion measured from DS test. Olson (2009) reported c_{ds} for partially saturated RMS graded sand as 2.1 kPa at $\gamma_{dry} < 16.0 \text{ kN/m}^3$ and ϕ_{crit} as 43.6° .

Olson performed 19 DS tests and provided τ_p/σ_N and $(\psi_p)_{p.sat}$ data for partially saturated RMS graded sand. The data were digitized and plotted in Fig. 3.21. The nonlinear regression for τ_p/σ_N vs. $(\psi_p)_{p.sat}$ has $r^2 = 0.91$ and the resulting regression equation is

$$\frac{\tau_p}{\sigma_N} = \exp(0.027(\psi_p)_{p.sat} - 0.453) \quad (3.16)$$

The calculated ϕ_{ds-p} from Eqn. 3.15 is converted to, ϕ_{ps-p} using the relationship derived by Olson (2009) as

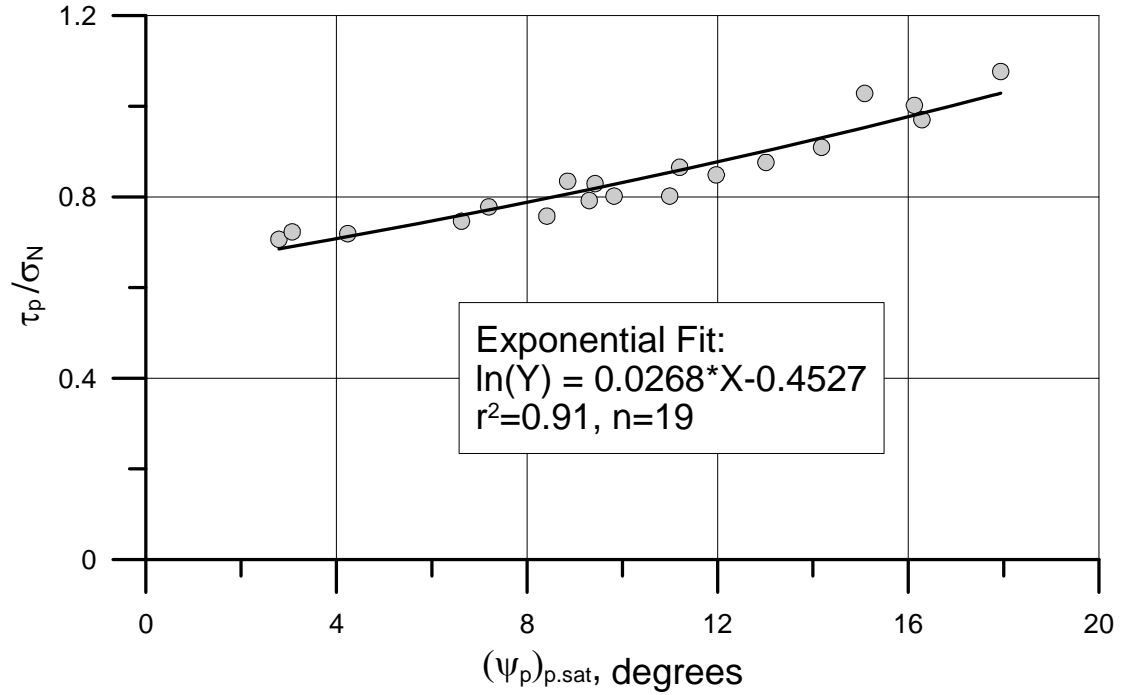
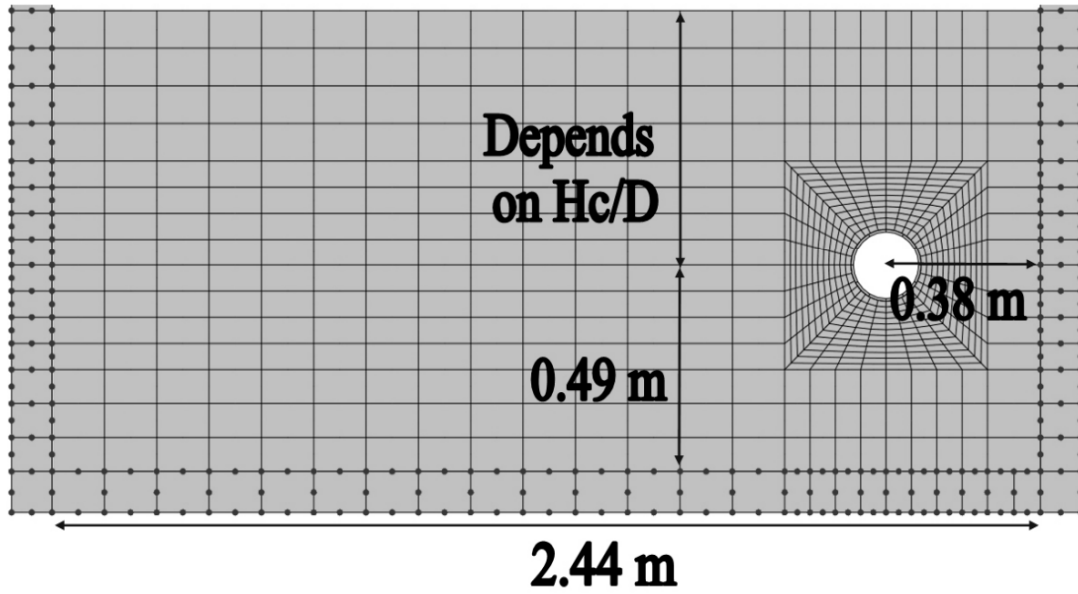


Figure 3.21 Plot of τ_p/σ_N vs. $(\psi_p)_{p.sat}$

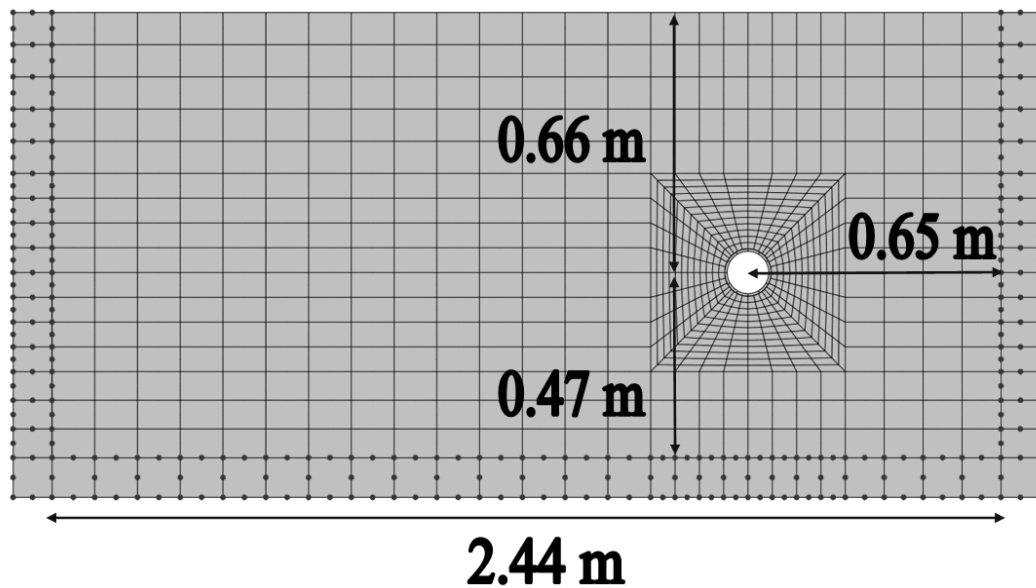
$$\sin \phi_{ps-p} = \frac{\frac{\tau_p}{\sigma_N}}{\left[1 + \frac{\tau_p}{\sigma_N} \tan(\psi_p)_{p.sat} + \frac{c_{ps} \cot \phi_{ps-p}}{\sigma_N} \right] \cos(\psi_p)_{p.sat}} \quad (3.17)$$

in which c_{ps} is a cohesion in plane strain parameters. Equation 3.17 is a transcendental equation and ϕ_{ps-p} must be solved iteratively. Olson (2009) showed that Eqn. 3.17 reduces to Eqn. 3.4 for zero cohesion in dry sand.

The FE mesh was developed to replicate the geometry and material properties of the soil, pipe and experimental facilities in partially saturated RMS graded sand tests. Figure 3.23 shows the geometry of the numerical model for analyses of partially saturated RMS graded tests referred to a) Olson 2-D Moist 3, 5, and 6 test



a) Olson 2-D Moist
3, 5, and 6 Test (2009)



b) Olson 2-D Moist 1 Test (2009)

Figure 3.22 Geometry of the Partially Saturated RMS Graded Sand Test (Olson, 2009)

(2009), and b) Olson 2-D Moist 1 test (2009). Olson performed tests with two different boxes with an inner length of 2.44 m, pipe length = 2.44 m, and pipe wall thickness = 6.4 mm. For the 2-D Moist Tests 3, 5, and 6, $H_{bt} = 0.49$ m, $H_{bk} = 0.38$ m, $D = 174$ mm, and H_c was varied to obtain different H_c/D . For the 2-D Moist Test 1, $H_{bt} = 0.47$ m, $H_{bk} = 0.65$ m, $D = 124$ mm, and $H_c = 0.66$ m.

The γ_d measured by Olson (2009) was used with Eqn. 3.16 to evaluate $(\psi_p)_{p.sat}$, where σ_N is taken as σ_{vc} , which is the vertical total stress at the pipe centerline. With $\tan(\psi_p)_{p.sat}$ estimated relative to σ_{vc} , Eqns 3.17, 3.18, and 3.19 were used to evaluate ϕ_{ps-p} .

As discussed in Section 3.7, the model proposed by Anastasopoulos, et al. (2007) is used to represent strain softening, and a FORTRAN subroutine prepared by Robert and Soga (2009) was used to apply the softening behavior in the 2-D FE simulation of soil-pipeline interaction. From the partially saturated RMS graded DS test (Olson 2009) and Eqn. 3.13, a value of $\gamma_f^p = 0.4$ is calculated. Olson (2009) reported ϕ_{crit} for partially saturated RMS graded sand as 43.6° and soil cohesion for plane strain, $c_{ps} = 1.2$ kPa. Olson (2009) reported that no cohesion was observed in DS tests for partially saturated RMS graded sand at large displacements. To represent the c_{ps} at large displacement (c_{ps-ld}), the model was set to linearly diminish c_{ps} to residual values at 0, from the plastic strain at ϕ_{ps-p} to γ_f^p . A small residual values of $c_{ps-ld} = 0.1$ kPa at large displacements was used to promote numerical stability. Sensitivity analyses were performed with different c_{ps-ld} values to show that the range of $c_{ps-ld} = 0.1$ kPa had negligible effect on the results.

Table 3.4 summarizes the test dimensions and soil properties associated with

the full scale 2-D tests with partially saturated RMS graded sand performed by Olson (2009).

Table 3.4 Summary of the Input Parameters Used in Finite Element Analyses of Partially Saturated RMS Graded Sand

Test No.	H _c /D	Diameter (mm)	Length (mm)	γ _{total} (kN/m ³)	γ _d (kN/m ³)	φ' _{ps-p} (degrees)	Ψ _p (degrees)
2-D Moist Test 3	3.5	0.174	2.44	16.7	15.9	44.0	13.0
2-D Moist Test 1	5.29	0.124	2.44	16.7	16.1	44.0	12.5
2-D Moist Test 6	6.5	0.174	2.44	16.5	15.8	43.4	9.2
2-D Moist Test 5	7.5	0.174	2.44	16.5	15.8	43.2	8.5

3.10 Comparison of Partially Saturated RMS Graded Soil Force vs. Displacement Curves for Analytical and Test Results.

Data obtained by Olson (2009) for partially saturated RMS graded sand from 4 large-scale 2-D tests were used to determine E_{70-H} according to K₇₀- procedure as discussed in Section 3.4.2. Using the σ_{vc} and γ_{total} from the 4 Olson moist tests, Eqn. 3.12 was used to predict E_{70-H} = 2500 kPa, 2400 kPa, 3700 kPa, and 3300 kPa for 2-D Moist Tests 1, 3, 5, and 6, respectively.

Comparisons between the analytical force vs. displacement plots using E_{70-H},

and the experimental force vs. displacement plots (Olson, 2009) are provided in Fig 3.23 for partially saturated RMS graded sand. The results have been plotted in dimensionless form. The predicted E_{70-H} using Eqn. 3.12 tends to under predict measured loads by 30 – 70 % in terms of pre-peak behavior. In general, E_{70-H} for partially saturated sand is stiffer than dry sand due to suction. The suggested simplified E_{70-H} for partially saturated sand is approximately $E_{70-H \text{ sat}} \cong 2E_{70-H}$. Using this approximation, the following empirical equation applies for the partially saturated RMS graded sand

$$\frac{E_{70-H \text{ sat}}}{P_a} = 2 \times 10^{-0.264} \left[\frac{\gamma_t}{\gamma_w} \left(\frac{\sigma_{vc}}{P_a} \right)^{0.075} \right]^{10.42} \quad (3.18)$$

Table 3.5 summarizes $E_{70-H \text{ sat}}$ associated with the full scale 2-D tests with partially saturated RMS graded sand performed by Olson (2009), in which $E_{70-H \text{ sat}}$ is determined by using Eqn. 3.18.

Table 3.5 Summary of $E_{70-H \text{ sat}}$ Used in Partially Saturated RMS Graded Sand Lateral Pipe Movement Simulation

Test No.	H_c/D	$E_{70-H \text{ sat}}$ (kPa)	Test No.	H_c/D	$E_{70-H \text{ sat}}$ (kPa)
2-D Moist Test 3	3.5	4700	2-D Moist Test 6	6.5	6600
2-D Moist Test 1	5.29	5000	2-D Moist Test 5	7.5	7400

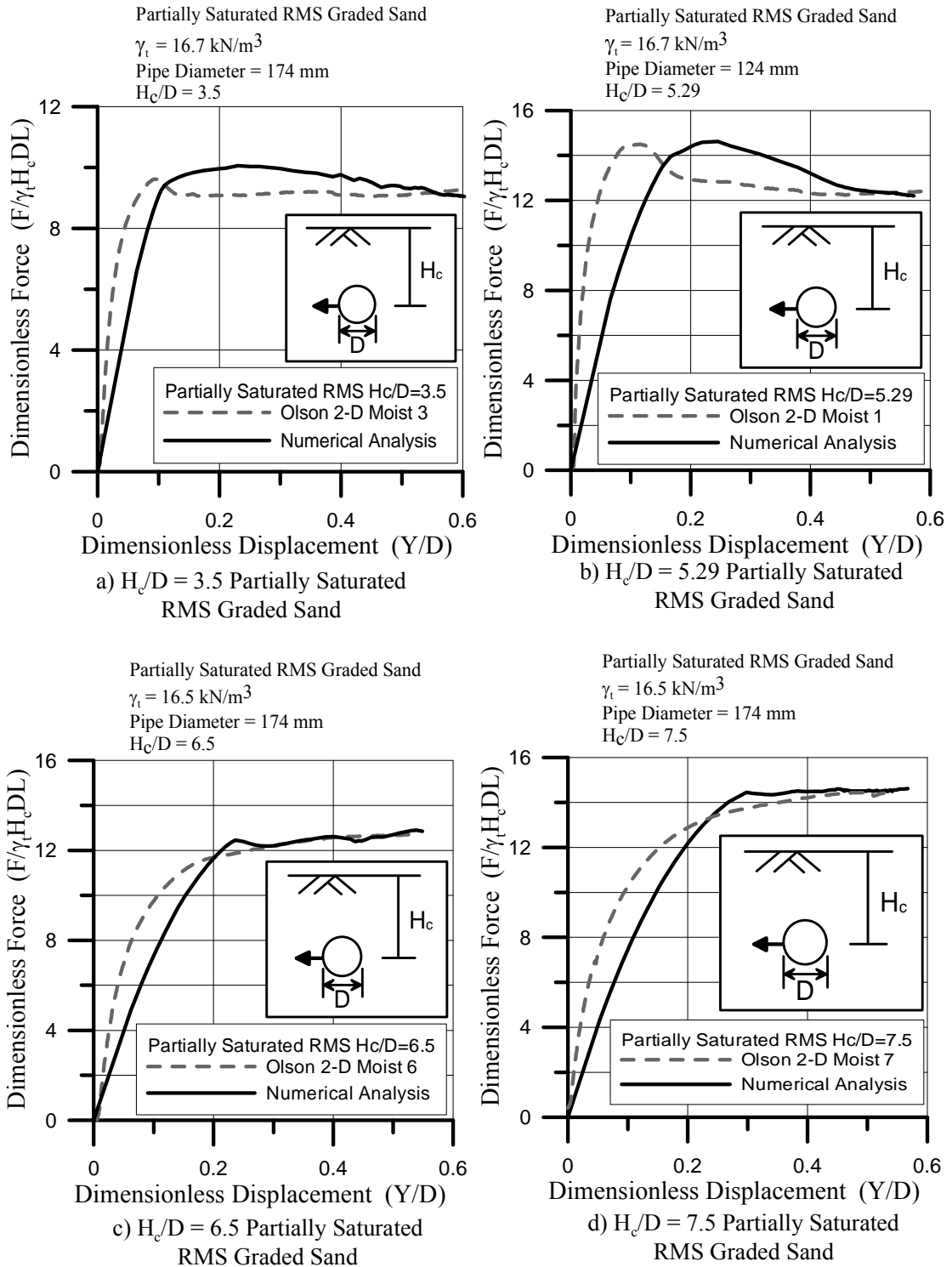


Figure 3.23 Dimensionless Force vs. Displacement Curves of Partially Saturated RMS Graded Sand Using E_{70-H}

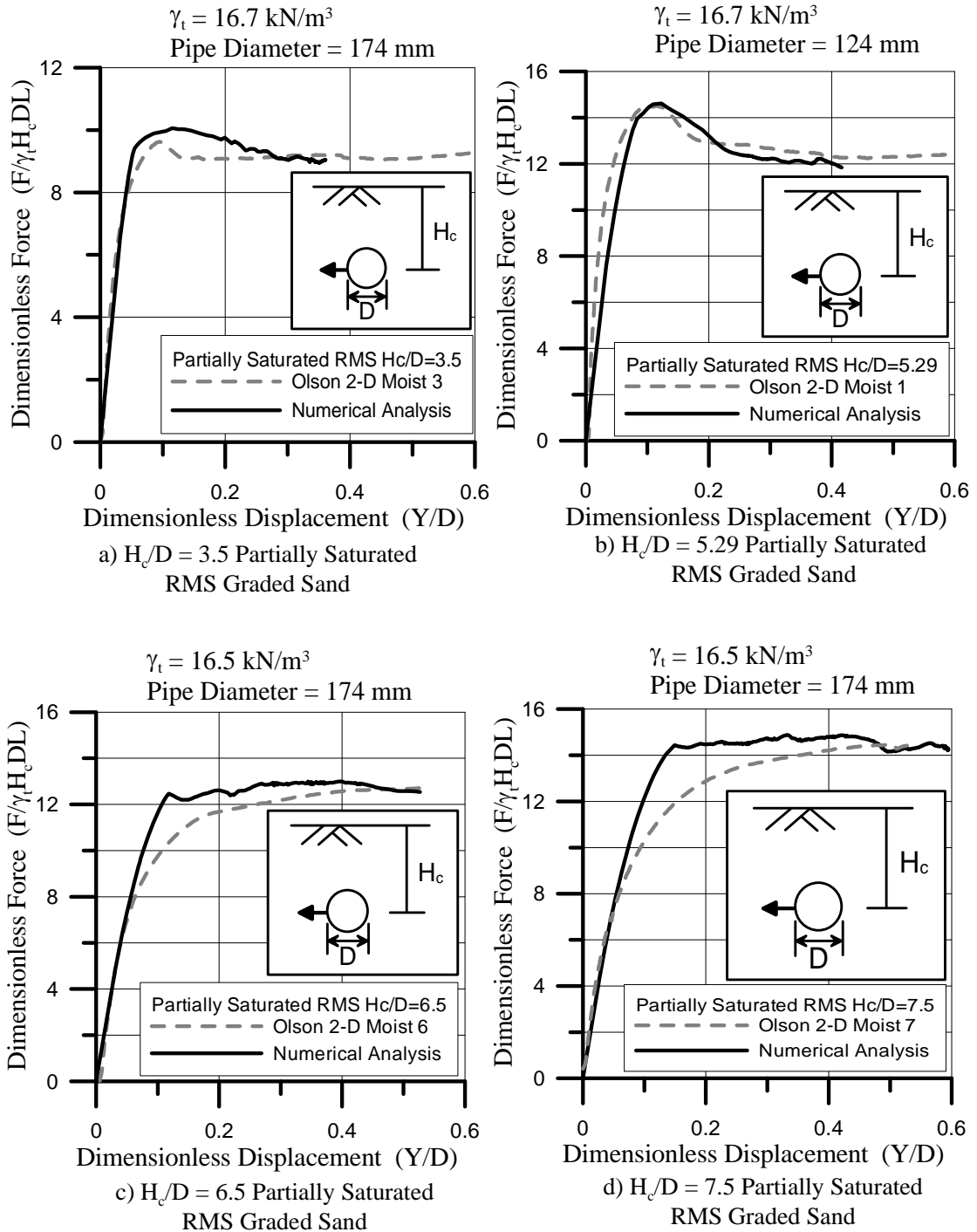


Figure 3.24 Dimensionless Force vs. Displacement Curves of Partially Saturated RMS Graded Sand Using $E_{70-H \text{ sat}}$

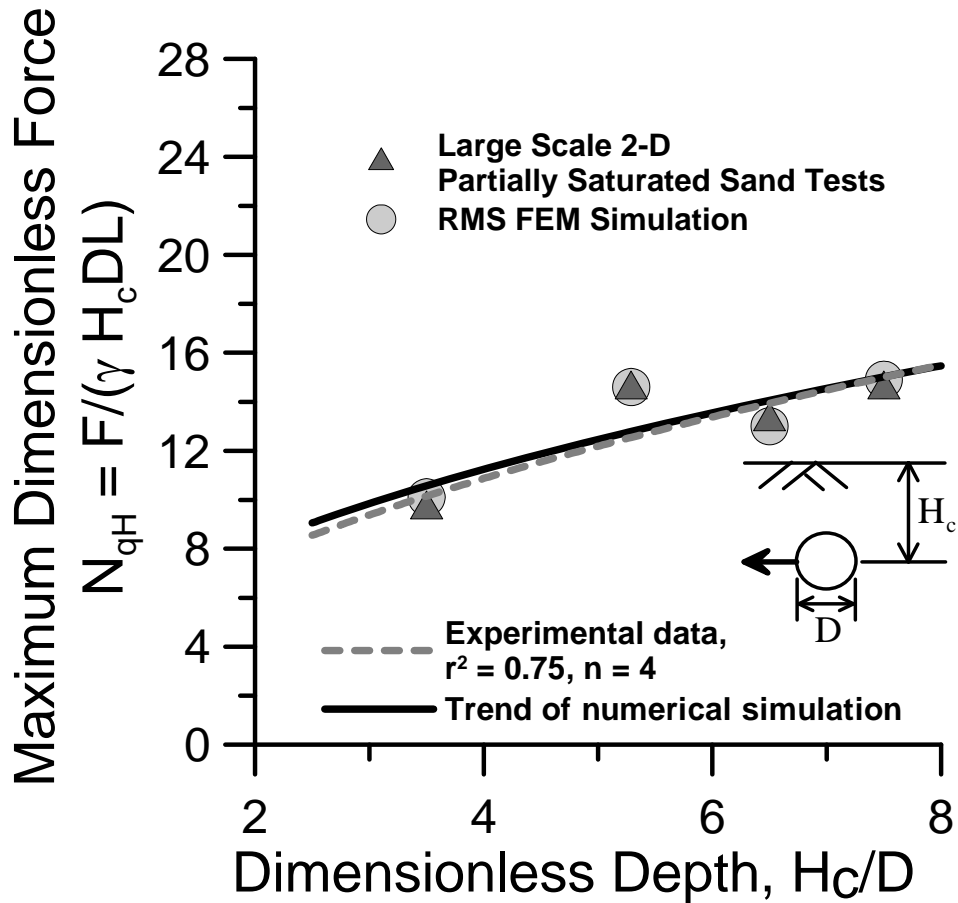


Figure 3.25 Plot of N_{qH} vs. H_c/D for Partially Saturated RMS Graded Sand

Figure 3.24 shows the dimensionless force vs. dimensionless displacement plots predicted by numerical simulation using the soil properties test dimensions in Table 3.4 and 3.5. The numerical simulations for partially saturated RMS graded sand shows favorable agreement with the experimental data for all Olson moist tests. The numerical simulation compares favorably in terms of pre-peak, peak force, and post-peak behavior. The numerical simulation results in a softer soil reaction within the equivalent elastic range for $H_c/D = 5.29$.

The FE analyses and 2-D test results for partially saturated RMS graded soil are compared in Fig. 3.25, in which maximum dimensionless force is plotted as a

function of dimensionless depth. There is an excellent agreement among the data for all H_c/D . In general, the FE analyses results differ from the measured dimensionless peak force by only $-1.5 \sim 8 \%$.

CHAPTER 4

LATERAL PIPE MOVEMENT IN SEMI-INFINITE SOIL AT VARIABLE DEPTHS

4.1 Introduction

In this chapter, the finite element (FE) models for simulating lateral pipe movement under experimental conditions are expanded to analyze soil-pipe interaction in a semi-infinite soil medium. The modeling procedures using infinite elements are described, and the semi-infinite soil medium results are compared with the numerical results presented in Chapter 3 as well as large-scale experimental measurements. FE simulations were run for layered semi-infinite soil conditions in which sand strength parameters were varied with depth and related to accurate assessments of normal stress, σ'_N . The results are compared with FE results for a more simple modeling process in which the sand friction and dilation angles are related only to the vertical effective stress at the pipe centerline. Finally, relationships between maximum lateral pipe force and pipe depth are developed for semi-infinite soil conditions and H_c/D increasing to 100.

4.2 Finite Element Model

FE analyses were run with a semi-infinite soil medium using 'infinite elements' as proposed by Ungless (1973) and Bettess (1977), and improved by Zienkiewicz et al. (1983). The infinite elements are defined over semi-infinite domains with decay functions and are mapped onto the finite element domain. These

infinite elements represent a semi-infinite soil medium and are attached to 8-node quadratic elements in closer proximity to the pipe. The infinite element formulations proposed by Zienkiewicz et al. (1983) are used in this study.

Figure 4.1 shows the typical geometry of the model used for simulating lateral soil-pipe interaction in both dry and partially saturated sand. In the figure, H_c is the depth from the top of the soil to the center of the pipe, and D is the external diameter of the pipe. As described in Chapter 3, 8-node biquadratic, plane strain, quadrilateral, reduced integration elements (element type CPE8R) were used to represent the soil around the pipe from A to B, and from the surface to 1.7-m – 2.6-m depth, depending

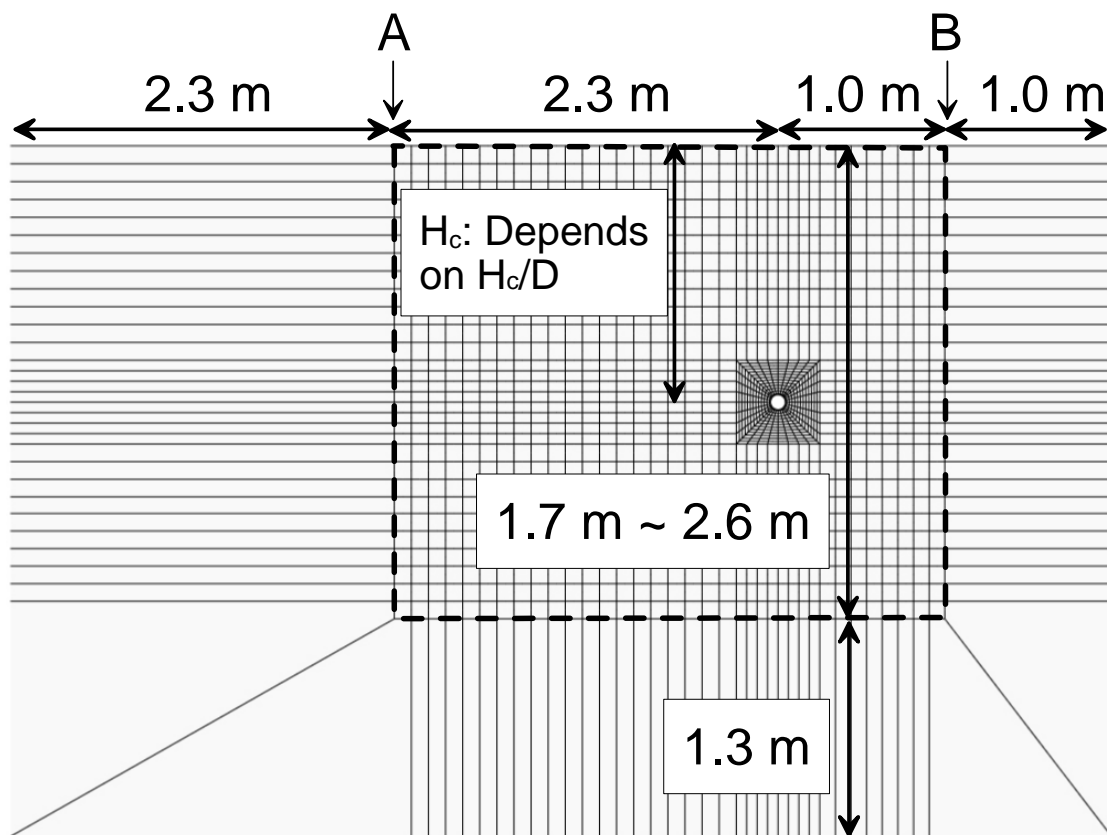


Figure 4.1 Geometry for the Numerical Analysis of Each Test

on the H_c/D conditions being analyzed. Five-node quadratic, plane strain, one-way infinite quadrilateral elements (element type CINPE5R) are used to represent the semi-infinite soil medium. The infinite elements are located outside of the CPE8R elements and are 2.3 m, and 1.0 m in width. The infinite elements at the base of the model are 1.3 m in height. The pipe was modeled as a rigid cylinder. The interface between the soil and pipe has a friction angle of $0.6 \phi'_{ds-p}$ on the basis of direct shear (DS) tests performed by Trautmann (1983) and Olson (2009). The interface interaction is modeled through surface-based contact, in which separation and slip between soil and pipe are allowed. A refined mesh was used within a distance of approximately two pipe diameters from the center of the pipe. The thickness of the elements within the refined mesh was taken as the shear band thickness observed during DS test (Roscoe, 1970; Vardoulakis and Graf, 1985; Muhlhaus and Vardoulakis, 1987; Bardet and Proubet, 1992; Huang, et al., 2002; Olson, 2009). Approximately 1482 to 4852 elements were used in the meshes to simulate different H_c/D conditions. The geostatic load is applied to the soil and pipe at the beginning of the analysis under $K_o = 1$ condition. Lateral pipe movement is expressed by imposing a lateral displacement boundary condition to all nodes in the pipe.

Input parameters for dry soil strength were obtained from the equations developed from DS tests results as discussed in Section 3.3. The peak angle of dilation, ψ_p was evaluated using Eqn. 3.2, where σ'_N is taken as σ'_{vc} , which is the vertical effective stress at the pipe centerline. With ψ_p estimated relative to σ'_{vc} , Eqns 3.3 and 3.7 were used to evaluate ϕ'_{ps-p} . Critical friction angle, ϕ'_{crit} , was selected as 38.6° for CU filter sand and 40.8° for dry RMS graded sand.

The FE analyses were performed for the same dry sand experimental results as

described in Chapter 3. Table 3.1 summarizes the input parameters used in lateral pipe movement analyses.

Input parameters for partially saturated soil strength were obtained from the equations developed from DS tests results as discussed in Section 3.9. The γ_d measured by Olson (2009) was used with Eqn. 3.16 to evaluate $(\psi_p)_{p.sat}$, where σ_N is taken as σ_{vc} , which is the vertical total stress at the pipe centerline. With $\tan(\psi_p)_{p.sat}$ estimated relative to σ_{vc} , Eqns 3.17, 3.18, and 3.19 were used to evaluate ϕ_{ps-p} . Olson (2009) reported ϕ_{crit} for partially saturated RMS graded sand as 43.6° and soil cohesion for plane strain, $c_{ps} = 1.2$ kPa. Olson (2009) reported that no cohesion was observed in DS tests for partially saturated RMS graded sand at large displacements. To represent the c_{ps} at large displacement (c_{ps-ld}), the model was set to linearly diminish c_{ps} to residual values at 0, from the plastic strain at ϕ_{ps-p} to γ_f^p . A small residual values of $c_{ps-ld} = 0.1$ kPa at large displacements was used to promote numerical stability. Sensitivity analyses were performed with different c_{ps-ld} values to show that the range of $c_{ps-ld} = 0.1$ kPa had negligible effect on the results.

As discussed in Section 3.7, the model proposed by Anastasopoulos, et al. (2007) was used to represent strain softening, and a FORTRAN subroutine prepared by Robert and Soga (2009) was used to apply the softening behavior in the 2-D FE simulation of soil-pipeline interaction. From DS test results from Olson (2009) and Eqn. 3.15, a value of $\gamma_f^p = 0.3$ and 0.4 were calculated for dry sand and partially saturated RMS graded sand, respectively. The FE analyses were performed for the same partially saturated RMS graded sand experimental results as described in Chapter 3. Table 3.4 summarizes the input parameters used in lateral pipe movement in partially saturated semi-infinite soil.

4.3 Comparison of Peak Forces for Semi-Infinite Soil and Experimental Simulations with Measured Peak Forces

Figure 4.2 plots the dimensionless maximum lateral forces from the FE analyses for a semi-infinite soil medium, N_{q-si} , vs. the dimensionless lateral forces measured in the large-scale experiments, N_{q-m} . The values of N_{q-m} were determined as described in Chapter 3. There is favorable agreement between N_{q-si} and N_{q-m} , with all N_{q-si} within $\pm 10\%$. In general, N_{q-si} for CU filter sand is larger than N_{q-m} by 1 – 7 %, whereas the N_{q-si} for RMS graded sand is smaller than N_{q-m} by 4 – 10 %. The average difference between N_{q-si} and N_{q-m} is 4.6 %, compared with a 5.1 % difference between the analytical and experimental results described in Chapter 3.

Figure 4.3 plots the dimensionless maximum lateral forces from the FE analyses for a semi-infinite soil medium, N_{q-si} , vs. the dimensionless lateral forces from the FE analyses of the large-scale tests, N_{q-e} . There is favorable agreement between N_{q-si} and N_{q-e} , with all N_{q-si} within $\pm 10\%$. In general, N_{q-si} is smaller than N_{q-e} by 0.1 – 2.9 %. The average difference between N_{q-si} and N_{q-e} is 1.9 %.

As illustrated in Figs. 4.2 and 4.3, N_{q-si} for the semi-infinite soil analyses are very close to N_{q-e} and N_{q-m} , with N_{q-si} about 2.2 % lower than N_{q-e} on average. It is instructive to examine the 2-D displacements from the semi-infinite soil and experimental simulations for the same pipe diameter, H_c/D , and soil properties.

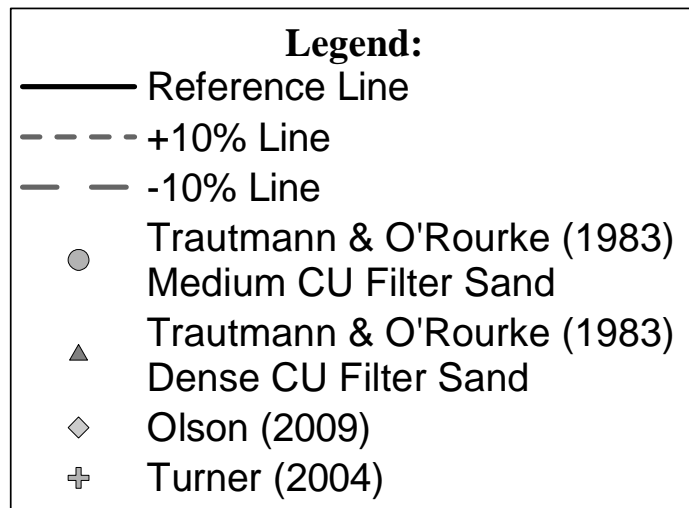
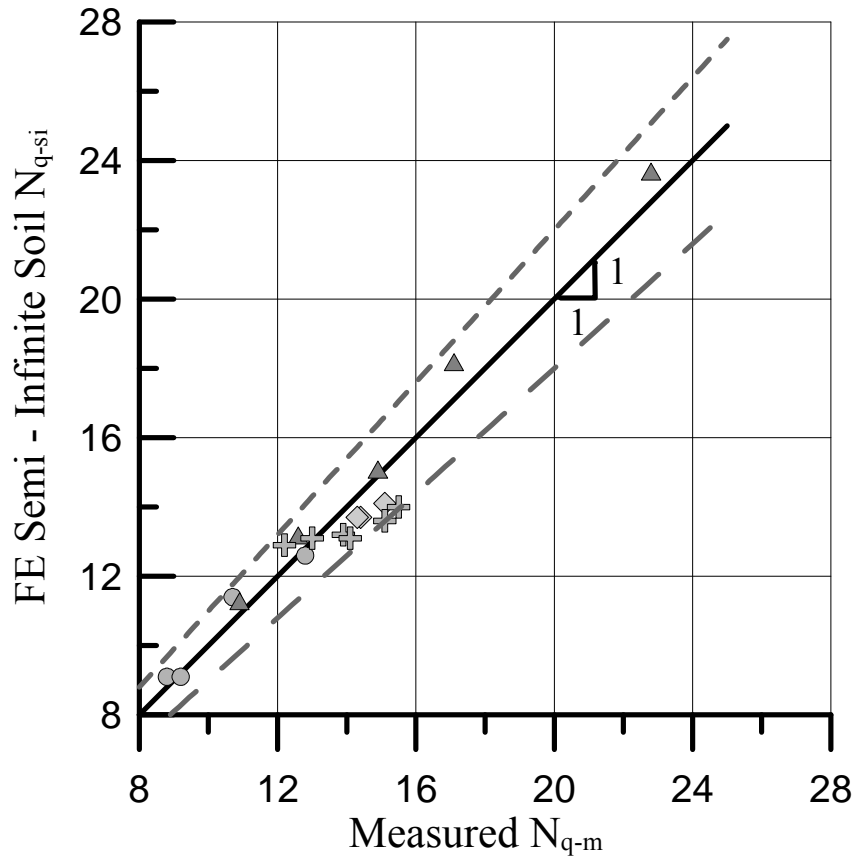


Figure 4.2 Comparison of FE Semi-Infinite Soil N_{q-si} vs. Measured N_{q-m}

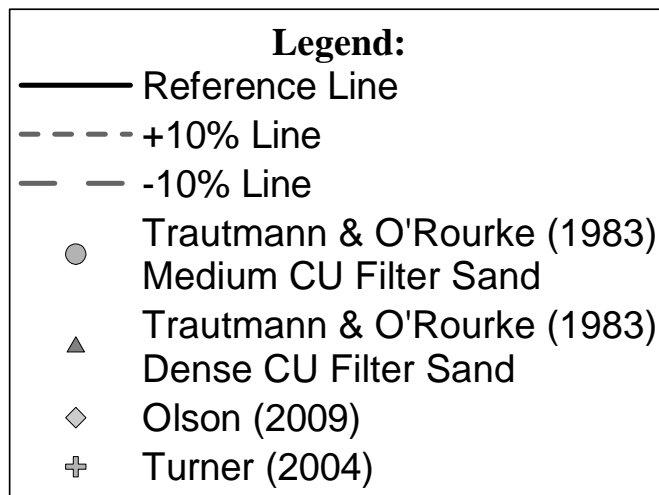
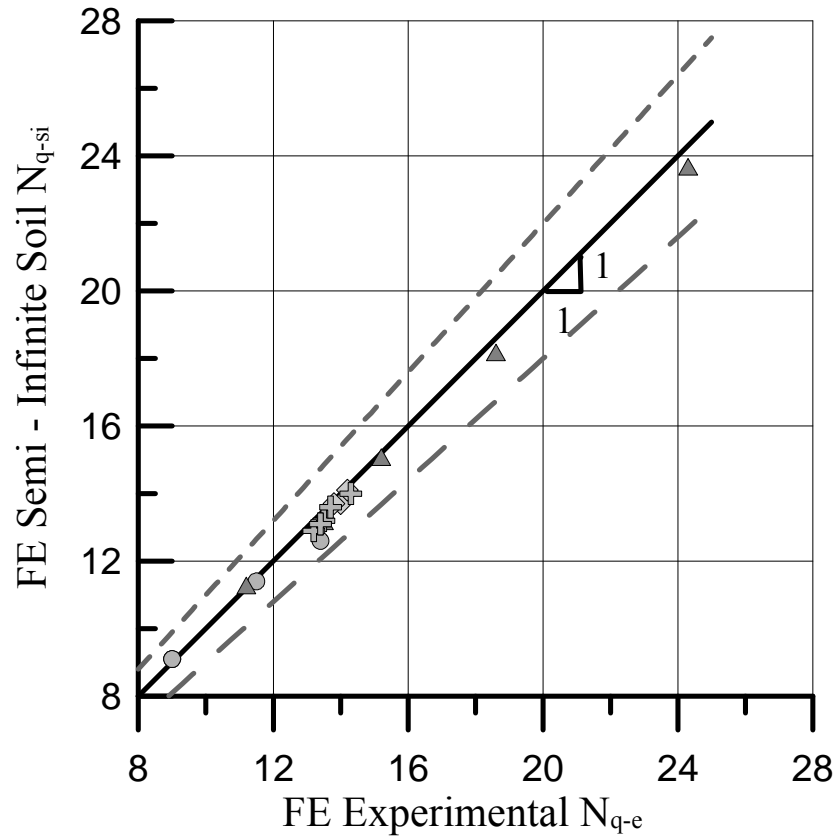


Figure 4.3 Comparison of FE Semi-Infinite Soil N_{q-si} vs. FE Experimental N_{q-e}

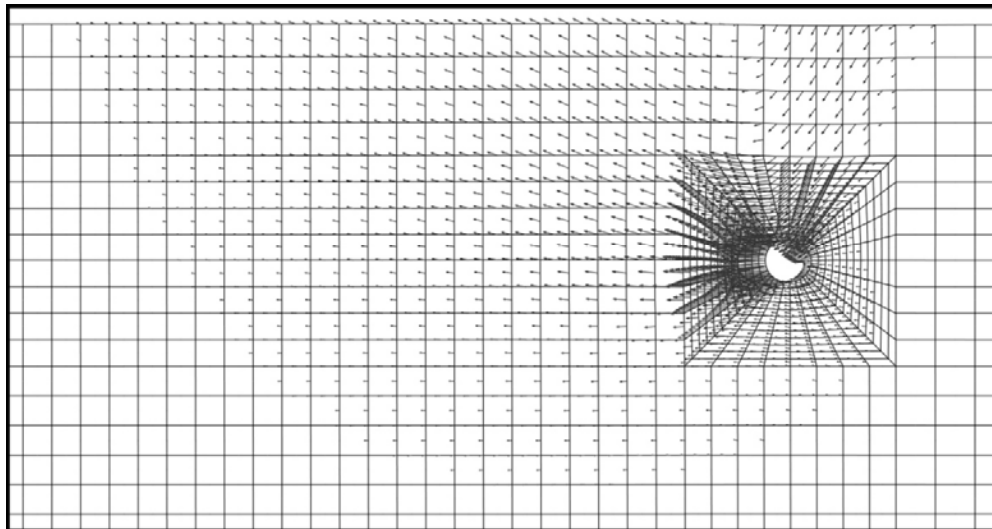
Figure 4.4 shows 2-D plots of soil displacement patterns for a pipe with $D = 102$ mm, $H_c/D = 5.5$ in very dense dry CU filter sand at peak load for semi-infinite soil and experimental simulations. The scales for vector displacement and cross-section dimensions are identical. There are notable differences in the magnitude and pattern of soil movement. The FE simulation of the large-scale experiments results in relatively large horizontal displacement near the base of the test basin due to horizontal sliding of soil along the experimental timber interface. In addition, relatively large soil movement occurs between the pipe and vertical test basin wall. Because the soil is modeled as a continuum with break-away boundary elements between the soil and wall, forward pipe movement causes lateral deformation of the relatively narrow soil column behind the pipe. This deformation leads to larger soil displacements compared with those of the semi-infinite soil mass model, with larger forward pipe movement at a slightly lower horizontal force. Under these conditions, the stiffness of the lateral force vs. displacement relationship for the experimental simulation is less than that for the semi-infinite soil.

In contrast, there are no large horizontal semi-infinite soil displacements behind the pipe due to the infinite lateral boundary conditions. The vectors of displacement are inclined, with a significant downward component of movement behind the pipe.

When compared with the actual displacements observed in the large-scale experiments (Trautmann, 1983; Turner, 2004), the semi-infinite model provides a better representation of dry soil movement behind the pipe, but does not account for horizontal soil sliding along the base of the experimental test box. Hence, both the semi-infinite and experimental simulations capture important aspects of the soil mass

Vector Scale
→
0.03 m

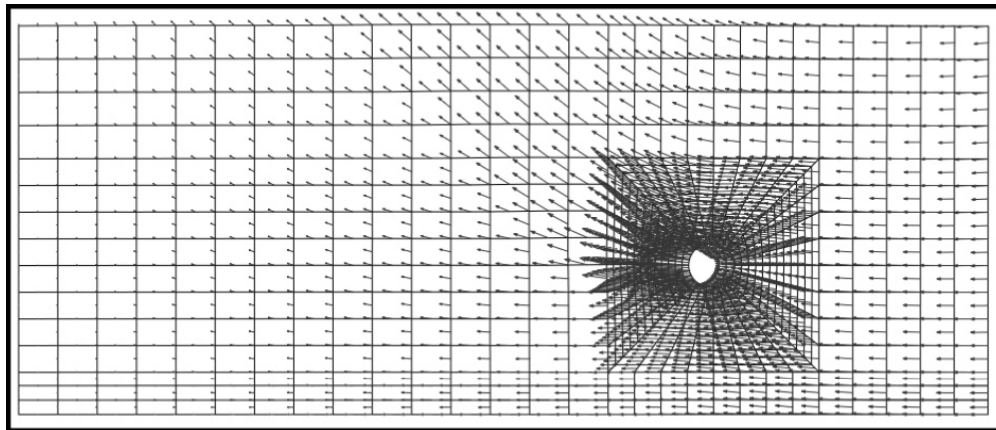
Cross-Section Scale
↔
0.2 m



a) Very Dense CU Filter Sand, $H_c/D = 5.5$
FE Semi-Infinite Soil

Vector Scale
→
0.03 m

Cross-Section Scale
↔
0.2 m



b) Very Dense CU Filter Sand, $H_c/D = 5.5$
Experimental Simulation

Figure 4.4 Displacement Pattern for Very Dense CU Filter Sand FE Semi-Infinite Soil
and Experimental Simulation at $H_c/D = 5.5$

movement in the actual experimental test basins, and the numerical results from both methods of analysis are clustered around the experimental data in Fig. 3.8 and 4.2 and are comparable to each other as shown in Fig. 4.3.

4.4 Comparison of Semi-Infinite Numerical and Experimental Results for Maximum Force at Variable Depths

Figure 4.5 compares N_{q-si} and N_{q-m} , in which the dimensionless force is plotted as a function of the dimensionless depth. N_{q-e} is also plotted in the figure for reference. There is a favorable agreement among the data for all H_c/D . In general N_{q-si} overpredicts N_{q-m} by 1 – 7 %. Overall, the average difference between N_{q-si} and N_{q-m} for dry CU filter sand is 3.3 %.

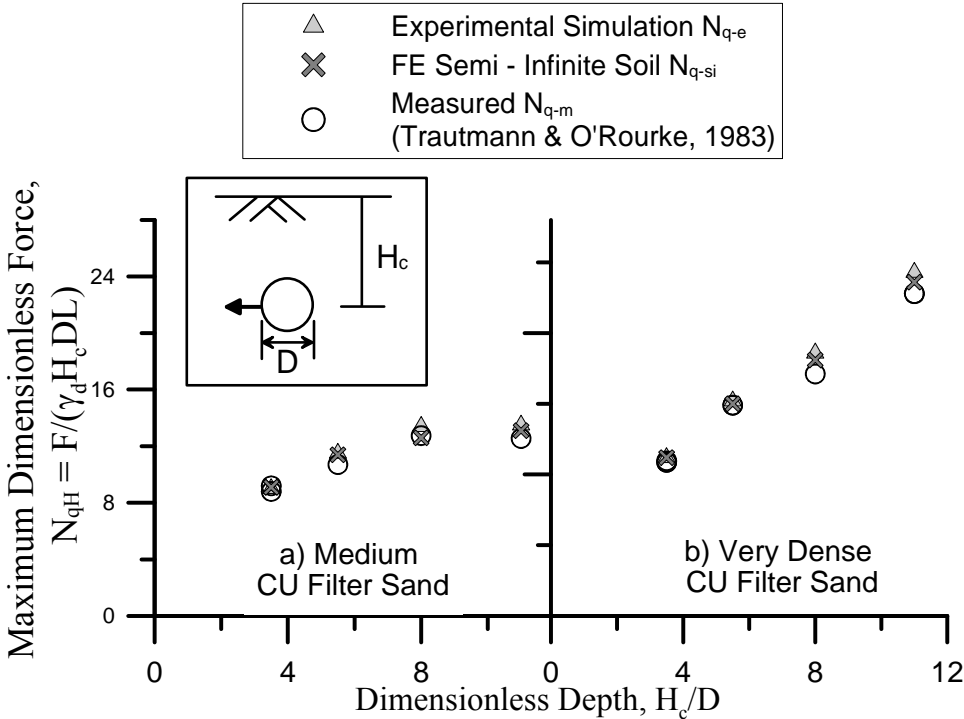


Figure 4.5 Comparison Plot of N_q vs. H_c/D for CU Filter Sand

Figure 4.6 summarizes N_{q-si} vs. H_c/D for all dry sand tests with CU filter and RMS graded sand. Both N_{q-si} and N_{q-m} are plotted for medium, dense, and very dense sand as characterized in Table 3.2. Nonlinear regression lines are plotted for the experimental data and semi-infinite soil numerical results pertaining to medium and very dense sand. Also plotted is the regression for dense sand semi-infinite soil numerical results. Experimental data for dense dry sand are available from Olson (2009) and Turner (2004) for $H_c/D = 5.5$ only. To produce a curve for dense sand, FE analyses were performed for $H_c/D = 3.5, 5.5, 8, 11$, and the regression line for those results is shown in the figure. The numerical results exceed measured peak forces by about 3.2 % for very dense sand, and 3.3 % for medium sand with $H_c/D \leq 11$.

4.5 Comparisons of Force vs. Displacement Curves for Semi-Infinite Soil and Experimental Simulations with Measured Force vs. Displacement Curves

Semi-infinite soil models were developed that used an equivalent modulus according to the K_{70} procedure discussed in Section 3.6.2. As discussed in Section 3.7, the model proposed by Anastasopoulos, et al. (2007) is used to represent strain softening behavior in the 2-D FE simulation of soil-pipeline interaction.

Comparisons of semi-infinite soil and experimental FE simulations with measured force vs. displacement plots are provided in Fig 4.7 to 4.9 for medium and very dense CU filter sand as reported by Trautmann (1983) and Trautmann and O'Rourke (1983) as well as RMS graded sand as reported by Olson (2009). The lateral pipe forces are shown as dimensionless force $F' = F/(\gamma_d H_c DL)$, and lateral pipe displacements are shown as dimensionless displacement $Y' = Y/D$.

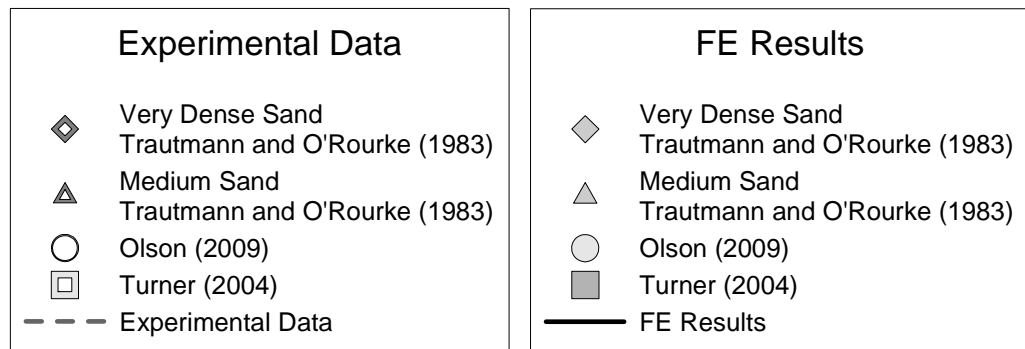
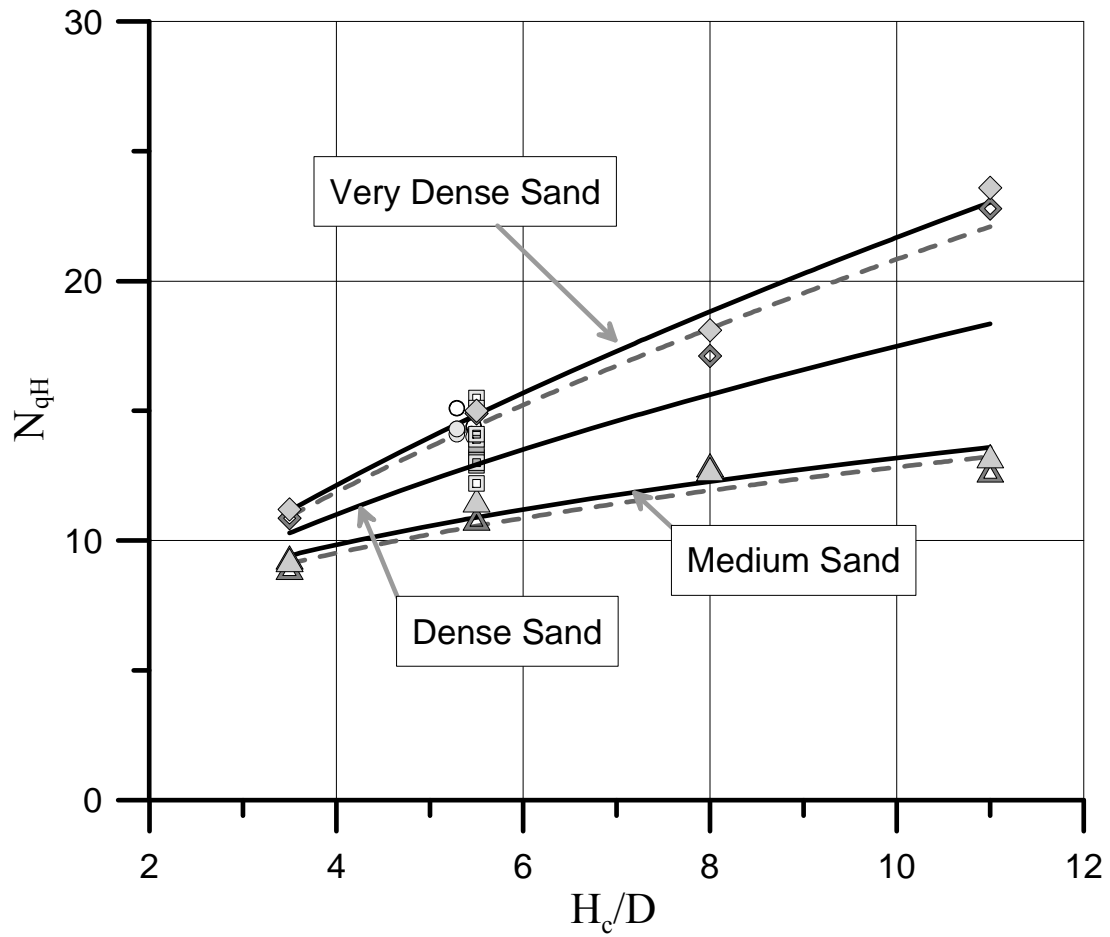


Figure 4.6 Summary Plot of N_{qH} vs. H_c/D for Infinite Field Boundary Condition FEA and FE Simulation of the Large-Scale Tests

The semi-infinite soil simulation results for medium CU filter sand shown in Fig. 4.7 are consistent with the data trends for all H_c/D but tend to over predict peak loads by 3 – 7 %. The predicted pre-peak behavior from the semi-infinite soil simulation is stiffer than that from the experimental simulation as discussed in Section 4.3. The semi-infinite soil simulations for very dense CU filter sand in Fig. 4.8 agree well with the experimental data for all H_c/D data. The analytical peak forces are larger than the measured forces by 1 – 6 %. The pre-peak behavior predicted by the semi-infinite soil simulations for dense CU filter sand is stiffer than the experimental simulation and shows better agreement with the experimental data.

Figure 4.9 shows the dimensionless force vs. dimensionless displacement plot predicted by the semi-infinite soil simulations for RMS graded sand compared with the dimensionless force vs. dimensionless displacement data for three 2-D tests of dry RMS graded sand performed by Olson (2009). Both the semi-infinite soil and large-scale test numerical simulations for dry RMS graded sand show favorable agreement with the experimental data. The numerical simulation results compare favorably in terms of peak force, and post-peak behavior. The analytical peak forces are within -7 – -4 % of the measured peak forces. As shown in the CU filter sand analyses, the pre-peak behavior predicted by the semi-infinite soil simulations is stiffer than the experimental simulation, as discussed in Section 4.3.

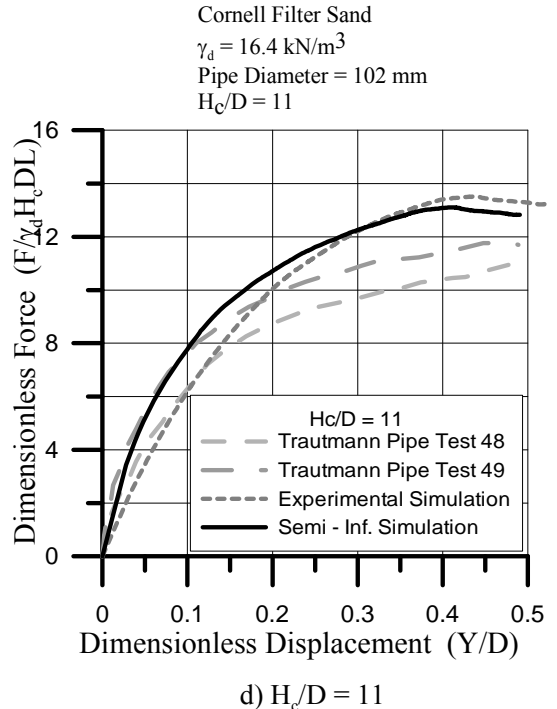
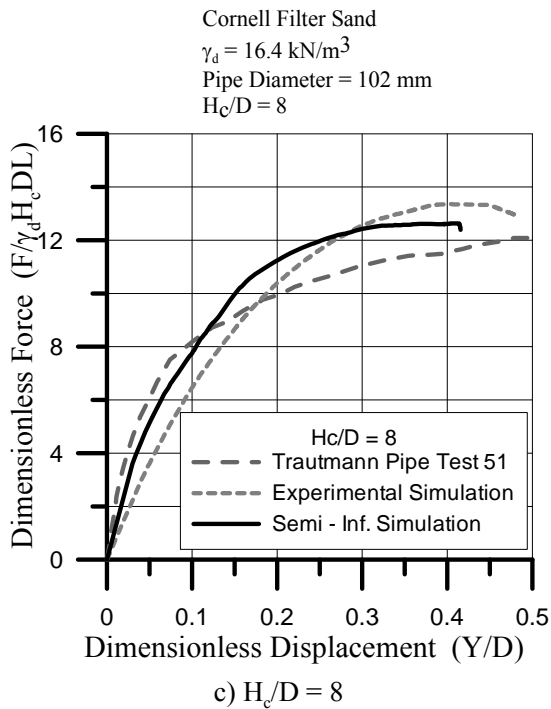
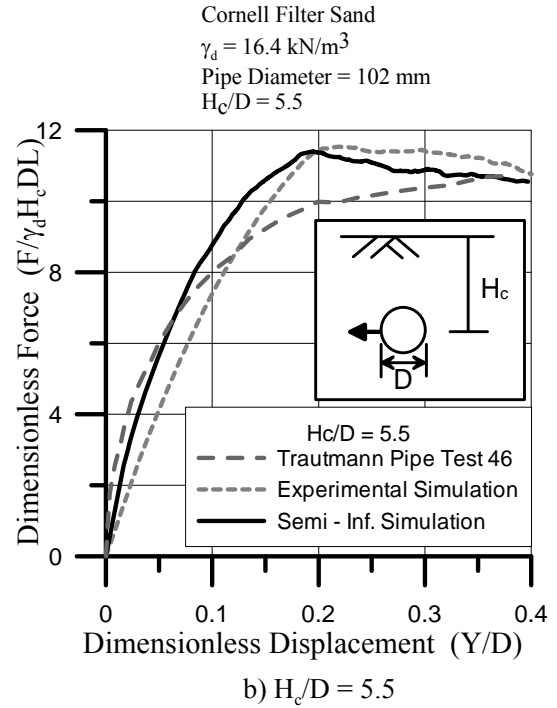
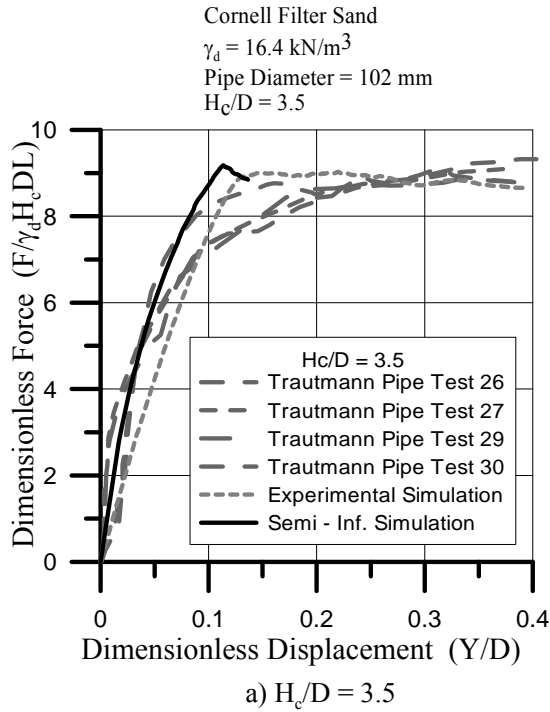


Figure 4.7 Dimensionless Force vs. Displacement Curves for Medium CU Filter Sand

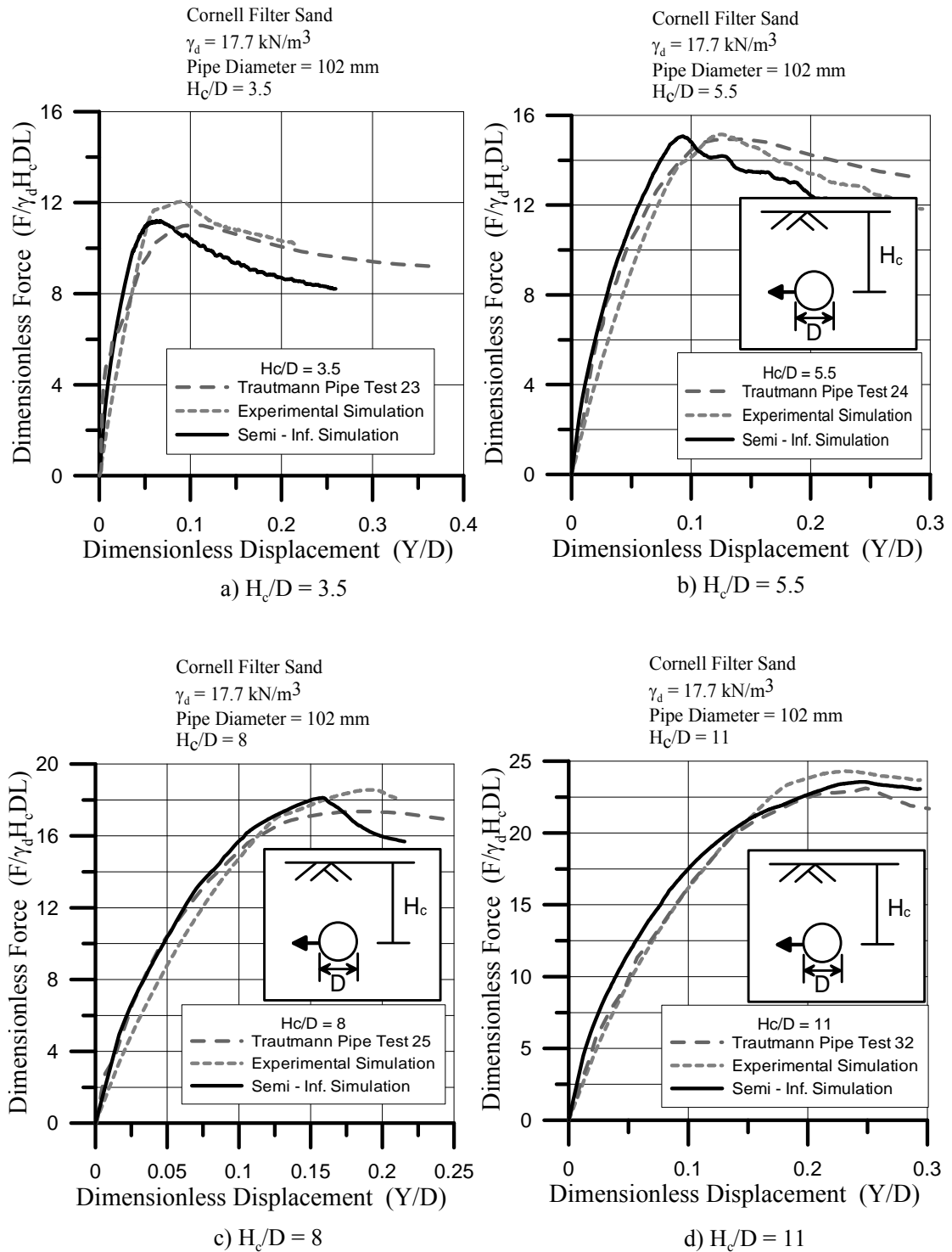


Figure 4.8 Dimensionless Force vs. Displacement Curves for Dense CU Filter Sand

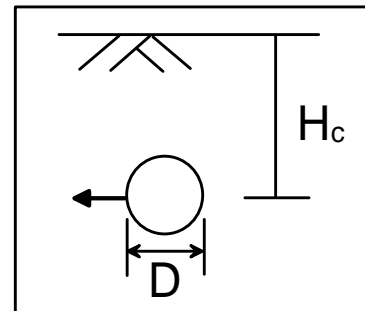
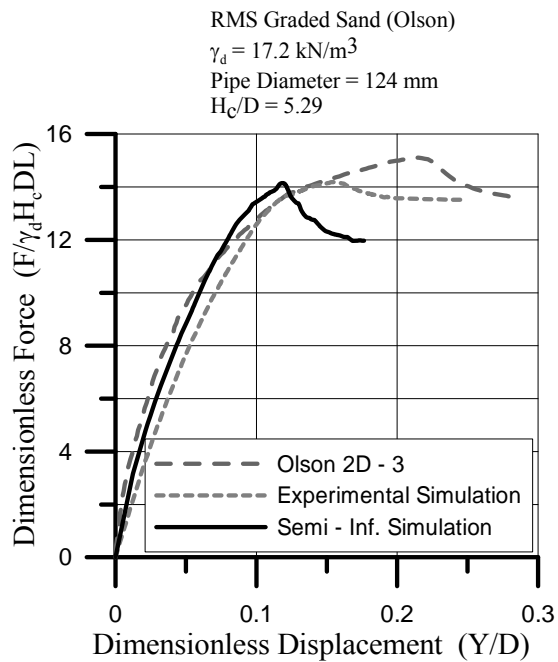
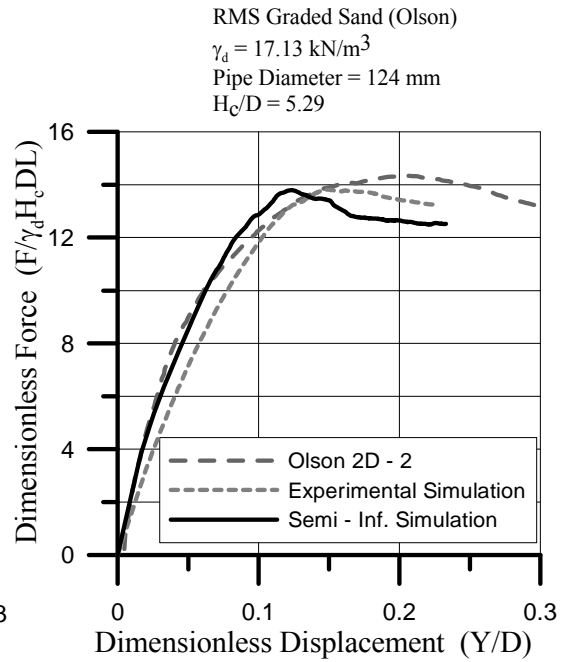
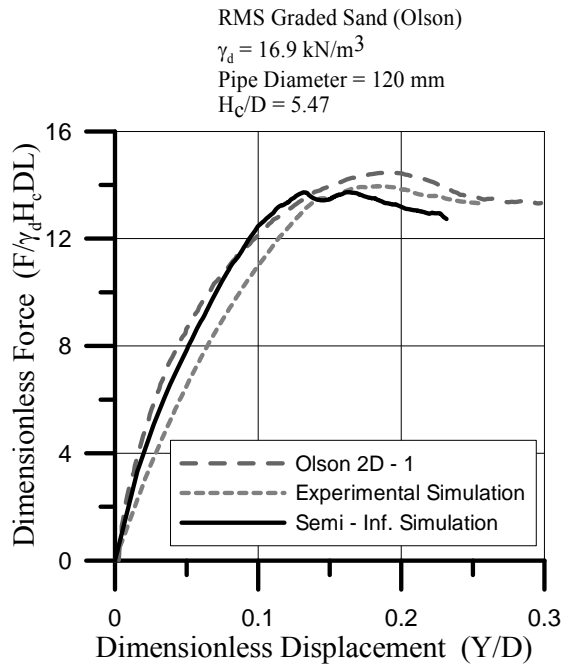


Figure 4.9 Dimensionless Force vs. Displacement Curves for RMS Graded Sand

4.6 Comparisons of Semi-Infinite Soil and Experimental Simulations with Measured Data for Partially Saturated RMS Graded Sand

The FE analyses were performed for the same partially saturated RMS graded sand experimental results as described in Section 3.9 and 4.2. Table 3.4 summarizes the input parameters used in lateral pipe movement in partially saturated semi-infinite soil. The semi-infinite partially saturated soil models were developed that used an equivalent modulus according to the K_{70} procedure discussed in Section 3.10. Table 3.5 summarizes $E_{70-H \text{ sat}}$ used in lateral pipe movement in partially saturated semi-infinite soil. As discussed in Section 3.7, the model proposed by Anastasopoulos, et al. (2007) is used to represent strain softening behavior in the 2-D FE simulation of soil-pipeline interaction. The model was set to linearly diminish c_{ps} to residual values at 0, from the plastic strain at ϕ_{ps-p} to γ_f^p and a small residual values of $c_{ps-ld} = 0.1$ kPa at large displacements was used to promote numerical stability.

Figure 4.10 compares the dimensionless force vs. dimensionless displacement curve for semi-infinite partially saturated soil, experimental simulations with measured data. The numerical simulations for semi-infinite partially saturated soil agree with the measured data for all Olson (2009) tests. The numerical simulations compare favorably in terms of pre-peak, peak force, and post-peak behavior. The numerical simulations, however, result in a softer soil reaction within the equivalent elastic range for $H_c/D = 5.29$. Overall, the predicted force-displacement behavior from the FE semi-infinite partially saturated soil compares very well with the measured data. Similar to the results of the dry sand simulations, the pre-peak behavior predicted for the semi-infinite partially saturated soil is stiffer than that of the FE simulations of the large-scale tests. The lower stiffness of the experimental

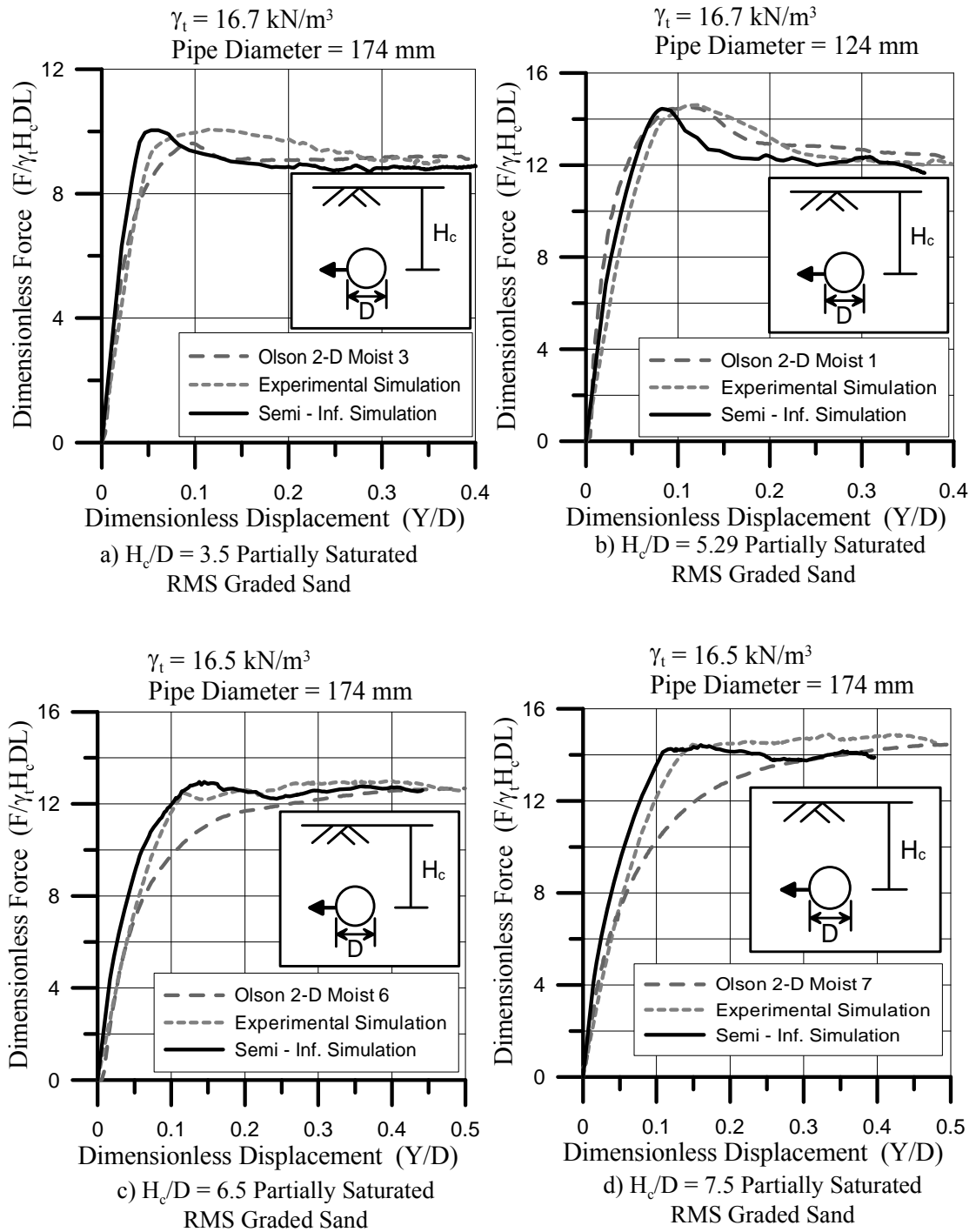


Figure 4.10 Dimensionless Force vs. Displacement Curves for Partially Saturated RMS Graded Sand

simulations is caused by relatively large deformation of the soil elements between the pipe and test box wall, as discussed in Section 4.3.

N_{q-si} and N_{q-m} of partially saturated RMS graded sand are compared in Fig. 4.11, in which dimensionless forces are plotted as a function of dimensionless depth. There is a favorable agreement among the data for all H_c/D . In general, N_{q-si} over predict N_{q-m} by 0.1 – 4 %. Overall, the average difference between N_{q-si} and N_{q-m} for partially saturated RMS graded sand is 2.3 % with $H_c/D \leq 7.5$.

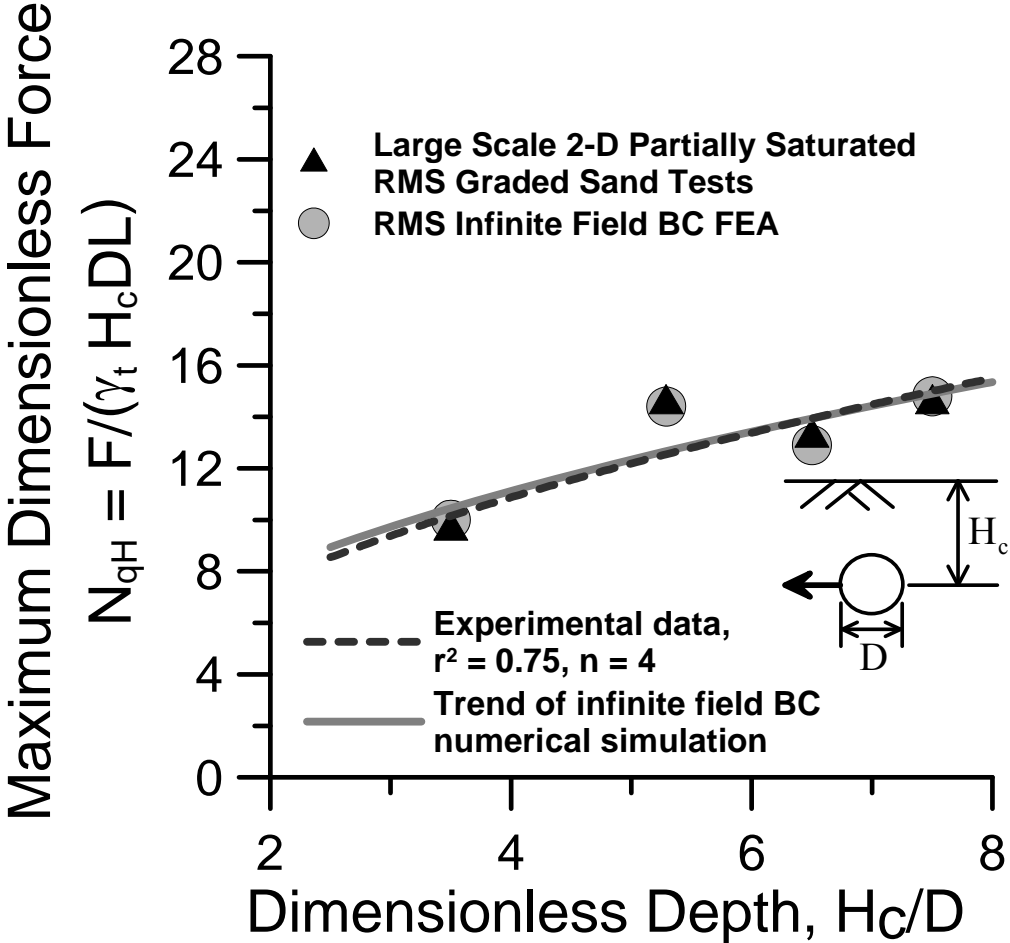


Figure 4.11 Plot of N_{qH} vs. H_c/D of Semi-Infinite Soil and Measured Data for Partially Saturated RMS Graded Sand

4.7 Refinements in Soil Strength Modeling

As described in Chapter 3, characterizing ψ_p in terms of a single σ'_{vc} is a simplification that does not account for variable ψ_p and ϕ'_{ps-p} with depth or link ψ_p with the appropriate σ'_N at any given depth. To evaluate the effects of more comprehensive characterization of soil strength, FE simulations were performed for layered soil conditions in which ψ_p and ϕ'_{ps-p} were varied with depth and σ'_N was estimated with greater accuracy. The modeling methods and FE results of this study are described under the subheadings that follow.

4.7.1 Depth Dependent Soil Strength Properties

DS tests performed by Olson (2009) showed that ψ_p and ϕ'_{ps-p} varies with depth. To model the spatial distribution of the depth effects on soil strength properties, the soil was divided into layers as shown in Fig. 4.12, and depth-dependent values of ψ_p and ϕ'_{ps-p} were assigned to each layer. The mesh geometry, interface friction, and modeling procedures are the same as those described in Chapter 3. Approximately 1300 to 1500 elements were used in the meshes to simulate different H_c/D conditions.

FE simulation with ψ_p and ϕ'_{ps-p} , that varies with depth, is referred to as the 'Depth Dependent Model', whereas FE simulation using ψ_p and ϕ'_{ps-p} linked to a single σ'_{vc} is referred to as 'Pipe Depth Dependent Model'. Figure 4.13 shows the dimensionless force vs. dimensionless displacement curve for both the Depth and Pipe Depth Dependent Model with $H_c/D = 5.5$ and 15. On average, the difference between the two models is 3.3 %, 1.9 %, and 1.6 % in terms of pre-peak, peak, and

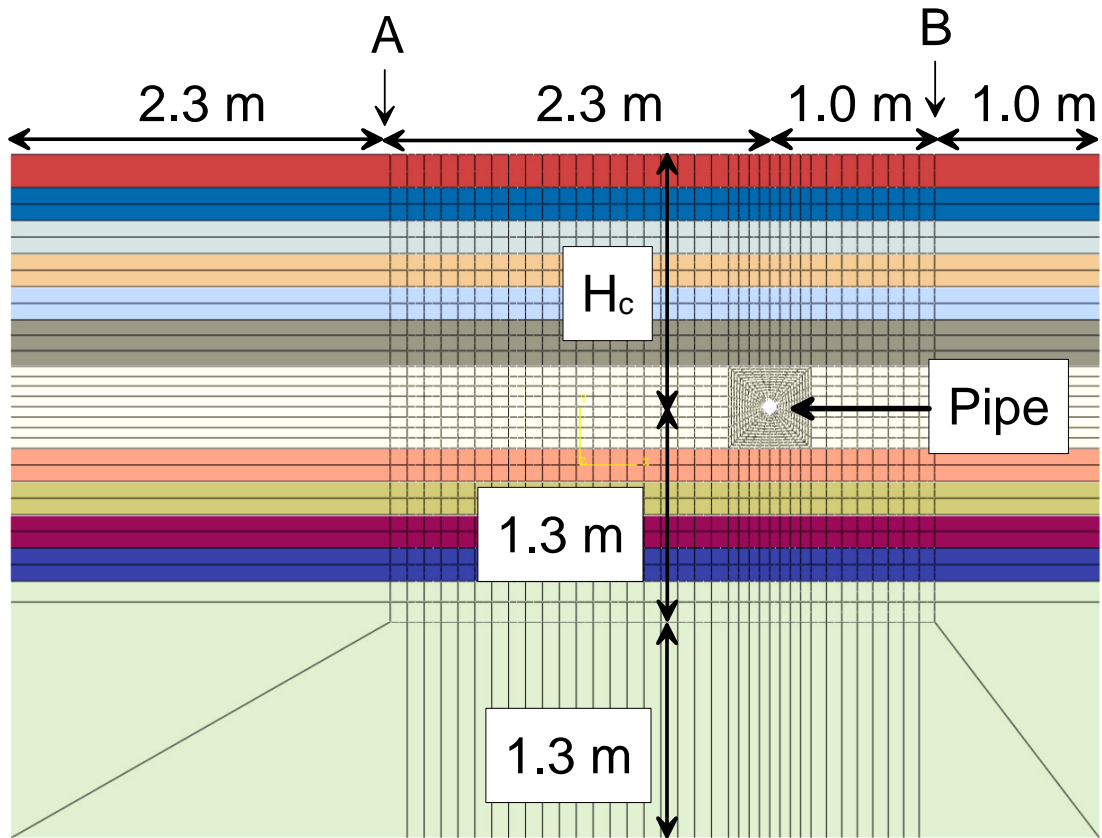


Figure 4.12 Geometry of Depth Dependent Soil Strength Properties Model

post-peak behavior, respectively. Because the comparisons show only 1.6 – 3.3 % difference in the results, the Depth Dependent Model can be replaced with the Pipe Depth Dependent Model, which is a more simple and straight forward characterization of ψ_p and ϕ'_{ps-p} .

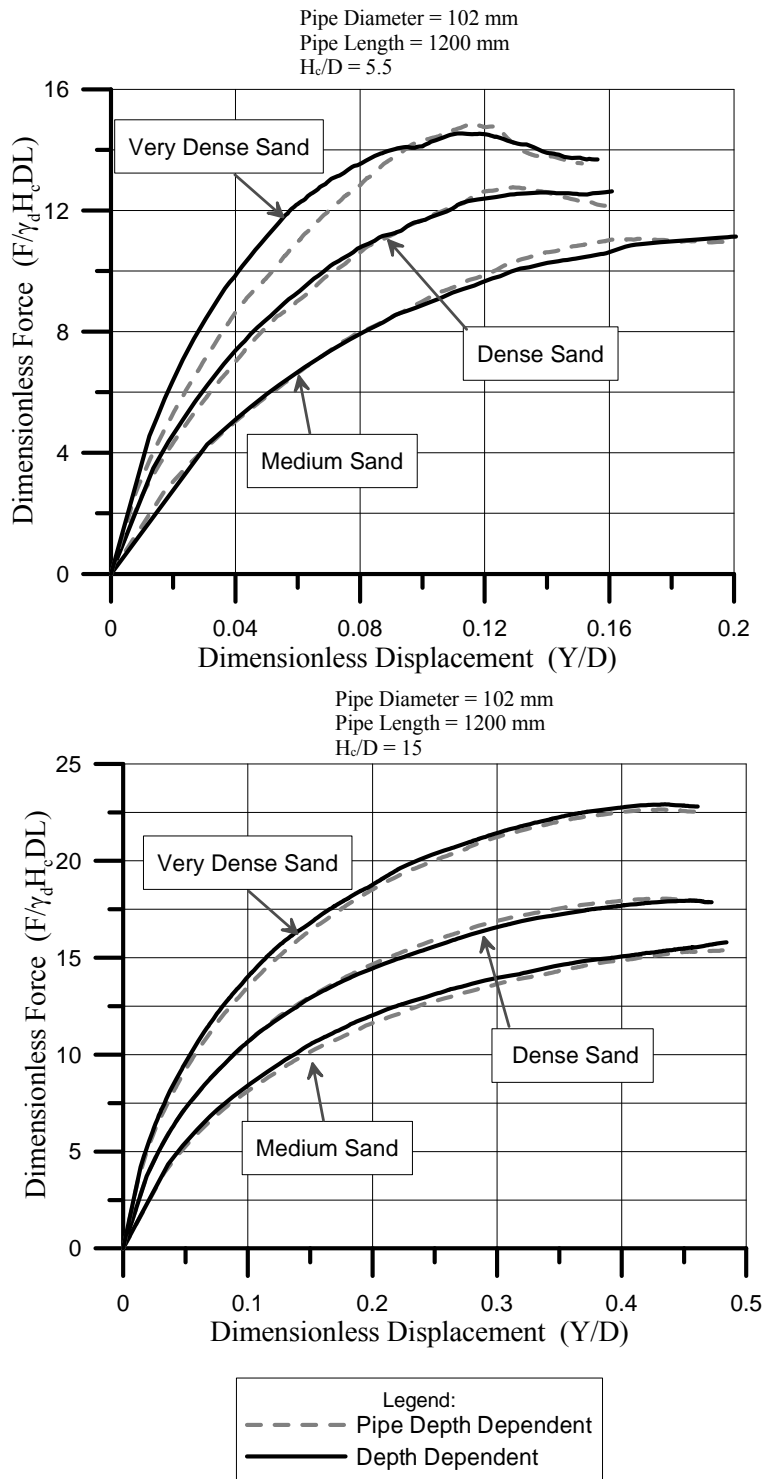


Figure 4.13 Dimensionless Force vs. Displacement Curve for Depth Dependent Model and Pipe Depth Dependent Model

4.7.2 σ'_N Reference Stress

In the Pipe Depth Dependent Model, σ'_{vc} is used as a proxy for σ'_N . The sand strength, however, is controlled by σ'_N , which will generally be larger than σ'_{vc} for soil elements at yield surrounding the pipe. It is therefore instructive to obtain force vs. displacement curves for simulations where the sand strength depends on σ'_N and compare them to similar curves where sand strength is related to σ'_{vc} to evaluate the difference in results associated with the two modeling procedures.

Figure 4.14 shows the relationship between σ'_N and the principal stresses at yield. From the figure, σ'_N can be calculated as

$$\sigma'_N = \frac{\sigma'_1 + \sigma'_3}{2} - \frac{\sigma'_1 - \sigma'_3}{2} \sin \phi'_{ps-p} \quad (4.1)$$

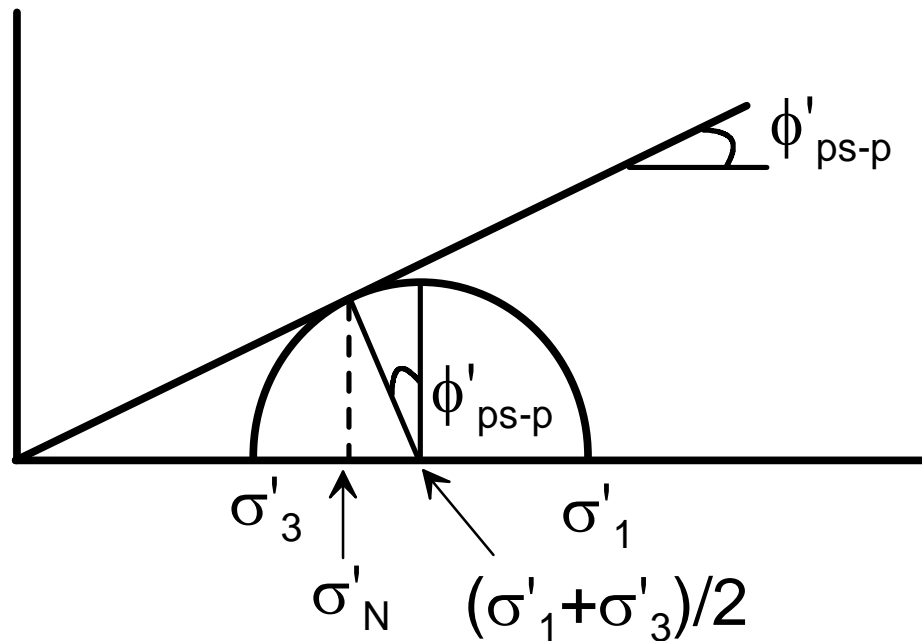


Figure 4.14 Relationship Between σ'_N and Principal Stresses

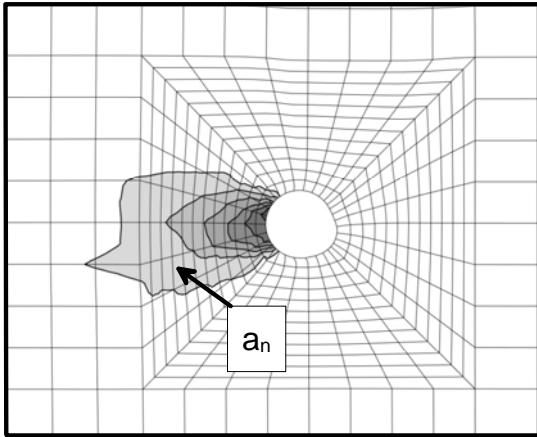
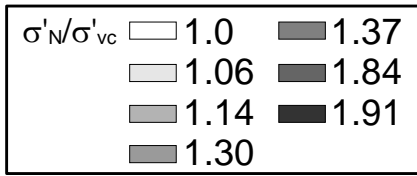
Figure 4.15 shows the contours of σ'_N/σ'_{vc} for lateral pipe displacement in medium and very dense sand at $H_c/D = 5.5$ and 15. Values of σ'_1 and σ'_3 around the pipe were analyzed, and σ'_N was calculated using Eqn. 4.1. Each area of σ'_N/σ'_{vc} was then measured and the weighted averages of σ'_N around the pipe were calculated by the following equation:

$$\sigma'_N = \left[\frac{\sum_n \left\{ \left(\frac{\sigma'_N}{\sigma'_{v0}} \right)_n a_n \right\}}{\sum_n a_n} \right] \sigma'_{v0} \quad (4.2)$$

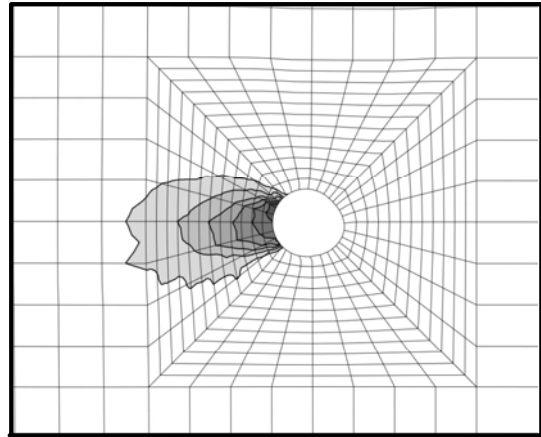
in which a_n is the area of each $(\sigma'_N/\sigma'_{v0})_n$.

The weighted averages of σ'_N were $1.16 \sigma'_{v0}$ and $1.12 \sigma'_{v0}$ for medium sand at $H_c/D = 5.5$ and 15, respectively. Likewise, the weighted averages of σ'_N were $1.15 \sigma'_{v0}$ and $1.11 \sigma'_{v0}$ for very dense sand at $H_c/D = 5.5$ and 15, respectively. The soil strength properties obtained from the weighted averages of σ'_N differ from those obtained from σ'_{vc} reference stress model by only 0.2 ~ 2.5 %.

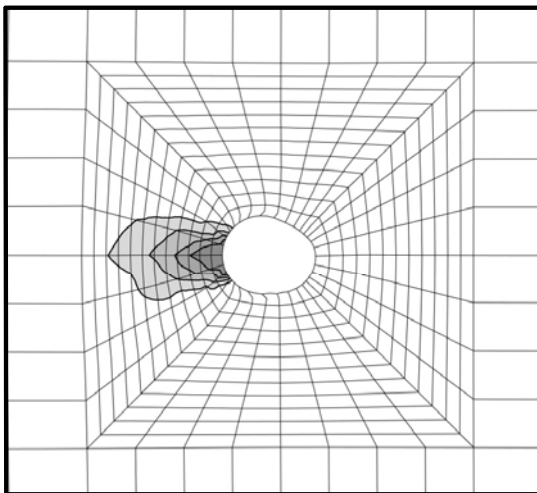
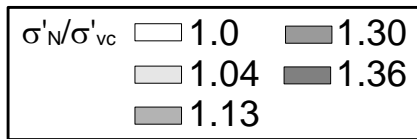
FE simulations were performed for both the σ'_N and σ'_{vc} reference stress models, and the resulting dimensionless force vs. displacement curves are shown in Fig. 4.16. The difference between results of the two models is less than 1 % for both $H_c/D = 5.5$ and 15. The predicted force of the σ'_{vc} reference stress model is slightly higher than that of the σ'_N model, and thus tends to produce conservative estimates for the analysis of pipeline deformation in the ground. As was the case for the depth dependent soil properties, the use of σ'_N to characterize sand strength produces only a



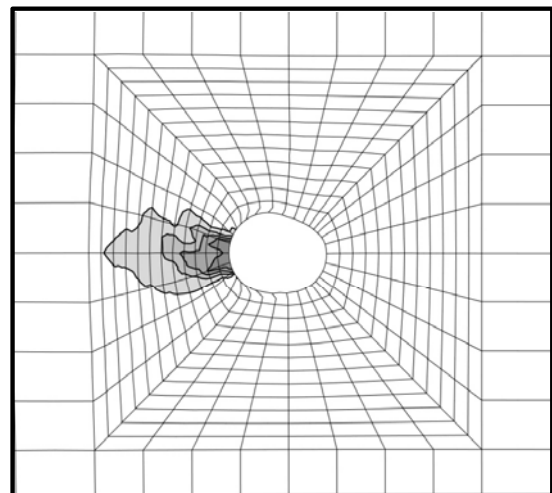
a) $H_c/D = 5.5$, Medium Sand



b) $H_c/D = 5.5$, Very Dense Sand



c) $H_c/D = 15$, Medium Sand



d) $H_c/D = 15$, Very Dense Sand

Figure 4.15 σ'_N/σ'_{vc} Plot for $H_c/D = 5.5$ and 15 at the Peak

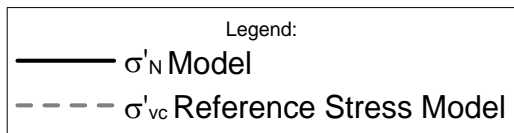
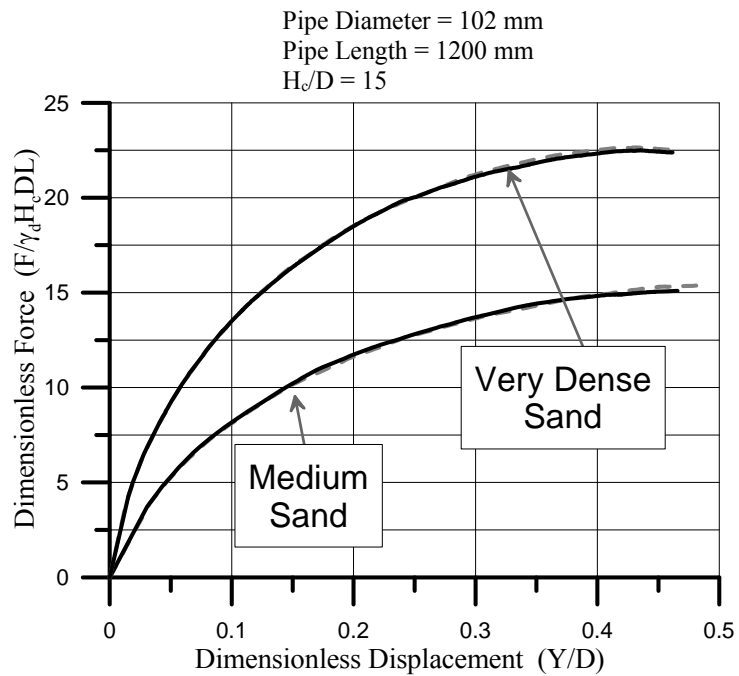
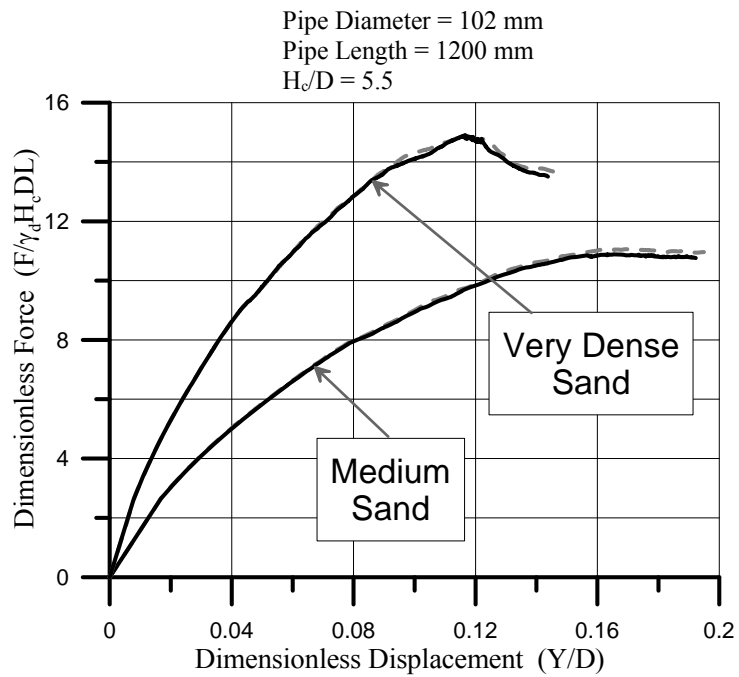


Figure 4.16 Dimensionless Force vs. Displacement Curve for σ'_N Model and σ'_{vc} Reference Stress Model

small change in the results compared with the Pipe Depth Dependent Model. Thus, the Pipe Depth Dependent Model is justified to production runs due to its simplicity and results consistent with more complex characterizations of strength.

4.8 Relationship Between Maximum Lateral Force and Pipe Depth

Yimsiri et al. (2004) analyzed the lateral force vs. displacement relationship for pipelines in dry sand under plane strain conditions. They showed that a limiting value of N_{qH} is reached at a particular value of H_c/D for each friction angle investigated. Large-scale test data obtained by Turner (2004) showed that N_{qH} reached a limiting value at $H_c/D = 15 - 20$.

To explore further lateral N_{qH} vs. H_c/D for underground pipe, FE simulations were performed for H_c/D varying from 3.5 to 100 for medium, dense, and very dense dry sand and for partially saturated sand. The analytical investigation and its results are described under the subheadings that follow.

4.8.1 Model Geometry and Properties for Maximum Dimensionless Lateral Force and Dimensionless Depth

Semi-infinite soil models described in Section 4.2 were used to investigate the relationship between N_{qH} and H_c/D for medium, dense, and very dense sand as characterized in Table 3.2. Input parameters for soil strength were obtained with the procedures described in Section 3.3.2. An equivalent modulus, according to the K_{70} procedure discussed in Section 3.6.2, and strain softening model described in Section 3.7 were used in the 2-D FE simulations of soil-pipeline interaction. Table 4.1

Table 4.1 Summary of the Input Parameters Used in Finite Element Analyses for
Maximum Force and Pipe Depth

Test No.	H_c/D	γ_d (kN/m ³)	ϕ'_{ds-p} (degrees)	Ψ_p (degrees)	ϕ'_{ps-p} (degrees)	E_{70-H} (kPa)
RMS3.5M	3.5	16.4	36.2	4.3	44.0	1300
RMS3.5D	3.5	17.1	38.8	8.3	46.8	2000
RMS3.5VD	3.5	17.7	41.1	11.7	49.1	3000
RMS5.5M	5.5	16.4	36.0	4.0	43.8	1800
RMS5.5D	5.5	17.1	38.5	7.7	46.4	2900
RMS5.5VD	5.5	17.7	40.6	10.9	48.6	4200
RMS8M	8	16.4	35.8	3.8	43.6	2400
RMS8D	8	17.1	38.2	7.3	46.1	3800
RMS8VD	8	17.7	40.2	10.3	48.2	5600
RMS11M	11	16.4	35.7	3.6	43.5	3100
RMS11D	11	17.1	38.0	7.0	45.9	4900
RMS11VD	11	17.7	39.9	9.8	47.9	7200
RMS15M	15	16.4	35.6	3.5	43.4	3900
RMS15D	15	17.1	37.7	6.6	45.6	6300
RMS15VD	15	17.7	39.6	9.4	47.5	9200
RMS20M	20	16.4	35.5	3.3	43.3	4900
RMS20D	20	17.1	37.6	6.4	45.4	7800
RMS20VD	20	17.7	39.3	9.0	47.3	11600
RMS30M	30	16.4	35.3	3.1	43.1	6700
RMS30D	30	17.1	37.3	6.0	45.2	10800
RMS30VD	30	17.7	39.0	8.5	46.9	15900
RMS100M	100	16.4	35.0	2.6	42.7	17300
RMS100D	100	17.1	36.6	5.0	44.5	27600
RMS100VD	100	17.7	38.0	7.1	45.9	35800

summarizes the input parameters used in the FE analyses of each large-scale test for lateral pipe movement. A Poisson's ratio, $\nu = 0.3$, was assumed for the sand and all simulations were performed with a nominal cohesion $c' = 0.1 - 0.3$ kPa to promote numerical stability.

4.8.2 Analytical Results of Lateral Maximum Dimensionless Force and Dimensionless Depth

Comparisons of N_{qH} vs. H_c/D for medium, dense, and very dense sand are shown in Fig. 4.17. The dimensionless equations $N_{qH} = F/(\gamma_d H_c DL)$ and H_c/D defines the lateral pipe forces and depth, respectively. The values of N_{qH} were determined as described in Chapter 3.

Turner (2004) performed three lateral pipe movement tests using mixed CU filter sand and RMS graded sand and a pipe diameter of 120 mm. For $H_c/D = 15.2$, Turner used $\gamma_d = 18.0$ kN/m³ and $\phi'_{ds-p} = 45.3^\circ - 46.6^\circ$ (approximately $\phi'_{ps-p} = 53.2^\circ$, $\psi_p = 10.5^\circ$). For $H_c/D = 19.2$, Turner carried out two experiments, using $\gamma_d = 17.8$ kN/m³, $\phi'_{ds-p} = 44.1^\circ - 44.9^\circ$ (approximately $\phi'_{ps-p} = 49.2^\circ$, $\psi_p = 9.3^\circ$) and $\gamma_d = 17.9$ kN/m³, $\phi'_{ds-p} = 44.4^\circ - 45.3^\circ$ (approximately $\phi'_{ps-p} = 50.1^\circ$, $\psi_p = 9.7^\circ$). Measured values of N_q from Turner (2004) are plotted in Fig. 4.17 for comparison. The measured N_q did not show a significant increase between $H_c/D = 15.2$ and 19.2, which is consistent with the analytical results. The, ϕ'_{ds-p} -values used in the experiments were 4 – 11 % larger than those used in the FE analyses performed for very dense sand. Turner's experimental values of N_{qH} are also 4 – 13 % higher than those obtained from the FE analyses for very dense sand, which reflect the higher strength soils used in the experimental study.

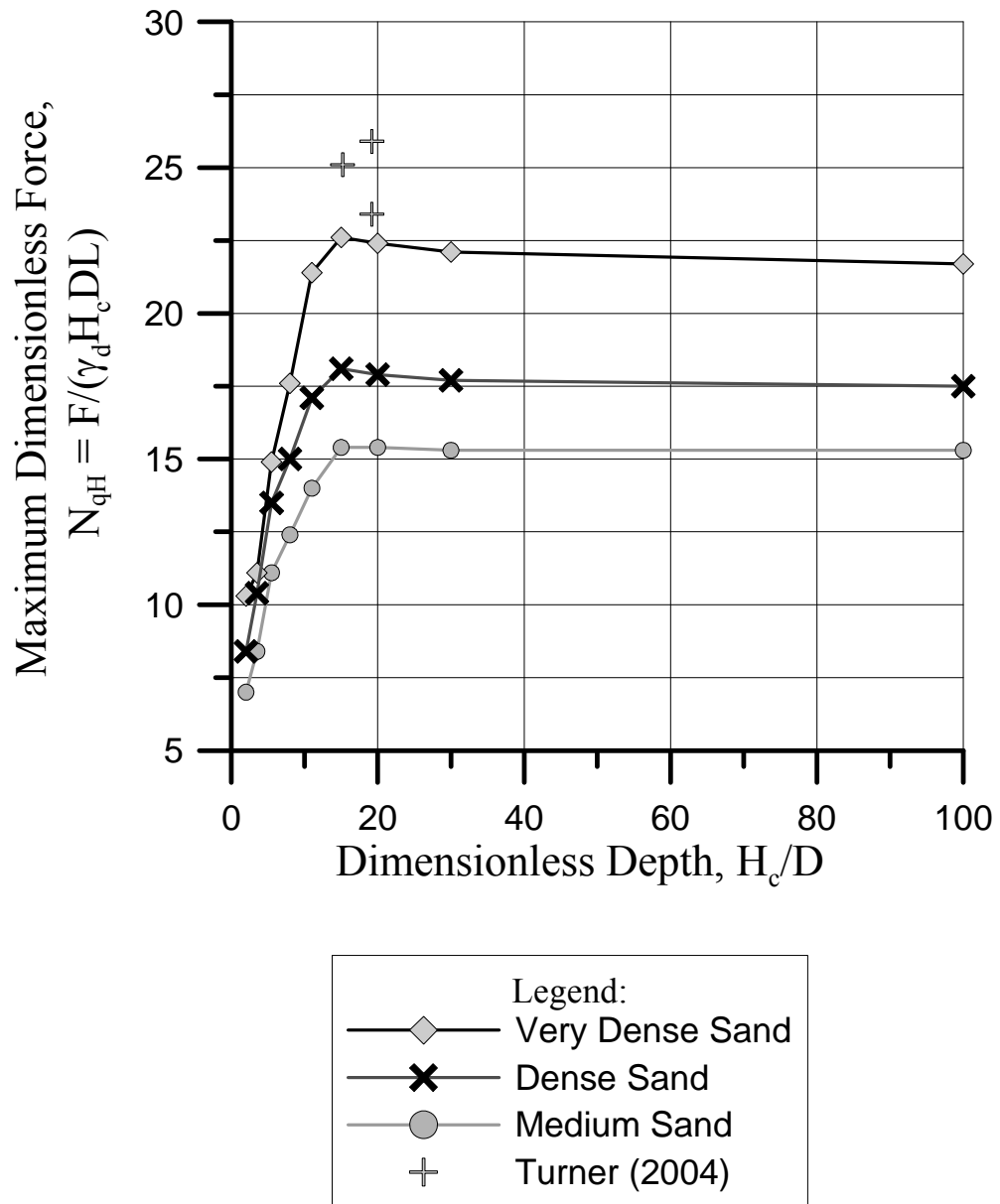


Figure 4.17 Summary Plot of N_{qH} vs. H_c/D for Lateral Pipe Movement

The FE simulations of lateral pipe movement show that N_{qH} reaches its maximum value at $H_c/D = 15 - 20$, and then decreases with increasing H_c/D . As shown in Fig. 4.17, from $H_c/D = 15$ to 100, N_{qH} decreases approximately by 0.6 %, 3.3 %, and 3.1 % for medium, dense, and very dense sand, respectively. The values of ϕ'_{ps-p} decrease approximately by 1.5 %, 2.6 %, and 3.4 % for medium, dense, and very dense sand, respectively, due to increasing confining stress at higher H_c/D values. Between $H_c/D = 15$ and 20, N_{qH} reaches its limiting values of approximately 15.4, 18.1, and 22.6 for medium, dense, and very dense sand, respectively. As illustrated in Fig. 4.17, N_{qH} increases steeply at shallower depths and remains relatively constant once H_c/D reaches a critical embedment ratio.

It is instructive to examine the 2-D displacements of lateral pipe movement from FE simulations at various depths to check soil deformation patterns relative to N_{qH} . Figure 4.18 through 4.21 show the displacement pattern for a pipe in medium sand with $D = 102$ mm and $H_c/D = 8 - 100$. Vector displacements less than 4 mm are removed from the figures for better visualization. The figures show that the soil displacement pattern at shallower depth is asymmetrically developed from the pipe to the surface, whereas the soil displacement pattern at greater depth is symmetrically developed around the pipe. When H_c/D increases to approximately 20, the soil deformation pattern becomes symmetric with respect to the pipe so that any further change in lateral force with increasing depth is related to changes in soil strength and not the geometric characteristics of the soil movement.

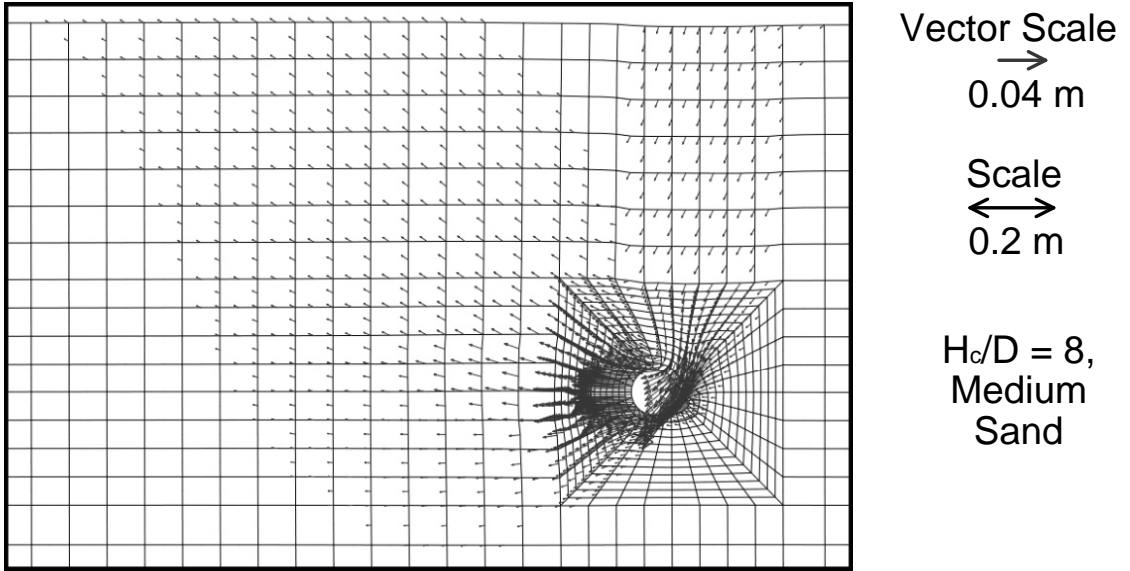


Figure 4.18 Displacement Pattern for Medium Sand at $H_c/D = 8$

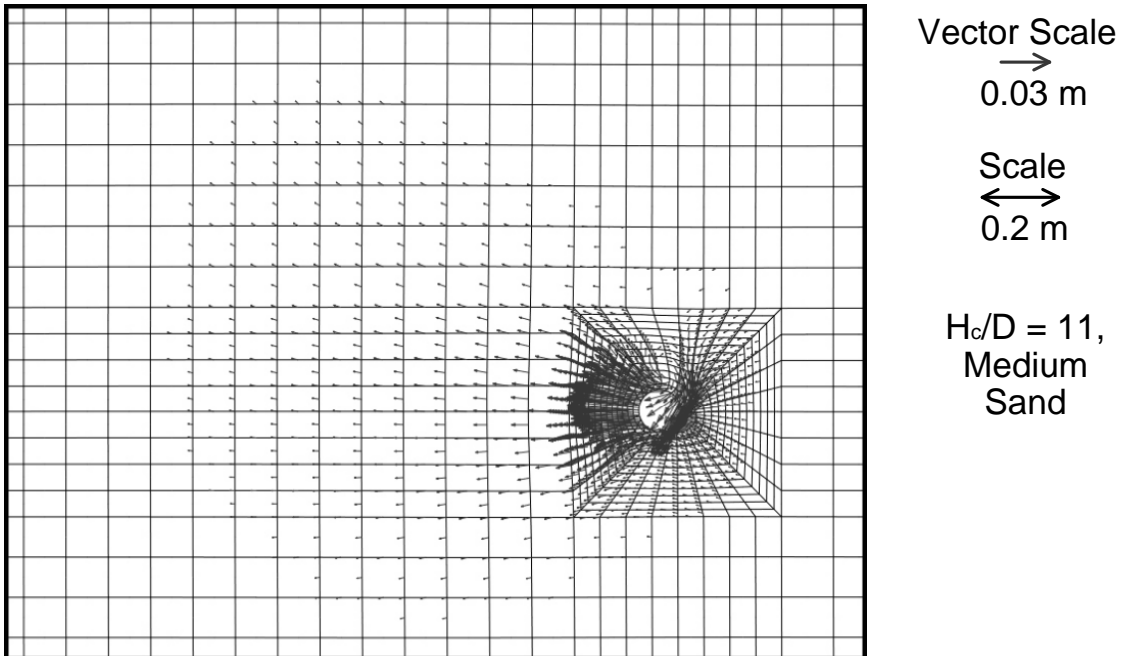
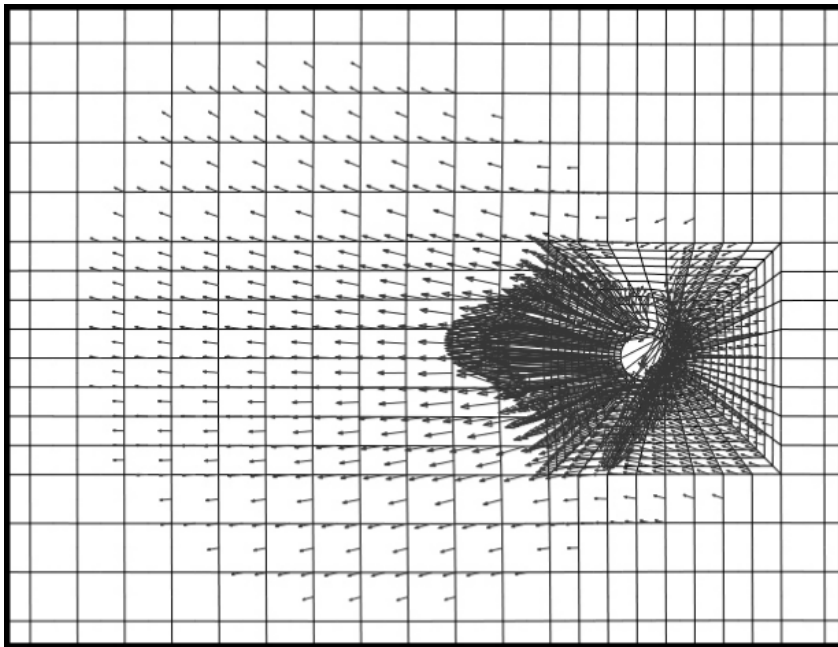


Figure 4.19 Displacement Pattern for Medium Sand at $H_c/D = 11$

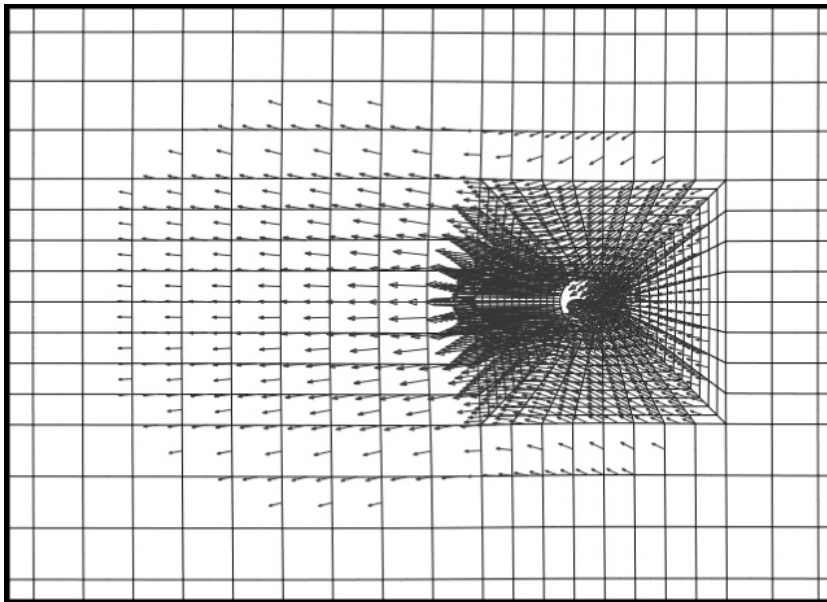


Vector Scale
 \longrightarrow
 0.02 m

Scale
 \longleftrightarrow
 0.2 m

$H_c/D = 15$,
 Medium
 Sand

Figure 4.20 Displacement Pattern for Medium Sand at $H_c/D = 15$



Vector Scale
 \longrightarrow
 0.02 m

Scale
 \longleftrightarrow
 0.2 m

$H_c/D = 100$,
 Medium
 Sand

Figure 4.21 Displacement Pattern for Medium Sand at $H_c/D = 100$

4.8.3 Analytical Results of Maximum Lateral Dimensionless Forces for Various Pipe Diameters

Additional FE analyses were run with various pipe diameters to investigate the effects increasing diameter on soil-pipe interaction at constant H_c/D . Figure 4.22 shows the geometry of the numerical model for simulating lateral soil-pipe interaction with various pipe diameters in dry sand. In the figure, H_c varies according to the H_c/D used in the simulation, and the distance from the pipe center to the bottom (boundary marked by C) of the model is 10 m. The closest distance from vertical pipe centerline to A and B in Fig. 4.22 is 20 m, and 10 m, respectively. The selected pipe diameters for this study were 500 mm and 900 mm, compared with 102 mm used in the production simulations. The pipe is modeled as a rigid cylinder with surface

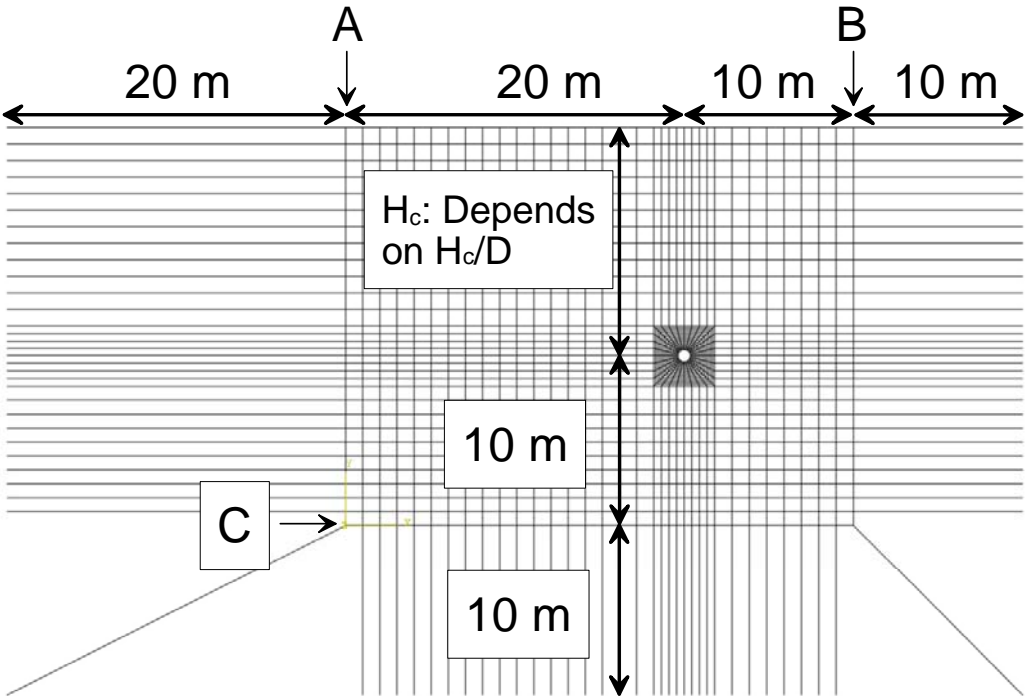


Figure 4.22 Geometry of the Numerical Model for Various Pipe Diameters

properties similar to those of ASTM Grade A-36 steel. The interface friction angle between the soil and pipe is taken as $0.6 \phi'_{ds-p}$ and a refined mesh is used within a distance of approximately two pipe diameters from the test pipe. Geostatic load is applied to the soil and pipe at the start of each simulation under $K_o = 1$ conditions. Pipe movement is expressed by imposing a lateral displacement boundary condition to all the nodes in the pipe.

Input parameters for soil strength were obtained from the procedure discussed in Section 3.3.2. An equivalent modulus according to the K_{70} procedure discussed in Section 3.6.2 and strain softening model described in Section 3.7 were used in the 2-D FE simulation of soil-pipeline interaction. Table 4.2 summarizes input parameters used in FE analyses for various pipe diameters. A Poisson's ratio, $\nu = 0.3$, was assumed for the sand, and all simulations were performed with a nominal cohesion $c' = 0.1 - 0.3$ kPa to promote numerical stability.

Figure 4.23 plots N_{qH} from the FE analyses for various pipe diameters. The dimensionless parameters, $N_{qH} = F/(\gamma_d H_c DL)$ and H_c/D , define the lateral pipe forces and depth, respectively. The plot shows diameter effects increasing with increasing γ_d , and decreasing with increasing H_c/D . For $D = 102$ mm and 900 mm, the maximum difference in N_{qH} is approximately 12 % for both dense and very dense sand. The effects of diameter become negligible in medium sand. N_{qH} for $D = 900$ mm converges to N_{qH} for $D = 102$ m at $H_c/D = 10 - 12$. The results for $D = 500$ mm fall between those of $D = 102$ mm and 900 mm and are skewed towards the results for $D = 102$ mm.

Table 4.2 Summary of the Input Parameters Used in Finite Element Analyses for
Various Pipe Diameters

Test No.	H_c/D	Diameter (m)	γ_d (kN/m ³)	ϕ'_{ds-p} (degrees)	ψ_p (degrees)	ϕ'_{ps-p} (degrees)	E_{70-H} (kPa)
9D2M	2	0.9	16.4	35.5	3.4	43.3	4400
9D3.5M	3.5	0.9	16.4	35.3	3.1	43.1	6800
9D5.5M	5.5	0.9	16.4	35.2	2.9	43.0	9800
9D8M	8	0.9	16.4	35.1	2.8	42.9	13100
9D15M	15	0.9	16.4	34.9	2.5	42.7	21500
9D2D	2	0.9	17.1	37.6	6.5	45.5	7300
9D3.5D	3.5	0.9	17.1	37.3	6.0	45.2	11300
9D5.5D	5.5	0.9	17.1	37.0	5.6	44.9	16200
9D8D	8	0.9	17.1	36.8	5.3	44.7	21700
9D15D	15	0.9	17.1	36.5	4.8	44.3	35600
9D2VD	2	0.9	17.7	39.5	9.2	47.4	11000
9D3.5VD	3.5	0.9	17.7	39.0	8.4	46.9	17100
9D5.5VD	5.5	0.9	17.7	38.6	7.9	46.5	24500
9D8VD	8	0.9	17.7	38.3	7.4	46.2	32900
9D15VD	15	0.9	17.7	37.8	6.8	45.7	54000
5D2D	2	0.5	17.1	38.0	7.1	46.0	4600
5D5.5D	5.5	0.5	17.1	37.4	6.1	45.3	10200
5D2VD	2	0.5	17.7	40.0	10.0	48.0	6900
5D5.5VD	5.5	0.5	17.7	39.1	8.6	47.0	15400

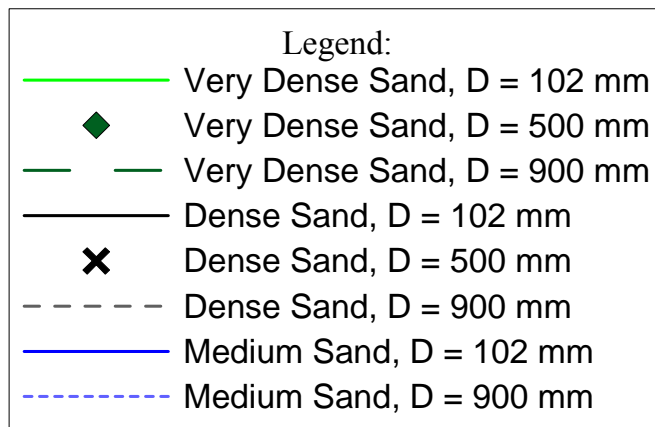
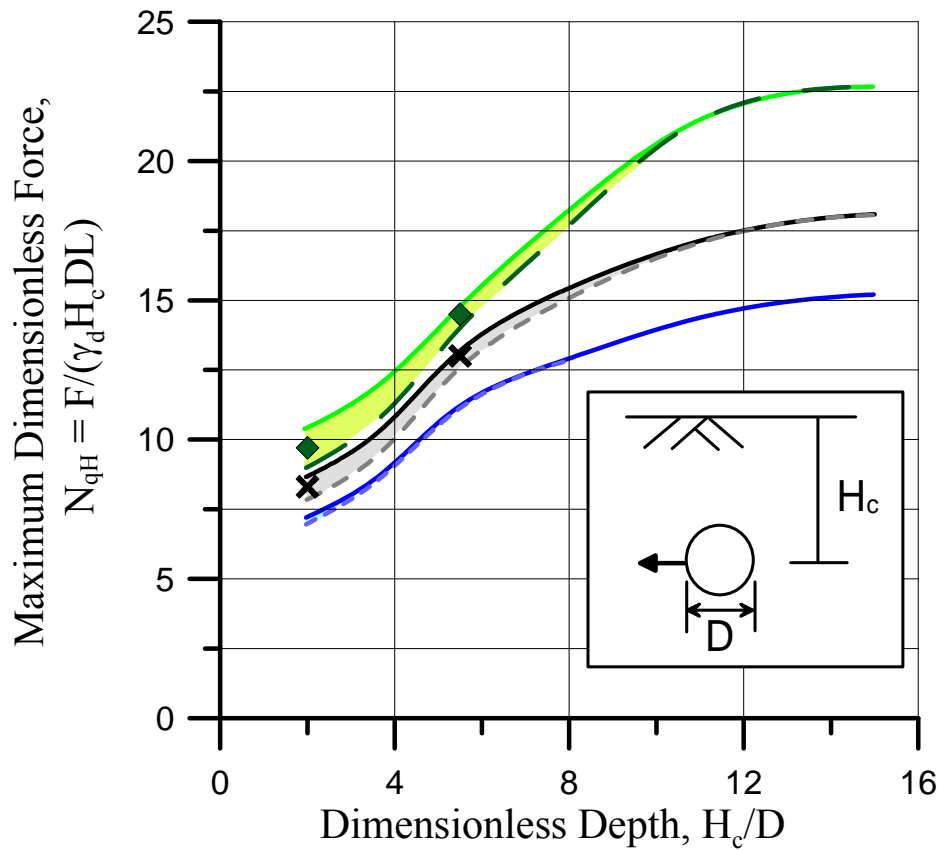


Figure 4.23 Summary Plot of N_{qH} vs. H_c/D for Various Pipe Diameters

The trends in the numerical results can be explained by the depth-dependent characteristics of soil strength for which ϕ'_{ps-p} and ψ_p increase rapidly at low σ'_{vc} . Especially when $H_c/D \leq 6$, increased D results in increased σ'_{vc} for constant H_c/D so that ϕ'_{ps-p} and ψ_p decrease, resulting in lower N_{qH} . This trend is amplified by increasing ϕ'_{ps-p} , which results in a more rapid reduction in strength with depth. For medium dense sand with little dilatancy, the effects of D are negligible.

4.8.4 Investigation of Maximum Dimensionless Lateral Force and Dimensionless Depth in Partially Saturated RMS Graded Sand

FE analyses were run with the semi-infinite soil model for partially saturated RMS graded sand as described in Section 3.9 and 4.2. Input parameters for soil strength and an equivalent $E_{70-H \text{ sat}}$ were obtained from the procedure discussed in Section 3.9. Table 4.3 summarizes the soil properties associated with the partially saturated sand 2-D simulations. Strain softening model described in Section 3.7 was used in the partially saturated sand 2-D FE simulation and the model was set to linearly diminish c_{ps} to residual values at 0, from the plastic strain at ϕ_{ps-p} to γ_f^p and a small residual values of $c_{ps-ld} = 0.1$ kPa at large displacements was used to promote numerical stability.

Figure 4.24 shows the analytical results of the maximum dimensionless force plotted with respect to the dimensionless depth of partially saturated RMS graded sand using the soil properties provided in Table 4.3. The values of N_q were determined as described in Chapter 3. Figure 4.24 show that N_{qH} has the maximum value between $H_c/D = 20$ and 30, slightly greater than that from the dry RMS graded sand simulations.

Table 4.3 Summary of the Input Parameters Used in Partially Saturated Sand Finite Element Analyses for Lateral Pipe Movement

Test No.	H _c /D	D (mm)	γ _{total} (kN/m ³)	γ _d (kN/m ³)	ψ _p (degrees)	φ _{ps-p} (degrees)	E _{70-H sat} (kPa)
RMSPS 3.5	3.5	102	16.5	15.8	17.6	44.2	2700
RMSPS 5.5	5.5	102	16.5	15.8	13.7	44.1	3800
RMSPS 8	8	102	16.5	15.8	11.1	43.8	5100
RMSPS 11	11	102	16.5	15.8	9.3	43.4	6600
RMSPS 15	15	102	16.5	15.8	7.8	43	8400
RMSPS 20	20	102	16.5	15.8	6.6	42.7	10500
RMSPS 30	30	102	16.5	15.8	5.2	42.2	14400
RMSPS 100	100	102	16.5	15.8	2.6	41.1	37000

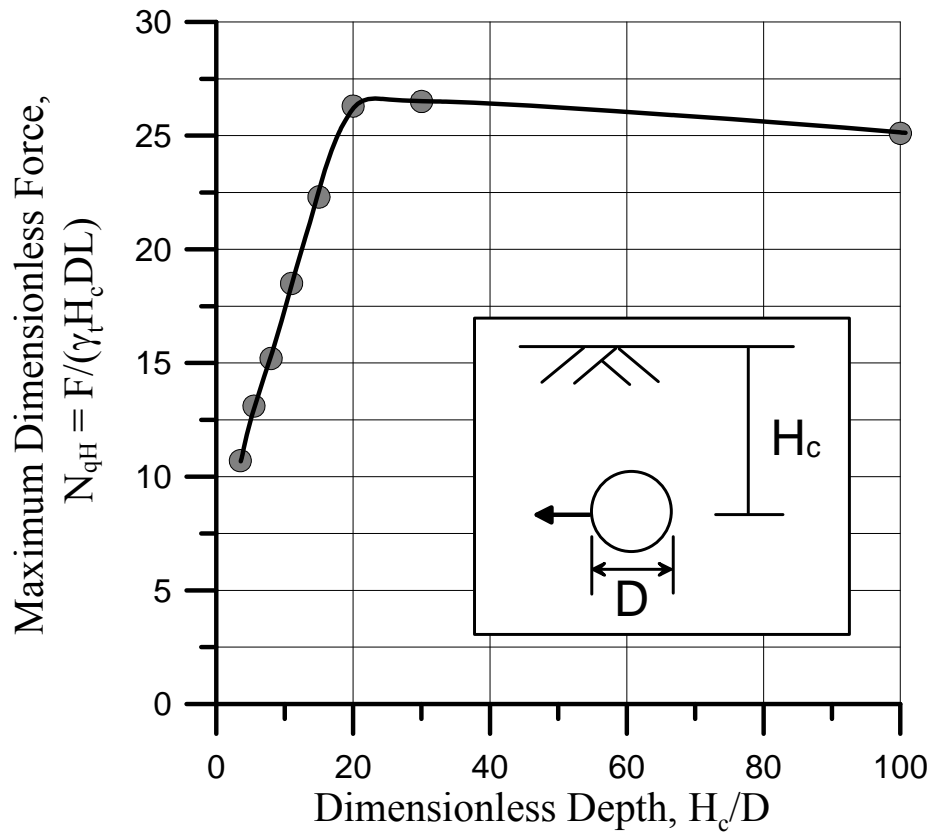


Figure 4.24 Lateral N_{qH} vs. H_c/D for Partially Saturated RMS Graded Sand

The overall trend of N_{qH} vs. H_c/D for partially saturated RMS graded sand is similar to that for dry sand. The N_{qH} decreases approximately 4.4 % from $H_c/D = 20$ to 100, and ϕ_{ps-p} decrease approximately 4.6 % at the same range of H_c/D . The figure indicates that a limiting value of N_{qH} , approximately equal to 26.5, is reached at critical embedment ratio between $H_c/D = 20$ and 30.

CHAPTER 5

VERTICAL UPWARD PIPE MOVEMENT

5.1 Introduction

A series of finite element (FE) analyses with ABAQUS 6.9 (2009) were performed to predict the peak force and to compare the measured peak forces with experimental results for vertical upward pipe movement. Comparing the results of numerical simulations and actual experiments is necessary to validate the numerical model. The experimental database used for the comparisons is derived from full-scale, 2-D tests on pipe buried in dry sand. The full-scale tests and test results for vertical upward pipe movement are described by Trautmann and O'Rourke (1983). In this chapter, the modeling procedures for vertical upward pipe movement are described. Next, relationships between maximum upward pipe force and pipe depth are developed for dry and partially saturated semi-infinite soil conditions with H_c/D varying from 5.5 to 100.

5.2 Finite Element Model and Soil Strength Properties

To facilitate the comparison of experimental and analytical results, both the measurements and numerical output are converted to dimensionless form. Figure 3.1 shows a typical dimensionless pipe force vs. displacement curve. The vertical axis is the vertical upward forces exerted on the pipe in dry sand, which is expressed as $F' = F / (\gamma_d H_c DL)$. The horizontal axis is the dimensionless pipe displacement expressed as $Z' = Z/D$, in which Z is the measured relative vertical upward displacement between

pipe and soil.

Each FE analyses mesh was developed to replicate the geometry and material properties of the soil, pipe, and experimental facilities in each test. Figure 5.1 shows the typical geometry of the numerical model, which is taken directly from the large-scale tests. In the figure, H_{bt} is the height from the pipe center to the interior box bottom, H_{bk} is the closest distance from the center of the pipe to the test box wall, H_c is the depth from the top of the soil to the center of the pipe, and D is the external diameter of the pipe. As described in Chapter 3, 8-node biquadratic, plane strain, quadrilateral, reduced integration elements (element type CPE8R) are used to represent the soil around the pipe. The pipe was modeled as a rigid cylinder with surface properties similar to those of ASTM Grade A-36 steel.

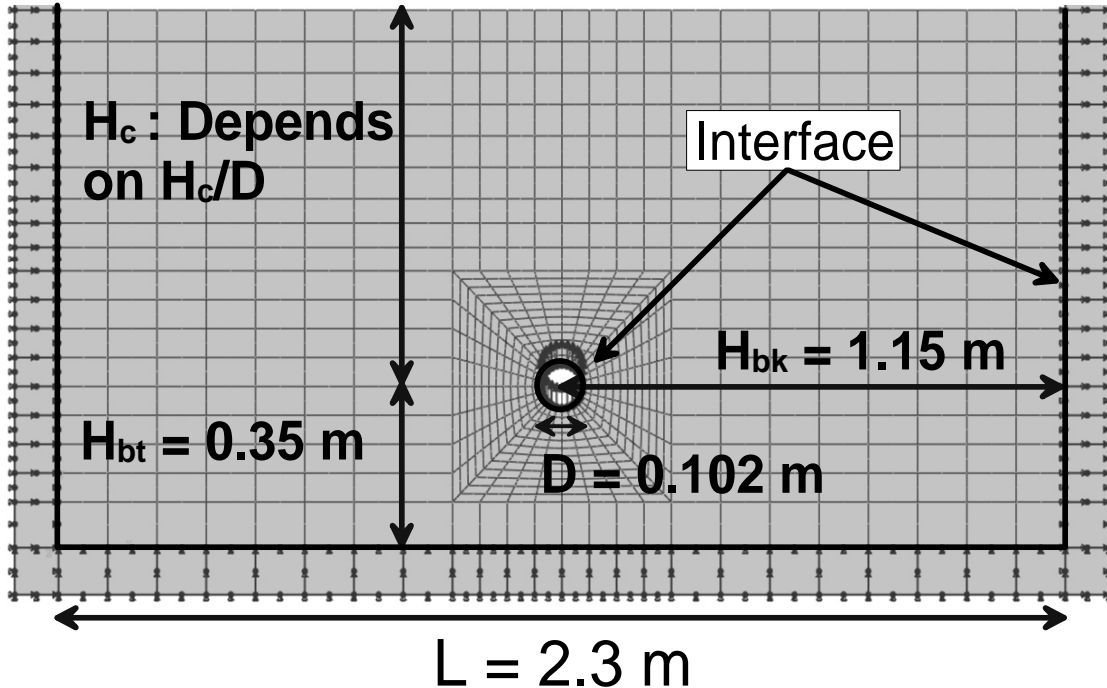


Figure 5.1 Geometry of the Finite Element Model for Upward Pipe Movement

A refined mesh was used within a distance of approximately two pipe diameters from the center of the pipe. As explained in Chapter 3, the thickness of the elements within the refined mesh was taken as the shear band thickness observed during DS tests. Approximately 700 to 900 elements were used in the meshes to simulate the different full-scale test conditions. A geostatic load was applied to the soil and pipe at the start of each simulation under $K_o = 1$ condition. Vertical upward pipe movement is generated by imposing a vertical upward displacement boundary condition on all the nodes of the pipe.

The interface between the soil and pipe has friction angle of $0.8 \phi'_{ds-p}$ on the basis of DS tests performed by Trautmann (1983). The interface interaction is modeled by the surface-based contact, in which the separation and slip between the soil and pipe is allowed.

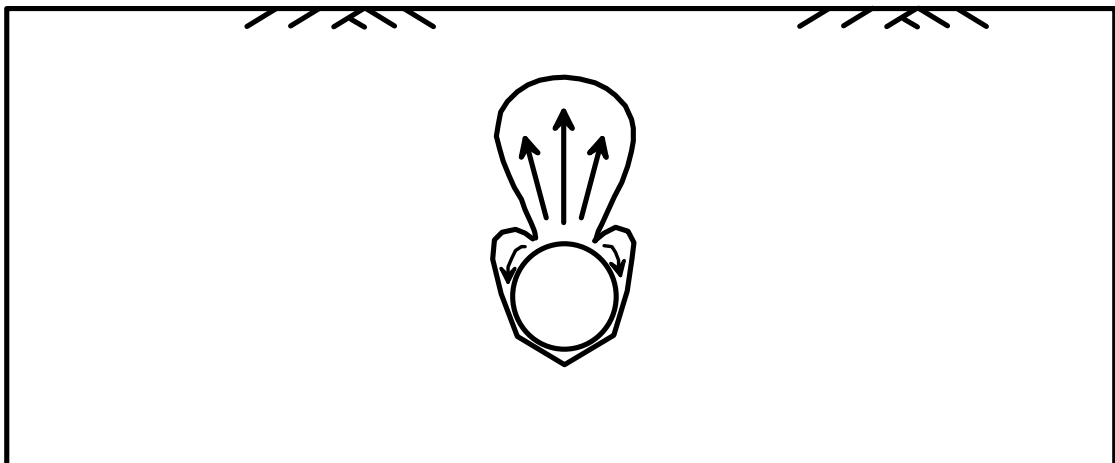


Figure 5.2 Displacement Field Interpretive Diagram for Upward Pipe Movement (Trautmann and O'Rourke, 1983)

Figure 5.2 shows the displacement field interpretive diagram for vertical upward pipe movement. In the experiments, the pipe was located at the center of the

test basin. Test measurements showed that soil displacement was confined to a relatively small zone surrounding the pipe. A sensitivity study was performed to determine how the peak upward force is affected by the interface elements between the soil/vertical test basin wall and soil/wooden base of the test basin. Because the study showed only 0.6 % difference in the results, the interface elements between the soil and the test basin were removed. Moreover, the nodes at the vertical boundaries were fixed in the x-direction and those at the base were fixed in the y-direction for all FE analyses of vertical upward pipe movement.

The input parameters required for vertical upward numerical analyses are similar to those required for lateral pipe movement. The peak angle of dilation, ψ_p was evaluated using Eqn. 3.2, where σ'_N is taken as σ'_{vc} , which is the vertical effective stress at the pipe centerline. With ψ_p estimated relative to σ'_{vc} , Eqns 3.3 and 3.7 were used to evaluate ϕ'_{ps-p} . Critical friction angle, ϕ'_{crit} , was selected as 38.6° for CU filter sand (Olson, 2009). Table 5.1 summarized input parameters used in vertical upward pipe movement FE analyses for CU filter sand. A Poisson's ratio, $\nu = 0.3$, was assumed for the sand.

5.3 Comparison of FE Analyses and Measured Peak Forces

Figure 5.3 shows the experimental data and analytical results in terms of vertical upward force vs. displacement for medium CU filter sand with $H_c/D = 1.5$. There are notable differences, especially in the maximum forces. The analytical dimensionless peak force, N_{q-e} , exceeds the measured dimensionless peak force, N_{q-m} , approximately by 42 %. The post-peak behavior of the experimental data shows that the force decreases approximately by 50 % from the peak, whereas the FE results

Table 5.1 Summary of the Input Parameters Used in Vertical Upward Pipe Movement
Finite Element Analysis for CU Filter Sand

Test No.	H_c/D	Diameter (mm)	Length (mm)	γ_d (kN/m ³)	Ψ_p (degrees)	ϕ'_{ds-p} (degrees)	ϕ'_{ps-p} (degrees)
T & O* 44	1.5	102	1200	16.4	7.1	37.0	43.9
T & O 43	4	102	1200	16.4	6.1	36.3	43.2
T & O 42	8	102	1200	16.4	5.5	35.9	42.8
T & O 41	13	102	1200	16.4	5.1	35.6	42.5
T & O 38	1.5	102	1200	17.7	17.4	44.1	51.1
T & O 37/50	4	102	1200	17.7	15.1	42.5	49.5
T & O 40	8	102	1200	17.7	13.6	41.5	48.5
T & O 39	13	102	1200	17.7	12.6	40.8	47.8

* T & O: Trautmann & O'Rourke (1983)

show a continuous decrease of only 20 % from the peak. The pattern of soil displacement at a shallower depth affected the uplift force and led to the differences between the N_{q-m} and N_{q-e} values.

The soil displacements measured for vertical upward pipe movement in the medium CU filter sand at $H_c/D = 1.5$ (Trautmann and O'Rourke, 1983) are shown in Fig. 5.4. As the pipe moved upward, the soil on the upper side of the pipe was pushed upward and outward. The soil at the sides moved downward and flowed into the void created under the pipe, in much the same manner described by Kananyan (1966) for uplift tests on disks. The maximum displacement above the pipe center at the soil surface was approximately 45 % of the vertical pipe displacement.

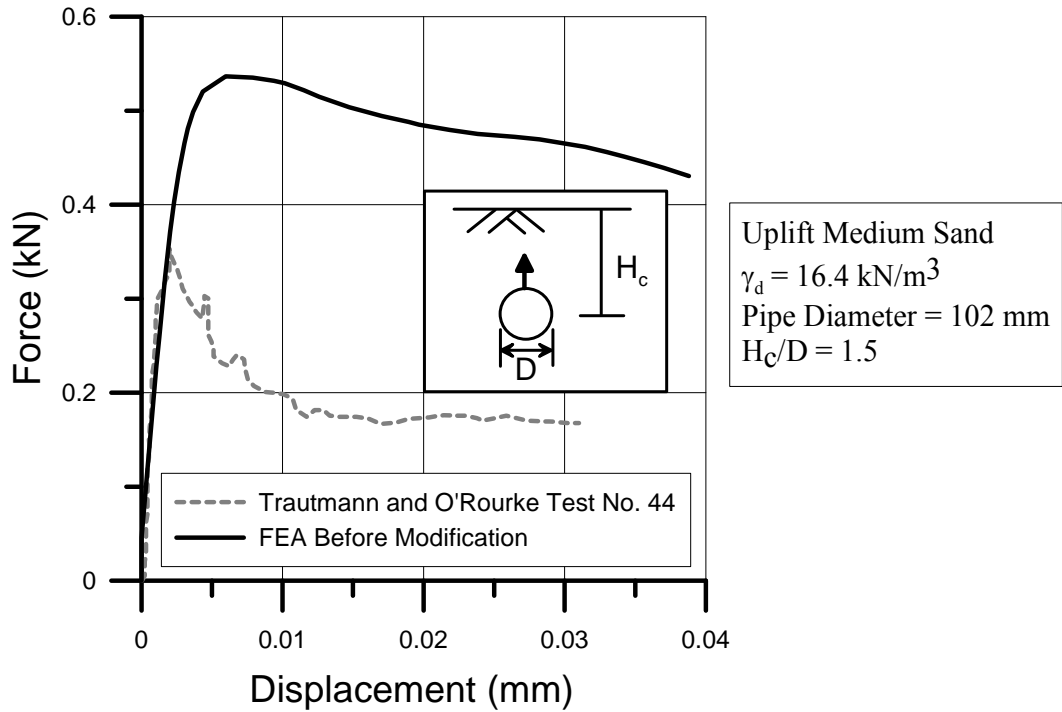


Figure 5.3 Force vs. Displacement Curve for Medium CU Filter Sand Vertical Upward Pipe Movement Test at $H_c/D = 1.5$

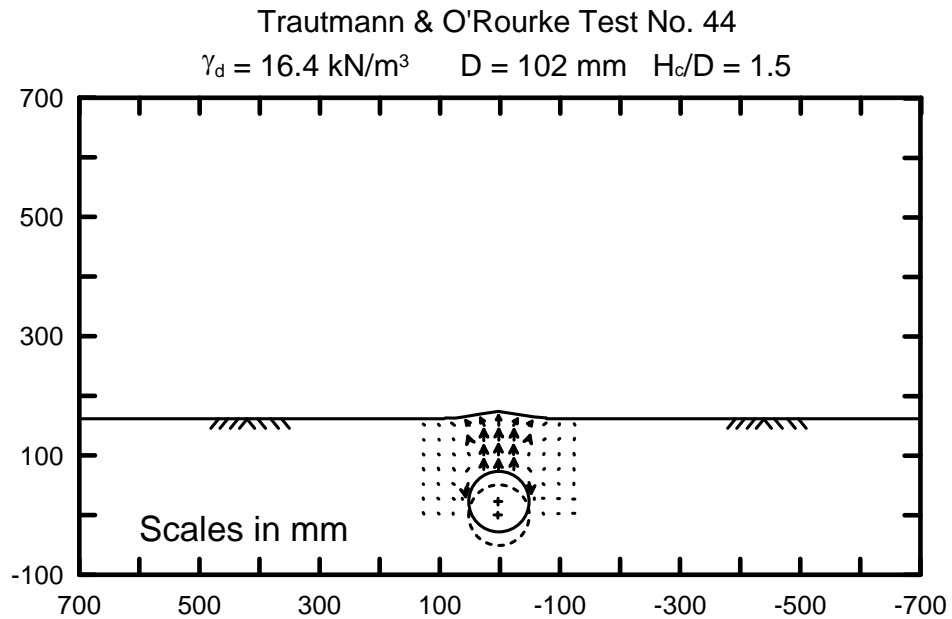


Figure 5.4 Displacement Field for Vertical Upward Pipe Movement Test in Medium Sand at $H_c/D = 1.5$ (Trautmann and O'Rourke, 1983)

Figure 5.5 shows deformed shape of FE mesh for vertical upward pipe movement in medium dense CU filter sand at $H_c/D = 1.5$. In the FE analysis, the maximum displacement of the soil surface was approximately equal to the vertical pipe displacement. In addition, the soil was modeled as a continuum so that the soil elements were not able to separate and flow into the void under the pipe. As a result, all soil elements directly above the pipe still contribute to weight and shear resistance, thus increasing the force on the pipe, especially at shallower depths.

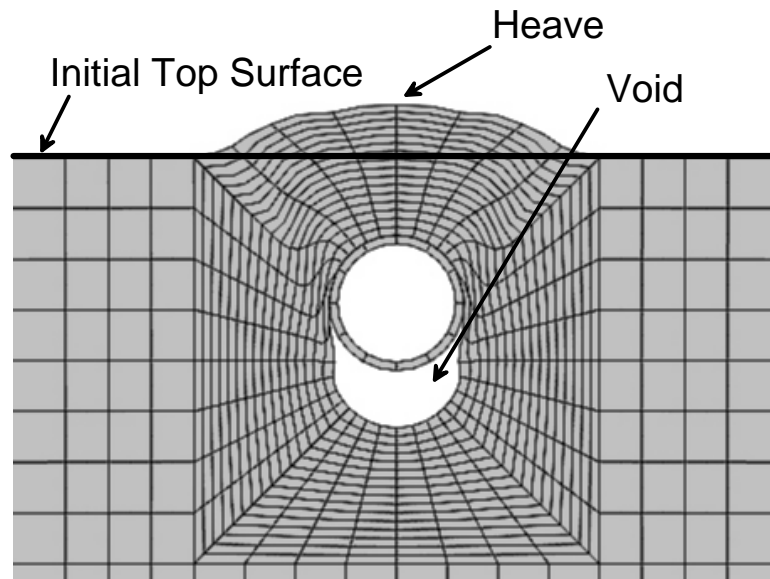


Figure 5.5 Deformed Shape of FE Analysis for Vertical Upward Pipe Movement Test in Medium Sand at $H_c/D = 1.5$

To eliminate the extra resistance, a modified simulation was developed by which the finite element mesh was adjusted to remain level during upward pipe movement. At $H_c/D = 1.5$, for example, the soil elements equivalent to 45 % of the pipe displacement were removed. In general, the area of the void under the pipe was approximately equal to the area of the removed elements. In this case, the maximum

displacement on the soil surface was approximately 45 % of the pipe displacement, which was consistent with the experimental measurement, as illustrated in Fig. 5.4.

Figure 5.6 shows the deformed shape of the FE mesh for medium sand at $H_c/D = 1.5$ for the modified mesh model. The actual area of removed soil was approximately 20 % larger than the void created under the pipe, and the maximum displacement on the soil surface was approximately 40 % of the vertical pipe displacement. Because the soil is modeled as a continuum, the modified numerical model is not able to account fully for soil that moves into the void beneath the pipe. The force acting on the pipe, however, results mainly from soil above the pipe, and

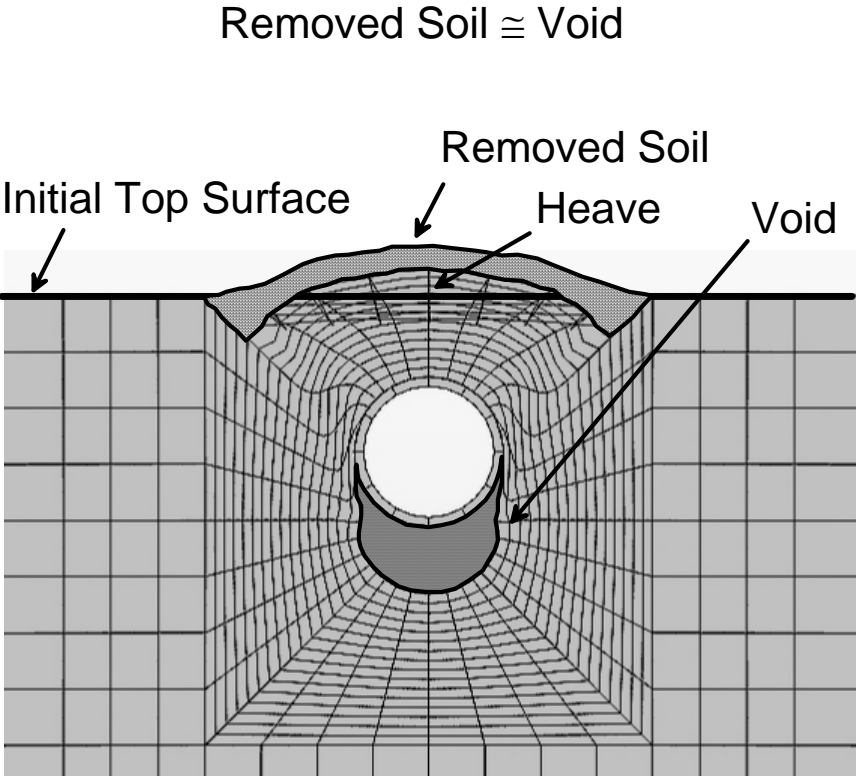


Figure 5.6 Deformed Shape of FE Analysis for Vertical Upward Pipe Movement Test
After Mesh Modification

removing the surface elements was enough to eliminate soil weight and shear strength so that the numerical results are consistent with the full-scale test observations.

Figure 5.7 shows force vs. displacement relationships for vertical upward pipe movement in medium and dense CU filter sand at $H_c/D = 1.5$ and 4 reported by Trautmann (1983) and Trautmann and O'Rourke (1983) in comparison with the results of the modified numerical simulations. In the figure, T & O represents the Trautmann and O'Rourke (1983) test. The vertical axis shows the upward force, and the horizontal axis shows the relative displacement between pipe and soil. The modified numerical simulation results are in favorable agreement with the experimental data for vertical upward pipe movement in medium and very dense sand at $H_c/D = 1.5$ and 4. The results from modified numerical simulations show sudden changes in the post-peak behavior as elements on the top surface were removed from the FE mesh. The irregular pattern of the upward forces matches that of the full-scale test measurements.

Finite element analyses without surface modification for $H_c/D = 8$ and 13 showed small surface displacement consistent with the experimental data. To identify the smallest H_c/D where unmodified FE analyses results compare favorably with experimental data, a series of unmodified FE analyses were performed to compare the FE dimensionless maximum vertical upward movement force, N_{qVU-e} , with the measured dimensionless maximum vertical upward movement force, N_{qVU-m} . Figure 5.8 shows the percentage difference between N_{qVU-m} and N_{qVU-e} with respect to N_{qVU-m} from the unmodified FE simulations vs. H_c/D . The unmodified FE analyses over predict N_{qVU-m} at shallower depths ($H_c/D = 1.5$ and 4) by 17 – 42 %, whereas the

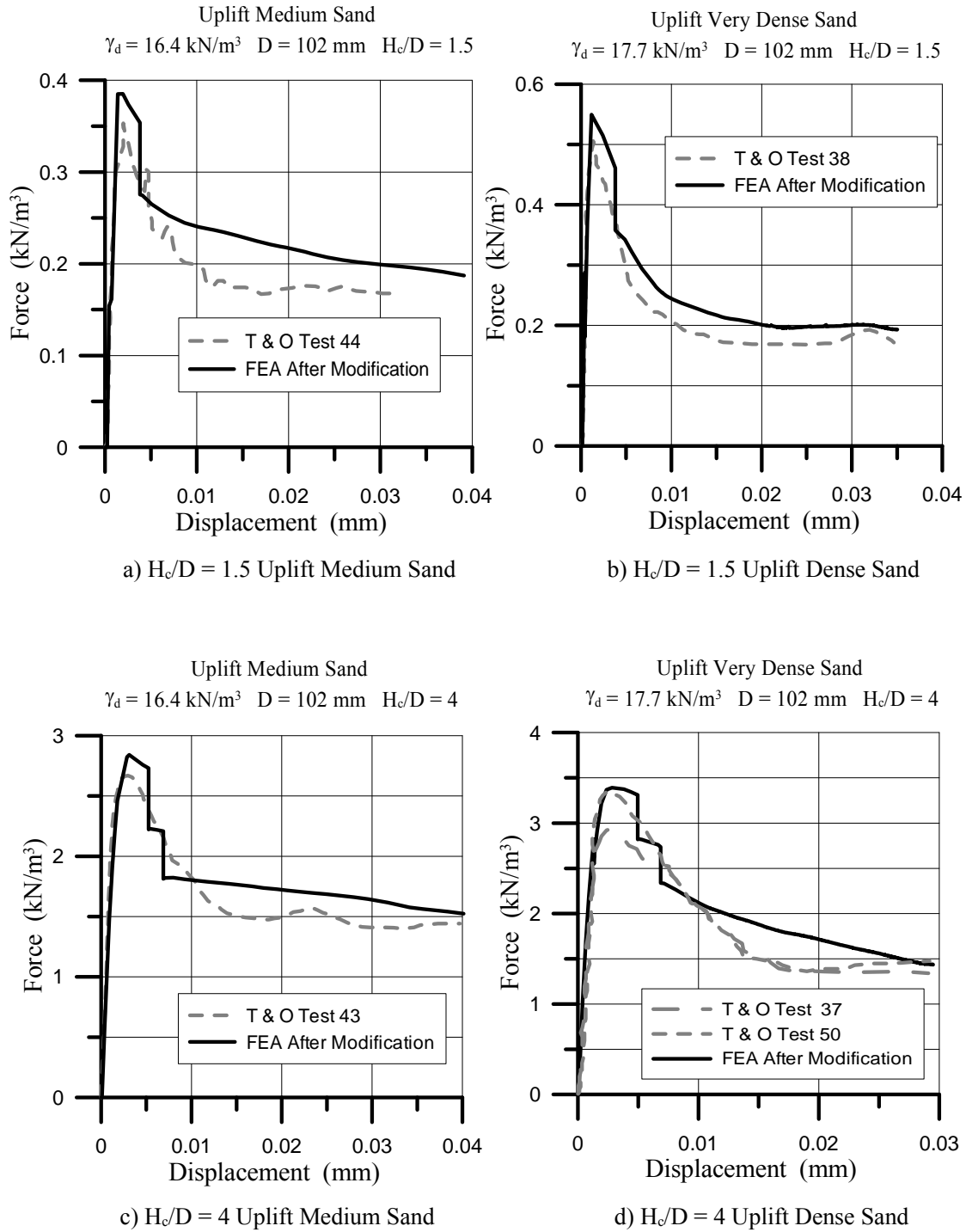


Figure 5.7 Force vs. Displacement Curve for Vertical Upward Pipe Movement Test in Medium and Very Dense Sand Test at $H_c/D = 1.5$ and $H_c/D = 4$

Uplift FEA Error Analyses

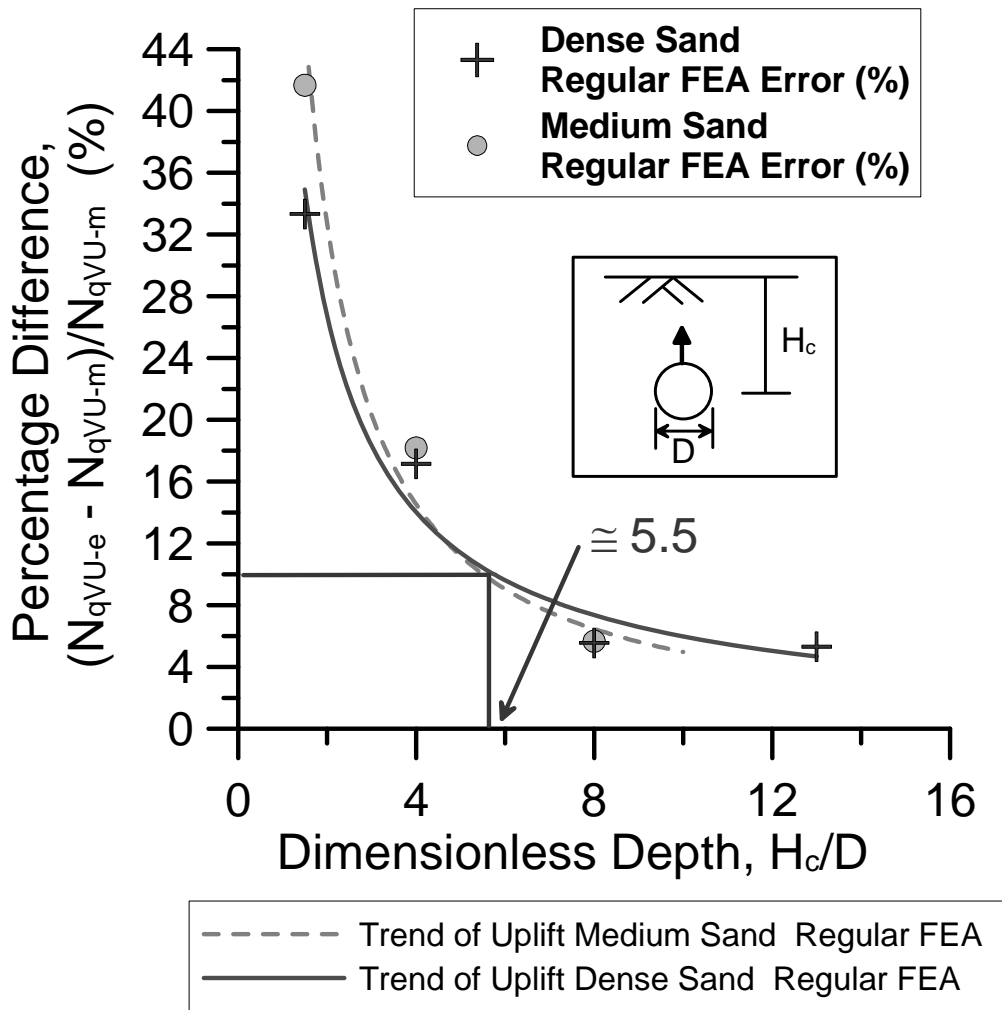


Figure 5.8 Comparisons of Vertical Upward N_{qvU-m} and N_{qvU-e} in Medium and Very Dense CU Filter Sand Using the Regular FEA

unmodified FE analyses predicts N_{qvU-m} reasonably well at for $H_c/D \geq 5.5$. The percentage differences for both medium and very dense sand become smaller than 10 % at $H_c/D \approx 5.5$. Therefore, the modified FE analyses are used for $H_c/D < 5.5$, and unmodified FE analyses are used for $H_c/D \geq 5.5$.

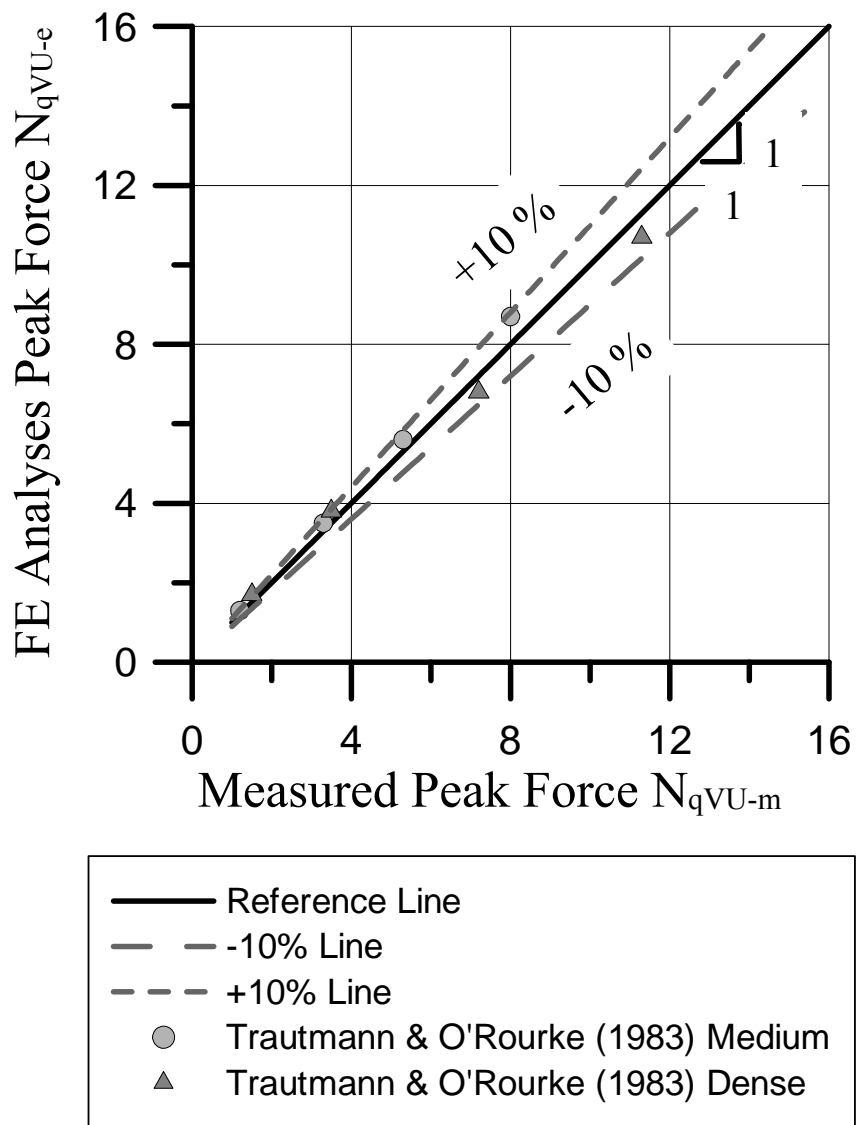


Figure 5.9 Comparisons of N_{qvU-m} and N_{qvU-e} for the Modified Mesh Model

Figure 5.9 shows N_{qvU-m} plotted with respect to N_{qvU-e} after the modification. The FEA and the measured dimensionless peak forces match reasonably well for the uplift test results. There are favorable agreements between N_{qvU-e} and N_{qvU-m} , with 88 % of N_{qvU-e} within $\pm 10\%$ of N_{qvU-m} . The average difference between N_{qvU-e} and N_{qvU-m} is 7.7 %.

Figure 5.10 compares the FE results and 2-D test measurements of Trautmann and O'Rourke (1983), in which the dimensionless force is plotted as a function of the dimensionless depth. There is a favorable agreement among the data for all H_c/D . In general the FE analyses results over predict N_{qVU-m} by 5 – 13 %. Overall, the average difference between the FE analyses and measured force for dry CU filter sand is 7.7 %.

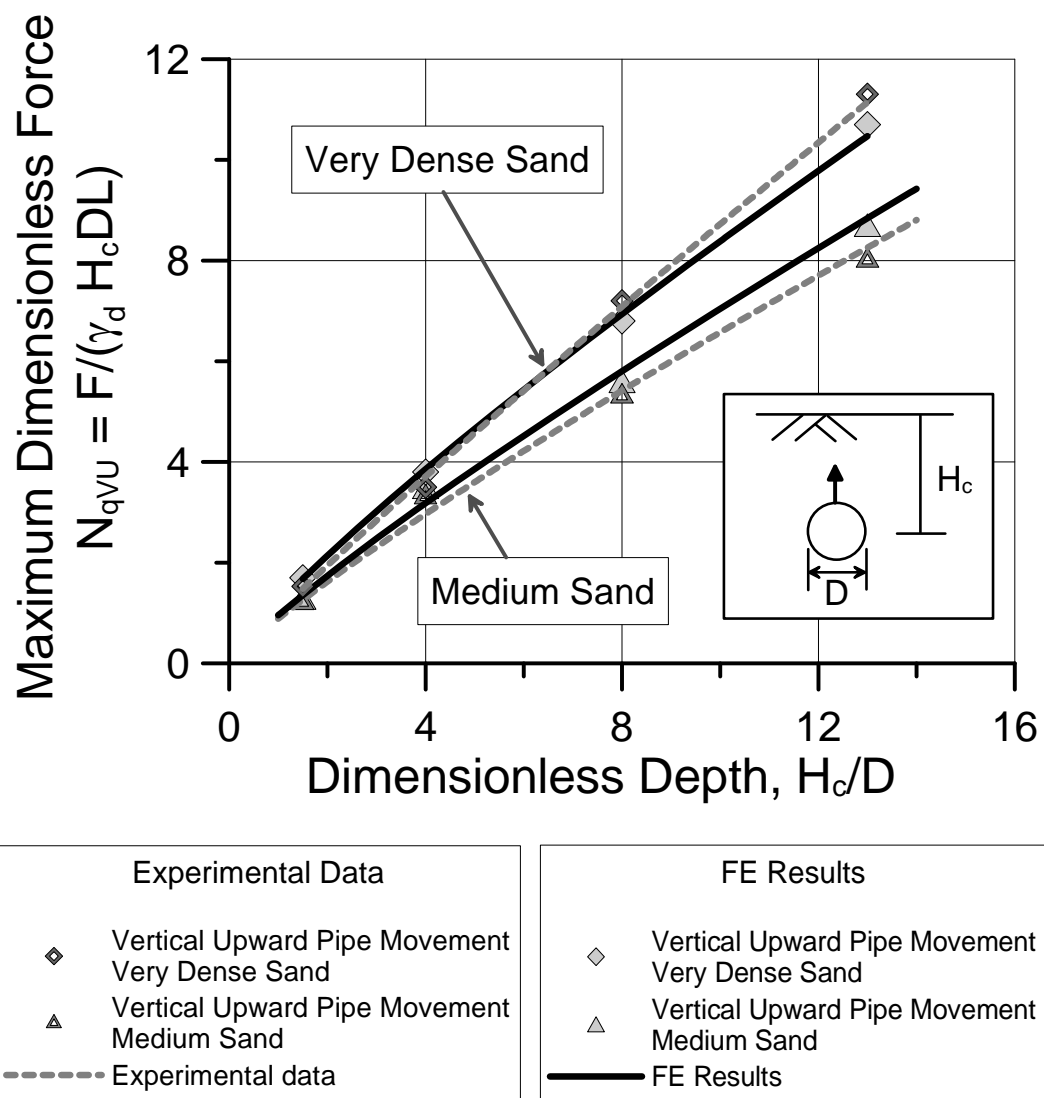


Figure 5.10 Plot of Vertical Upward Pipe Movement N_{qVU} vs. H_c/D

5.4 Young's Modulus for Vertical Upward Pipe Movement

As discussed in Chapter 3, the Mohr-Coulomb plasticity model in this work is based on representing the soil response as linear elastic until stresses in the soil are equal to and exceed the Mohr-Coulomb yield surface. Thus, an elastic modulus is required as one of the constituent soil properties. The model uses a constant elastic modulus to approximate the nonlinear stress-strain behavior of soil before yield, and thus provides a simplified “equivalent” representation of soil response to vertical upward pipe movement. The K_{70} approach discussed in Section 3.6.2 is used to approximate E_{70-VU} .

The equivalent modulus for vertical upward pipe movement was determined by running FE simulations with different values of E and the same strength parameters for each vertical upward pipe movement experimental data set from Trautmann & O'Rourke (1983) until the initial linear force vs. displacement response coincided with K_{70} .

In Fig. 5.11 equations following the form of Eqn. 3.8 fit to the Trautmann and O'Rourke (1983) test data for medium and very dense sand in which σ'_3 is expressed as σ'_{vc} . As discussed in Section 3.6.2, the experimental data in Fig. 5.11 shows that E_{70-VU} increases with increasing γ_d , for constant σ'_{vc} . Using the data from the Trautmann and O'Rourke (1983), the multiple linear regression analyses provide the following:

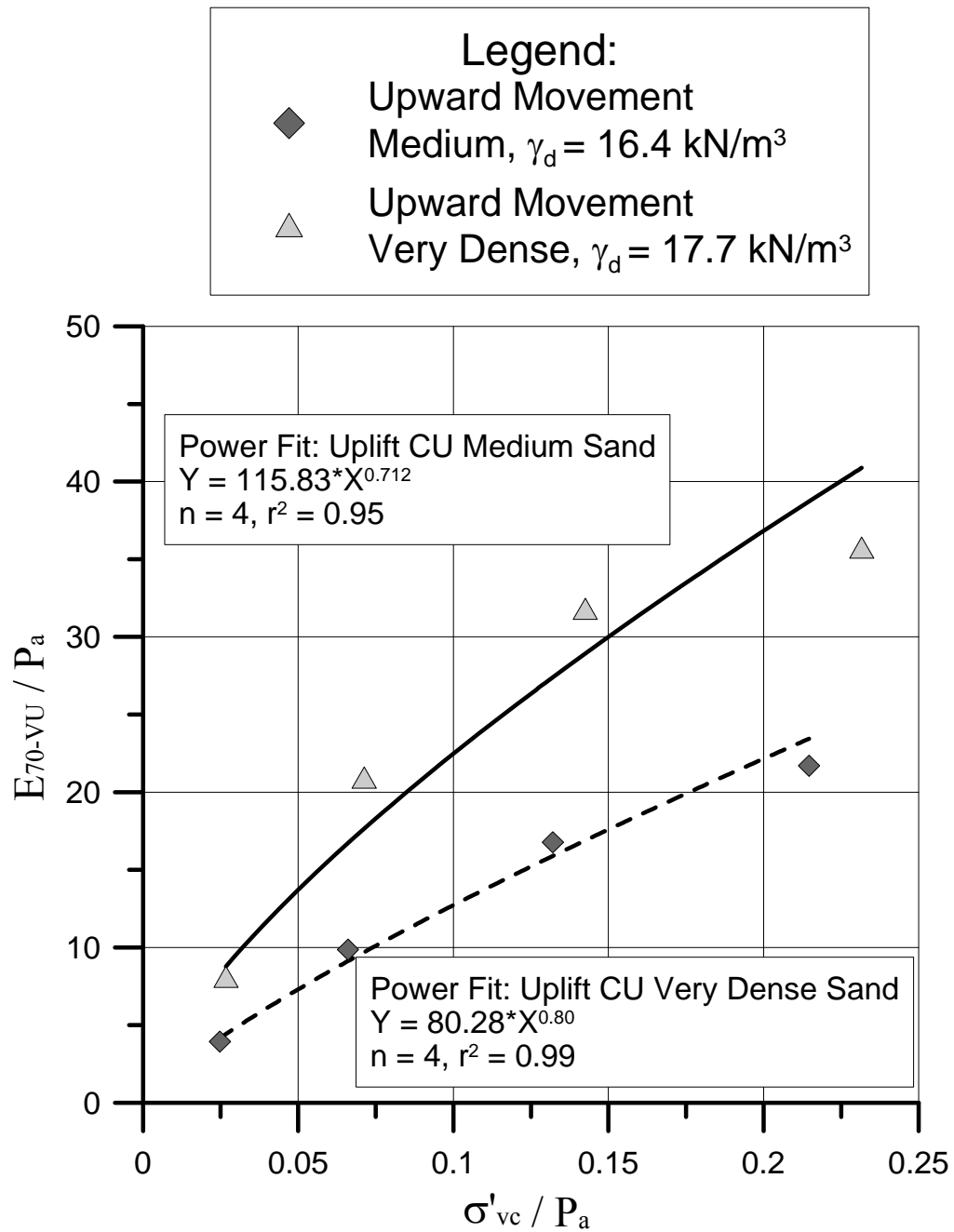


Figure 5.11 Relationships between E_{70-VU}/P_a and σ'_{vc}/P_a of Vertical Upward Pipe Movement Tests

$$\log \frac{E_{70-VU}}{P_a} = 0.481 + (7.061) \log \frac{\gamma_d}{\gamma_w} + (0.920) \log \frac{\sigma'_{vc}}{P_a} \quad (5.1)$$

in which log is for base 10. For this equation $r^2 = 0.95$, indicating a high degree of statistical significance.

Using the experimental data, Eqn 5.1 is re-written as

$$\frac{E_{70-VU}}{P_a} = 10^{0.481} \left[\frac{\gamma_d}{\gamma_w} \left(\frac{\sigma'_{vc}}{P_a} \right)^{0.130} \right]^{7.061} \quad (5.2)$$

The experimental data and Eqn. 5.2 are plotted in Fig. 5.12. The equation provides a close fit to the data, and thus provides a dependable way of re-producing the data trends. Table 5.2 summaries E_{70-VU} used in the vertical upward pipe movement simulation calculated from Eqn. 5.2.

Table 5.2 Summary of E_{70-VU} Used in Dry Vertical Upward Pipe Movement Simulations

Test No.	H_c/D	E_{70-VU} (kPa)	Test No.	H_c/D	E_{70-VU} (kPa)
T & O* 44	1.5	400	T & O 38	1.5	700
T & O 43	4	1000	T & O 37/50	4	1800
T & O 42	8	1800	T & O 40	8	3300
T & O 41	13	2800	T & O 39	13	5200

* T & O: Trautmann & O'Rourke (1983)

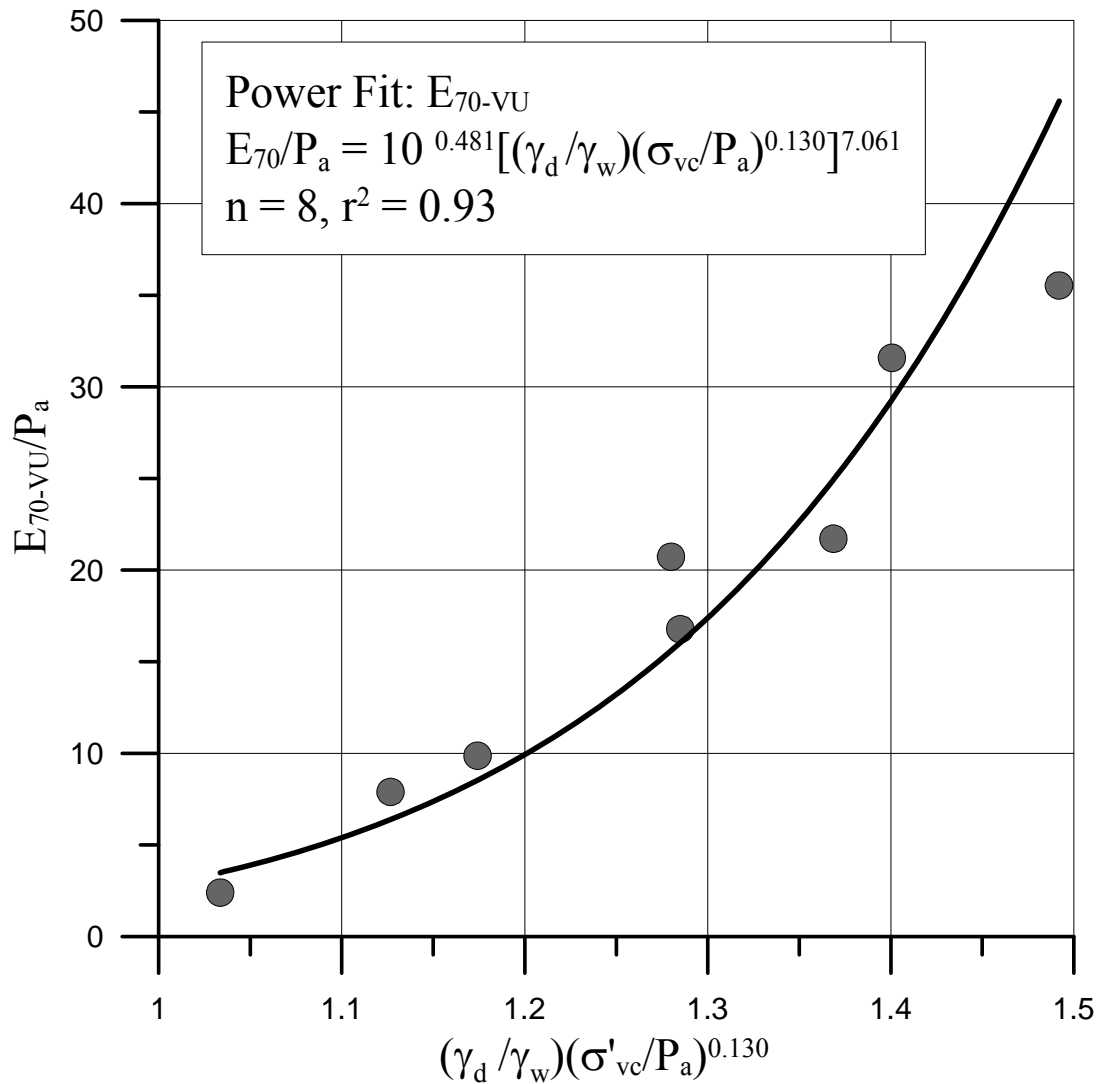


Figure 5.12 E_{70-VU} Multiple Linear Regression for γ_d and σ'_{vc} for Vertical Upward Pipe Movement

5.5 Comparison of Simulated and Measured Upward Force vs. Displacement Curves

Finite element models were developed that used input properties provided in Table 5.1 and 5.2. As discussed in Section 3.7, the model proposed by Anastasopoulos, et al. (2007) is used to represent strain softening behavior in the 2-D

FE simulation of soil-pipeline interaction.

Comparisons of FE simulations with measured force vs. displacement plots are provided in Figs. 5.13 and 5.15 for medium and very dense CU filter sand, respectively, reported by Trautmann (1983) and Trautmann and O'Rourke (1983). The vertical upward pipe forces are shown as dimensionless force $F' = F/(\gamma_d H_c DL)$, and lateral pipe displacements are shown as dimensionless displacement $Y' = Y/D$.

Comparisons between analytical and experimental force vs. displacement plots are provided in Figs. 5.14 and 5.15 for vertical upward pipe movement of medium and dense CU filter sand (Trautmann and O'Rourke 1983). The vertical upward pipe forces are shown as dimensionless force $F' = F/(\gamma_d H_c DL)$, and vertical upward pipe displacements are shown as dimensionless displacement $Z' = Z/D$. The vertical upward pipe movement numerical simulations for medium and very dense CU filter sand in Fig. 5.13 and 5.14 agree well with the test data for all H_c/D in terms of pre-peak, peak, and post-peak behavior. Overall, the analytical results are consistent with the data trends for all H_c/D , but tend to over predict peak loads for medium dense sand by 6 – 9 % at $H_c/D = 1.5 - 13$, and for dense sand by 9 – 13 % at $H_c/D = 1.5 - 4$. The analytical simulations under estimate the peak loads for dense sand by 5 – 6 % at $H_c/D = 8 - 13$.

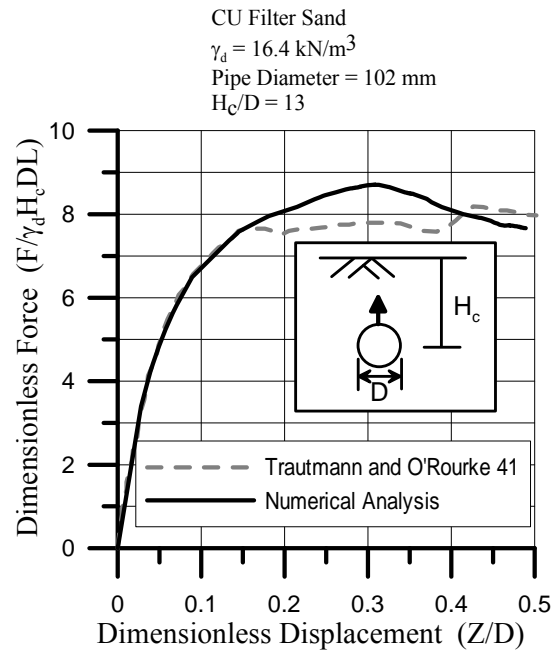
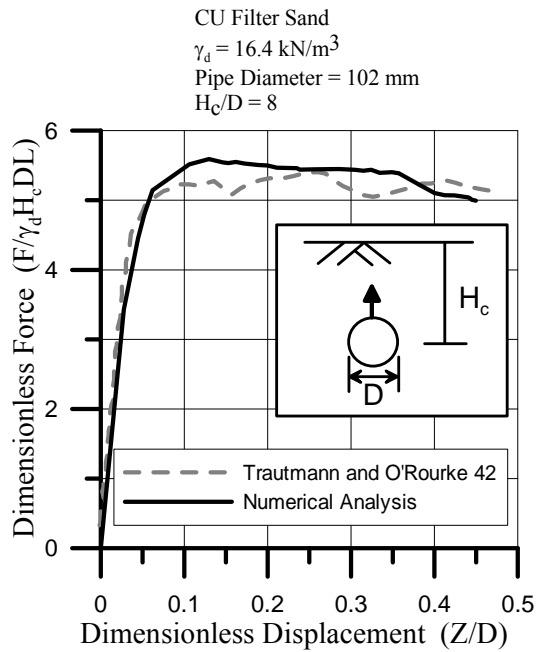
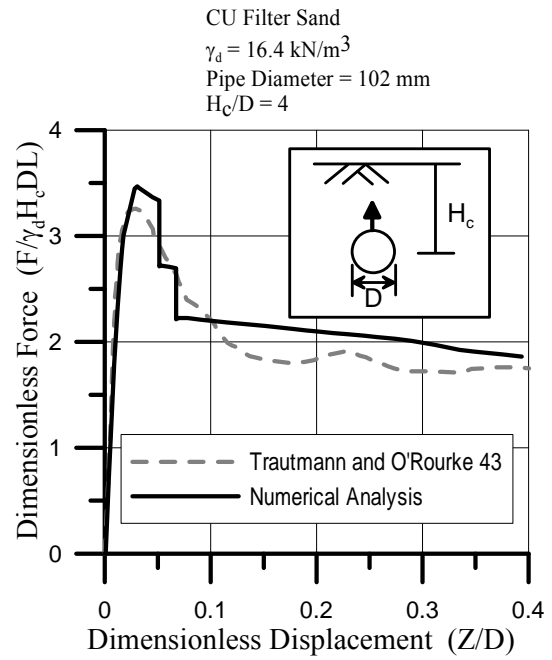
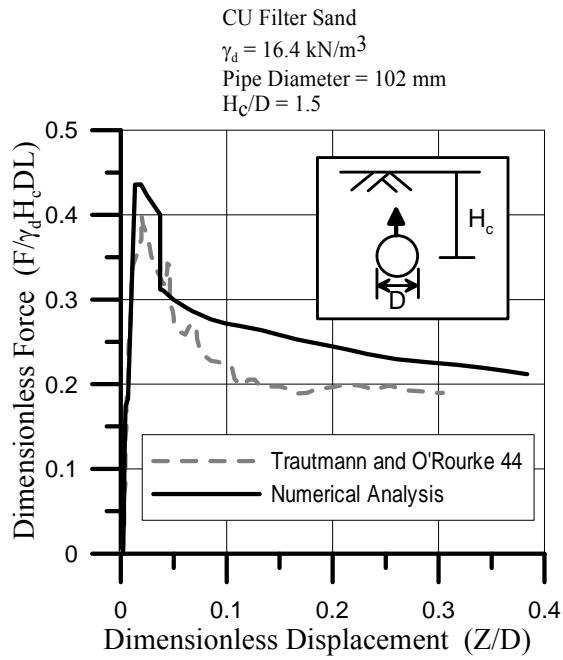


Figure 5.13 Vertical Upward Movement Dimensionless Force vs. Displacement
 Curves for Medium CU Filter Sand

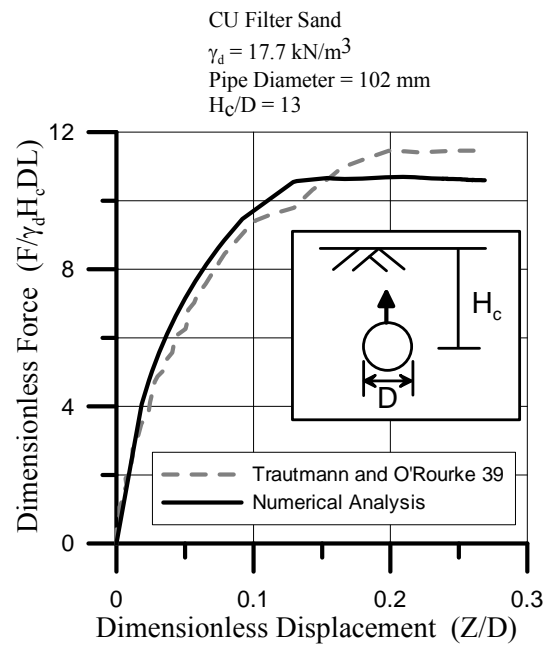
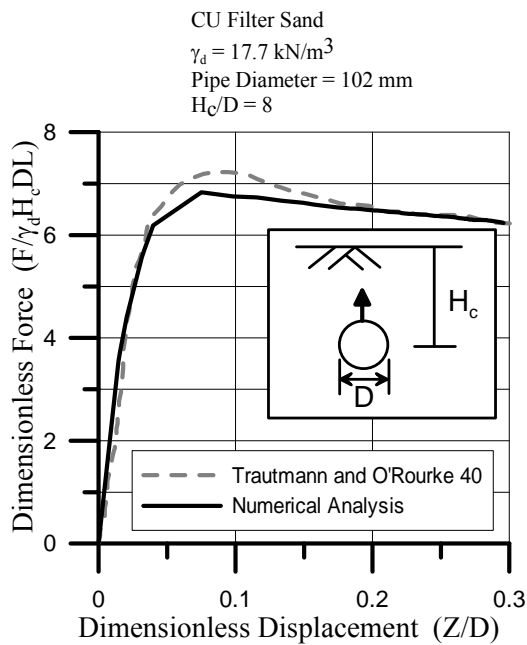
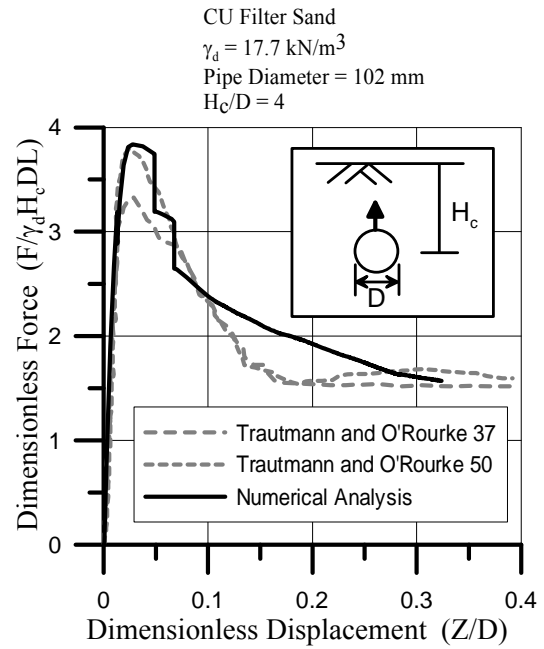
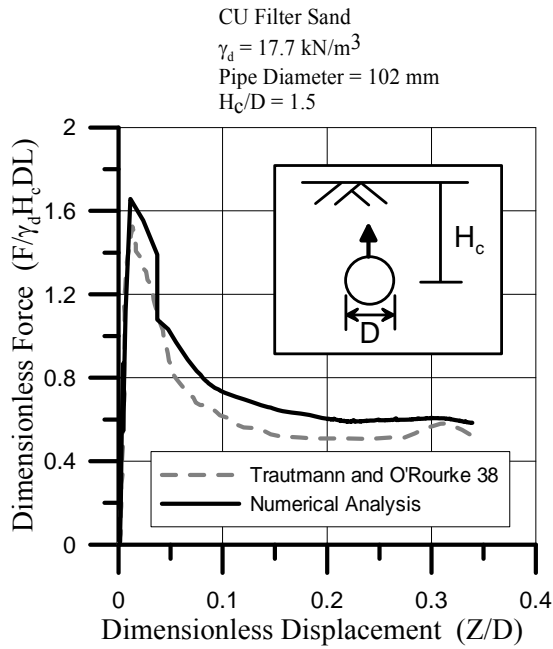


Figure 5.14 Vertical Upward Movement Dimensionless Force vs. Displacement
 Curves for Very Dense CU Filter Sand

5.6 Relationship Between Maximum Vertical Upward Force and Pipe Depth

Semi-infinite soil models were used to investigate the relationship between maximum vertical upward and downward pipe force and pipe depth for $H_c/D = 3.5 - 100$ for medium, dense, and very dense sand as characterized in Table 3.2. Figure 5.15 shows the typical geometry of the model used for simulating vertical upward soil-pipe interaction in both dry and partially saturated sand. The same FE model was used for vertical downward pipe movement, as explained in Chapter 6. As described in Chapter 3, 8-node biquadratic, plane strain, quadrilateral, reduced integration elements (element type CPE8R) were used to represent the soil around the pipe.

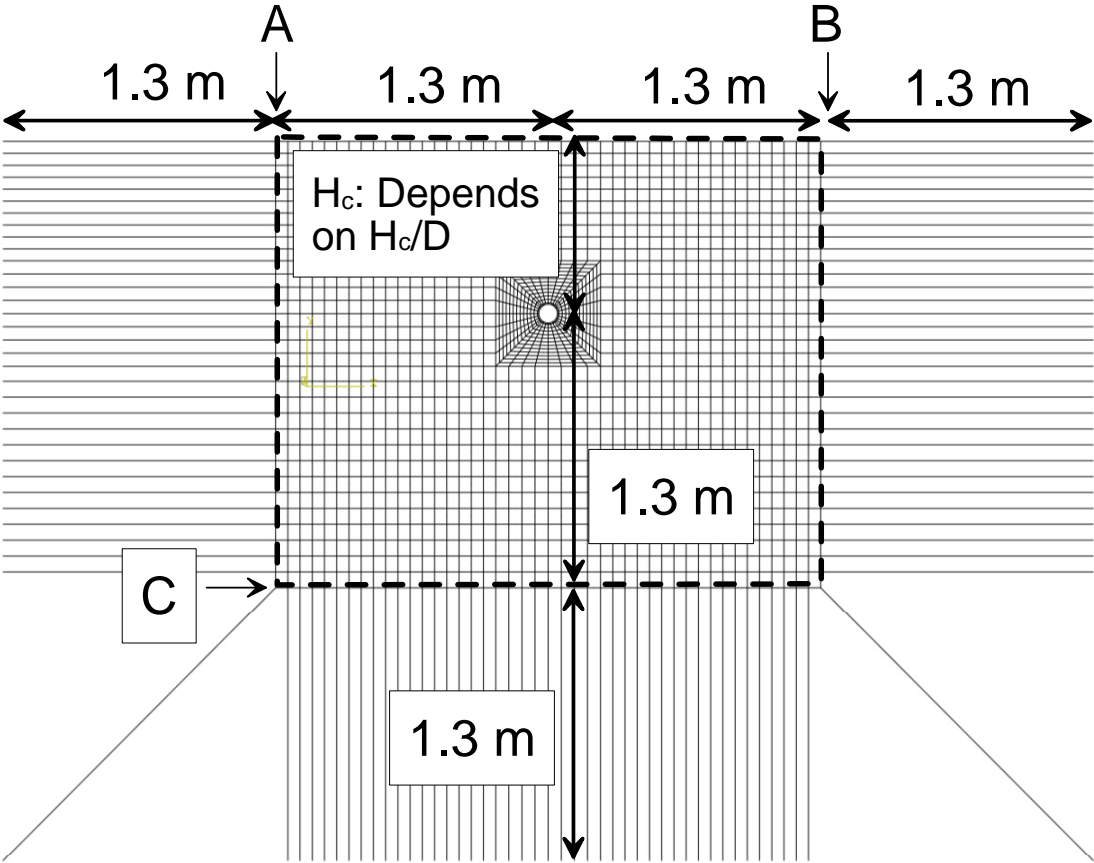


Figure 5.15 Finite Element Model for Upward Pipe Movement in Dry RMS Graded Sand

Five-node quadratic, plane strain, one-way infinite quadrilateral elements (element type CINPE5R) were used to represent the semi-infinite soil medium and were located outside of the CPE8R elements (boundary marked by A, B, and C).

Input parameters for soil strength were obtained from the procedure discussed in Section 3.3.2. An equivalent modulus according to the K_{70} procedure discussed in Section 5.4 and strain softening model described in Section 3.7 were used in the vertical upward 2-D FE simulations. A Poisson's ratio, $\nu = 0.3$, was assumed for the sand and all simulations were performed with a nominal cohesion $c' = 0.1 - 0.3$ kPa to promote numerical stability.

Table 4.1 summarizes input parameters used in FE analyses, and Table 5.3 summarizes the calculated E_{70} from Eqn. 5.2 for vertical upward pipe movement simulations. The notation ‘_UP’ indicates vertical upward pipe movement.

Comparisons of vertical upward N_{qVU} vs. H_c/D for medium, dense, and very dense sand are shown in Fig. 5.16. The dimensionless parameters $N_{qVU} = F/(\gamma_d H_c DL)$ and H_c/D defines the lateral pipe forces and depth, respectively. The values of N_{qVU} were determined as described in Chapter 3.

The FE simulations of vertical upward pipe movement show that N_{qVU} reaches its maximum value at $H_c/D = 30$ at values approximately equal to 14.4, 16.7, and 20.3 for medium, dense, and very dense sand, respectively.

Table 5.3 Summary of E_{70-VU} for Vertical Upward Pipe Movement Simulations

Test No.	H_c/D	E_{70-VU} (kPa)	Test No.	H_c/D	E_{70-VU} (kPa)
RMS5.5M_UP	5.5	1300	RMS20D_UP	20	5800
RMS8M_UP	8	1800	RMS30D_UP	30	8500
RMS11M_UP	11	2400	RMS100D_UP	100	25500
RMS15M_UP	15	3200	RMS5.5VD_UP	5.5	2300
RMS20M_UP	20	4200	RMS8VD_UP	8	3300
RMS30M_UP	30	6100	RMS11VD_UP	11	4400
RMS100M_UP	100	17300	RMS15VD_UP	15	5900
RMS5.5D_UP	5.5	1800	RMS20VD_UP	20	7700
RMS8D_UP	8	2500	RMS30VD_UP	30	11100
RMS11D_UP	11	3400	RMS100VD_UP	100	33600
RMS15D_UP	15	4500			

5.7 Analytical Results of Maximum Vertical Upward Dimensionless Forces for Various Pipe Diameters

Additional FE analyses were run with various pipe diameters to investigate the effects increasing diameter on soil-pipe interaction at constant H_c/D . Figure 5.17 shows the geometry of the numerical model for simulating vertical upward soil-pipe interaction with various pipe diameters in dry sand. The model is similar to that shown in Fig. 5.15 except the dimensions. The selected pipe diameters for this study were 900 mm, compared with 102 mm used in the production simulations. Because of the increased pipe size, the mesh dimensions are ten times larger than those shown in Fig. 5.15

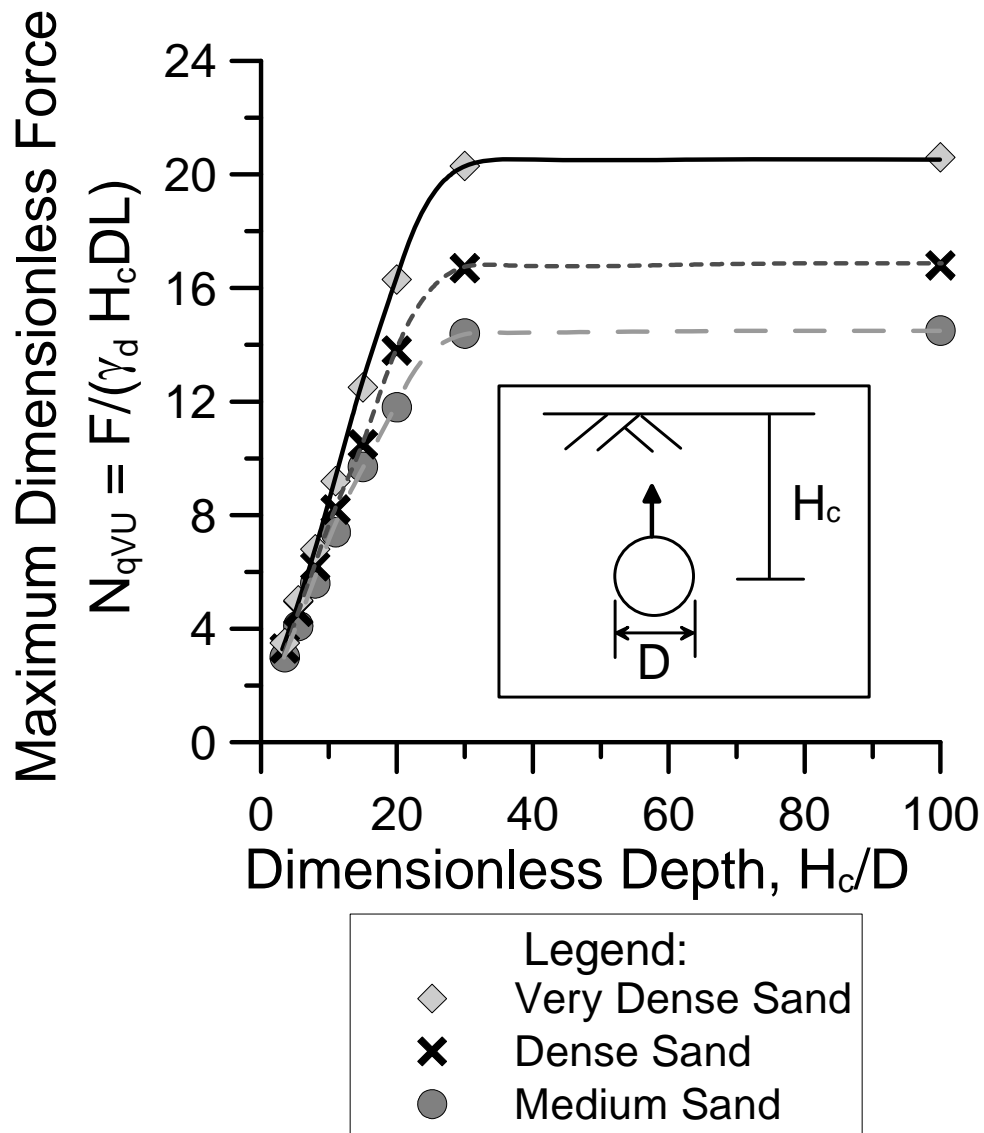


Figure 5.16 Summary Plot of N_{qvU} vs. H_c/D for Vertical Upward Pipe Movement

Input parameters for numerical simulation, including soil strength and modulus are the same as those described in Section 4.8.3. As previously described, $\nu = 0.3$ was assumed for the sand and a nominal cohesion $c' = 0.1 - 0.3$ kPa was used in the simulations for numerical stability.

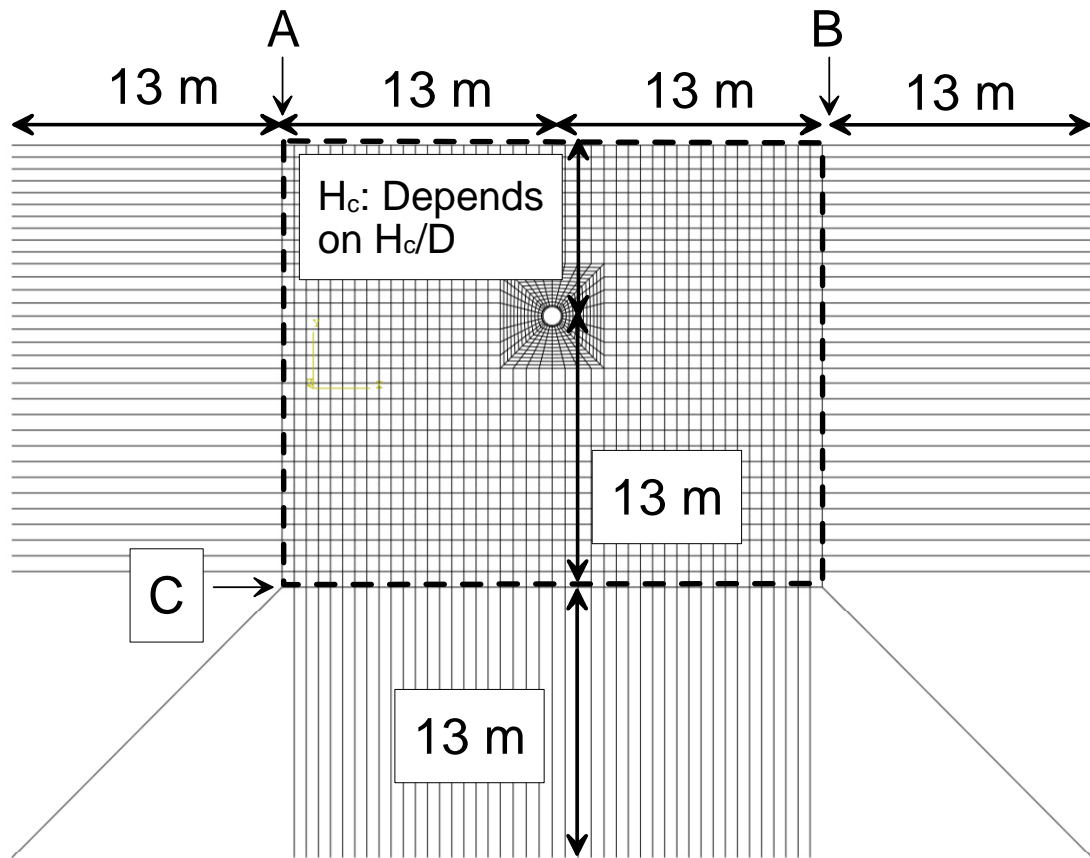


Figure 5.17 Geometry of the Vertical Upward Pipe Movement Numerical Model for Various Pipe Diameters Simulation

Figure 5.18 plots N_{qVU} from the FE analyses for various pipe diameters. The dimensionless parameters, $N_{qVU} = F/(\gamma_d H_c DL)$ and H_c/D , define the vertical upward pipe forces and depth, respectively. The plot shows diameter effects increasing with increasing γ_d , and decreasing with increasing H_c/D . For $D = 102$ mm and 900 mm, the maximum difference in N_{qVU} at $H_c/D = 2$ is approximately 12 % for both dense and very dense sand. As discussed in Section 4.8.3, the effects of diameter become negligible in medium sand and not shown in the figure. N_{qVU} for $D = 900$ mm converges to N_{qVU} for $D = 102$ m at $H_c/D = 8 - 11$.

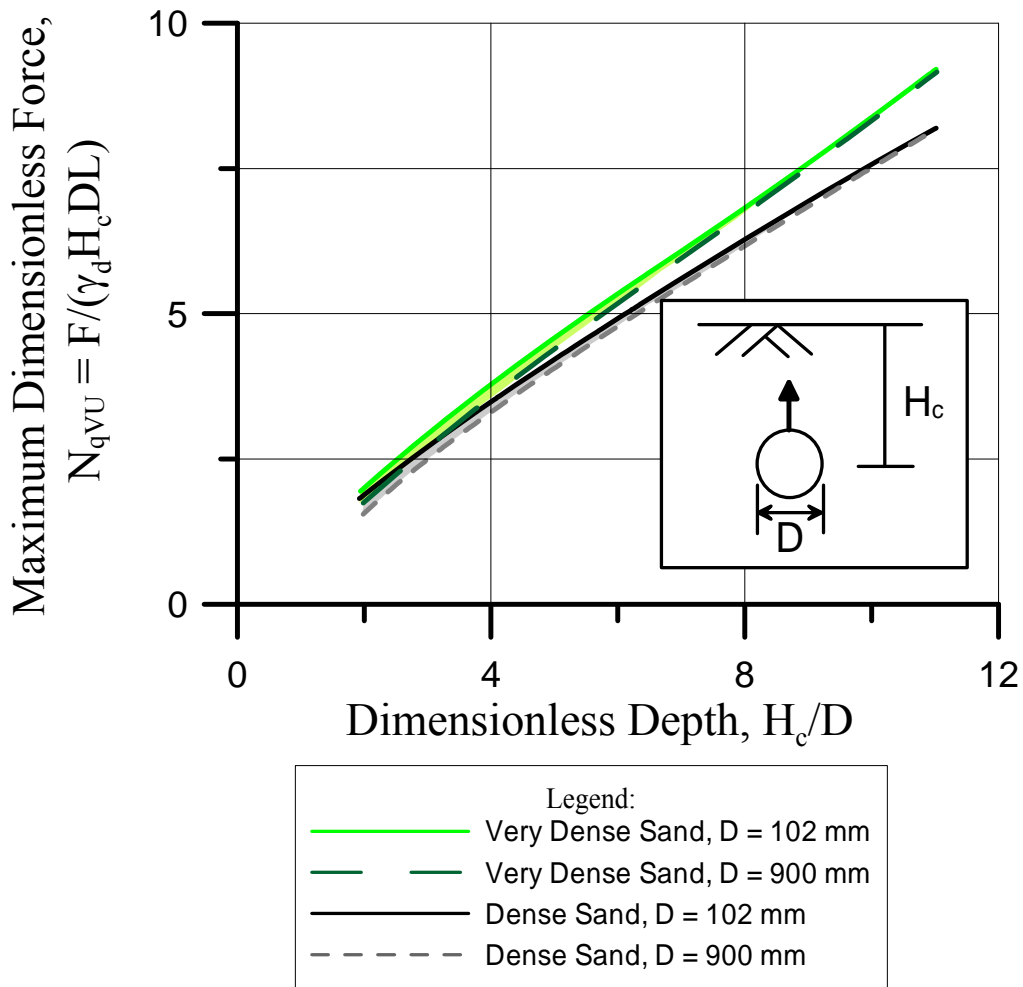


Figure 5.18 Summary Plot of N_{qvU} vs. H_c/D for Various Pipe Diameters

5.8 Analytical Results of Maximum Vertical Upward Force in Partially Saturated RMS Graded Sand

FE analyses were run with the semi-infinite soil model for partially saturated RMS graded sand as described in Sections 3.9 and 5.6. Input parameters for soil strength were obtained from the procedure described in Section 3.9. As discussed in Chapter 3, the suggested simplified E_{70} for partially saturated sand is $E_{70-H \text{ sat}} \approx 2 E_{70-H}$.

Using this approximation, $E_{70-H \text{ sat}}$ for vertical upward pipe movement in partially saturated sand is calculated using the following equation:

$$\frac{E_{70-H \text{ sat}}}{P_a} = 2 \times 10^{0.481} \left[\frac{\gamma_d}{\gamma_w} \left(\frac{\sigma'_{vc}}{P_a} \right)^{0.130} \right]^{7.061} \quad (5.3)$$

Table 4.3 summarizes the soil properties associated with the vertical upward pipe movement 2-D simulations in partially saturated sand. The strain softening model described in Section 3.7 was used in the FE simulation and the model was adjusted for a linear decrease in c_{ps} to 0, from the plastic strain at ϕ_{ps-p} to γ_f^p . A small residual value of $c_{ps-ld} = 0.1$ kPa at large displacements was used to promote numerical stability.

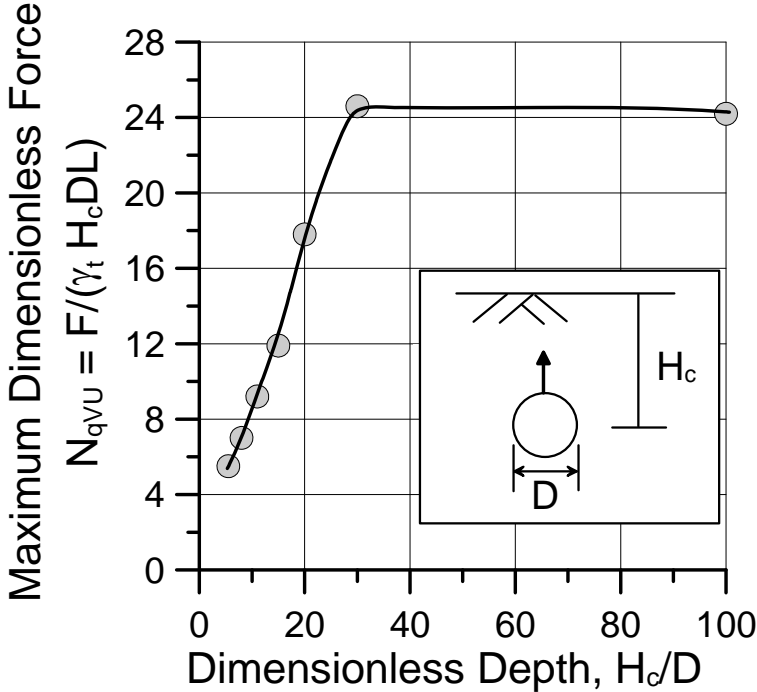


Figure 5.19 Vertical Upward N_{qvU} vs. H_c/D for Partially Saturated RMS Graded Sand

Figure 5.19 shows N_{qVU} plotted with respect to H_c/D of partially saturated sand for vertical upward pipe movement. The values of N_{qVU} were determined as described in Chapter 3. The figure shows that N_{qVU} reaches its maximum value of 24.6 at $H_c/D = 30$.

CHAPTER 6

VERTICAL DOWNWARD PIPE MOVEMENT

6.1 Introduction

In this chapter, the finite element (FE) models for simulating vertical downward pipe movement under plane strain conditions are described. Because there are no large-scale experimental results for downward pipe movement, the numerical modeling procedures are evaluated with respect to full-scale field measurements of pile and drilled shaft load vs. settlement behavior. Numerical simulations of 2-D deep foundations were performed and compared the maximum reaction forces from the model with the forces predicted by conventional bearing capacity formulations for deep foundations to validate the model. The lower and upper bound of strain compatible secant modulus for vertical downward pipe movement was investigated to determine the appropriate modulus which provided a ρ_{L1} and ρ_{L2} consistent with load test statistics.

6.2 Finite Element Model and Soil Strength Properties

Semi-infinite FE soil models described in Section 5.6 were used to investigate the relationship between maximum vertical downward pipe force and pipe depth for medium, dense, and very dense sand as characterized in Table 3.2. Figure 5.16 shows the typical FE model geometry used for simulating both vertical downward and upward soil-pipe interaction in dry and partially saturated sand.

Input parameters for soil strength were obtained with the procedures described in Section 3.3.2. The peak angle of dilation, ψ_p was evaluated using Eqn. 3.2, where σ'_N is taken as σ'_{vc} , which is the vertical effective stress at the pipe centerline. With ψ_p estimated relative to σ'_{vc} , Eqns 3.3 and 3.7 were used to evaluate ϕ'_{ps-p} . Critical friction angle, ϕ'_{crit} , was selected as 40.8° for dry RMS graded sand.

6.3 Analytical Results of Maximum Vertical Downward Force in Dry Sand

The FE results for force vs. pipe settlement differ from those for lateral and upward pipe movement, for which there is generally (but not always) a clear maximum load. For downward pipe movement, the vertical load continues to increase at relatively high loading levels with no clear maximum value.

To evaluate the effective maximum load for pipe settlement, the methods recommended for the interpretation of deep and shallow foundation load tests (Hirany and Kulhawy, 1998, 1989, and 2002; Akbas and Kulhawy, 2009) were used. Vertical downward movements of both pipe and deep foundations in medium to very dense sand result in a strain hardening type behavior with a gradual increase in vertical load at high levels of settlement. A typical load-settlement curve for an axial compression foundation test is shown in Fig. 6.1 (Akbas and Kulhawy, 2009). The geometric characteristics of this curve are similar for both deep and shallow foundations (Hirany and Kulhawy, 2002; Akbas and Kulhawy, 2009). To help interpret the vertical force vs. settlement relationships, L_1 is defined at the end of the initial linear region of the curve, and L_2 is defined at the beginning of the final linear region. The settlement associated with L_1 is referred to as ρ_{L1} and that associated with L_2 is referred to as ρ_{L2} . The vertical force associated with L_2 is called the failure threshold, Q_{L2} , after Akbas

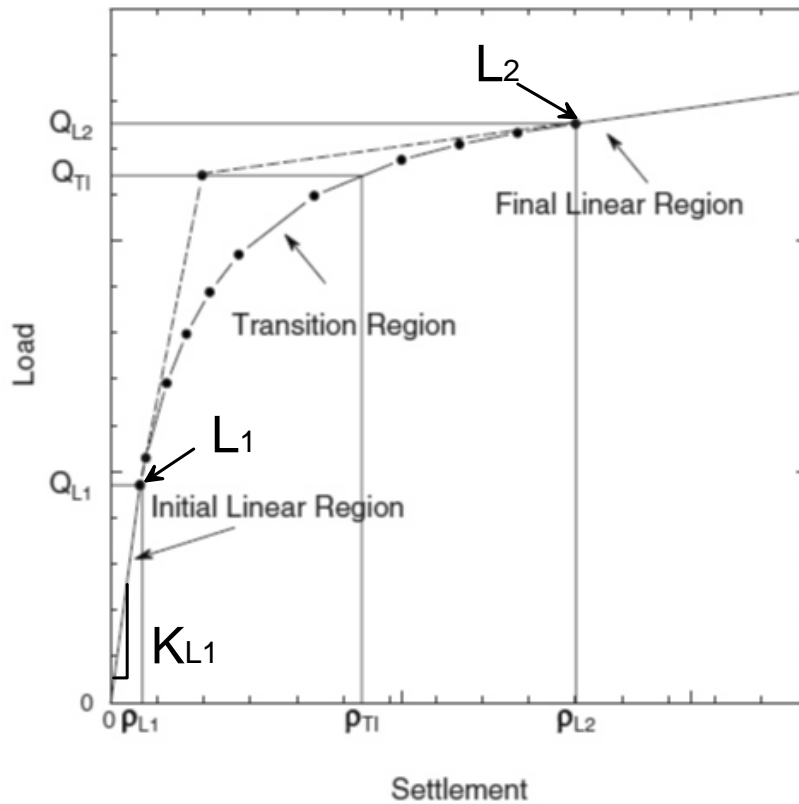


Figure 6.1 Typical Load-Settlement Curve of Axial Compression Test on Foundation

(After Akbas and Kulhawy, 2009)

and Kulhawy (2009) [shown as Q_{L2} in Fig. 6.1], and is used to obtain the dimensionless maximum downward pipe movement force, N_{qVD} .

It was found that Q_{L2} depends on the Young's modulus for vertical downward movement, E_{VD} , with larger Q_{L2} resulting from larger E_{VD} . For lateral and vertical upward pipe movement, this is not the case. The peak pipe force is relatively insensitive to the choice of modulus under lateral and vertical upward displacement, although the actual force vs. displacement relationship is closely related to the modulus.

To determine Q_{L2} , the fraction of mobilized soil strength, α , was needed to estimate the strain compatible modulus at peak pipe force. The range of α from 0.7 to 0.9 was taken from Table A.2 in Appendix A. This appendix describes how strain compatible moduli are estimated for vertical uplift, lateral, and vertical downward pipe displacement. The modulus associated with $\alpha = 0.8$ (mid range of $0.7 \leq \alpha \leq 0.9$) was applied through Eqn. A.9 for medium, dense, and very dense sand to obtain the strain compatible $E_{\alpha\text{-VD}}$ at peak pipe force.

Figure 6.2 presents the FE results for the maximum dimensionless vertical downward force for medium, dense, and very dense sand for $H_c/D = 2 - 100$. As $H_c/D \rightarrow 0$, there is a finite value of N_{qVD} associated with the resistance to vertical movement of a pipe buried at a depth of half its external diameter. This value is analogous to the bearing capacity of a shallow foundation with width equal to D at the ground surface.

The FE simulations of vertical downward pipe movement show that N_{qVD} reaches its limiting value between $H_c/D = 8$ and 15 at values approximately equal to 16.3, 18.7, and 23.7 for medium, dense, and very dense sand, respectively. As shown in Fig. 6.2, from $H_c/D = 11$ to 100, N_{qVD} decreases slightly by approximately 1.7 %, 2.1 %, and 2.4 % for medium, dense, and very dense sand, respectively. At the same time, ϕ'_{ps-p} decreases approximately by 1.8 %, 3.1 %, and 4.2 % for medium, dense, and very dense sand, respectively, due to increasing confining stress at higher H_c/D .

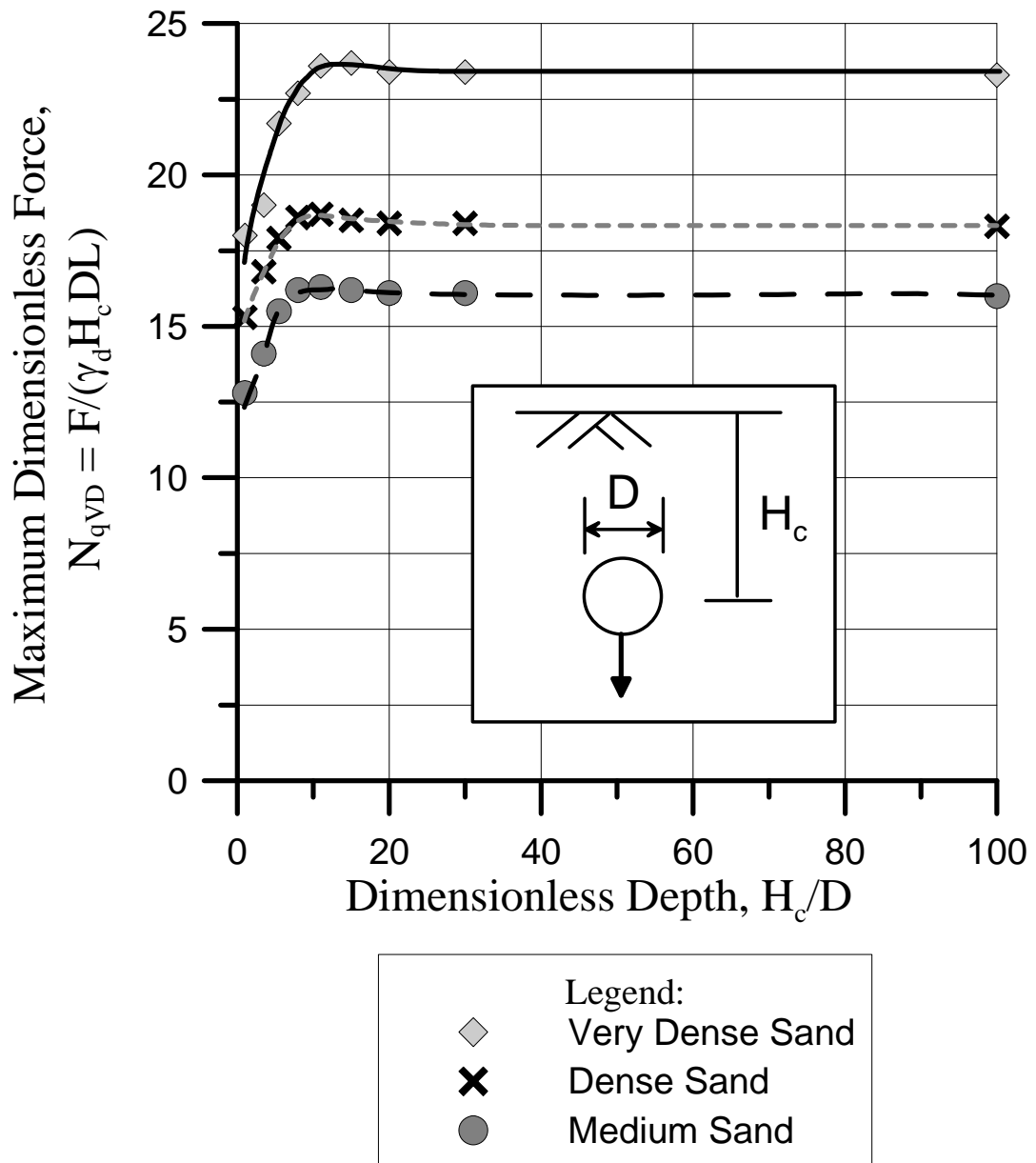


Figure 6.2 Summary Plot of N_{qVD} vs. H_c/D for Vertical Downward Pipe Movement

6.4 Comparison Between Pipe Peak Force and the Bearing Capacity for Deep Foundations

Guidelines for the seismic design of oil and gas pipelines have recommended that the maximum vertical force associated with downward pipe movement be estimated by conventional bearing capacity formulations (ASCE, 1984). No full-scale experimental validation for this recommendation has been performed. It is of interest therefore to compare the maximum vertical pipe force from bearing capacity theory with the peak pipe force resulting from the FE simulations.

6.4.1 Deep Foundation Bearing Capacity

The maximum tip resistance of a deep foundation, Q_{tc} , is calculated as

$$Q_{tc} = q_{ult} A_{tip} \quad (6.1)$$

in which q_{ult} = the maximum bearing capacity at the tip, and A_{tip} = area of the base of the foundation. Kulhawy et al. (1983) have shown that, for drained conditions with $H_c/D \geq 5$, q_{ult} can be estimated as

$$q_{ult} = q N_q \xi_{qr} \xi_{qs} \xi_{qd} \quad (6.2)$$

in which q = vertical effective stress at H_c , N_q = bearing capacity factor, ξ_{qr} = rigidity factor, ξ_{qs} = shape factor, and ξ_{qd} = depth factor.

The maximum tip resistance force from Eqns. 6.1 and 6.2, Q_{tc-c} , are calculated and summarized in Appendix C for medium, dense, and very dense sand as characterized in Table 3.2 for $H_c/D = 8, 11, 15, 20,$ and 30 . The peak dimensionless force from the FE analyses associated with the Q_{L2} values previously described, Q_{tc-fea} , are plotted vs. the bearing capacity values, Q_{tc-c} , for $H_c/D = 8 - 30$ in Fig. 6.3. The values of Q_{tc-fea} were determined as described in Section 6.2. As shown in the figure, there is a substantial difference between Q_{tc-c} and Q_{tc-fea} , with Q_{tc-fea} approximately 1/3 of Q_{tc-c} .

The failure threshold force for 2-D pipe settlement, Q_{tc-fea} , is consistently lower than the bearing capacity force, Q_{tc-c} , for a deep foundation by a large margin. This discrepancy can be explained qualitatively by recognizing that downward pipe movement is accompanied by soil displacement into the void that develops above the pipe. Movement of soil into a zone above the pipe is markedly different from soil movement during deep foundation settlement. The continuous deep foundation prevents soil displacement into a zone above the tip, and thus provides substantially higher constraint on soil deformation with associated higher resistance to tip penetration of the soil mass.

Force vs. displacement measurements from centrifuge tests of pipeline response to normal faulting are described by Abdoun, et al (2008). They compared the maximum force generated by downward pipe movement over the footwall of the normal fault with the maximum force from conventional bearing capacity equations, and showed that the measured force was substantially lower. Their measurements indicate a vertical reaction force approximately one-tenth of the conventional bearing capacity force.

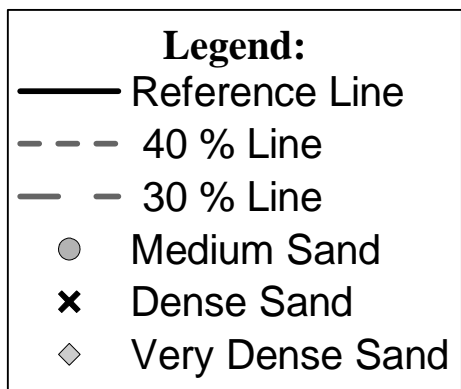
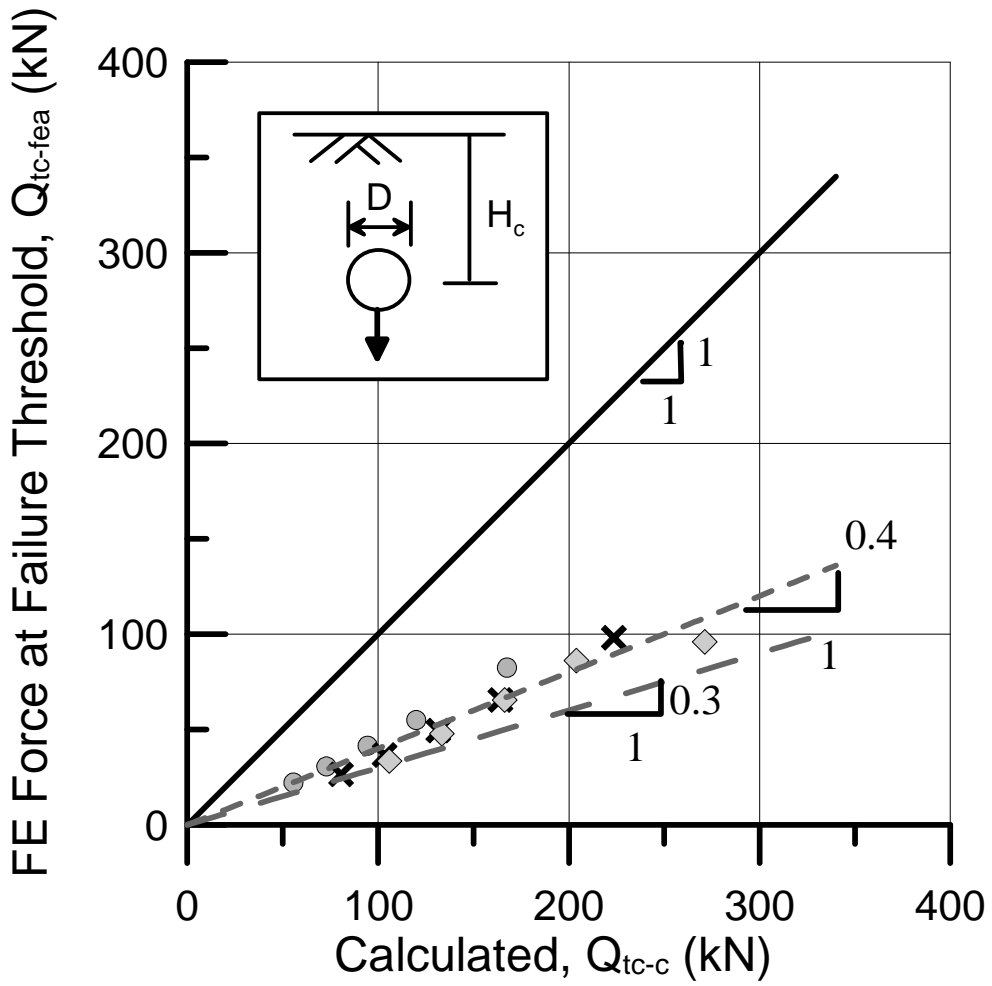


Figure 6.3 Comparison of Q_{tc} and Q_{tc-fea}

6.4.2 Finite Element Model for Deep Foundations

Because experimental data are sparse for downward pipe movement and are lacking entirely for 2-D conditions of downward movement, empirical confirmation of the FE pipe results cannot be obtained directly. However, numerical simulations of 2-D deep foundation bearing elements can be performed, and the failure threshold forces so obtained checked against the theoretical bearing capacity forces. If the FE results for deep foundation maximum tip resistance compare favorably with the theoretical bearing capacities, such agreement provides for validation of the numerical model for deep foundation bearing capacity assessment. The model can then be used for direct comparison between FE results for pipe and deep foundation settlements to quantify the differences in behavior for these two conditions of soil-structure interaction.

To evaluate deep foundation tip resistance, a new FE model was developed as shown in Fig. 6.4. The model is similar to that described in Section 5.6 except for the frictionless foundation at the center of the mesh. As described in Chapter 5, CEP8R elements are used to represent the soil inside the dashed line. CINPE5R elements were used to represent the semi-infinite soil medium and were located outside of the CPE8R elements.

Figure 6.5 shows an enlarged view of region A with more detailed boundary conditions and mesh arrangements. Because the largest soil deformations are expected near the periphery of the deep foundation, the mesh is dense in this region. The interface between the soil and the lower half of the circular foundation tip has a friction angle of $0.6 \phi'_{ds-p}$, as described previously in Chapter 4. The nodes in region

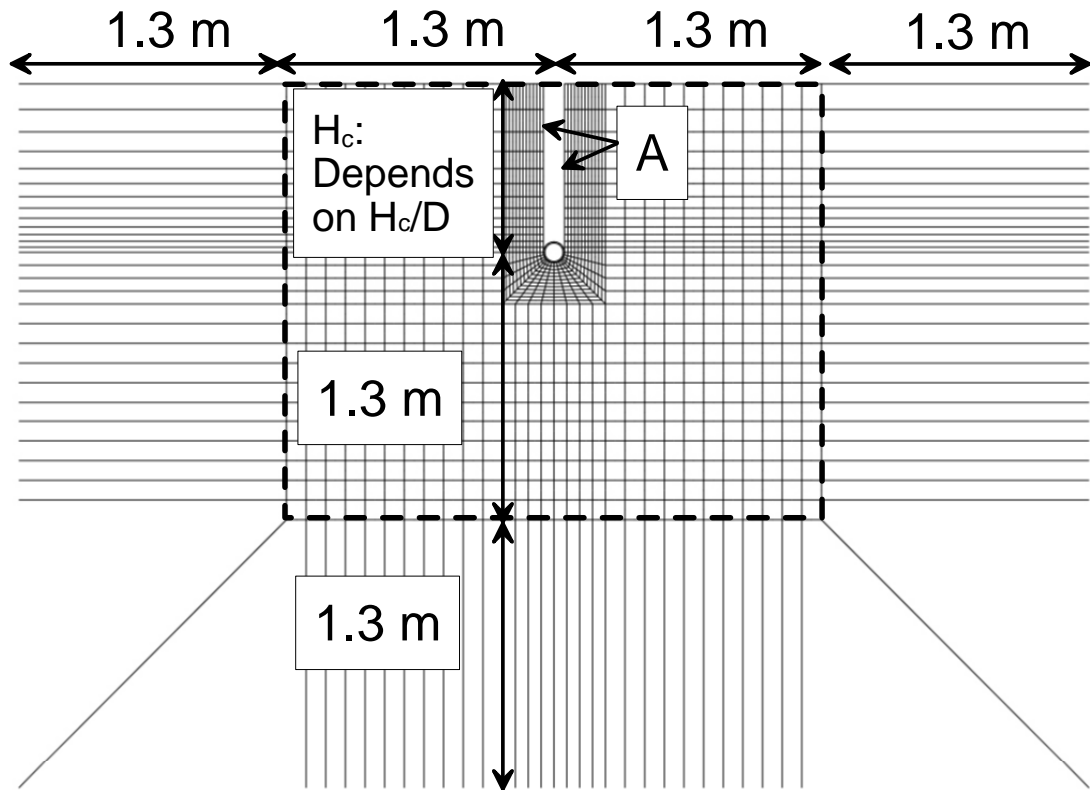


Figure 6.4 FE Model for Deep Foundation

A were fixed horizontally but unrestrained in the vertical direction to form a rigid frictionless surface.

A prime source of uncertainty associated with Q_{tc-c} is related to the rigidity factor, ξ_{qr} , which depends on the modulus, E . To evaluate the strain compatible $E_{\alpha-vD}$ at peak force, the range of α from 0.7 to 0.9 (lower and upper bound value) was used from Table A.2. The modulus associated with this range of α was applied through Eqn. A.9 for medium, dense, and very dense sand with $H_c/D = 8 - 20$ to obtain the strain compatible $E_{\alpha-vD}$ at peak force. Table 6.1 summarizes lower and upper bound of $E_{\alpha-vD}$ for select cases of sand density and H_c/D .

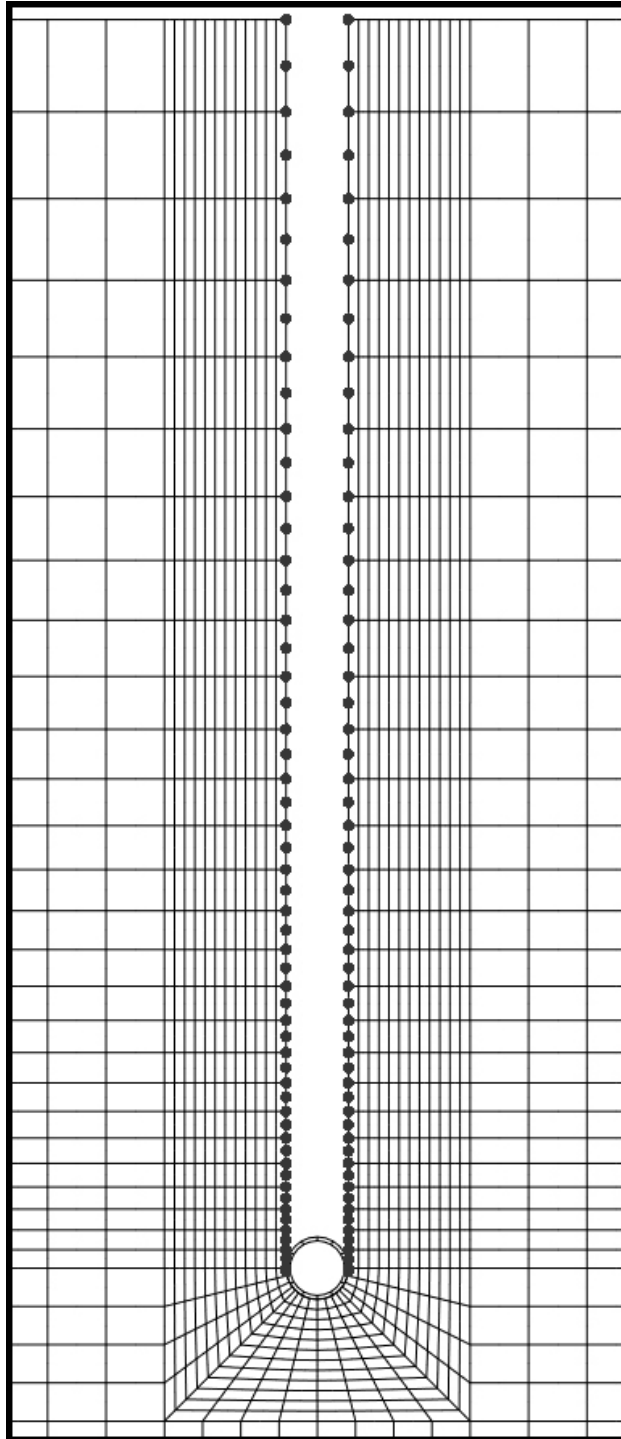


Figure 6.5 Detailed Boundary Conditions at A

Table 6.1 Upper and Lower Bound $E_{\alpha-VD}$ for Select Case of Sand Density and H_c/D

H_c/D	Sand Type	$E_{\alpha-VD}$ (kPa)	
		Lower Bound	Upper Bound
8	Medium	2300	8100
11	Medium	2900	9500
11	Very Dense	7600	21300
15	Dense	5900	17000
20	Very Dense	10300	27100

Figure 6.6 shows a plot of Q_{tc-d} from the deep foundation FE simulations vs. Q_{tc-c} for the same sand and H_c/D conditions. The Q_{tc-d} from the FE analyses and the Q_{tc-c} from the bearing capacity formulations (see Appendix C) were calculated for a strain compatible secant modulus, E_{α} , associated with $\alpha = 0.8$ (mid range value from Table A.2). The initial modulus, E_i , was estimated as described in Appendix C (Eqn. C.8) $E_i = K p_a (\sigma'_3/p_a)^n$, for which K and n were taken from data summarized by Wong and Duncan database for medium ($\phi' = 41.0 - 43.9^\circ$), dense ($\phi' = 44.0 - 46.4^\circ$), and very dense ($\phi' = 46.5 - 50.0^\circ$) sand. Average values of (K, n) were calculated from the Wong and Duncan (1974) for medium, dense, and very dense sand as $(550, 0.65)$, $(800, 0.55)$, and $(1000, 0.45)$, respectively. In this way, the same process for computing the strain compatible modulus was used with the same empirical database for both the FE simulations and bearing capacity formulations, thus providing for a comparison of vertical downward force unbiased by the selection process for modulus.

The Q_{tc-d} from the FE analyses for a deep foundation plot approximately 8 % above the 1:1 slope of the Q_{tc-c} vs. Q_{tc-d} plot. A favorable agreement between Q_{tc-c} and Q_{tc-d} shows that the FE model gives results that agree with conventional bearing capacity predictions within a reasonable range of ξ_{qr} and $E_{\alpha-VD}$ -values for the different sand densities studied in this work.

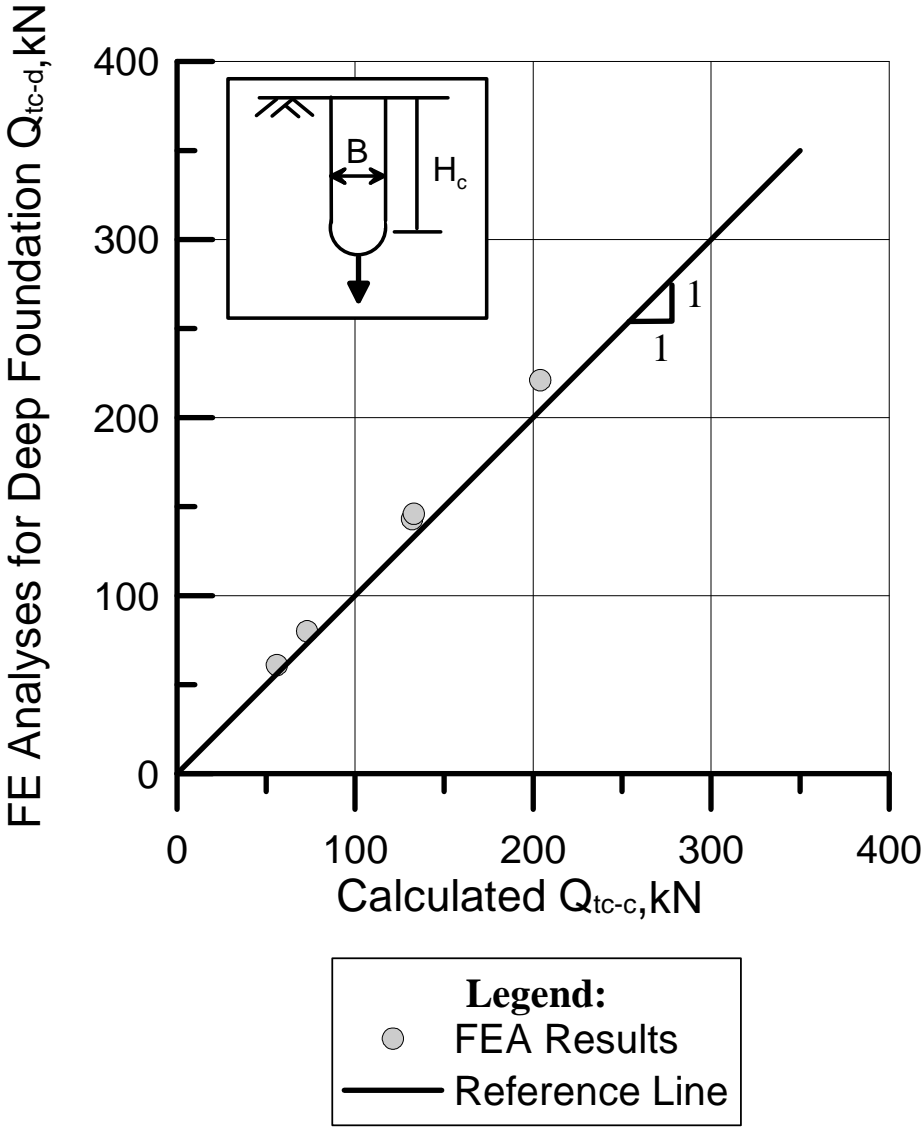
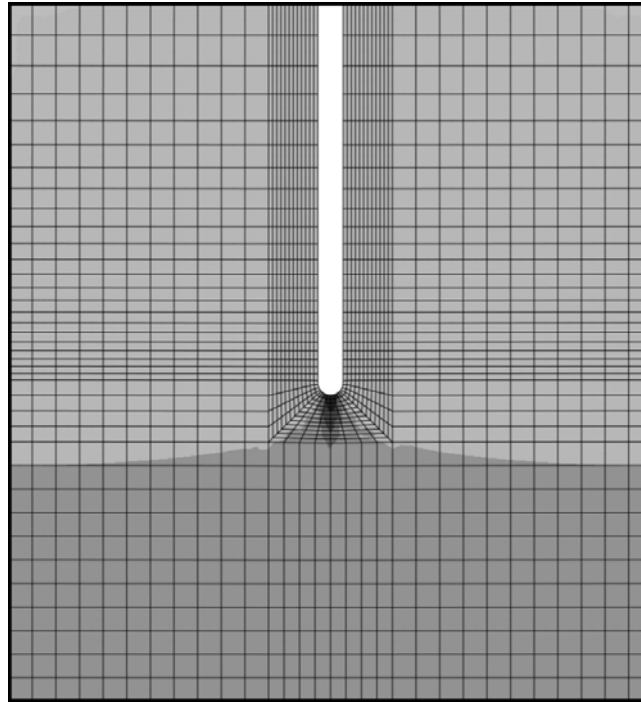
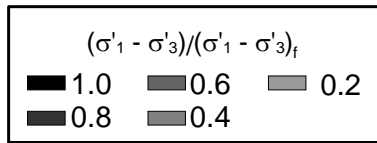


Figure 6.6 Comparison of Q_{tc-c} and Q_{tc-d}

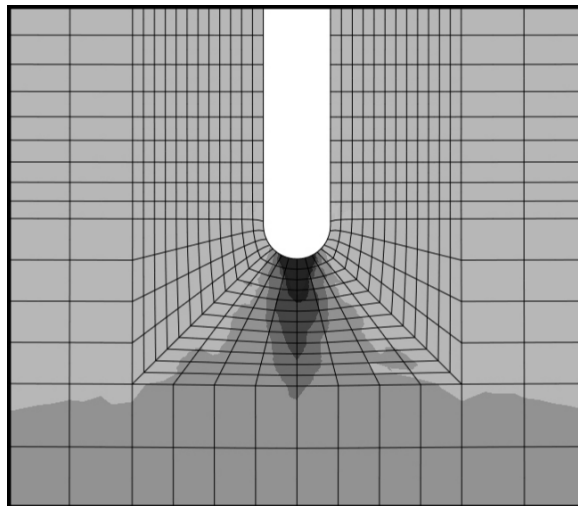
6.5 Young's Modulus for Vertical Downward Pipe Movement

Field load test data are presented for the vertical force vs. settlement behavior of shaft and pile foundations in Appendix D. The results do not include the effects of frictional resistance between the sides of the deep foundation and adjacent soil. Hence, the test results are for conditions similar to those simulated in the FE models shown in Figs 6.4 and 6.5. As discussed in Appendix D, the average values of ρ_{L1} and ρ_{L2} (see Fig. 6.1) for the test data are 0.22 % D and 5.94 % D, respectively. These values are close to ρ_{L1} and ρ_{L2} of 0.23 % D and 5.39 % D, respectively, reported by Akbas and Kulhawy (2009) for 205 load tests on shallow foundations, and are reasonably consistent with data for drilled shafts (Hirany and Kulhawy, 1988), where the average ρ_{L1} and ρ_{L2} were found to be 0.40 % D and 4 % D, respectively.

Figures 6.7 and 6.8 show contours of $(\sigma'_1 - \sigma'_3)/(\sigma'_1 - \sigma'_3)_f$ at the peak vertical downward force for a deep foundation and pipe with the same bearing dimensions obtained from FE analyses for $H_c/D = 15$ and dense sand. A mesh convergence study, based on stress response, was performed to determine whether the meshes shown in Fig. 6.7 and 6.8 were satisfactory. The study showed that the FE analyses converges and the results are satisfactory. As shown in the figures, the highest levels of principal stress difference are within a bulb-shaped zone that extends one and a half to two diameters below both the deep foundation and the pipe. A systematic comparison of FE results for deep foundations and pipes at various H_c/D , and sand densities, with a circular bearing contact surface show similar stress distributions beneath the bearing surfaces, as illustrated in Figs. 6.7 and 6.8. Given that FE deep foundation results agree well with bearing capacity prediction and there is close similarity in stress distribution for the pipe and deep foundation conditions,

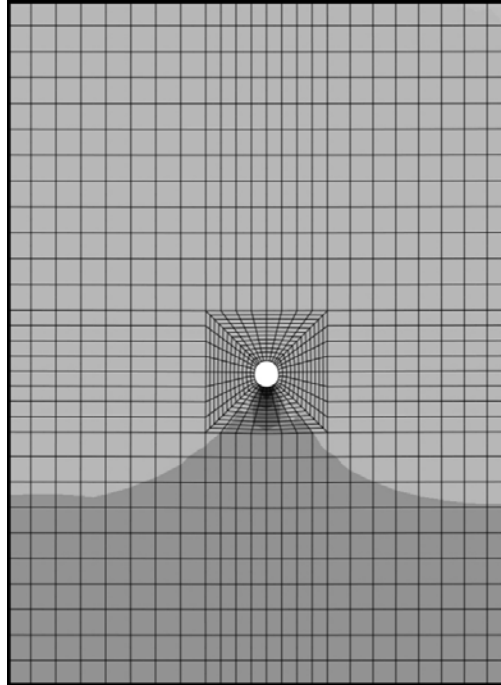
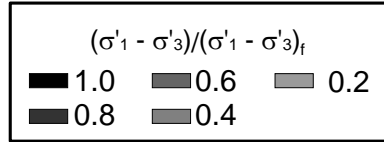


a) Entire Mesh
 $H_c/D = 15$, Dense Sand

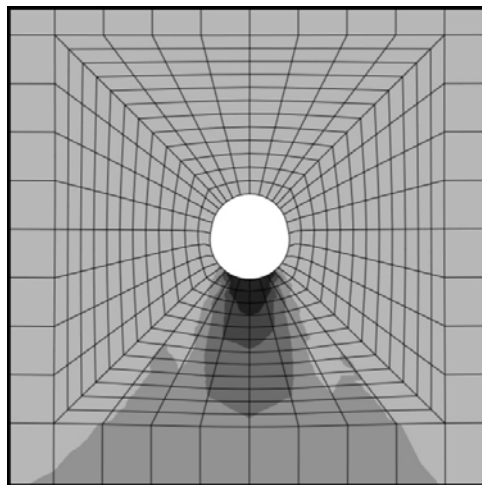


b) Mesh Adjacent to Deep Foundation Tip

Figure 6.7 Contour of $(\sigma'_1 - \sigma'_3)/(\sigma'_1 - \sigma'_3)_f$ for Deep Foundation in Dense Sand at
 Maximum Load



a) Entire Mesh
 $H_c/D = 15$, Dense Sand



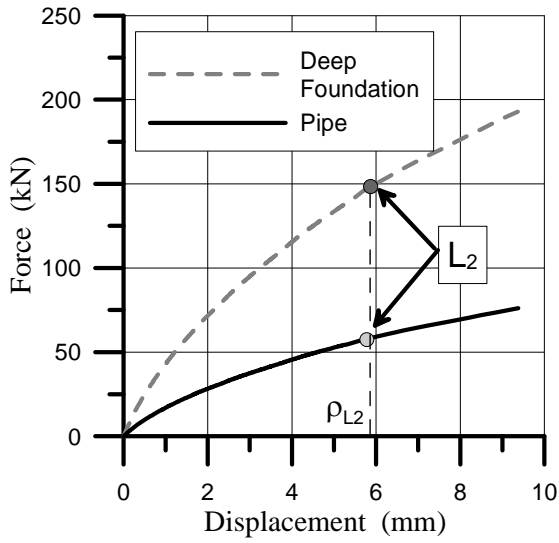
b) Mesh Adjacent to Pipe

Figure 6.8 Contour of $(\sigma'_1 - \sigma'_3)/(\sigma'_1 - \sigma'_3)_f$ for Vertical Downward Pipe in Dense Sand at Maximum Load

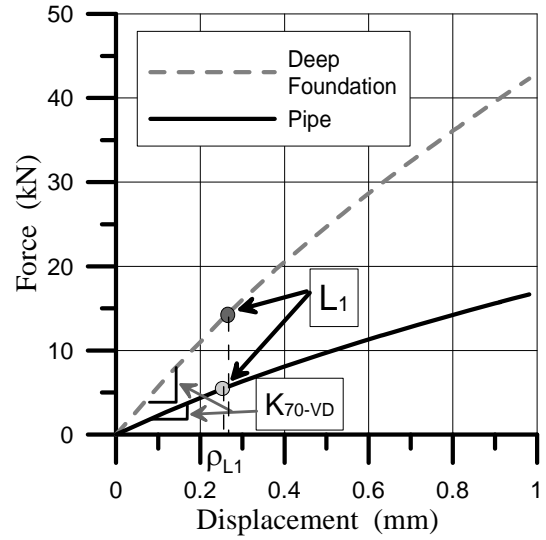
the FE results for the deep foundation are used to obtain strain compatible $E_{\alpha\text{-VD}}$ for vertical pipe movement where bearing surface, sand density, and depth are the same.

Strain compatible $E_{\alpha\text{-VD}}$ associated with $\alpha = 0.8$ from FE deep foundation analyses were used to predict the maximum downward pipe force for the medium, dense, and very dense sands at various H_c/D . Having $E_{\alpha\text{-VD}}$ associated with $\alpha = 0.8$, the force vs. settlement curve was checked to see if it provides a ρ_{L1} and ρ_{L2} consistent with load test statistics. From the 24 simulations performed with strain compatible $E_{\alpha\text{-VD}}$ for $\alpha = 0.8$, an average value of $\rho_{L1} = 0.19 \% D$ and $\rho_{L2} = 5.83 \% D$ were obtained, which are relatively close to $\rho_{L1} = 0.22 \% D$ and $\rho_{L2} = 5.94 \% D$, summarized for field test data in Appendix D, as well as $\rho_{L1} = 0.23 \% D$ and $\rho_{L2} = 5.39 \% D$ reported by Akbas and Kulhawy (2009).

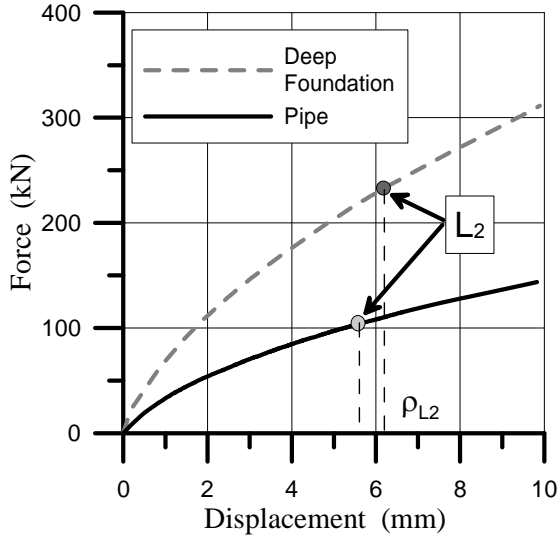
Figure 6.9 shows typical vertical force vs. settlement results for a pipe and a frictionless deep foundation. The results are for very dense sand, with $D = 102 \text{ mm}$ and $H_c/D = 11$ and 20 . The plots a-1) and b-1) show an enlarged view of the linear portion of the force vs. settlement curve for $H_c/D = 11$ and $H_c/D = 20$, respectively. The plots also show ρ_{L1} , ρ_{L2} , as well as K_{L1} , which is the slope of the linear portion of the curve. From these plots, $\rho_{L1} = 0.0019 D - 0.0024 D$ and $\rho_{L2} = 0.057 D - 0.062 D$ are obtained for both the deep foundation and the pipe, respectively. Please note that Q_{L2} is the failure threshold load. As discussed in Section 6.3, Q_{L2} is approximately 30 – 40 % of Q_{L2} for the deep foundation. Similarly, K_{L1} for the pipe is approximately 30 – 40 % of the K_{L1} for the deep foundation.



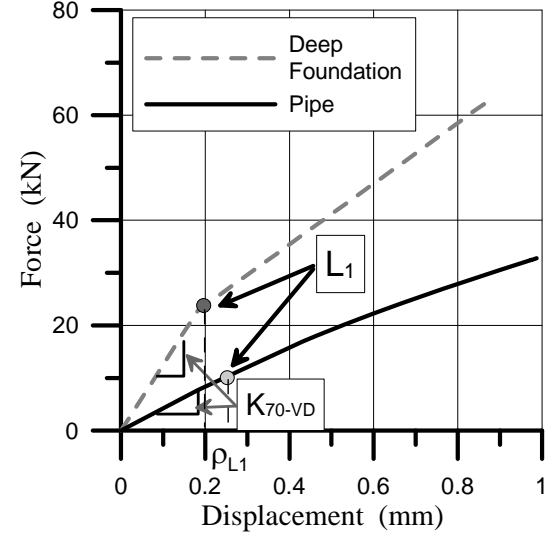
a) Very Dense Sand
 $H/D = 11$



a-1) Enlarged View



b) Very Dense Sand
 $H/D = 20$



b-1) Enlarged View

Figure 6.9 Typical Vertical Force vs. Settlement Results for a Pipe and Vertical Tip
 Resistance of a Frictionless Deep Foundation

6.6 Analytical Results of Maximum Vertical Downward Force for Various Pipe Diameters

Additional FE analyses were run with various pipe diameters to investigate the effects increasing diameter on soil-pipe interaction at constant H_c/D . Figure 5.17 shows the geometry of the numerical model for simulating vertical downward soil-pipe interaction with various pipe diameters in dry sand. The selected pipe diameters for this study were 900 mm, compared with 102 mm used in the production simulations.

Input parameters for numerical simulation, including soil strength, are the same as those described in Section 4.8.3. An equivalent modulus discussed in Section 6.4 and strain softening model described in Section 3.7 were used in the 2-D FE simulation of soil-pipeline interaction. As previously described, $\nu = 0.3$ was assumed for the sand and a nominal cohesion $c' = 0.1 - 0.3$ kPa was used in the simulations for numerical stability.

Figure 6.10 plots N_{qVD} from the FE analyses for various pipe diameters. The dimensionless parameters, $N_{qVD} = F/(\gamma_d H_c D L)$ and H_c/D , define the vertical downward pipe forces and depth, respectively. The plot shows diameter effects increasing with increasing γ_d , and decreasing with increasing H_c/D . For $D = 102$ mm and 900 mm, the maximum difference in N_{qVD} is approximately 33 % for both dense and very dense sand. N_{qVD} for $D = 900$ mm converges to N_{qVU} for $D = 102$ m at $H_c/D = 20 - 30$, with very little difference between the values at $H_c/D \geq 12$.

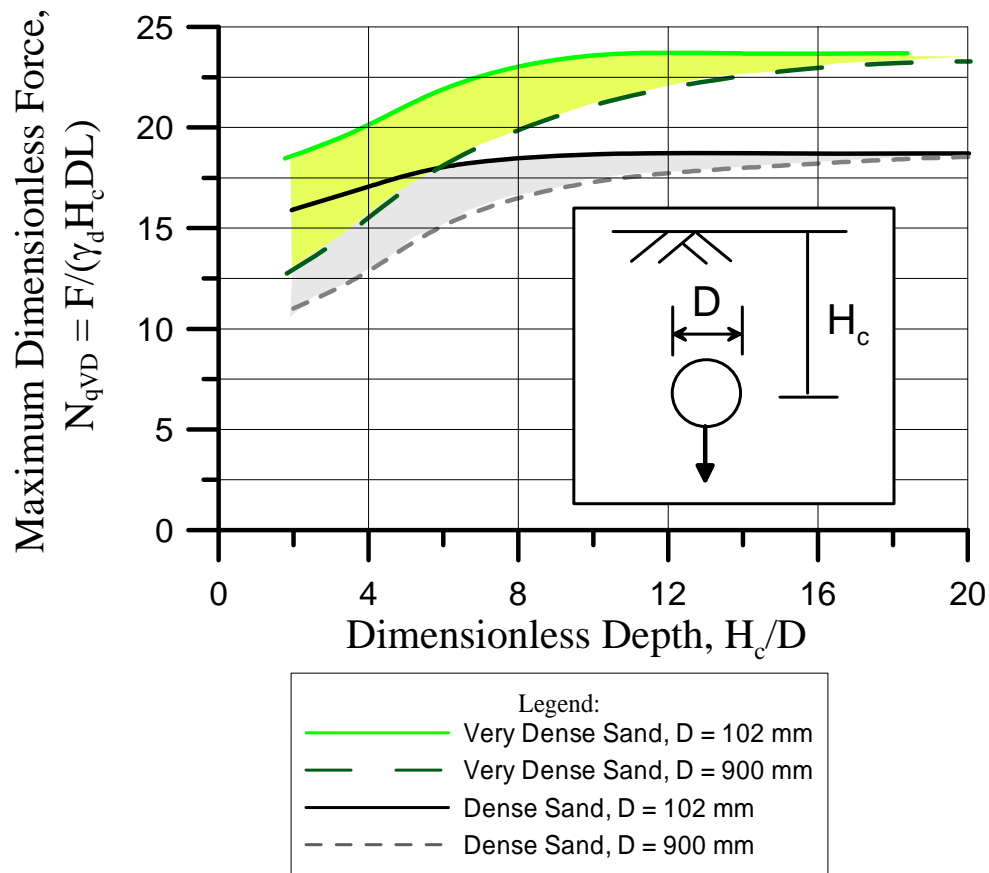


Figure 6.10 Summary Plot of N_{qVD} vs. H_c/D for Various Pipe Diameters

6.7 Analytical Results of Maximum Vertical Downward Force in Partially Saturated RMS Graded Sand

FE analyses were run with the semi-infinite soil model for partially saturated RMS graded sand as described in Sections 3.9 and 5.6. Input parameters for soil strength were obtained from the procedure described in Section 3.9. As discussed in Chapter 3, the suggested strain compatible simplified $E_{\alpha-VD}$ for partially saturated sand is approximately twice higher than that for dry sand.

Table 4.3 summarizes the soil properties associated with the vertical

downward pipe movement 2-D simulations in partially saturated sand. The strain softening model described in Section 3.7 was used in the FE simulation and the model was adjusted for a linear decrease in c_{ps} to 0, from the plastic strain at ϕ_{ps-p} to γ_f^p . A small residual value of $c_{ps-id} = 0.1$ kPa at large displacements was used to promote numerical stability.

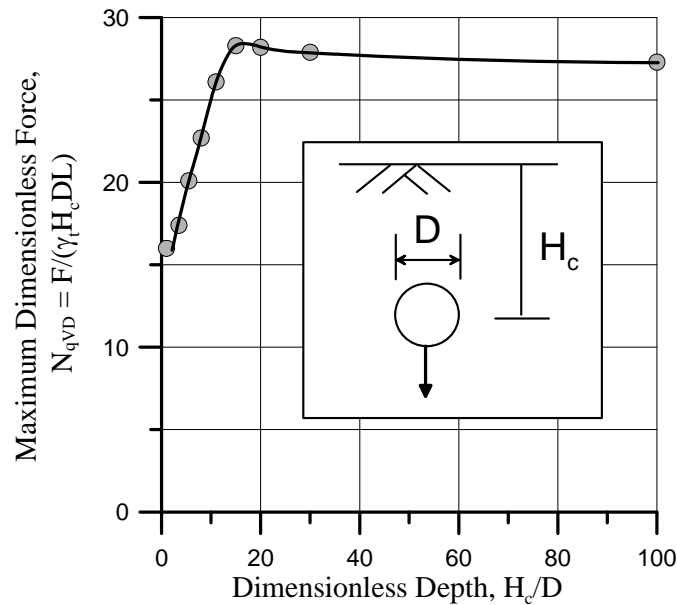


Figure 6.11 Vertical Downward N_{qVD} vs. H_c/D for Partially Saturated RMS Graded Sand

Figure 6.11 shows N_{qVD} plotted with respect to H_c/D for vertical downward pipe movement in partially saturated sand. The overall trend of N_{qVD} vs. H_c/D for partially saturated RMS graded sand is similar to that for dry sand. The N_q decreases approximately 3.5 % from $H_c/D = 15$ to 100, and ϕ_{ps-p} decrease approximately 4.4 % at the same range of H_c/D . The figure indicates that a limiting value of N_{qVD} , approximately equal to 28.3, is reached at critical embedment ratio between $H_c/D = 15$ and 20.

CHAPTER 7

OBLIQUE PIPE MOVEMENT AND GUIDELINES FOR PRACTICE

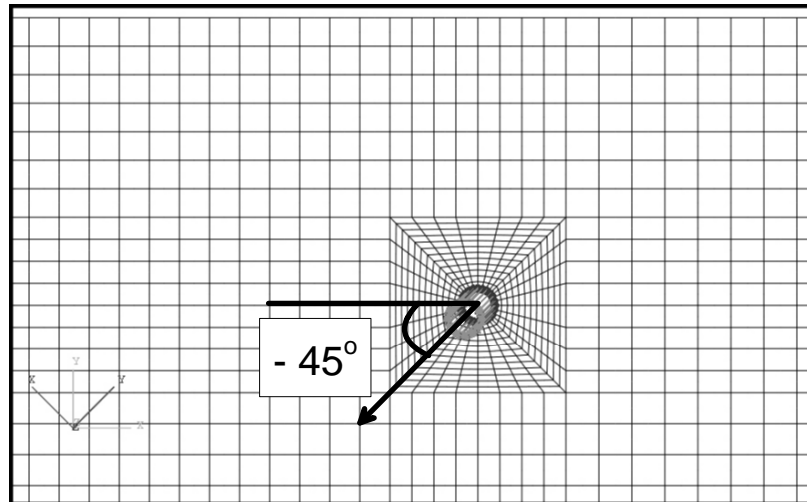
7.1 Introduction

A series of finite element (FE) analyses with ABAQUS 6.9 (2009) were performed to predict the maximum force on the pipe subject to oblique relative displacement with both downward and upward components of movement. The relationship between maximum lateral pipe force and pipe depth are developed for semi-infinite soil conditions and H_c/D increasing to 100. The analytical results from simulations of lateral, upward, downward, and oblique pipe movement are normalized with respect to maximum lateral force, and the normalized maximum forces are provided on 360° plots that can be used predict maximum pipe loads for medium to very dense dry and partially saturated sand at various H_c/D . Guidance is also provided for choosing the appropriate elastic modulus for elasto-plastic modeling at any orientation of pipe, and for direct estimation of the force vs. displacement relationships at any depth and orientation for one-dimensional modeling of soil-pipeline interaction.

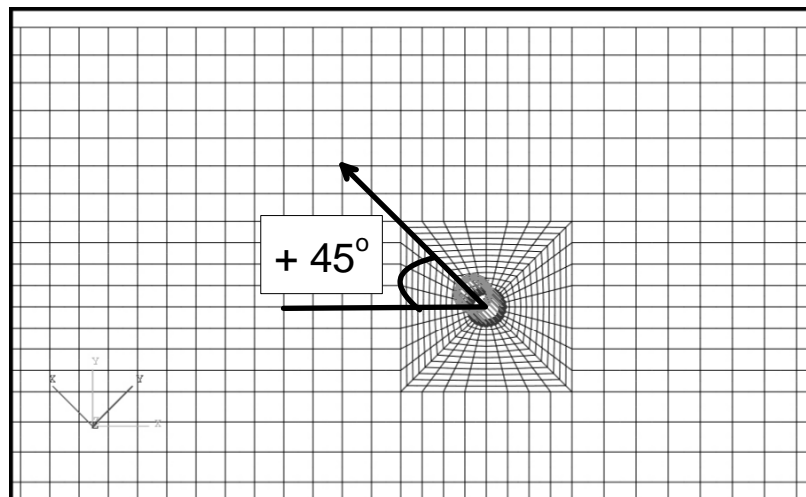
7.2 Analytical Results for Maximum Oblique Force in Dry Sand

The semi-infinite soil models described in Section 4.2 were used to investigate the relationship between maximum oblique forces and H_c/D for medium, dense, and very dense sand as characterized in Table 3.2. Input parameters for soil strength were obtained with the procedures described in Section 3.3.2. Figure 4.1 shows the typical

geometry of the model used for simulating oblique pipe movement in both dry and partially saturated sand. The pipe was displaced an angle of -45° and $+45^\circ$ with respect to the horizontal for oblique downward and oblique upward FE analyses, respectively. The graphical representation of pipe movement is shown in Fig. 7.1 for a) oblique downward and b) oblique upward movement, respectively.



a) Oblique Downward



b) Oblique Upward

Figure 7.1 Directions for Oblique Pipe Movement

7.3 Peak Dimensionless Force Associated with Oblique Pipe Movement

Comparisons of the dimensionless maximum oblique downward pipe movement force, N_{qOD} , with respect to H_c/D for medium, dense, and very dense sand are shown in Fig. 7.2. The dimensionless parameters $N_{qOD} = F/(\gamma_d H_c DL)$ and H_c/D define the pipe force and depth, respectively. Numerical results for $H_c/D = 2, 3.5, 5.5, 8, 11, 15, 20, 30,$ and 100 are presented in the figure. The values of N_{qOD} were determined as described in Chapter 3. The FE simulations of oblique downward pipe movement show that N_{qOD} reaches its maximum value at $H_c/D = 11 - 15$, and then decreases very slightly with increasing H_c/D . As shown in Fig. 7.2, from $H_c/D = 15$ to 100 , N_q decreases approximately by 1.3 %, 1.6 %, and 2.0 % for medium, dense, and very dense sand, respectively. In parallel, ϕ'_{ps-p} decreases approximately by 1.5 %, 2.6 %, and 3.4 % for medium, dense, and very dense sand, respectively, due to increasing confining stress at higher H_c/D values. Limiting values of N_{qOD} are reached between $H_c/D = 11$ and 15 at 16.0, 18.2, and 22.9 for medium, dense, and very dense sand, respectively.

Figure 7.3 shows the dimensionless maximum oblique upward pipe movement force, N_{qOU} , plotted with respect to H_c/D [$H_c/D = 3.5, 5.5, 8, 11, 15, 20, 30,$ and 100] for medium, dense, and very dense sand. The figure shows that N_{qOU} reaches its maximum value at $H_c/D = 20 - 30$ and then decreases slightly with increasing H_c/D . For example, from $H_c/D = 30$ to 100 , N_{qOU} decreases approximately by 0.6 %, 0.6 %, and 0.9 % for medium, dense, and very dense sand, respectively. Meanwhile, ϕ'_{ps-p} decreases approximately by 0.9 %, 1.6 %, and 2.1 % for medium, dense, and very dense sand, respectively. Limiting values of N_{qOU} are reached between $H_c/D = 20$ and 30 at 14.9, 17.1, and 21.4 for medium, dense, and very dense sand, respectively.

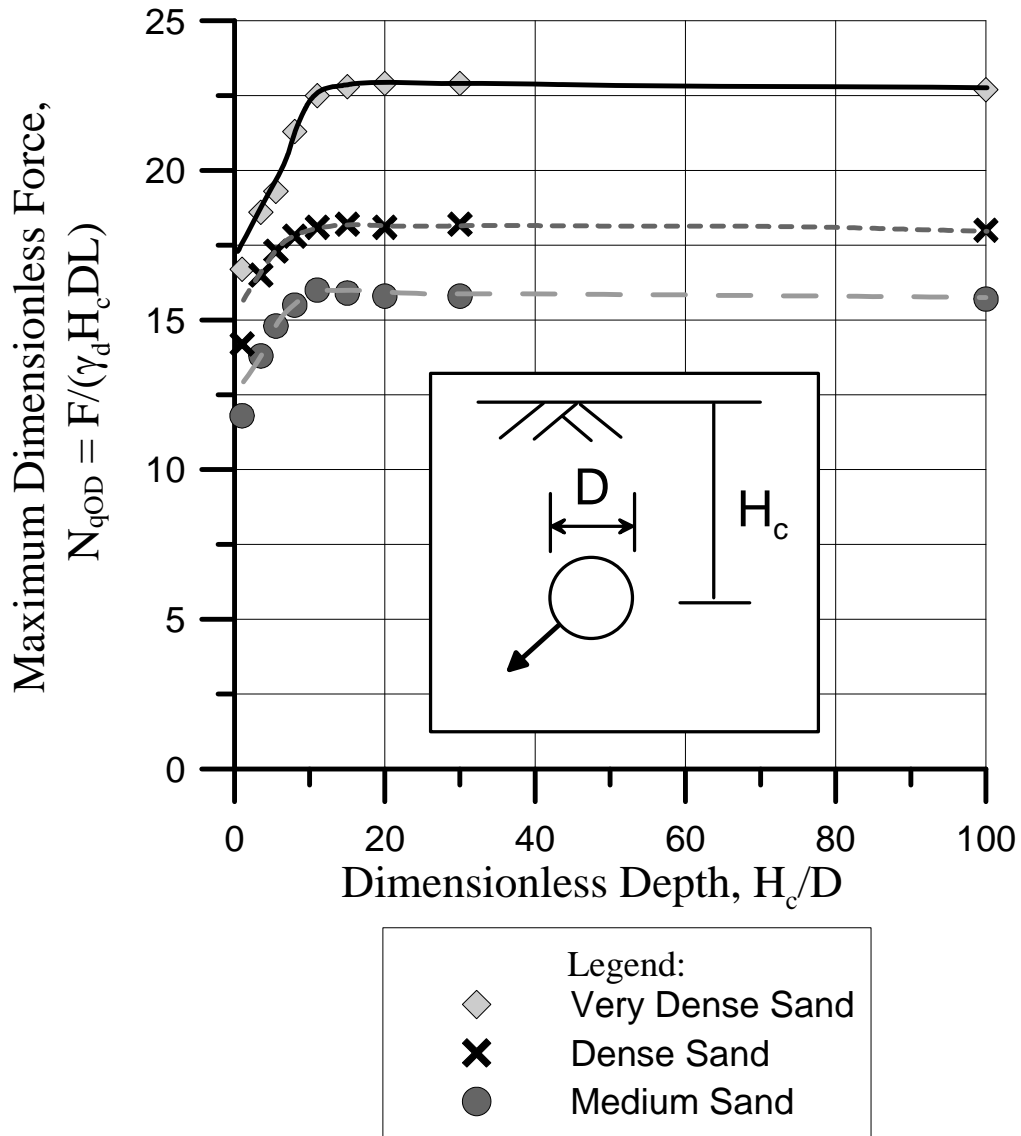


Figure 7.2 Summary Plot of N_{qOD} vs. H_c/D for Oblique Downward Pipe Movement

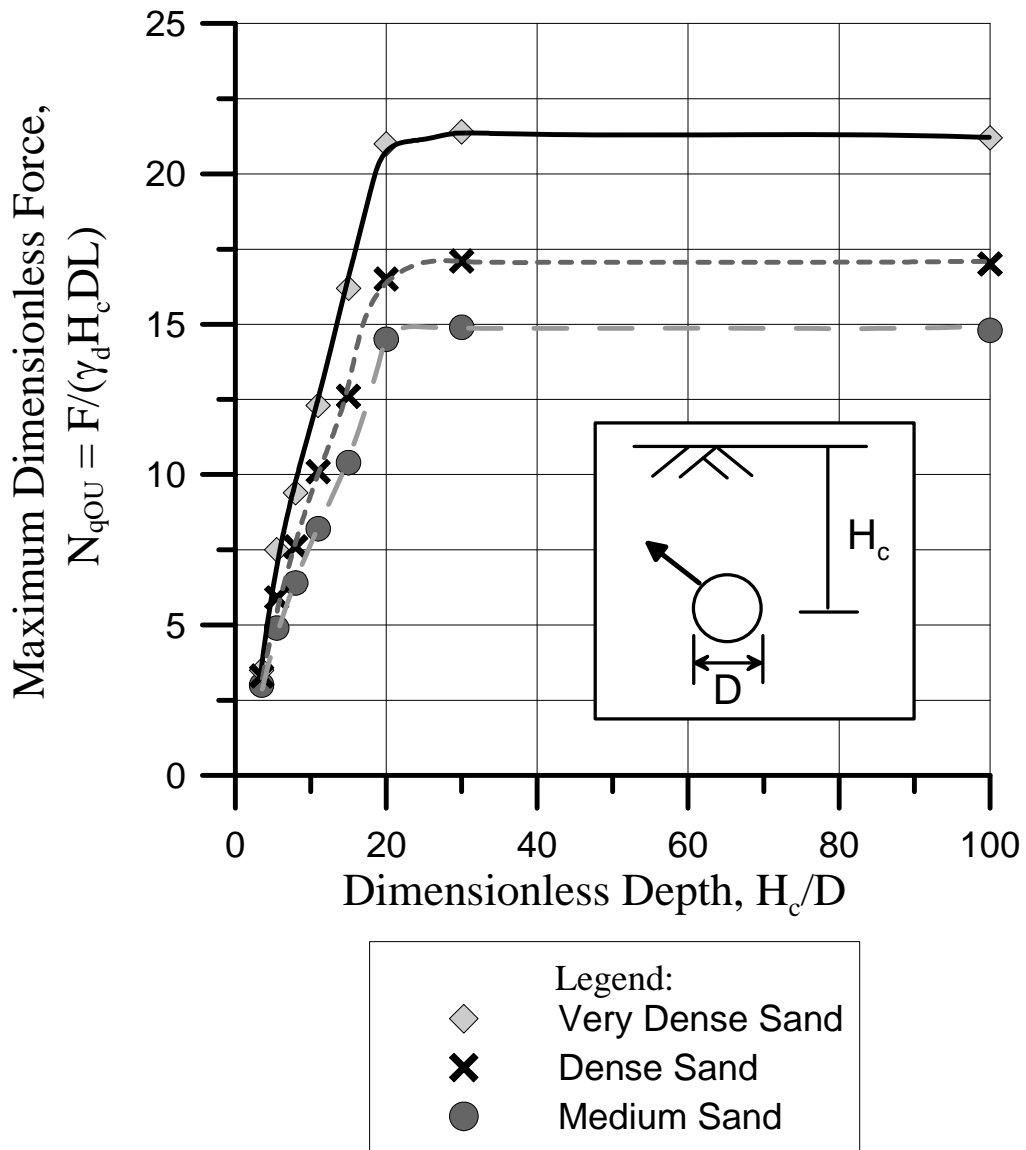


Figure 7.3 Summary Plot of N_{qOU} vs. H_c/D for Oblique Upward Pipe Movement

7.4 Relationship Between Force and Pipe Movement Direction

In this section, the maximum load for lateral, vertical upward, vertical downward, and 45° oblique orientations are combined to provide a relationship between force and any pipe movement direction as described under the subheadings that follow.

7.4.1. Simplified Approach

Equations for estimating the maximum oblique pipe force from known horizontal and vertical forces have been proposed (ASCE, 1984) on the basis of recommendations by Nyman (1982) and Meyerhof (1973). These equations for the maximum dimensionless pipe force are

$$N_{qOD} = iN_{qVD} \quad (7.1)$$

and

$$N_{qOU} = iN_{qVU} \quad (7.2)$$

in which

$$i = 1 + \left(\frac{0.25\alpha}{90^\circ - 0.75\alpha} \right) (i_u - 1) \quad (7.3)$$

and N_{q-OD} , N_{q-VD} , N_{q-OU} , and N_{q-VU} are the maximum dimensionless oblique downward, vertical downward, oblique upward, and vertical upward force, respectively, α is the angle of movement with respect to the horizontal; and i_u is the ratio of lateral N_{qH} to vertical N_{qV} , expressed as

$$i_u = \frac{N_{qH}}{N_{qV}} \quad (7.4)$$

Figure 7.4 plots the dimensionless oblique downward force from FE analyses, N_{qOD-e} , with respect to the dimensionless force, N_{qOD-s} , given by the simplified approach embodied in Eqn. 7.1. All comparisons are made for oblique forces at $\alpha = -45^\circ$. There is favorable agreement between N_{qOD-e} and N_{qOD-s} , with all N_{qOD-e} within $\pm 10\%$ of N_{qOD-s} . The average difference between N_{qOD-e} and N_{qOD-s} is 2.1%.

Similarly, Fig. 7.5 plots the dimensionless oblique upward force from FE analyses, N_{qOU-e} , with respect to N_{qOU-s} , given by the simplified approach embodied in Eqn. 7.2. All comparisons are made for oblique forces at $\alpha = +45^\circ$. There is favorable agreement between N_{qOU-e} and N_{qOU-s} , with all N_{qOU-e} within $\pm 10\%$ of N_{qOU-s} . The average difference between N_{qOU-e} and N_{qOU-s} is 4.9%.

7.4.2. Visualization of Maximum Dimensionless Force and Movement Direction

The FE maximum dimensionless force for lateral, vertical upward/downward, and $\pm 45^\circ$ oblique orientations are combined in a series of graphs for visualizing the variation in maximum pipe force for any movement direction under plane strain conditions. The analytical results are normalized with respect to maximum dimensionless lateral force, N_{qH} , and the normalized maximum forces are provided on 360° plots that can be used to predict maximum pipe loads for medium to very dense dry sand at various H_c/D .

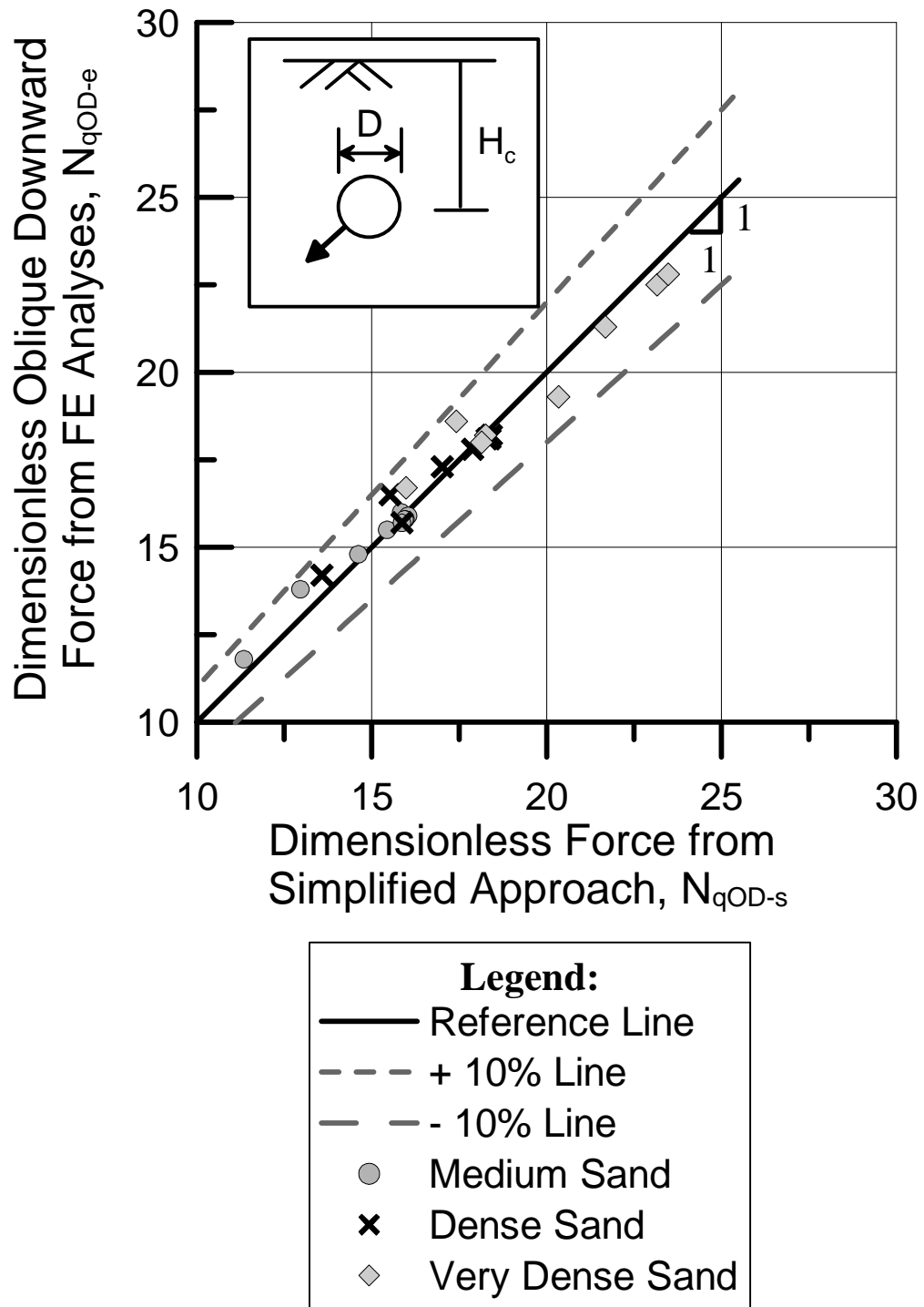


Figure 7.4 Comparison of N_{qOD-e} and N_{qOD-s}

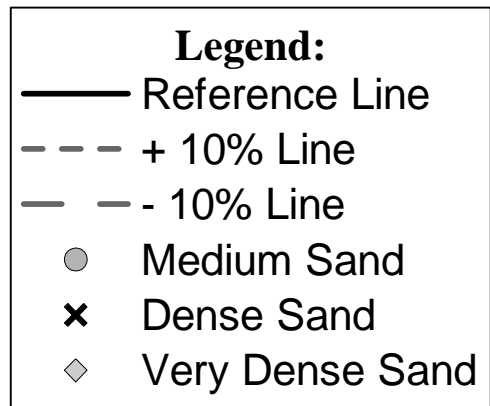
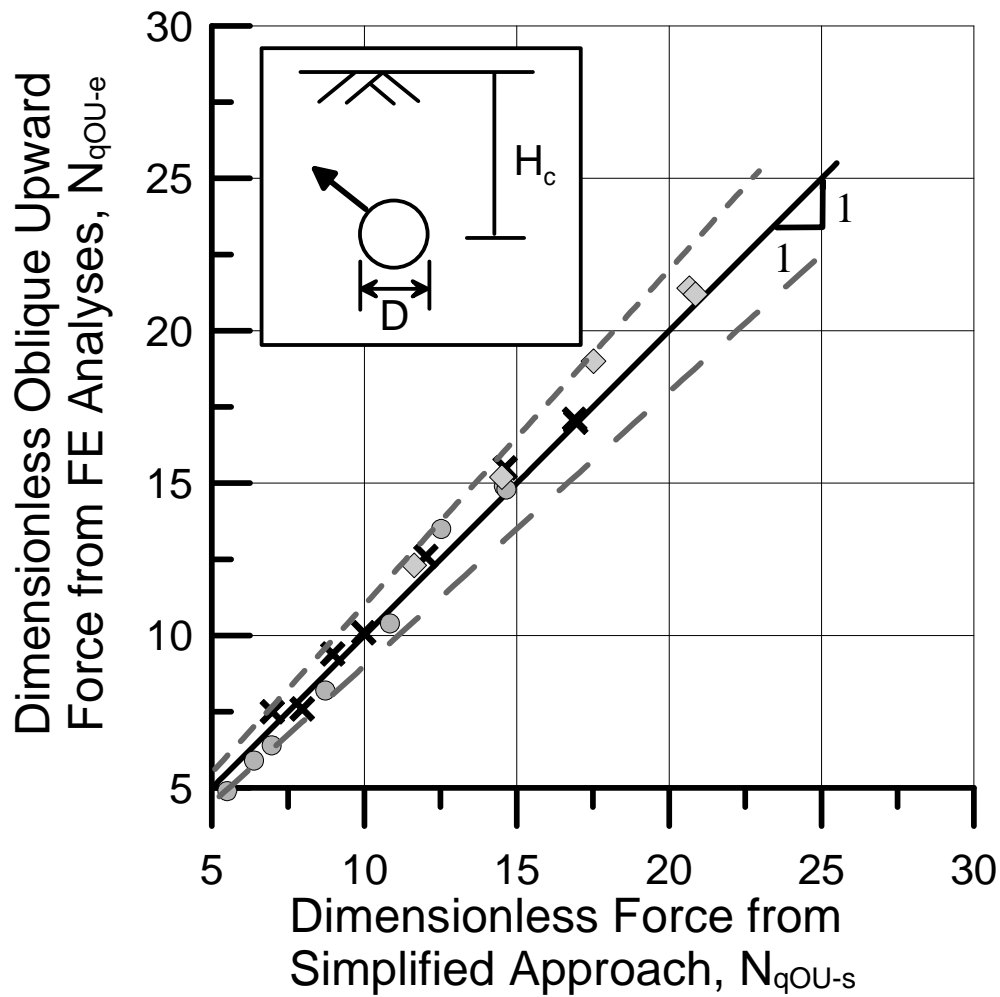


Figure 7.5 Comparison of N_{qOU-e} and N_{qOU-s}

Figures 7.6 and 7.7 show the ratio of maximum dimensionless force at any orientation and maximum lateral dimensionless force, N_q/N_{qH} , plotted in polar coordinates for $H_c/D = 3.5 - 100$. The dimensionless force ratio, N_q/N_{qH} has a unique value for a given H_c/D and direction of pipe movement, which does not depend on sand density and associated friction angles. This aspect of the relationships is illustrated in Fig. 7.9, which compares N_q/N_{qH} for medium and very dense sands. These sand densities represent the greatest difference in soil strength that was investigated in this work. Approximately 81 % of N_q/N_{qH} values are within ± 10 % of the line of equality. The average difference between the two ratios is 4.9 %.

Figures 7.6 and 7.7 show that at low values of H_c/D , the plots are asymmetric about the horizontal axis, with low N_q/N_{qH} associated with upward pipe movement and high N_q/N_{qH} associated with downward pipe movement. As H_c/D increases, the plots become increasingly more symmetric about the horizontal axis. At $H_c/D = 30$ the graph is nearly symmetric, and at $H_c/D = 100$, the graph is a circle. The perfect symmetry at $H_c/D = 100$ is achieved because at great depth, maximum force is identical in all directions for homogeneous soil.

It should be recognized that N_q/N_{qH} at $H_c/D \leq 15$ is unique for any given H_c/D , γ_d , and pipe movement direction only if D is constant. As explored in the previous sections of this work, there is a dependency of N_q on D for constant shallow H_c because of confining stress effects on the friction angle. A correction factor to cover different diameters can be obtained from the treatment of diameter effects for N_{qH} , N_{qVU} , and N_{qVD} in Chapters 4, 5, and 6, respectively.

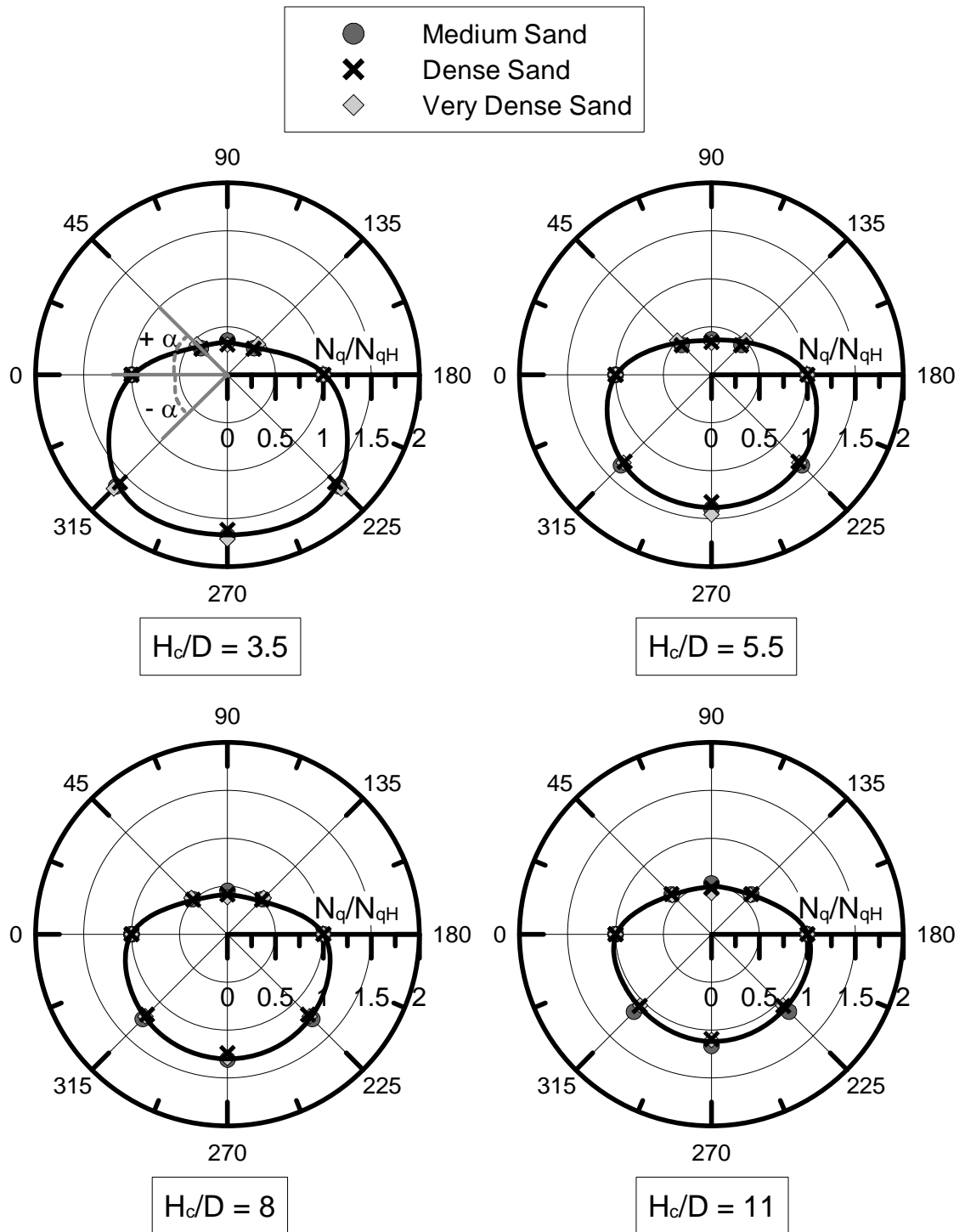


Figure 7.6 Visualization of N_q/N_{qH} for $H_c/D = 3.5 - 11$

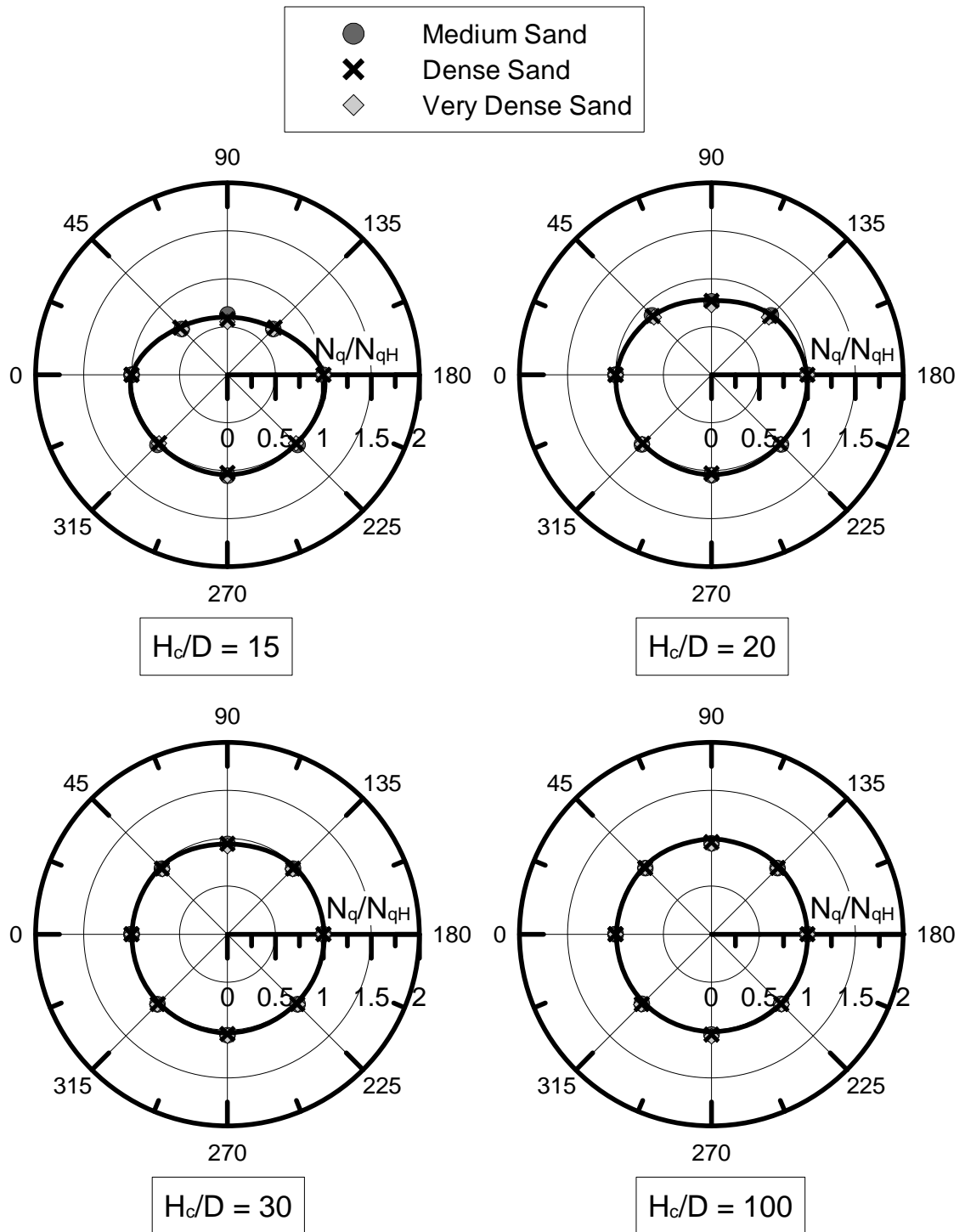


Figure 7.7 Visualization of N_q/N_{qH} for $H_c/D = 15 - 100$

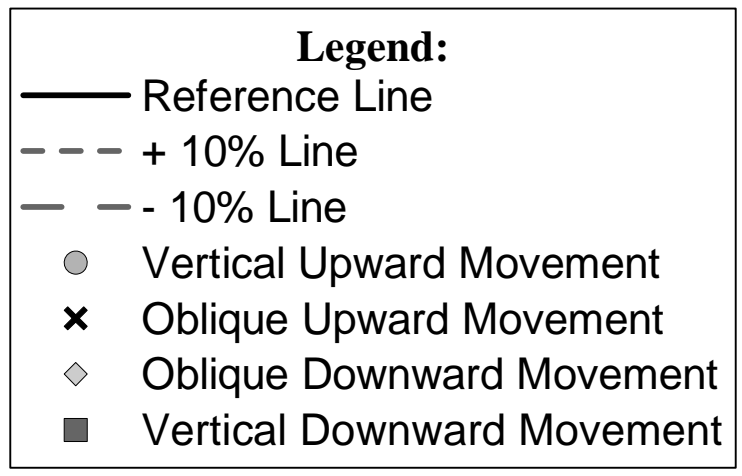
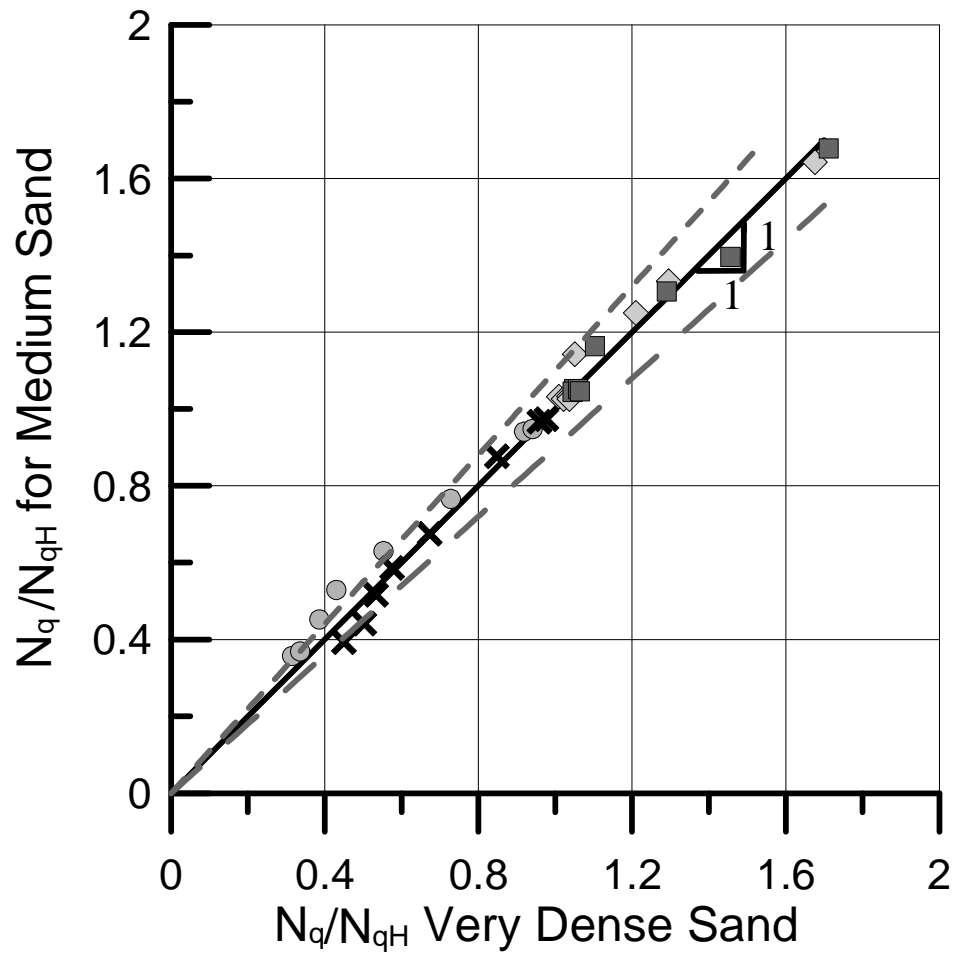


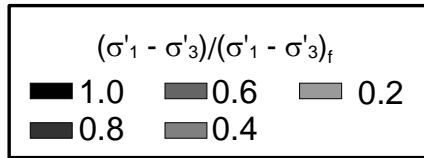
Figure 7.8 Comparison of N_q/N_{qH} of Medium and Very Dense Sand

7.5 Relationship Between Young's Modulus and Pipe Movement Direction

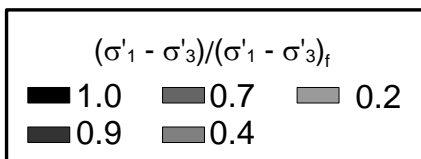
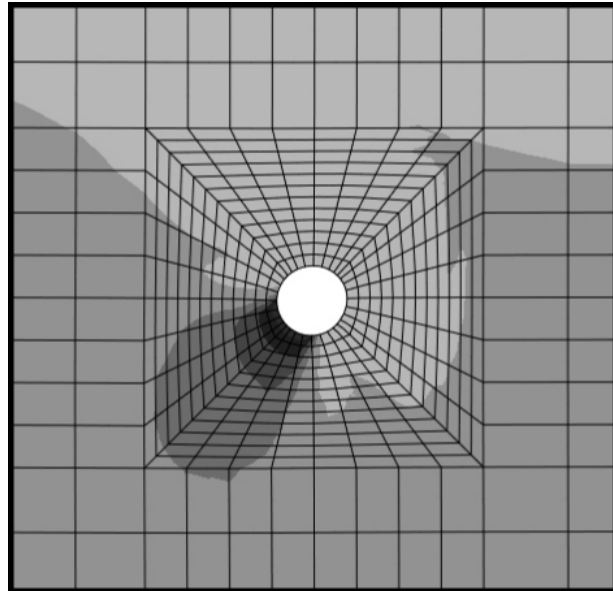
Finite element results were evaluated to estimate the strain compatible E_α at peak pipe force for oblique pipe movement. Figure 7.9 shows typical contours of $(\sigma'_1 - \sigma'_3)/(\sigma'_1 - \sigma'_3)_f$ from FE analyses of the peak oblique pipe force in dense sand at $H_c/D = 11$. The highly stressed zones at one and two pipe diameters from the pipe were used to perform two separate calculations of the mobilized soil strength fraction at peak pipe force, α , with Eqn. A.11, from which lower and upper bound values of the strain compatible modulus at peak pipe force, E_α , were obtained. The range of α for dense sand at $H_c/D = 11$ is 0.75 – 0.85 and 0.85 – 0.95 for oblique downward and upward pipe movement, respectively. The procedure for evaluating the mobilized soil strength fraction at peak force, described in Appendix A, was applied systematically to FE results for oblique pipe movement in medium, dense, and very dense sands at H_c/D from 5.5 to 20. Generalizing from the results of all analyses, it appears that $0.75 \leq \alpha \leq 0.85$ for oblique downward pipe movement and $0.85 \leq \alpha \leq 0.95$ for oblique upward pipe movement. Table 7.1 summarizes the range of α for various direction of pipe movement for dry sands under plane strain conditions.

Table 7.1 Summary of Mobilized Soil Strength Fraction at Peak Pipe Force, α , and Various Pipe Movements

Relative Pipe-Soil Movement	Mobilized Soil Strength Fraction, α
Vertical Upward	$0.90 \leq \alpha \leq 0.95$
45° Oblique Upward	$0.85 \leq \alpha \leq 0.95$
Lateral	$0.90 \leq \alpha \leq 0.95$
45° Oblique Downward	$0.75 \leq \alpha \leq 0.85$
Vertical Downward	$0.70 \leq \alpha \leq 0.90$



a) Mesh Adjacent to Pipe
 Oblique Upward
 Pipe Movement
 $H_c/D = 11$, Dense Sand



b) Mesh Adjacent to Pipe
 Oblique Downward
 Pipe Movement
 $H_c/D = 11$, Dense Sand

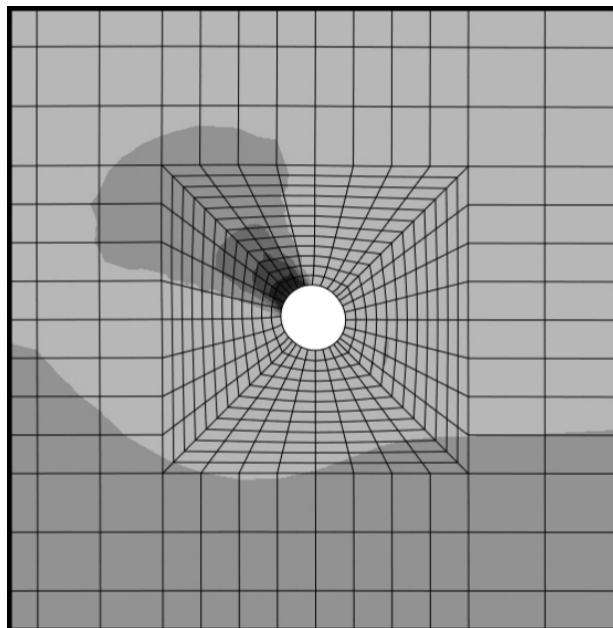


Figure 7.9 Contour of $(\sigma'_1 - \sigma'_3)/(\sigma'_1 - \sigma'_3)_f$ for Dense Sand at Peak Pipe Force for Oblique Pipe Movement

For the movement directions listed in Table 7.1, one can select α , from which the strain compatible modulus, E_α , at peak pipe force can be estimated from Eqn. A.9, which is given as $E_\alpha = E_i (1 - \alpha)$. The initial tangent modulus, E_i , can be estimated from Eqn. 3.8, using data summarized by Duncan and Chang (1970) and Wong and Duncan (1974). Alternatively, for lateral and upward vertical pipe movement, E_{70-H} and E_{70-VU} can be estimated from Eqns. 3.12 and 5.2, respectively, which have been derived from large-scale test data.

7.6 Peak Dimensionless Force for Oblique and Vertical Downward Pipe Movement in Partially Saturated RMS Graded Sand

The similar numerical model used in the dry oblique pipe movement study discussed in the previous Section 7.2 is used to investigate N_{qOD} and N_{qOU} in the partially saturated RMS graded sand used in the large-scale testing at various H_c/D . The dimensions of the model including the pipe diameter are identical to that used in dry oblique pipe movement analytical study. Input parameters for soil strength are similar to that used in Section 4.7.6. In the analyses for partially saturated RMS graded sand, the total unit weight of the sand γ_{total} , as well as ϕ_{ds-p} , and ϕ_{ps-p} are used in the analyses. Summarized input parameters used in partially saturated sand for oblique pipe movement FE analyses are presented in Table 4.3. Soil cohesion for plane strain condition is selected as $c_{ps} = 1.2$ kPa (Olson, 2009) and a small residual values of $c_{ps-ld} = 0.1$ kPa is used to promote numerical stability. A Poisson's ratio of 0.3 is assumed, and the model is set to linearly diminish c_{ps} to c_{ps-ld} , from the plastic strain at ϕ_{ps-p} to γ_f^p .

The FE analyses results of oblique pipe movement in partially saturated RMS

graded sand are shown in Fig. 7.10 and 7.11. The procedure explained in Chapter 3 and 6 is used to obtain N_{qOU} , and N_{qOD} , respectively. Figure 7.10 show that a limiting value of N_{qOD} is reached between $H_c/D = 20 - 30$ at 27.4. The N_{qOD} decreases with increasing H_c/D after the maximum value of N_{qOD} . For example, N_{qOD} decreases approximately 2.9 % and ϕ_{ps-p} decrease approximately 3.7 % from $H_c/D = 20$ to 100.

Figure 7.11 show that a limiting value of N_{qOU} is reached between $H_c/D = 25 - 30$ at 25.1. The N_{qOU} decreases with increasing H_c/D after the maximum value of N_{qOD} . For example, N_{qOU} decreases approximately 1.2 % and ϕ_{ps-p} decrease approximately 2.6 % from $H_c/D = 30$ to 100.

Figure 7.12 plots N_{qOD-e} and N_{qOU-e} with respect to N_{qOD-s} and N_{qOU-s} in partially saturated sand. N_{qOD-s} and N_{qOU-s} are given by the simplified approach embodied in Eqn. 7.1 and 7.2, respectively. There is favorable agreement between the FE analyses and the simplified approach, with all the FE analyses within ± 10 % of the simplified approach. The average difference between N_{qOD-e} and N_{qOD-s} is 2.7 %, and N_{qOU-e} and N_{qOU-s} is 3.7 %.

7.7 Force vs. Displacement Relationships for One Dimensional Modeling of Soil-Pipeline Interaction

Pipeline analysis for soil-structure interaction under permanent ground deformation is often performed with one-dimensional FE models to represent the pipeline and soil force vs. displacement relationships that are mobilized by various types of ground movement. As described by ASCE (1984), soil pipeline interaction

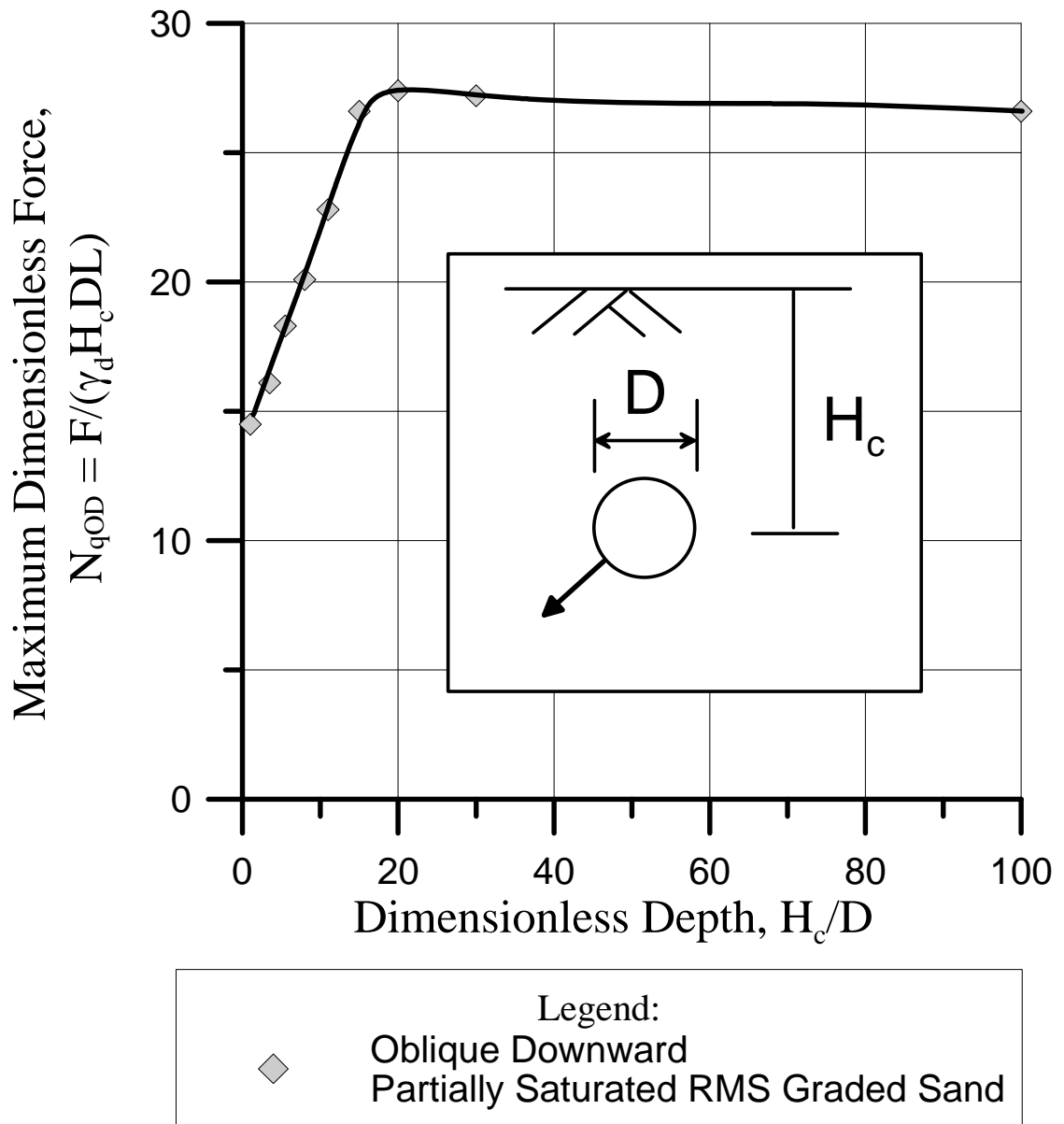


Figure 7.10 Summary Plot of N_{qOD} vs. H_c/D of Oblique Downward Pipe Movement in Partially Saturated RMS Graded Sand

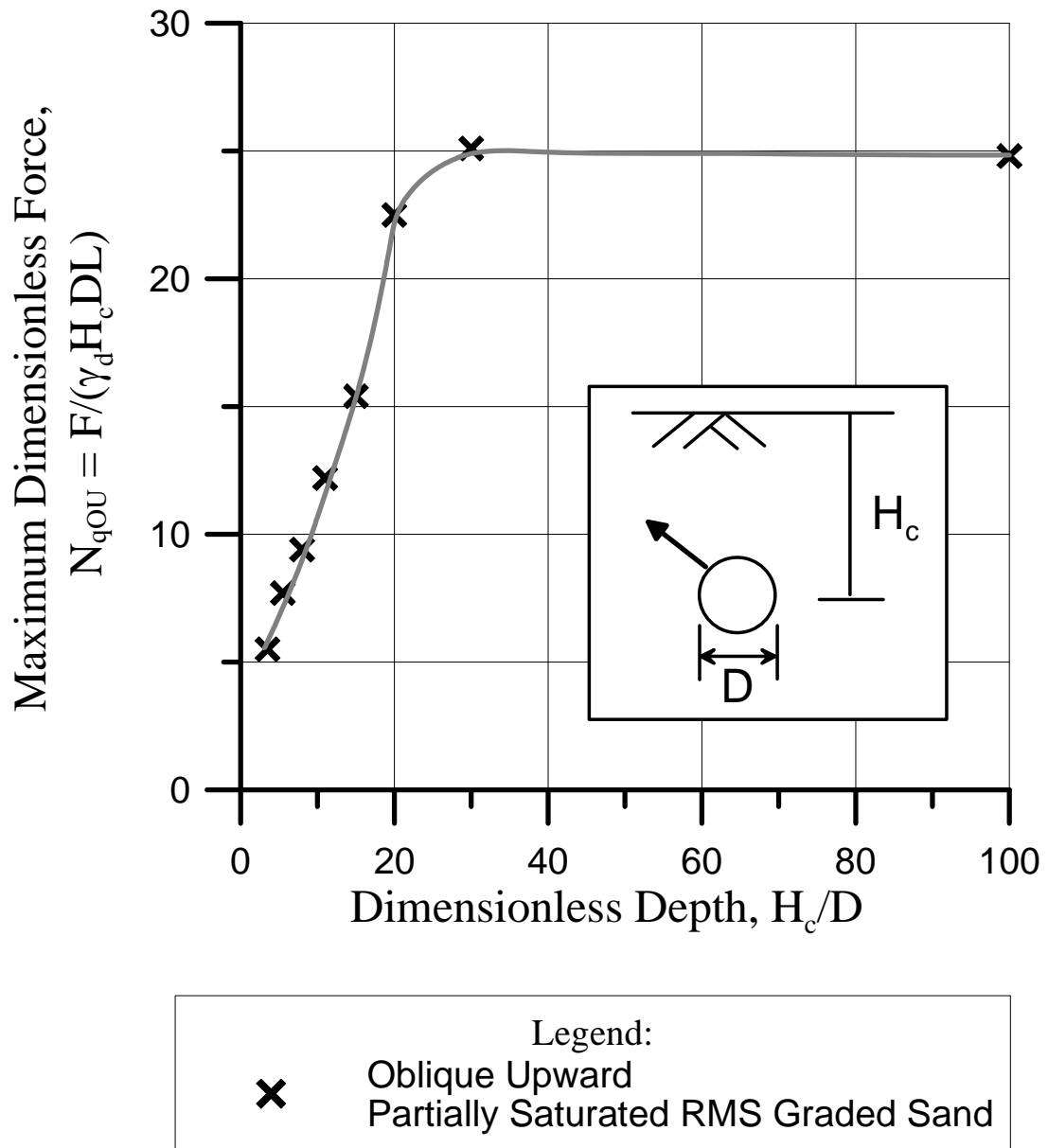


Figure 7.11 Summary Plot of N_{qOU} vs. H_c/D for Oblique Upward Pipe Movement in Partially Saturated RMS Graded Sand

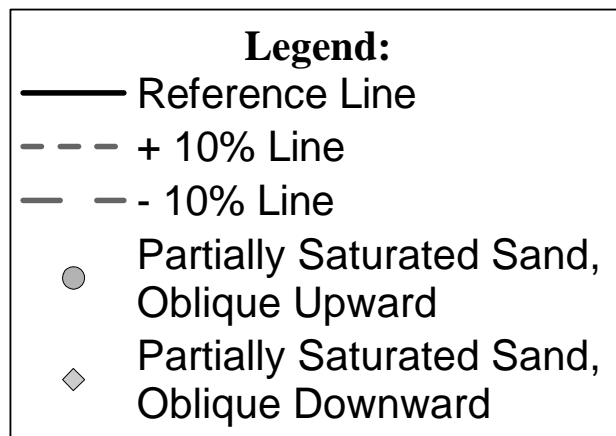
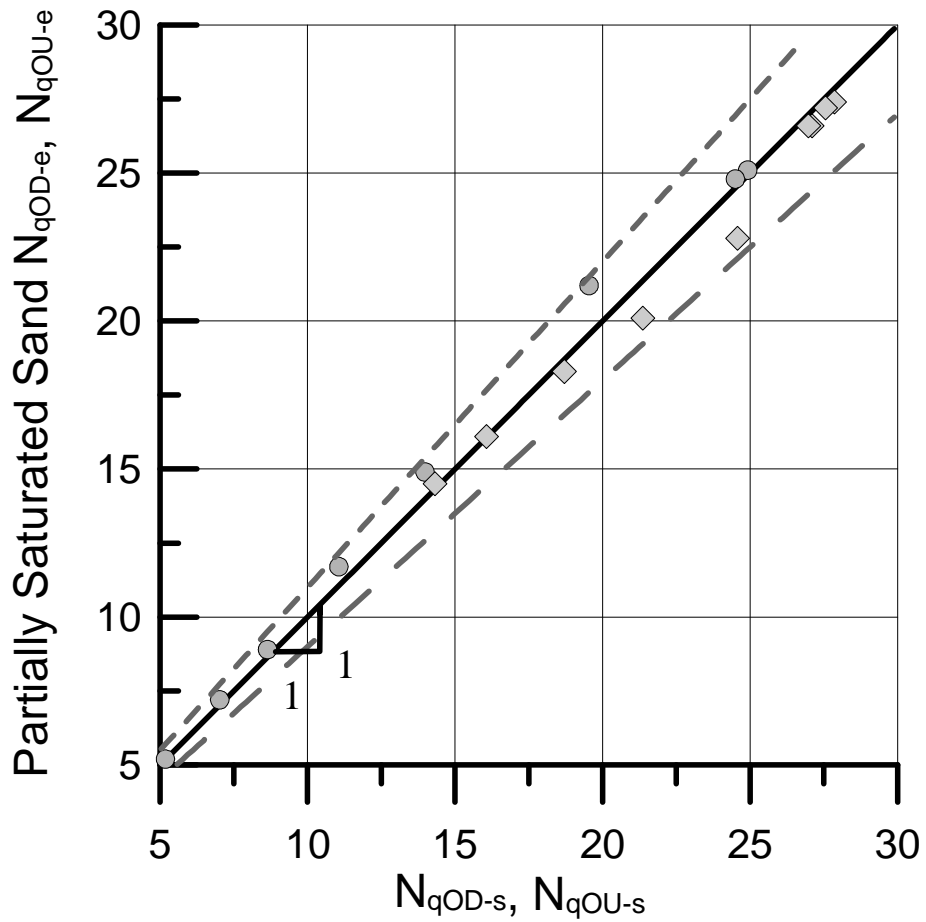
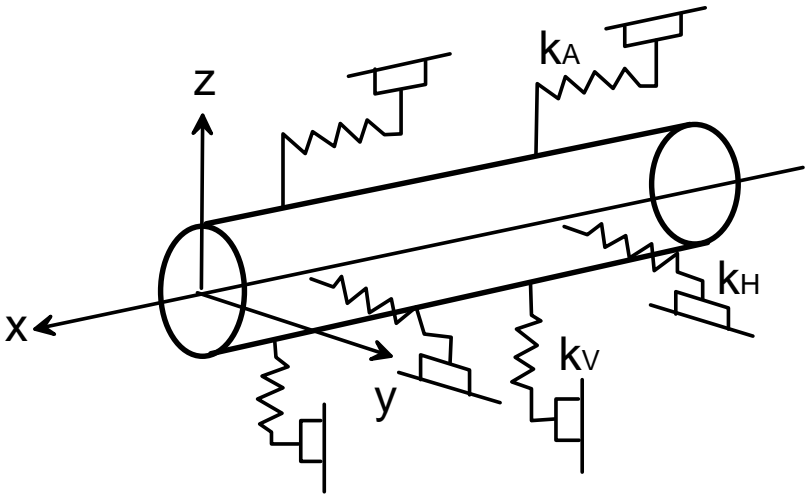
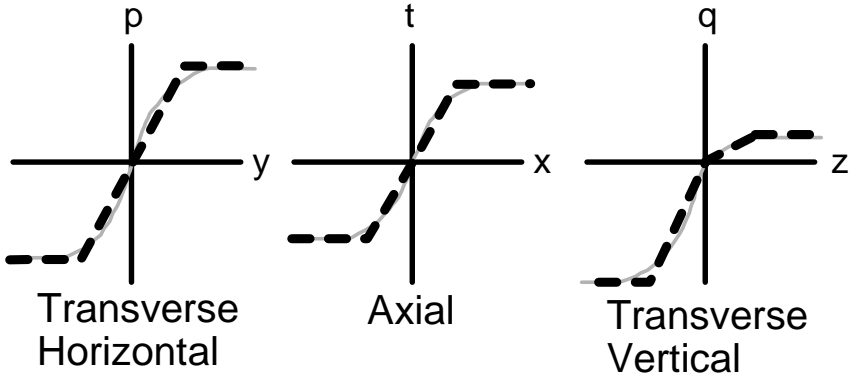


Figure 7.12 Comparison of FE Analyses and Simplified Approach

is represented by components in the axial, transverse horizontal, and transverse vertical directions, as schematically represented by the soil springs in Fig. 7.13.



a) Idealized Structural Model



b) Soil Load-Deformation Relationships

Figure 7.13 Soil Load and Restraints (ASCE, 1984)

The force vs. displacement relationships for transverse force on pipelines subjected to differential ground movement can be represented by a rectangular hyperbola for the nonlinear characterization of force vs. displacement or by a simple bilinear relationship between force and displacement (Trautmann and O'Rourke, 1983;

ASCE, 1984; Trautmann et al., 1985; Turner, 2004). Nonlinear and bilinear force vs. displacement relationships for 1-D FE modeling of soil-pipeline interaction are developed from the analytical and experimental work described in this study, and are presented for lateral, vertical upward, vertical downward, and oblique pipe movements under the subheadings that follow.

7.8.1 Lateral Pipe Movement

Following the procedure proposed by Trautmann and O'Rourke (1983), the force vs. displacement relationship can be modeled by a rectangular hyperbola. Normalizing the force vs. displacement curves with respect to the maximum lateral dimensionless force, N_{qH} , and the dimensionless displacement associated with maximum force, Y_{fH}/D , the data were plotted on transformed axes. The displacement Y_{fH} is replotted in Fig. 7.14 as the ratio Y_{fH}/H_c . As shown in the figure, representative values of Y_{fH}/H_c are 3.7 %, 2.7 %, and 2.1 % for medium, dense, and very dense sand, respectively. Figure 7.15 shows the average hyperbolic relationship for selected data from each test. The representative hyperbolic models for lateral pipe movement was found to be

$$F'_H = \frac{Y'_H}{0.20 + 0.82Y'_H} \quad (7.5)$$

in which $F'_H = (F/\gamma_d H_c DL)/N_{qH}$, $Y'_H = (Y_H/D)/(Y_{fH}/D)$, F = the force measured at each increment of displacement, and Y_H = horizontal displacement. Equation 7.5 is close to the expression of $F'_H = Y'_H/(0.17 + 0.83 Y'_H)$ reported by Trautmann and O'Rourke (1985) for lateral pipe movement in dry CU filter sand based on the experimental data.

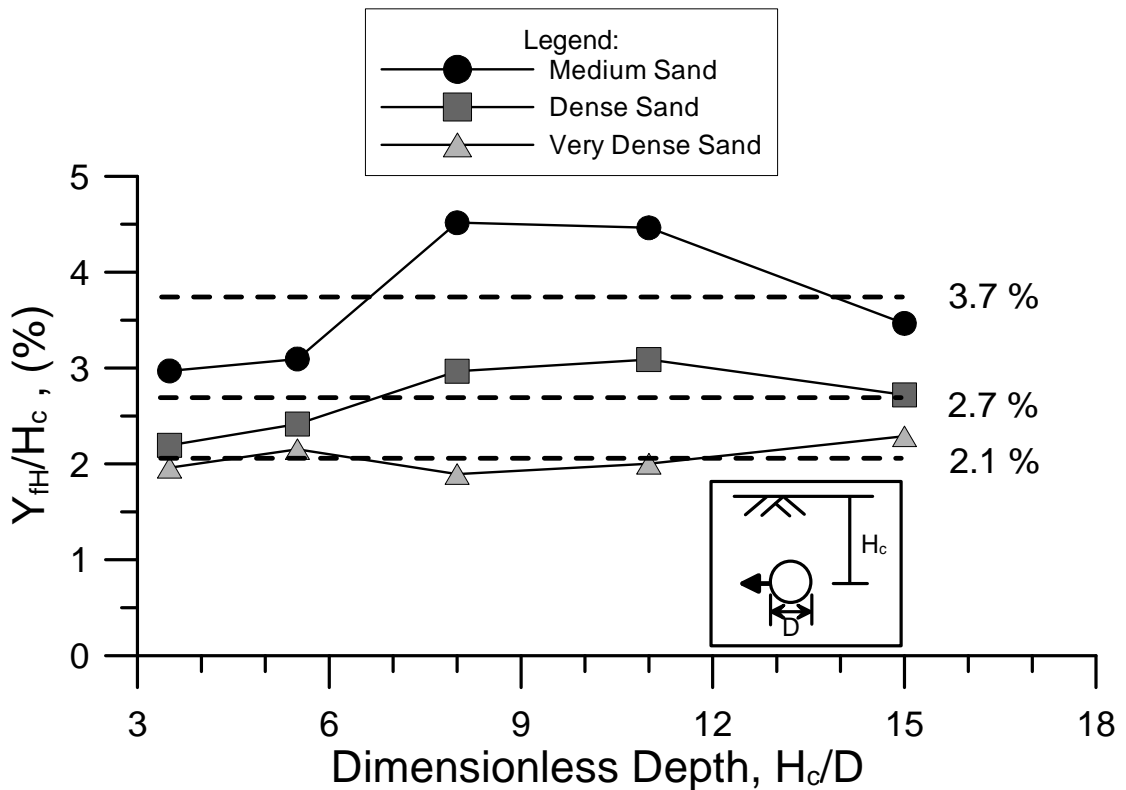


Figure 7.14 Y_{FH}/H_c vs. H_c/D Plots for Lateral Pipe Movement

Using this relationship and appropriate values of N_{qH} and Y_{FH}/D , a force vs. displacement relationship can be constructed for any combination of pipe diameter, depth, and soil density.

Some computer programs use a bilinear force vs. displacement relationship to model soil behavior. The bilinear force vs. displacement model consists of an initial elastic portion and a plastic portion. The initial elastic portion has a slope of K_{70H} and the plastic portion represents the limiting value of maximum pipe force. To select the slope of K_{70H} , the method proposed by Thomas (1978) and used by Truatmann & O'Rourke (1983) was applied to the force vs. displacement response of the pipe. As explained in Chapter 3, bisecting the experimental pipe-displacement

plot by a K_{70} -line results in approximately equal areas between K_{70} and the nonlinear data plot below and above the 70 % peak force value.

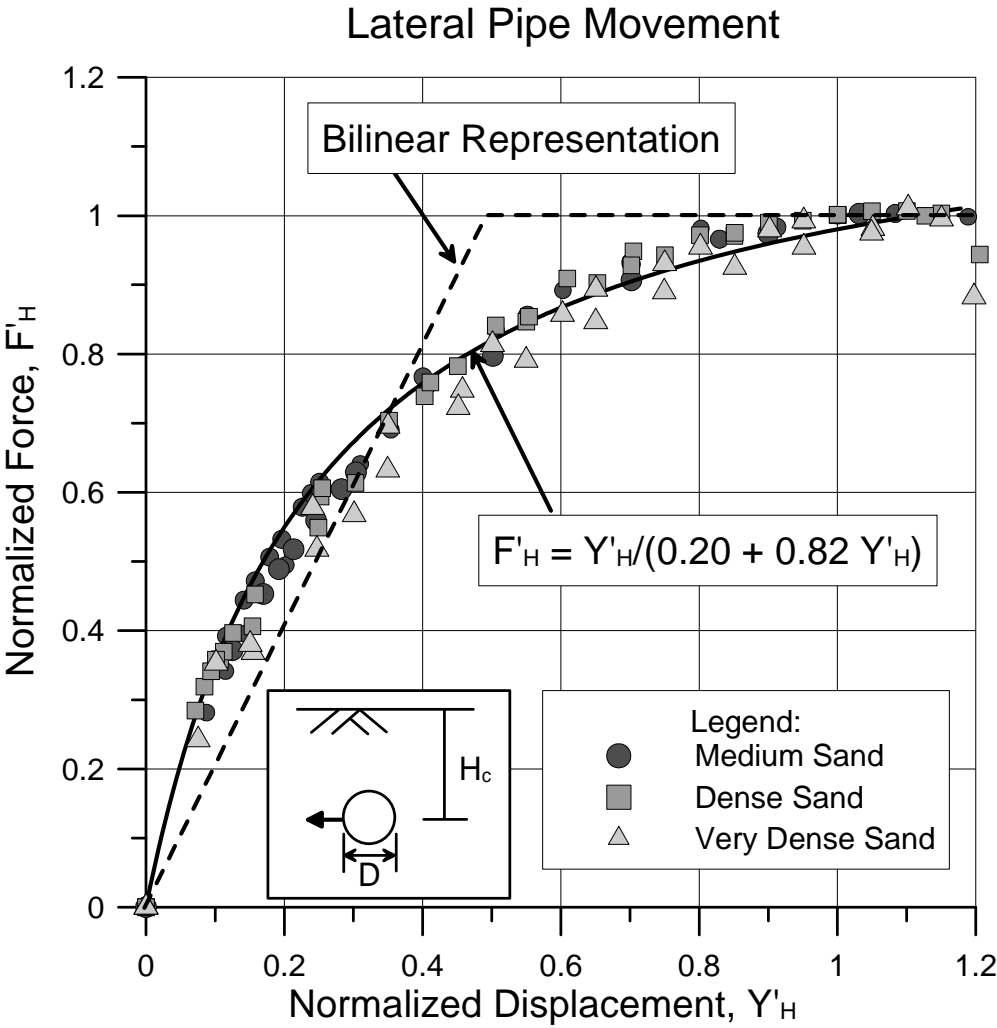


Figure 7.15 Force vs. Displacement Relationships for One Dimensional Modeling of Soil-Pipeline Interaction for Lateral Pipe Movement

As shown in Fig 7.15, a bilinear representation based on K_{70H} results in a maximum force at a normalized displacement of 0.5. This value is close to 0.4 reported by Trautmann and O’rourke (1985). From the observation, the displacement

at maximum force for the bilinear relationship is half of the Y_{fH}/D and can be defined as

$$C_{KH} = \left(\frac{0.5Y_{fH}}{D} \right)^{-1} \quad (7.6)$$

K_{70H} is then given by the following equation:

$$K_{70H} = C_{KH} N_{qH} \gamma_d DL \quad (7.7)$$

The displacement Y_{fH} is provided in Fig. 7.14 for medium, dense, and very dense sand.

7.8.2 Vertical Upward Pipe Movement

As explained in Section 7.8.1, the force vs. displacement relationship for vertical upward pipe movement can be modeled by a rectangular hyperbola. Normalizing the force vs. displacement curves with respect to the maximum vertical upward dimensionless force, N_{qVU} , and Y_{fVU}/D , the data were plotted on transformed axes. The displacement Y_{fVU} is replotted in Fig. 7.16 as the ratio Y_{fVU}/H_c . As shown in the figure, representative values of Y_{fVU}/H_c are 1.3 %, 1.1 %, and 1.0 % for medium, dense, and very dense sand, respectively. Figure 7.17 shows the average hyperbolic relationship for selected data from each test. The representative hyperbolic models for vertical upward pipe movement was found to be

$$F'_{vU} = \frac{Y'_{vU}}{0.16 + 0.85Y'_{vU}} \quad (7.8)$$

in which $F'_{vU} = (F/\gamma_d H_c DL)/N_{qvU}$, $Y'_{vU} = (Y_{vU}/D)/(Y_{fvU}/D)$, and Y_{vU} = vertical upward displacement. Equation 7.8 is close to the expression of $F'_{vU} = Y'_{vU}/(0.07 + 0.93 Y'_{vU})$ reported by Trautmann et al., (1985) for vertical upward pipe movement in dry CU filter sand based on the experimental data. Using this relationship and appropriate values of N_{qvU} and Y_{fvU}/D , a force vs. displacement relationship can be

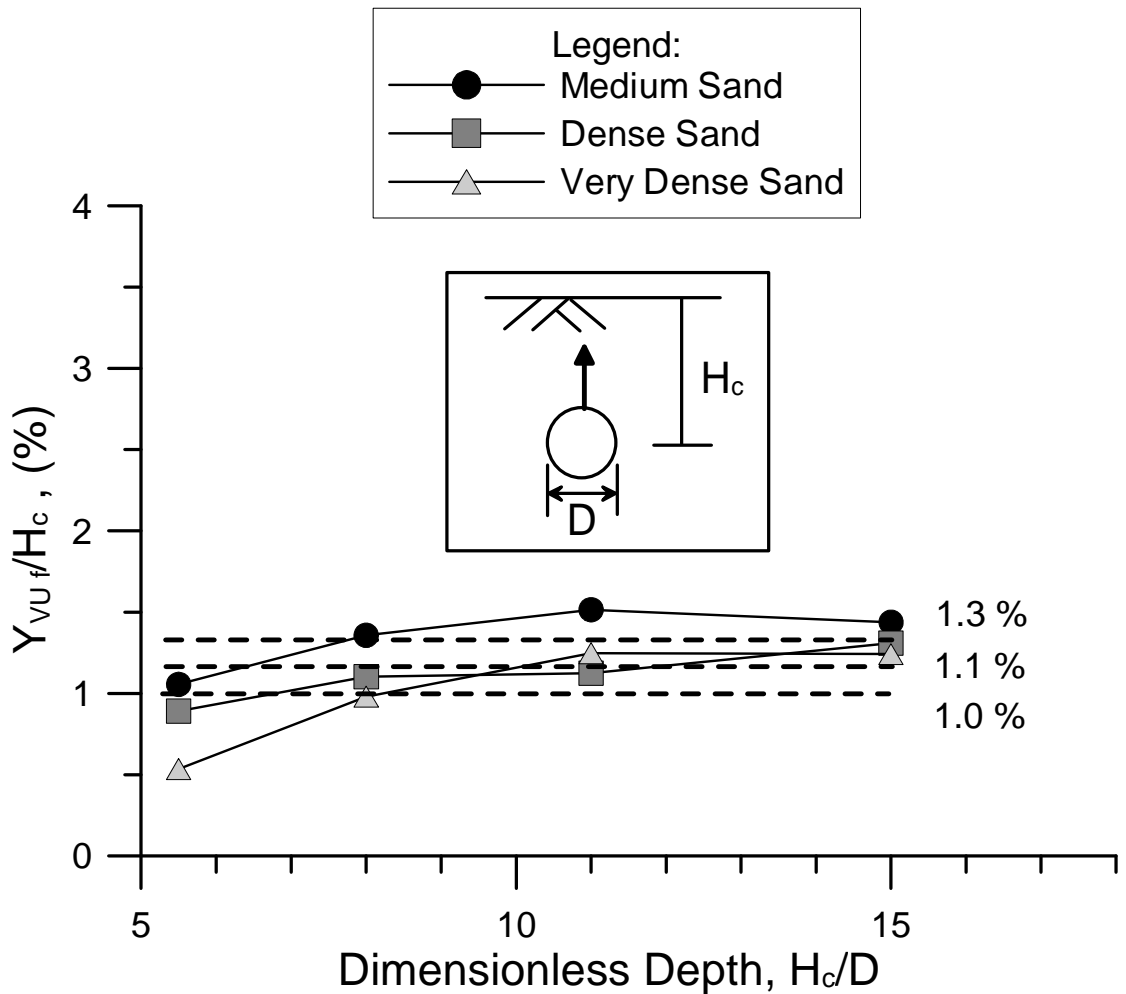


Figure 7.16 Y_{fvU}/H_c vs. H_c/D Plots for Vertical Upward Pipe Movement

constructed for any combination of pipe diameter, depth, and soil density.

Similar to lateral pipe movement, a bilinear representation of force vs. displacement for vertical upward pipe movement is plotted in Fig. 7.17. As shown in the figure, a bilinear representation based on K_{70VU} results in a maximum force at a normalized displacement of 0.3. This value is close to 0.2 reported by Trautmann et al., (1985). From the observation, the displacement at maximum force for the bilinear relationship is 0.3 times the Y_{fVU}/D and can be defined as

$$C_{KVU} = \left(\frac{0.3Y_{fVU}}{D} \right)^{-1} \quad (7.9)$$

K_{70VU} is then given by the following equation:

$$K_{70VU} = C_{KVU} N_{qVU} \gamma_d DL \quad (7.10)$$

The displacement Y_{fVU} is provided in Fig. 7.16 for medium, dense, and very dense sand.

7.8.3 Vertical Downward Pipe Movement

As explained in Section 7.8.1, the force vs. displacement relationship for vertical downward pipe movement can be modeled by a rectangular hyperbola. Normalizing the force vs. displacement curves with respect to the maximum vertical downward dimensionless force, N_{qVD} , and Y_{fVD}/D , the data were plotted on

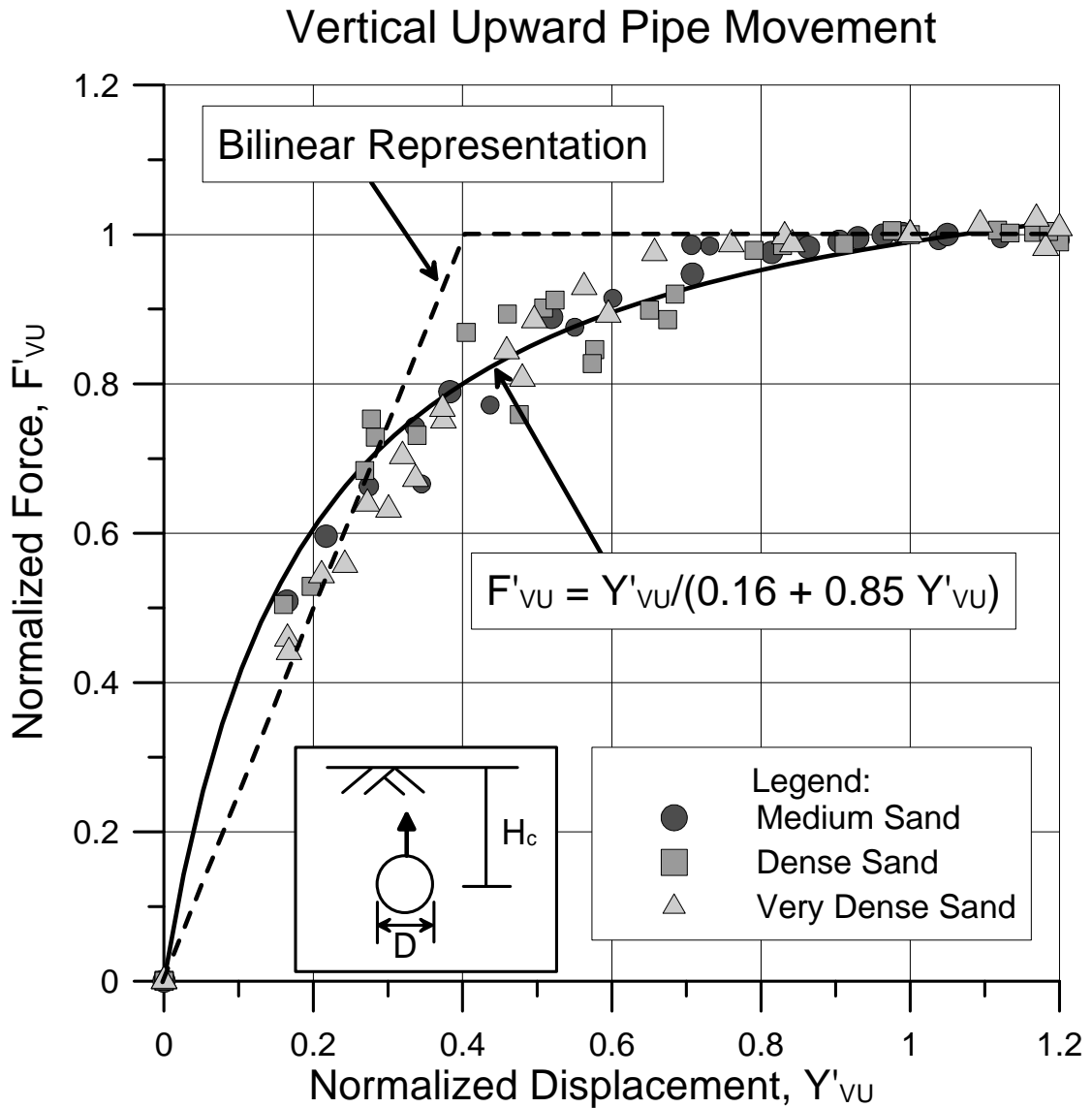


Figure 7.17 Force vs. Displacement Relationships for One Dimensional Modeling of Soil-Pipeline Interaction for Vertical Upward Pipe Movement

transformed axes. The displacement Y_{fVD} is replotted in Fig. 7.18 as the ratio Y_{fVD}/H_c . As shown in the figure, representative values of Y_{fVD}/H_c are 0.81 %, 0.79 %, and 0.75 % for medium, dense, and very dense sand, respectively. Figure 7.19 shows the average hyperbolic relationship for selected data from each test. The representative hyperbolic model for vertical downward pipe movement was found to be

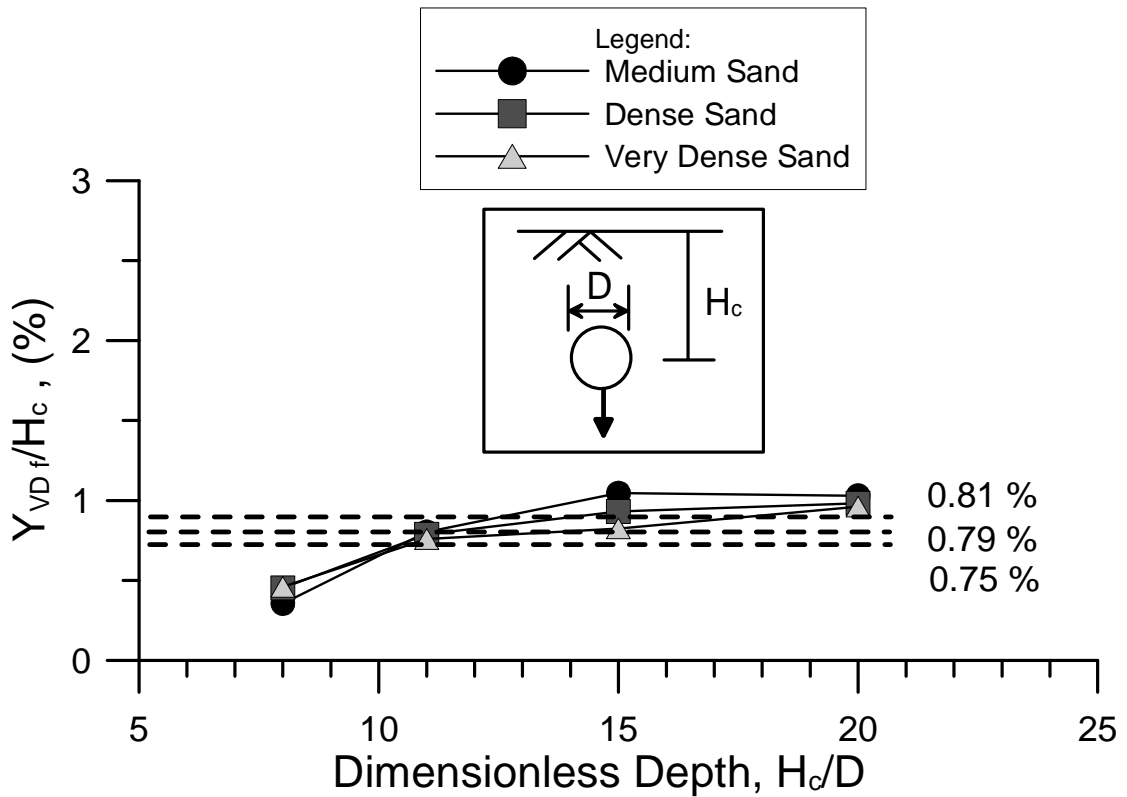


Figure 7.18 Y_{fVD}/H_c vs. H_c/D Plots for Vertical Downward Pipe Movement

$$F'_{VD} = \frac{Y'_{VD}}{0.53 + 0.46Y'_{VD}} \quad (7.11)$$

in which $F'_{VD} = (F/\gamma_d H_c DL)/N_{qVD}$, $Y'_{VD} = (Y_{VD}/D)/(Y_{fVD}/D)$, and Y_{VD} = vertical downward displacement. Using this relationship and appropriate values of N_{qVD} and Y_{fVD}/D , a force vs. displacement relationship can be constructed for any combination of pipe diameter, depth, and soil density.

Similar to lateral pipe movement, a bilinear representation of force vs. displacement for vertical downward pipe movement is plotted in Fig. 7.19. As shown in the figure, a bilinear representation based on K_{70VD} results in a maximum

Vertical Downward Pipe Movement

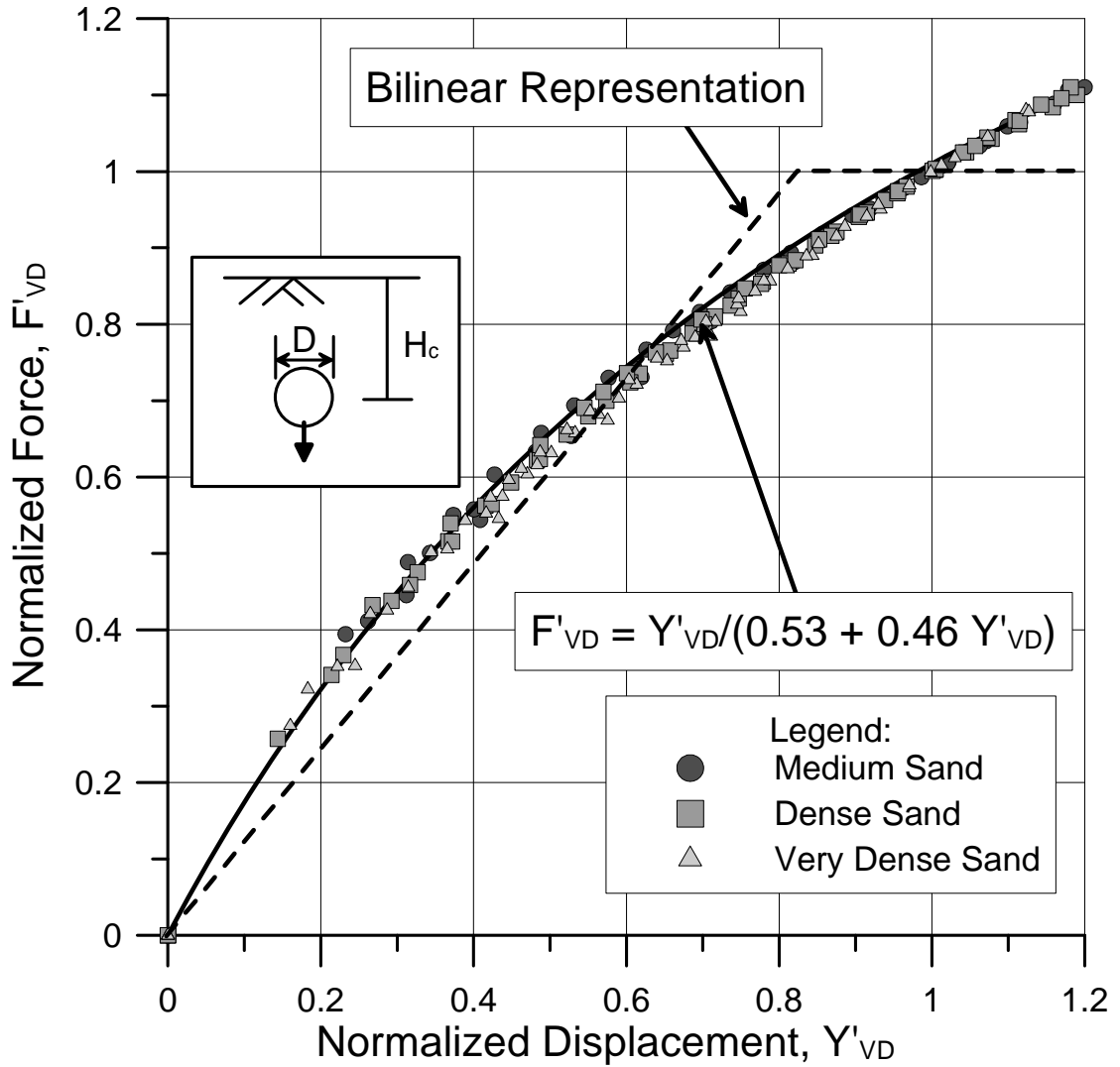


Figure 7.19 Force vs. Displacement Relationships for One Dimensional Modeling of Soil-Pipeline Interaction for Vertical Downward Pipe Movement

force at a normalized displacement of 0.6. From the observation, the displacement at maximum force for the bilinear relationship is 0.6 times the Y_{fVD}/D and can be defined as

$$C_{KVD} = \left(\frac{0.6Y_{fVD}}{D} \right)^{-1} \quad (7.12)$$

K_{70VD} is then given by the following equation:

$$K_{70VD} = C_{KVD} N_{qVD} \gamma_d DL \quad (7.13)$$

The displacement Y_{fVD} is provided in Fig. 7.18 for medium, dense, and very dense sand.

7.8.4 Oblique Downward Pipe Movement

The force vs. displacement relationship for oblique downward pipe movement can be modeled by a rectangular hyperbola. Normalizing the force vs. displacement curves with respect to the maximum oblique downward dimensionless force, N_{qOD} , and Y_{fOD}/D , the data were plotted on transformed axes. The displacement Y_{fOD} is replotted in Fig. 7.20 as the ratio Y_{fOD}/H_c . As shown in the figure, representative values of Y_{fOD}/H_c are 0.44 %, 0.07 %, and 0.06 % for medium, dense, and very dense sand, respectively. Figure 7.21 shows the average hyperbolic relationship for selected data from each test. The representative hyperbolic models for oblique downward pipe movement was found to be

$$F'_{OD} = \frac{Y'_{OD}}{0.53 + 0.46Y'_{OD}} \quad (7.14)$$

in which $F'_{OD} = (F/\gamma_d H_c DL)/N_{qOD}$, $Y'_{OD} = (Y_{OD}/D)/(Y_{fOD}/D)$, and Y_{OD} = oblique

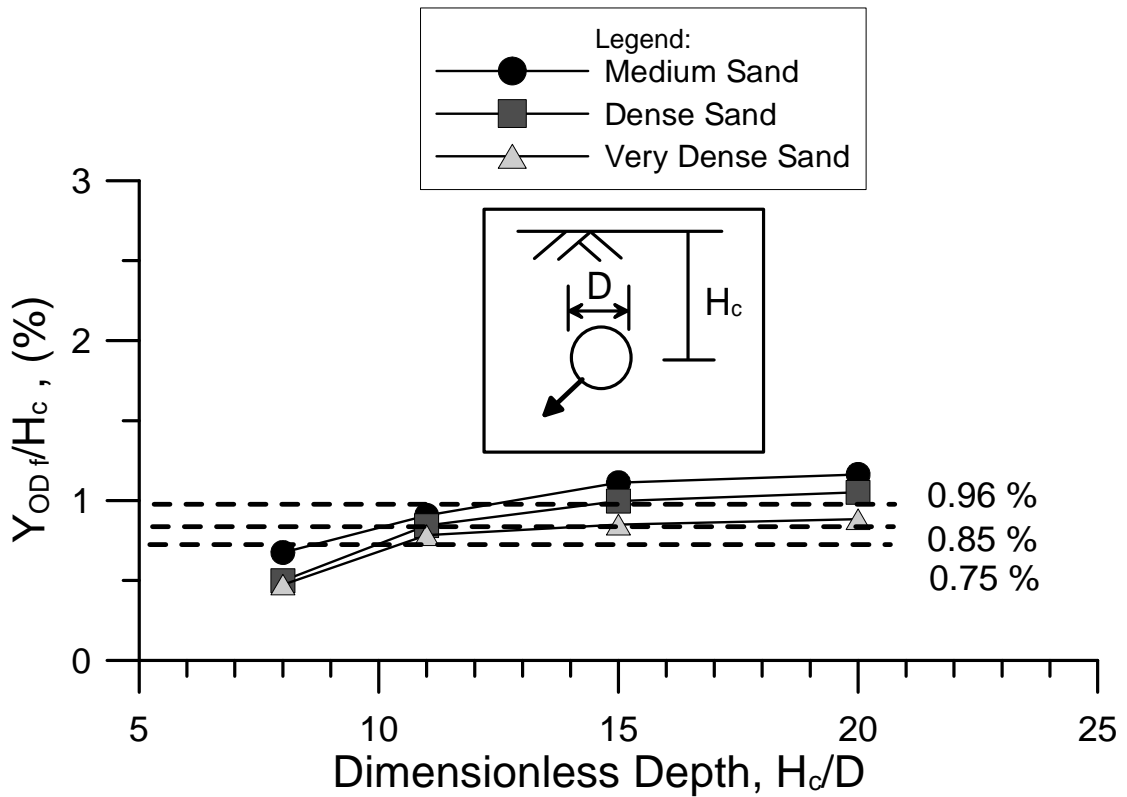


Figure 7.20 Y_{fOD}/H_c vs. H_c/D Plots for Vertical Downward Pipe Movement

downward displacement. Using this relationship and appropriate values of N_{qOD} and Y_{fOD}/D , a force vs. displacement relationship can be constructed for any combination of pipe diameter, depth, and soil density.

A bilinear representation of force vs. displacement for oblique downward pipe movement is plotted in Fig. 7.21. As shown in the figure, a bilinear representation based on K_{70OD} results in a maximum force at a normalized displacement of 0.55. From the observation, the displacement at maximum force for the bilinear relationship is 0.55 times the Y_{fOD}/D and can be defined as

Oblique Downward Pipe Movement

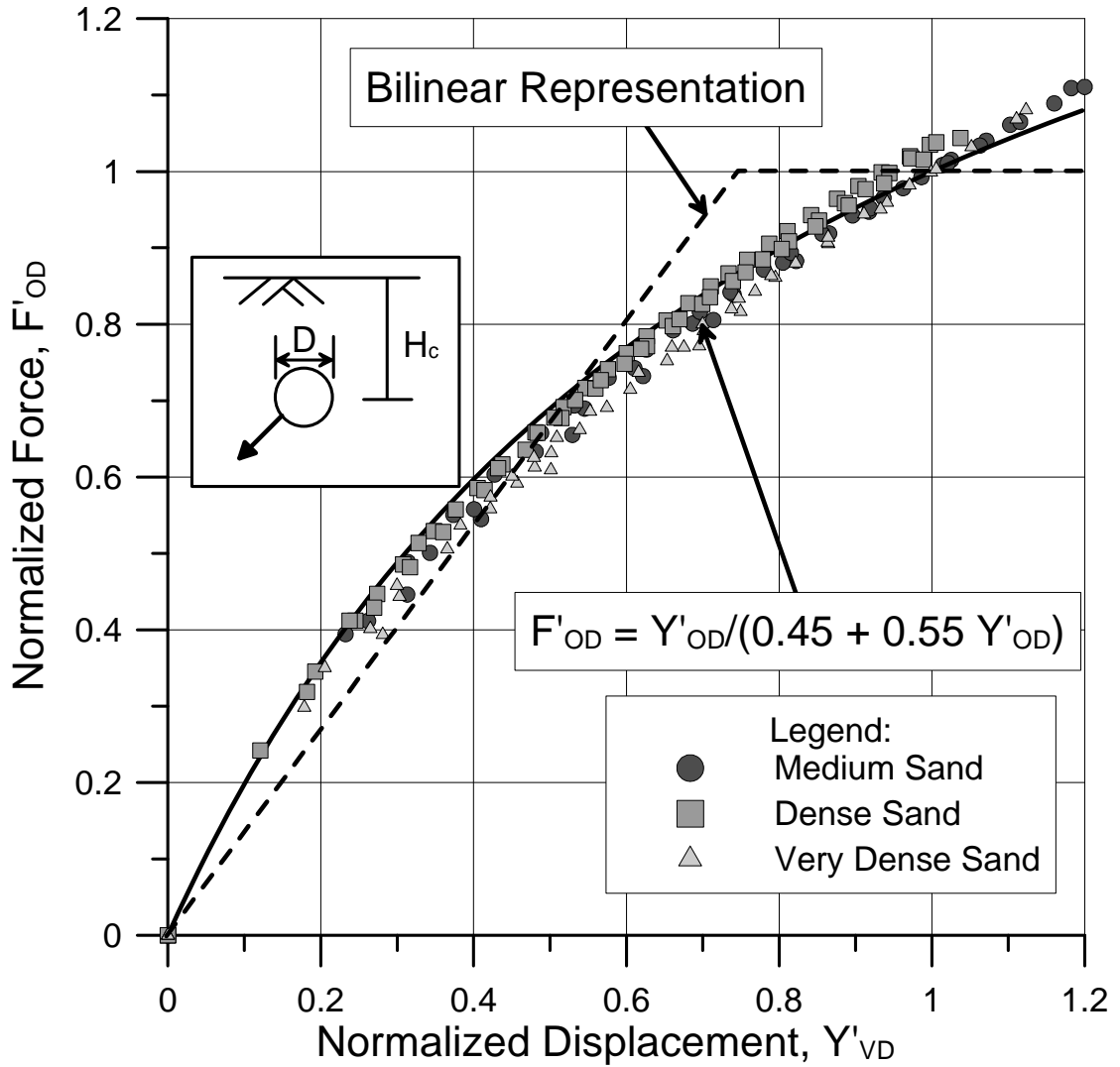


Figure 7.21 Force vs. Displacement Relationships for One Dimensional Modeling of Soil-Pipeline Interaction for Oblique Downward Pipe Movement

$$C_{KOD} = \left(\frac{0.55 Y_{fOD}}{D} \right)^{-1} \quad (7.15)$$

K_{70OD} is then given by the following equation:

$$K_{70OD} = C_{KOD} N_{qOD} \gamma_d DL \quad (7.16)$$

The displacement Y_{fOD} is provided in Fig. 7.20 for medium, dense, and very dense sand.

7.8.5 Oblique Upward Pipe Movement

The force vs. displacement relationship for oblique upward pipe movement can be modeled by a rectangular hyperbola. Normalizing the force vs. displacement curves with respect to the maximum oblique upward dimensionless force, N_{qOU} , and Y_{fOU}/D , the data were plotted on transformed axes. The displacement Y_{fOD} is replotted in Fig. 7.22 as the ratio Y_{fOU}/H_c . As shown in the figure, representative values of Y_{fOU}/H_c are 1.7 %, 1.3 %, and 1.2 % for medium, dense, and very dense sand, respectively. Figure 7.23 shows the average hyperbolic relationship for selected data from each test. The representative hyperbolic models for oblique upward pipe movement was found to be

$$F'_{OU} = \frac{Y'_{OU}}{0.21 + 0.81Y'_{OU}} \quad (7.14)$$

in which $F'_{OU} = (F/\gamma_d H_c DL)/N_{qOU}$, $Y'_{OU} = (Y_{OU}/D)/(Y_{fOU}/D)$, and Y_{OU} = oblique upward displacement. Using this relationship and appropriate values of N_{qOU} and Y_{fOU}/D , a force vs. displacement relationship can be constructed for any combination of pipe diameter, depth, and soil density.

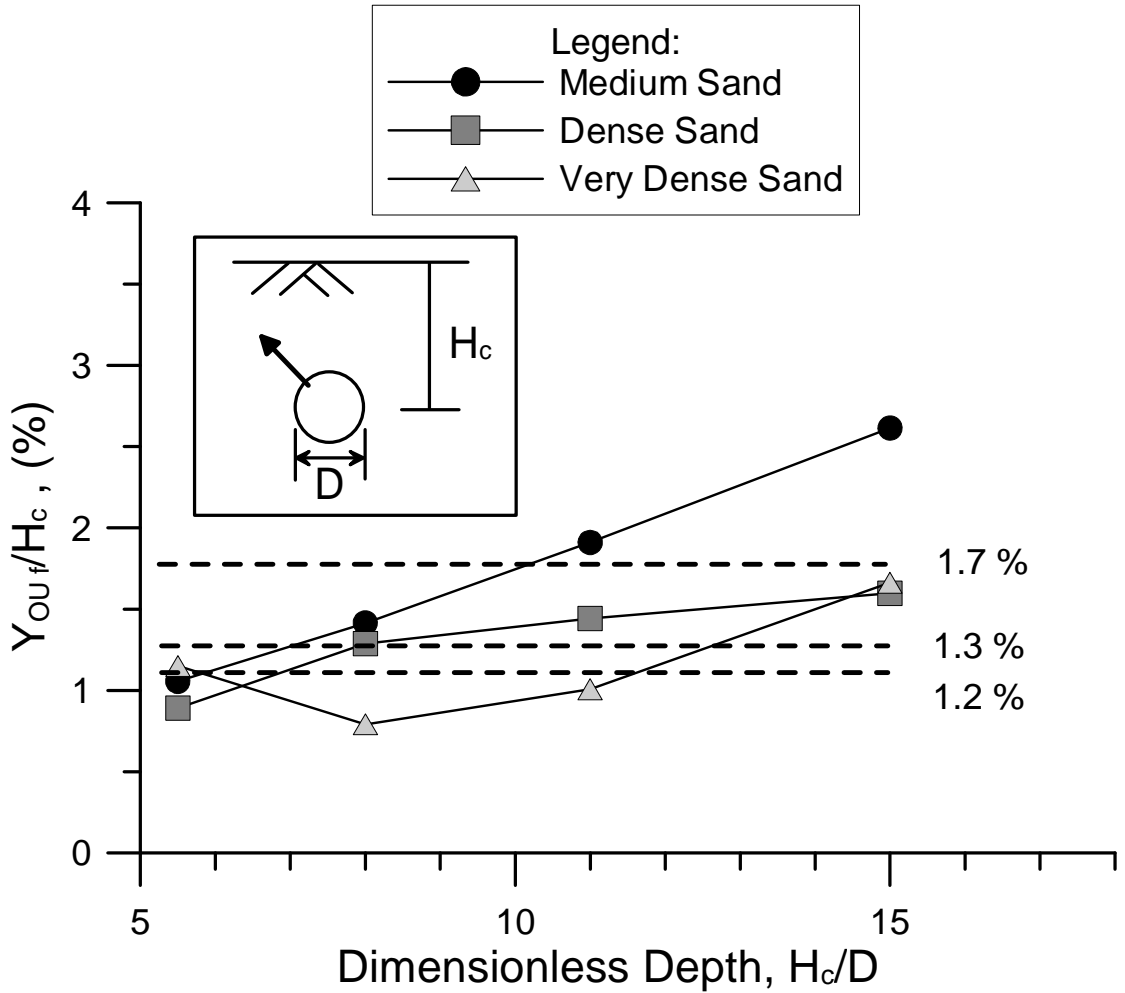


Figure 7.22 Y_{fOU}/H_c vs. H_c/D Plots for Vertical Downward Pipe Movement

A bilinear representation of force vs. displacement for oblique upward pipe movement is plotted in Fig. 7.23. As shown in the figure, a bilinear representation based on K_{70OU} results in a maximum force at a normalized displacement of 0.4. From the observation, the displacement at maximum force for the bilinear relationship is 0.4 times the Y_{fOU}/D and can be defined as

$$C_{KOU} = \left(\frac{0.4Y_{fOU}}{D} \right)^{-1} \quad (7.15)$$

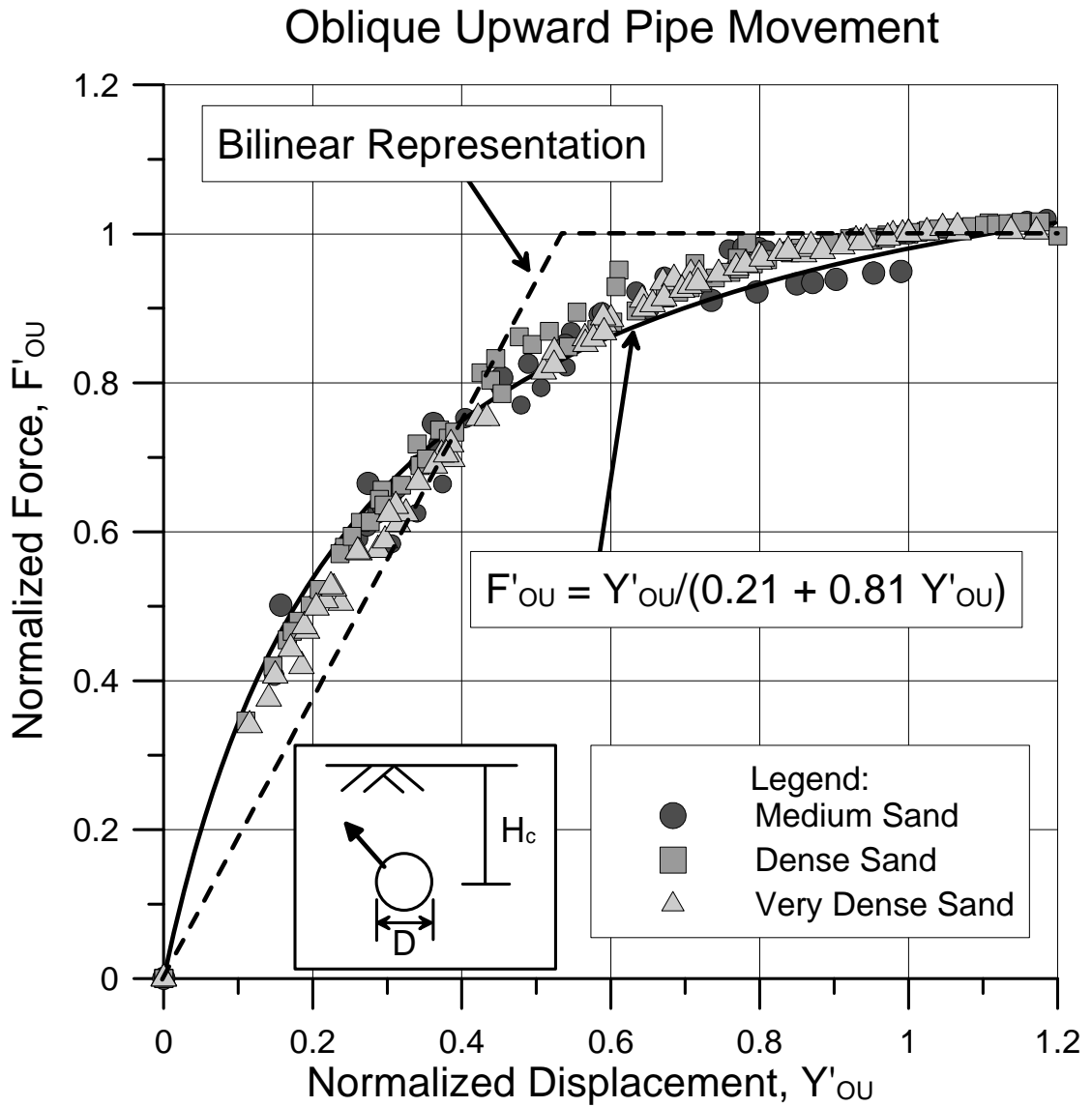


Figure 7.23 Force vs. Displacement Relationships for One Dimensional Modeling of Soil-Pipeline Interaction for Oblique Downward Pipe Movement

K_{70OU} is then given by the following equation:

$$K_{70OU} = C_{KOU} N_{qOU} \gamma_d DL \quad (7.16)$$

The displacement Y_{fOU} is provided in Fig. 7.22 for medium, dense, and very dense sand.

CHAPTER 8

SUMMARY AND CONCLUSIONS

8.1 Introduction

This study has focused on soil-structure interaction of underground pipelines subject to relative displacement between pipe and soil under 2-D plane strain conditions. Finite element (FE) analyses of lateral, vertical upward, vertical downward, and oblique pipe movement have been performed. This chapter provides a summary of major research findings associated with this dissertation. The sections that follow summarize the research findings related to 1) comparison of finite element and experimental results for lateral pipe movement; 2) lateral pipe movement in semi-infinite soil at various depths; 3) vertical upward pipe movement; 4) vertical downward pipe movement; 5) oblique pipe movement; and 6) guidelines for practice. The final section provides a discussion of research needs and future research directions.

8.2 Comparison of Finite Element and Experimental Results for Lateral Pipe Movement

A series of finite element (FE) analyses with ABAQUS 6.9 (2009) were performed to predict the peak force and to compare the measured peak forces with experimental results. The experimental database used for the comparisons was derived from full-scale, 2-D tests on pipe buried in dry and partially saturated sand. The input soil strength parameters for the FE simulations were obtained from DS tests

performed by Olson (2009) and strain softening of the soil was represented by applying the model proposed by Anastasopoulos, et al. (2007).

The soil strength modeling used in this research accounts for changes in the sand peak angle of dilatancy, ψ_p , as a function of the confining stress and initial dry soil density, γ_d , based on the experimental results of Olson (2009). Because the peak plane strain friction angle, ϕ'_{ps-p} , is related to ψ_p as well as the critical angle of shear resistance, ϕ'_{crit} , ϕ'_{ps-p} will also vary as a function of confining stress. A simplified analytical approach was developed in which ϕ'_{ps-p} was related only to the vertical effective stress at the pipe centerline. The FE results for this approach were compared with the results of FE analyses in which ϕ'_{ps-p} was varied with depth and related to the more accurate reference stress, σ'_N , representing the normal stress at maximum obliquity. The difference between the simplified approach and more accurate representation was less than 3.3 %, thus showing that the simplified approach provides a suitable method of analysis. A similar analytical approach was adapted for partially saturated conditions using total stress strength parameters for plane strain cohesion, c_{ps} , and friction angle, ϕ_{ps-p} .

For both dry and partially saturated sand, the dimensionless lateral force from FE analyses and the 2-D large-scale test results of Trautmann and O'Rourke (1983) and Olson (2009) are in very favorable agreement for depth-to-diameter ratios, H_c/D , that vary from 3.5 to 11. In general, the FE analyses results over predict the measured dimensionless peak force by a small, but conservative, margin of 2 – 7 %.

To determine the elastic modulus that represents the force-displacement relationship before yield, the K_{70} approach proposed by Thomas (1978) and applied by

Trautmann & O'Rourke (1983) was used. The equivalent modulus for lateral pipe movement, E_{70-H} , was determined by running FE simulations with different values of E and the same strength parameters for each experimental data set from Trautmann & O'Rourke (1983) and Olson (2009) until the initial linear force displacement response coincided with K_{70} . Then, multiple linear regression analyses were performed on E_{70-H} , σ'_{vc} , and γ_d to obtain an expression for predicting E_{70-H} as a function of σ'_{vc} and γ_d .

8.3 Lateral Pipe Movement in Semi-Infinite Soil at Various Depths

The modeling process was expanded to account for lateral soil-pipe interaction within a semi-infinite soil medium. Comparisons of experimental FE analyses and semi-infinite FE analyses show that the dimensionless maximum lateral forces from the semi-infinite FE analyses are smaller than those from the experimental FE analyses by 2 %. The displacement patterns for semi-infinite FE analyses and experimental FE analyses are also compared. When compared with the actual displacements observed in the large-scale experiments (Trautmann, 1983; Turner, 2004), the semi-infinite model provides a better representation of dry soil movement behind the pipe, but does not account for horizontal soil sliding along the base of the experimental test box.

Semi-infinite soil models were used to investigate the relationship between maximum lateral dimensionless force, N_{qH} , and H_c/D for medium, dense, and very dense sand. The FE analyses of lateral pipe movement show that N_{qH} reaches its maximum value of approximately 15, 18, and 23 for medium, dense, and very dense sand, respectively, at $H_c/D = 15 - 20$. For partially saturated RMS graded sand, the

FE analyses of lateral pipe movement show that N_{qH} reaches its maximum value of 27 at $H_c/D = 30$.

Additional FE analyses were run with various pipe diameters to investigate the diameter effect on soil-pipe interaction at constant H_c/D . The results show that the diameter effect increases when γ_d increases, but decreases when H_c/D increases. For constant H_c/D , the pipe depth increases as D increases so that the elevated confining stress with depth reduces the dilatancy contribution to sand shear strength. For $D = 102$ mm and 900 mm, the maximum difference in N_{qH} is approximately 12 % for both dense and very dense sand. The effects of diameter are negligible in medium sand.

The 2-D displacements of lateral pipe movement from FE simulations at various depths were investigated to check soil deformation patterns relative to N_{qH} . The soil displacement pattern at shallower depth is asymmetrically developed from the pipe to the surface, whereas the soil displacement pattern at greater depth is symmetrically developed around the pipe. When H_c/D increases to approximately 20, the soil deformation pattern becomes symmetric with respect to the pipe so that any further change in lateral force with increasing depth is related to changes in soil strength and not the geometric characteristics of the soil movement.

8.4 Vertical Upward Pipe Movement

A simulation procedure was developed to account for the effects of soil movement during upward pipe displacement. The predicted maximum dimensionless forces from FE analyses match those from the large-scale tests for H_c/D

= 1.5 – 13. The FE results compare favorably with the measured maximum dimensionless forces, with values 5 – 13 % higher than the experimental forces.

A procedure similar to that used for lateral pipe movement was used to determine the equivalent modulus for vertical upward pipe movement, E_{70-VU} . Multiple linear regression analyses were also performed on E_{70-VU} , σ'_{vc} , and γ_d to obtain an expression for predicting E_{70-VU} as a function of σ'_{vc} and γ_d .

Semi-infinite soil models were used to investigate the relationship between maximum vertical upward pipe force and various pipe depths for medium, dense, and very dense sand. The FE simulations of vertical upward pipe movement show that N_{qVU} reaches its maximum value of approximately 14, 17, and 20 for medium, dense, and very dense sand, respectively, at $H_c/D = 30$. For partially saturated sand, N_{qVU} reaches its maximum value of approximately 25 at $H_c/D = 20 - 30$.

Additional FE analyses were run with various pipe diameters to investigate the diameter effect on soil-pipe interaction at constant H_c/D . Similar to the lateral pipe movement results, the vertical upward pipe movement results show that the diameter effect increases when γ_d increases, but decreases when H_c/D increases. For $D = 102$ mm and 900 mm, the maximum difference in N_{qVU} is approximately 11 % for both dense and very dense sand.

8.5 Vertical Downward Pipe Movement

The numerical model is modified to account for vertical downward soil-pipe interaction within a semi-infinite soil medium. To evaluate the effective maximum

load for pipe settlement, N_{qVD} , the methods recommended for the interpretation of deep and shallow foundation load tests (Hirany and Kulhawy, 1998, 1989, and 2002; Akbas and Kulhawy, 2009) were used.

The FE simulations of vertical downward pipe movement show that N_{qVD} reaches its maximum value of 16, 19, and 24 for medium, dense, and very dense sand, respectively, at $H_c/D = 8 - 15$. For partially saturated sand, N_{qVD} reaches its maximum value of approximately 28 at $H_c/D = 15 - 20$.

The failure threshold forces for 2-D vertical downward pipe movement are 30 – 40 % of the bearing capacity forces. Force vs. displacement measurements from centrifuge tests of pipeline response to normal faulting (Abdoun, et al., 2008) show that the measured force associated with vertical downward pipe movement was approximately one-tenth of the conventional bearing capacity force. The vertical downward pipe movement is accompanied by soil displacement into the void that develops above the pipe. In the case of a deep foundation, however, the continuous deep foundation prevents soil displacement into a zone above the tip, and thus provides substantially higher constraint on soil deformation with associated higher resistance to tip penetration of the soil mass.

Because experimental data are sparse for downward pipe movement, it is difficult to verify the FE analyses results. To check the validity of the model, numerical simulations of 2-D deep foundations are performed. The FE failure threshold forces of the foundations are then checked against the theoretical bearing capacity forces. The FE results compare favorably with the theoretical bearing capacity forces, with values about 5 % higher than the theoretical bearing capacity

forces, proving that the FE analyses provides reasonable estimate for deep foundations.

The strain compatible secant modulus for vertical downward pipe movement, $E_{\alpha\text{-VD}}$, associated with $\alpha = 0.8$ was used to predict $N_{q\text{VD}}$ for the medium, dense, and very dense sands at various H_c/D . The resulting force vs. displacement relationships for downward pipe movement were checked to see if they provides a ρ_{L1} and ρ_{L2} consistent with load test statistics. From the 24 simulations performed with $E_{\alpha\text{-VD}}$ related to $\alpha = 0.8$, average values were obtained for ρ_{L1} , the displacement at the end of the initial linear part of the load vs. displacement plot, and ρ_{L2} , the displacement at the beginning of the final linear part of the load vs. displacement plot. Values of $\rho_{L1} = 0.19\% D$ and $\rho_{L2} = 5.83\% D$ were obtained, which are relatively close to $\rho_{L1} = 0.22\% D$ and $\rho_{L2} = 5.94\% D$, obtained from field load test data summarized in Appendix D.

Additional FE analyses were run with various pipe diameters to investigate the diameter effect on soil-pipe interaction at constant H_c/D . The FE results show that the diameter effect increases when γ_d increases, and decreases when H_c/D increases. For $D = 102$ mm and 900 mm, the maximum difference in $N_{q\text{VD}}$ is approximately 30 %.

8.6 Oblique Pipe Movement

To develop a comprehensive basis for evaluating force vs. displacement relationships for underground pipelines, the modeling process is expanded to account for oblique movement of the pipe. Numerical simulations were performed for pipe displacement, with both upward and downward movement components, at an angle of

45° with respect to the horizontal. The FE simulations of oblique downward pipe movement show that the dimensionless maximum oblique downward pipe force, N_{qOD} , reaches its maximum value of 16, 18, and 23 for medium, dense, and very dense sand, respectively, at $H_c/D = 11 - 15$. For partially saturated sand, N_{qOD} reaches its maximum value of 27 at $H_c/D = 20 - 30$. The FE simulations of oblique upward pipe movement show that the dimensionless maximum oblique upward pipe movement force, N_{qOU} , reaches its maximum value of 15, 17, and 21 for medium, dense, and very dense sand, respectively, at $H_c/D = 20 - 30$. For partially saturated sand, N_{qOU} reaches its maximum value of 25 at $H_c/D = 25 - 30$.

Equations for estimating the maximum oblique pipe force from known horizontal and vertical forces have been proposed (ASCE, 1984) on the basis of recommendations by Nyman (1982) and Meyerhof (1973). The comparisons oblique forces from FE analyses compare favorably with those given by the proposed equations with only a 2 – 5 % difference between them.

8.7 Guidelines for Practice

The FE maximum dimensionless force for lateral, vertical upward/downward, and $\pm 45^\circ$ oblique orientations are combined in a series of graphs for visualizing and for modeling soil-pipeline force for any movement direction under plane strain conditions. The analytical results are normalized with respect to N_{qH} . The dimensionless force ratio, N_q/N_{qH} has a unique value for a given H_c/D and direction of pipe movement, which does not depend on sand density and associated friction angles. The plots of N_q/N_{qH} are asymmetric about the horizontal axis and the plots become symmetric about the horizontal axis, as H_c/D increases. Confining stress effects on

ϕ'_{ps-p} , and therefore, there is a dependency of N_q on the diameter for constant shallow H_c . A correction factor to cover different diameters can be obtained from the treatment of diameter effects for N_{qH} , N_{qVU} , and N_{qVD} .

Finite element results were evaluated to estimate the strain compatible secant modulus, E_α , at peak pipe force for various pipe movement directions. The range of the mobilized soil strength fraction at peak pipe force, α , for lateral, vertical upward/downward, and $\pm 45^\circ$ oblique orientations is provided. As H_c/D increases, the range of α converges to $0.7 \leq \alpha \leq 0.9$ for any pipe movement.

Hyperbolic and bilinear representations of force vs. displacement curves for various pipe movements are provided for simple 1-D numerical analyses. For a problem requiring a high degree of accuracy, the hyperbolic model provides better representations of soil-pipe behavior than the bilinear model. However, the bilinear model provides a quick and easy estimation of force with reasonable accuracy.

8.8 Future Research Directions

The purpose of this research is to evaluate soil-pipeline interaction under 2-D conditions with readily accessible constitutive models. In ABAQUS, the most widely used model for soil behavior is the MC plasticity model. When using the MC model in this work, direct shear strength data for sand were converted to plane strain strength parameters in accordance with the procedure described by Davis (1968), Olson (2009), and O'Rourke (2010). Moreover, strain softening of the soil was represented by applying the model proposed by Anastasopoulos, et al. (2007). To best describe the soil-pipeline interaction with the MC elasto-plastic model, it was

found that a strain compatible modulus is required. The selection of a strain compatible modulus requires an assessment of the fraction of mobilized peak soil strength within the highly stressed soil zone adjacent to the pipe at peak pipe force.

There are alternative models that describe the stress-strain behavior before and after the soil yield. Examples include the hyperbolic stress-strain relationship proposed by Duncan (1980), the hierarchical approach proposed by Desai, et al. (1986), the Nor-Sand model originally developed by Jefferies (1993) and used by Yimsiri, et al. (2004), and the CLoE model described and used by Chambon, et al. (2005). Future research should be focused on applying other models and/or developing a more appropriate model to account for the stress-strain relationship at any level of soil displacement.

Data from centrifuge tests of buried pipeline response to normal fault movement (Abdoun, et al., 2008) show that the measured force associated with vertical downward pipe movement was substantially lower than the maximum force calculated with conventional bearing capacity formulation. Finite element analyses in this work show that the failure threshold force for 2-D vertical downward pipe movement is consistently lower than conventional bearing capacity values. There are no experiments to verify the accuracy of the FE analyses results for vertical downward pipe movement. It would be beneficial for the validation of this model to have experiments similar to those performed by Trautmann and O'Rourke (1983), Turner (2004), and Olson (2009) in the vertical downward direction for pipe movement.

Because there are limited data available for partially saturated sand, only dry strength parameters were considered in this research. In partially saturated sand,

even small changes in grain size characteristics can substantially alter the soil suction and the total stress strength parameters of the sand surrounding the pipe. Moreover, the resistance of partially saturated sand with respect to pipe movement is greater than that of dry sand for equivalent conditions of soil density and vertical stress (Olson, 2009; O'Rourke, 2010). Therefore, to gain a greater understanding of soil-pipe behavior, more experiments and numerical analyses in partially saturated sand conditions are required.

It would be valuable to study the force vs. displacement relationship of pipes in trenches with different geometries and different backfill properties to determine the geometric configuration and backfill material specifications that minimize the force imposed on the pipe under permanent ground deformation. The effects of special measures, such as the use of light weight backfill, flowable fill, and expanded polystyrene, should also be evaluated with FE simulations and full-scale tests to validate and qualify the analytical process.

Additional research on soil-pipeline interaction is needed for clays and silts subject to undrained loading. Full-scale tests and numerical simulations are required to evaluate and design for this type of interaction.

APPENDIX A

STRAIN-COMPATIBLE MODULUS

A.1 Introduction

Implicit in using an elasto-plastic model to predict lateral force vs. displacement at maximum pipe load is the selection of E to be strain compatible with the level of stress in the soil at the peak pipe load. This appendix shows how the secant modulus, E_{sec} , of sand is related to the fraction of the peak soil strength mobilized at maximum lateral pipe force. The results of finite element (FE) analyses are evaluated using the relationship between secant modulus and mobilized peak soil strength.

A.2 Derivation of Secant Modulus Associated with Stress Levels

Duncan and Chang (1970) have shown that the stress-strain curve of sand can be approximated by hyperbola. The proposed hyperbolic equation is

$$\frac{\varepsilon}{(\sigma'_1 - \sigma'_3)} = a + b\varepsilon \quad (\text{A.1})$$

in which σ'_1 and σ'_3 are the major and minor principal stress, ε is the strain, and a and b are defined in Fig. A.1. In the figure, E_i is the initial tangent modulus and $(\sigma'_1 - \sigma'_3)_{\text{ult}}$ is the asymptotic value of the principal stress difference which the stress-strain curve approaches at infinite strain.

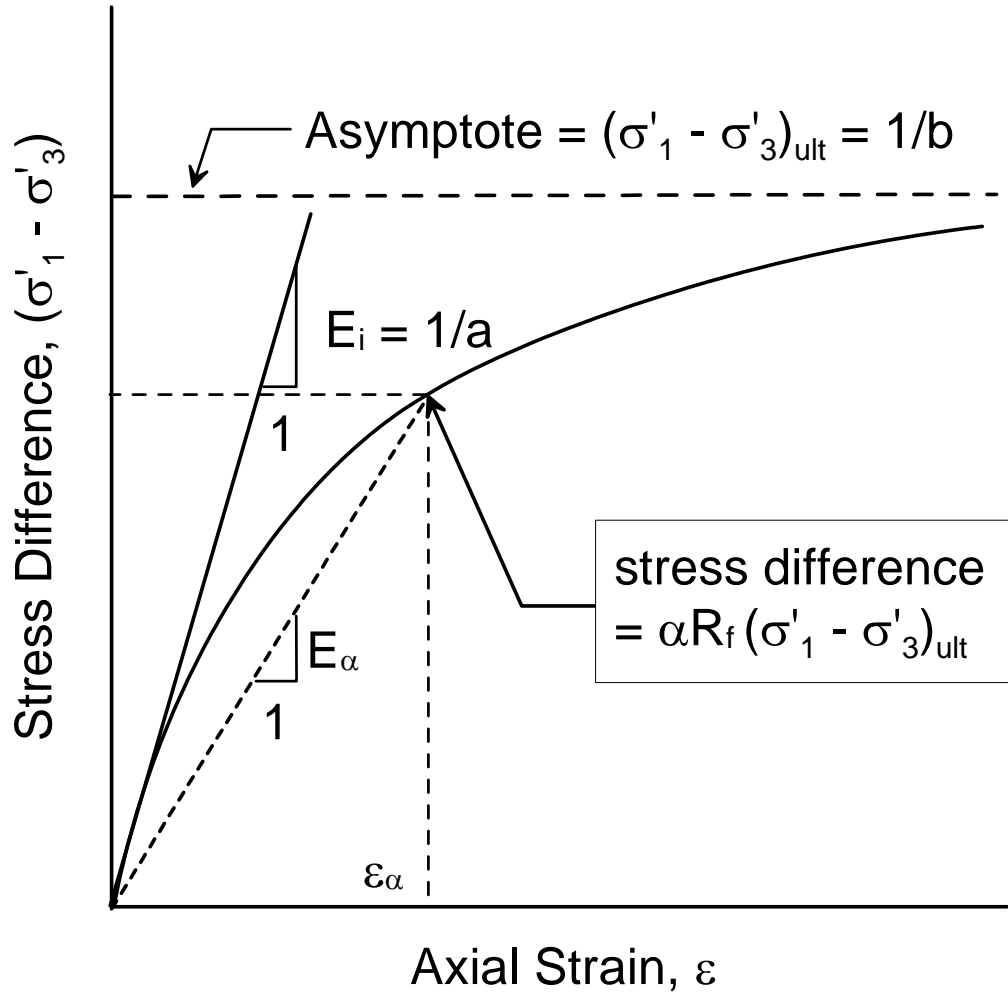


Figure A.1 Hyperbolic Stress-Strain Curve (After Duncan and Chang, 1970)

As shown in Fig. A.1, the hyperbola remains below $(\sigma'_1 - \sigma'_3)_{ult}$ within all finite values of strain. The stress difference at the maximum lateral pipe force, $(\sigma'_1 - \sigma'_3)_f$, is expressed as

$$(\sigma'_1 - \sigma'_3)_f = R_f (\sigma'_1 - \sigma'_3)_{ult} \quad (A.2)$$

in which R_f is a reduction factor. The value of $R_f = 0.9$ reported by Trautmann and O'Rourke (1983) was used in this study.

If α is the fraction of the peak soil strength mobilized at maximum lateral pipe force, Eqn. A.2 can be re-written as

$$\alpha(\sigma'_1 - \sigma'_3)_f = \alpha R_f (\sigma'_1 - \sigma'_3)_{ult} \quad (\text{A.3})$$

$$\alpha(\sigma'_1 - \sigma'_3)_f = \frac{\alpha R_f}{b} \quad (\text{A.4})$$

From Eqns A.1 and A.4, the soil strain related to α , ε_α , is expressed as

$$\frac{b\varepsilon_\alpha}{\alpha R_f} = a + b\varepsilon_\alpha \quad (\text{A.5})$$

$$\varepsilon_\alpha = \frac{a}{b} \frac{\alpha R_f}{(1 - \alpha R_f)} \quad (\text{A.6})$$

Combining the definitions of a and b with Eqn. A.6,

$$\varepsilon_\alpha = \frac{(\sigma'_1 - \sigma'_3)_{ult}}{E_i} \frac{\alpha R_f}{(1 - \alpha R_f)} \quad (\text{A.7})$$

Referring the Fig. A.1, the secant modulus related to α , E_α , is the slope of the straight line from the origin to $(\alpha R_f (\sigma'_1 - \sigma'_3)_{ult}, \varepsilon_\alpha)$, expressed as

$$E_\alpha = \frac{\alpha R_f (\sigma'_1 - \sigma'_3)_{ult}}{\varepsilon_\alpha} \quad (\text{A.8})$$

Combining Eqns A.7 and A.8, results in

$$E_{\alpha} = (1 - \alpha R_f) E_i \quad (\text{A.9})$$

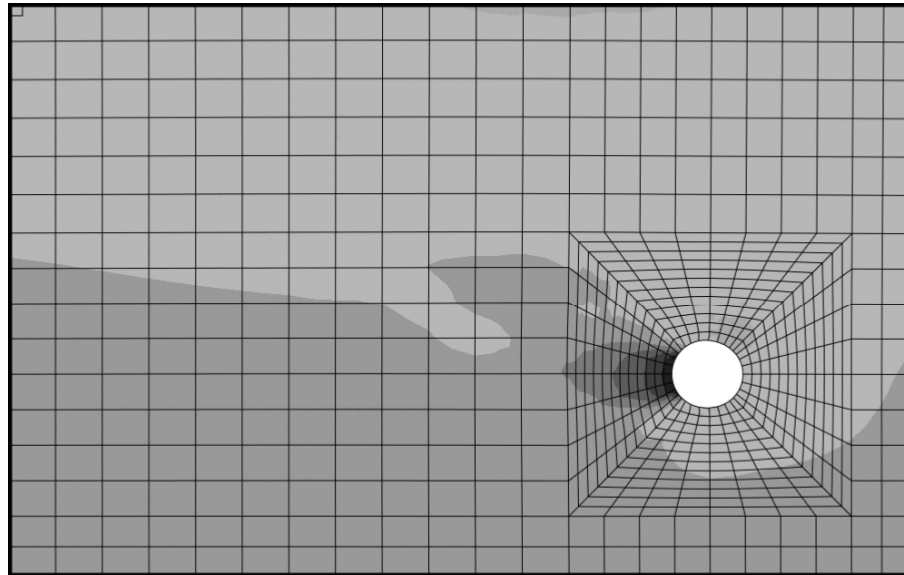
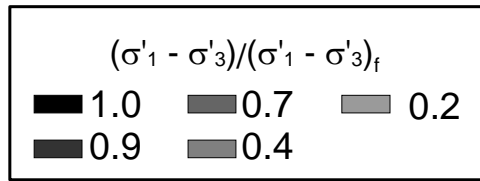
from which the ratio of the strain compatible modulus, E_{α} , mobilized at α , to the initial modulus, E_i , is

$$\frac{E_{\alpha}}{E_i} = (1 - \alpha R_f) \quad (\text{A.10})$$

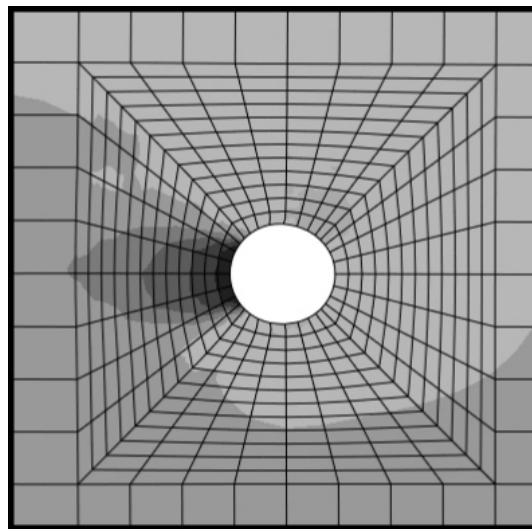
In this way, E_{sec} associated with any percentage of the maximum stress level can be calculated from the initial tangent modulus.

A.3 Relationship Between Secant Modulus and Mobilized Fraction of Soil Strength

Finite element results were evaluated to estimate the relationship between E_i and E_{sec} at maximum pipe load. Figure A.2 shows a typical contour pattern of $(\sigma'_1 - \sigma'_3)/(\sigma'_{1f} - \sigma'_{3f})$ FE analysis at the peak horizontal pipe load in dense RMS graded sand at $H_c/D = 5.5$. As shown in the figure, the highest levels of principal stress difference are within a bulb-shaped zone that extends one to two diameters from the pipe. Each area of $(\sigma'_1 - \sigma'_3)/(\sigma'_{1f} - \sigma'_{3f})$ within the bulb of elevated principal stress difference was measured and the weighted average of $(\sigma'_1 - \sigma'_3)/(\sigma'_{1f} - \sigma'_{3f})$, α , around the pipe was calculated by the following equation:



a) Entire Mesh
 $H_c/D = 5.5$, Dense Sand



b) Mesh Adjacent to Pipe

Figure A.2 Contour of $(\sigma'_1 - \sigma'_3)/(\sigma'_1 - \sigma'_3)_f$ for Dense CU Filter Sand at Maximum Pipe Load

$$\alpha = \frac{\sum_n \left\{ \left[\frac{(\sigma'_1 - \sigma'_3)}{(\sigma'_1 - \sigma'_3)_f} \right]_n a_n \right\}}{\sum_n a_n} \quad (\text{A.11})$$

in which a_n is the area of each $[(\sigma'_1 - \sigma'_3)/(\sigma'_1 - \sigma'_3)_f]_n$.

Using the relationship proposed by Janbu (1963) between E_i , and minor principal effective stress, σ'_3 , as $E_i = K p_a (\sigma'_3/p_a)^n$, Duncan and Chang (1970) and Wong and Duncan (1974) summarized K and n -values obtained from triaxial tests on sand, and reported mid-range values of K and n equal to 800 and 0.55 for dense sand. The vertical effective stress at the center of the pipe, σ'_{vc} , was used as a proxy for σ'_3 , and the highly stressed zones at one and two pipe diameters from the pipe were used to perform two separate calculations of α with Eqn. A.11, from which lower and upper bound values of E_α were obtained. The range of α for dense sand at $H_c/D = 5.5$ is 0.83 – 0.95, corresponding to $E_\alpha = 3200 - 5600$ kPa, which was calculated with Eqn A.9 and the Janbu expression for E_i above.

Figure A.3 shows the histogram of the moduli back-calculated for $H_c/D = 5.5$ in dense sand (see Chapter 3) from the data obtained with 9 large-scale tests (Turner, 2004; Olson, 2009). Lower and upper bound values of E_α are also shown on the figure. The back-calculated moduli were determined by the K_{70} -procedure discussed in Section 3.6. The mean value of E_{70-H} from 9 large-scale tests is 3200 kPa and the standard deviation is 480 kPa whereas the lower and upper bound values of E_α are 3200 kPa and 5600 kPa, respectively. The lower bound value of E_α is consistent with the experimentally determined values. Similar assessments were performed for

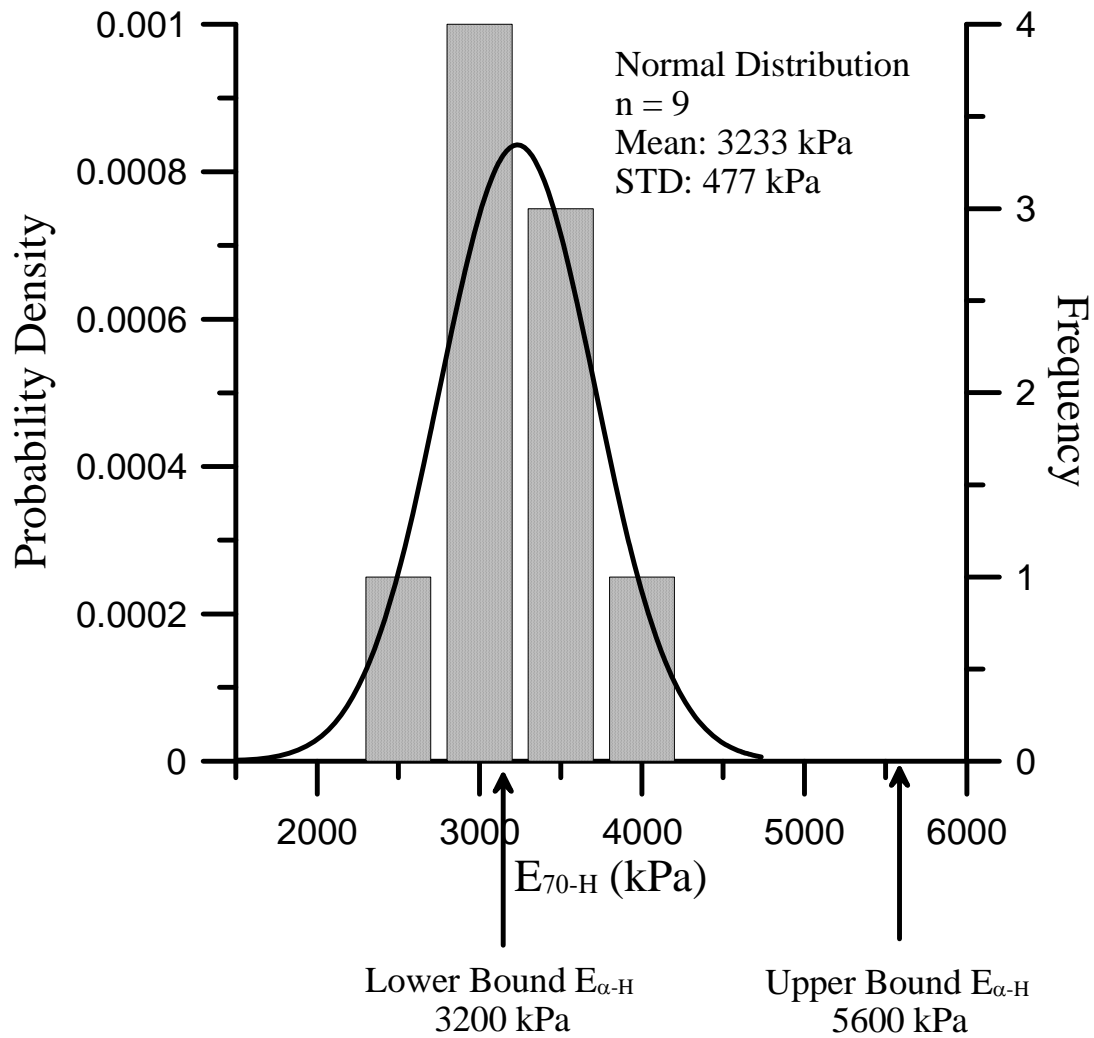


Figure A.3 Histogram of $E_{\alpha-H}$ from Turner (2004) and Olson (2009) Test and the Lower and Upper Bound of Computed $E_{\alpha-H}$

medium CU filter sand at $H_c/D = 3.5, 8,$ and 11 to compare E_α and the back-calculated moduli from the large-scale test data (Trautmann and O'Rourke, 1983). Table A.1 summarizes the results for medium CU filter sand at $H_c/D = 3.5, 8,$ and 11 . Similar to the results for dense sand, the lower bound value of E_α is consistent with the experimentally determined values for all cases.

Table A.1 Summary of $E_{\alpha-H}$ for Medium Sand at Various H_c/D

Hc/D	$E_{\alpha-H}$ (kPa)		E_{70-H} (kPa)
	Lower Bound	Upper Bound	
3.5	1300	2100	1300
8	2200	4200	2400
11	2800	5000	3100

A.4 Mobilized Soil Strength Fraction for Horizontal, Vertical Upward, and Vertical Downward Pipe Movement

The procedure for evaluating the mobilized soil strength fraction at peak force, described in the previous section, was applied systematically to FE results for horizontal pipe movement in medium, dense, and very dense sands at H_c/D from 3.5 to 11. Generalizing from the results of all analyses, it appears that $0.9 \leq \alpha \leq 0.95$ for horizontal pipe movement.

A similar assessment procedure was performed for vertical upward and downward pipe movement in sand, and the combined results are summarized in Table A.2. For vertical upward pipe movement, a range of α from FE results was used to estimate the strain compatible $E_{\alpha-VU}$ at peak pipe force. This $E_{\alpha-VU}$ was compared with the E_{70-VU} back-calculated from matching FE and measured force vs. displacement relationships to further narrow and refine the range of α in Table A.2. For vertical downward movement, a range of α from FE results for deep foundations was used to estimate the strain compatible $E_{\alpha-VD}$ at peak pipe force. The peak vertical downward force associated with $E_{\alpha-VD}$ at the midrange of estimated moduli was compared with the theoretical bearing capacity force calculated for rigidity factors

representing upper and lower bounds on $E_{\alpha\text{-VD}}$. The resulting favorable comparison, discussed in Chapter 6, confirms that the ranges of α for vertical downward pipe movement in Table A.2 are consistent with widely used bearing capacity formulations. As described in Chapter 7, the range of α for lateral and vertical upward pipe movement converges to that for vertical downward pipe movement in deep embedment condition.

Table A.2 Summary of Mobilized Soil Strength Fraction at Peak Pipe Force, α

Relative Pipe-Soil Movement	Mobilized Soil Strength Fraction, α
Lateral	$0.9 \leq \alpha \leq 0.95$
Vertical Upward	$0.91 \leq \alpha \leq 0.98$
Vertical Downward	$0.7 \leq \alpha \leq 0.9$

APPENDIX B

THEORETICAL BACKGROUND OF INFINITE ELEMENTS

B.1 Introduction

Finite element (FE) analyses were run with a semi-infinite soil medium using ‘infinite element’ as described in Chapter 4. This appendix reviews the theoretical background of the infinite element, and its content is consistent with the theoretical basis provided by Zienkiewicz et al. (1983).

B.2 Theoretical Background of Infinite Element

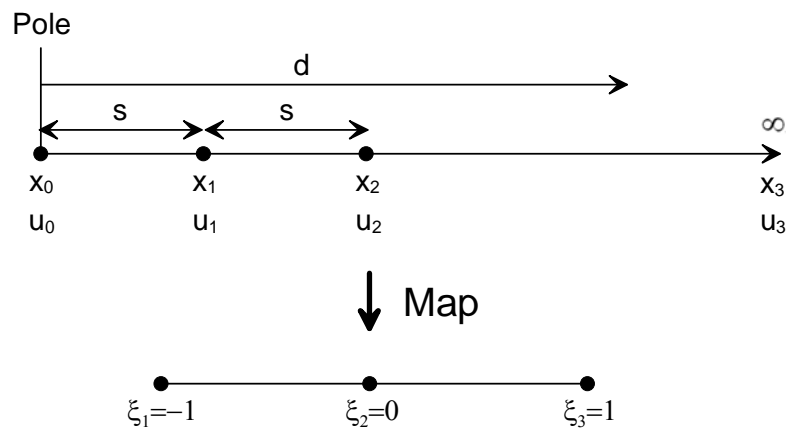


Figure B.1 Mapped Infinite Element for 1-D Element

The brief concept of the mapped infinite element can be explained by considering a simple one dimensional element as shown in Fig. B.1. It is assumed that the solution at infinity is linear and is based on displacement component u_i with respect to distance d measured from a pole, x_0 . The displacement component at the

far field converges to 0 as d grows to infinity, and the displacement component at the pole increases to infinity as d converges to 0. Consider an infinite element from node x_1 to x_2 and extending from x_2 to x_3 . The node x_1 lies at the interface between the finite and infinite element, and apart from the pole with distance $d = s$. The distance from the pole to the node x_2 is $2l_p$ and x_3 lies at infinity. This element is now mapped on to a finite domain $-1 \leq \xi \leq 1$, as illustrated in Fig. B.1. The mapping function chosen by Zienkiewicz et al. (1983) is

$$x = N_0(\xi)x_0 + N_2(\xi)x_2 \quad (\text{B.1})$$

where

$$N_0(\xi) = \frac{-\xi}{1-\xi} \quad \text{and} \quad N_2(\xi) = \frac{1}{1-\xi} \quad (\text{B.2})$$

An important condition of choosing the shape function $N_0(\xi)$ and $N_2(\xi)$ is that

$$N_0(\xi) + N_2(\xi) = 1 \quad (\text{B.3})$$

It is essential that the mapping should be independent of any change in the origin of the co-ordinate system (Zienkiewicz et al., 1983). Therefore, any shift of node in the origin by Δx results in the new co-ordinates as

$$\begin{aligned} x^N_0 &= x_0 + \Delta x \\ x^N_2 &= x_2 + \Delta x \end{aligned} \quad (\text{B.4})$$

For any chosen ξ , it is necessary that

$$x^N = x + \Delta x \quad (\text{B.5})$$

Combining Eqn. B.4 and Eqn. B.5 with Eqn. B.1 gives

$$x + \Delta x = N_0(\xi)(x_0 + \Delta x) + N_2(\xi)(x_2 + \Delta x) \quad (\text{B.6})$$

resulting in

$$\Delta x = (N_0(\xi) + N_2(\xi))\Delta x \quad (\text{B.7})$$

Equation B.7 is satisfied only if Eqn. B.3 is true. Thus, the relationship between the shape function $N_0(\xi)$ and $N_2(\xi)$ shown in Eqn. B.3 is required, so that the mapping is not affected by any shift of the node.

Using the Eqn. B.1, the corresponding ξ_i are

$$\begin{aligned} \xi_1 = -1 &\rightarrow x = \frac{x_0}{2} + \frac{x_0}{2} = x_1 \\ \xi_2 = 0 &\rightarrow x = x_2 \\ \xi_3 = 1 &\rightarrow x = \frac{-\xi}{1-\xi}x_0 + \frac{1}{1-\xi}x_2 = \infty = x_3 \end{aligned} \quad (\text{B.8})$$

The node x_1 can be any point between the nodes x_0 and x_2 . The expression for node x_1 can be written as

$$x_1 = cx_2 + (1-c)x_0 \quad (\text{B.9})$$

Usually, c in Eqn. B.9 is taken as 0.5, so that x_1 is defined at the center of x_0 and x_2 .

Using the mapping function described above, an unknown function F_u in the mapped domain can be expressed with ξ . F_u can be approximated with a standard polynomial function as follows

$$F_u = a_0 + a_1\xi + a_2\xi^2 + a_3\xi^3 + \dots \quad (\text{B.10})$$

Solving Eqn. B.1, ξ can be expressed as

$$\xi = \frac{x - x_2}{x - x_0} = 1 - \frac{x_2 - x_0}{x - x_0} \quad (\text{B.11})$$

From Eqn. B.9 and for $c = 0.5$,

$$x_1 - x_0 = x_2 - x_1 = s \quad (\text{B.12})$$

The relationship between x_0 , x_1 , and x_2 expressed in Eqn. B.12 is illustrated in Fig. B.1.

If we let $d = x - x_0$ as shown in Fig. B.1, Eqn. B.11 can be re-written as

$$\xi = 1 - \frac{2s}{d} \quad (\text{B.13})$$

The displacement component u can be expressed as

$$u = \frac{1}{2} \xi(\xi - 1)u_1 + (1 - \xi^2)u_2 \quad (\text{B.14})$$

Please note that Eqn. B.14 gives $u = 0$ at $\xi = 1$, where d approaches to infinity. Combine Eqn. B.13 and Eqn. B.14 gives

$$u = (-u_1 + 4u_2)\frac{s}{d} + (2u_1 - 4u_2)\left(\frac{s}{d}\right)^2 \quad (\text{B.15})$$

which includes $\frac{1}{d}$ and $\frac{1}{d^2}$ behavior. Similarly, $\frac{1}{d^3}$ behavior can be included by cubic interpolation of the displacement component, u , with respect to ξ , and can be expressed as

$$u = -\frac{1}{3} \xi(\xi - 1)\left(\xi - \frac{1}{2}\right)u_1 - 2(1 - \xi^2)\left(\xi - \frac{1}{2}\right)u_2 + \frac{8}{3} \xi(1 - \xi^2)u_3 \quad (\text{B.16})$$

Combining Eqn. B.13 and Eqn. B.16 gives

$$u = \left(-\frac{1}{3}u_1 - 4u_2 + \frac{32}{3}u_3\right)\frac{s}{d} + (-2u_1 + 20u_2 - 32u_3)\left(\frac{s}{d}\right)^2 + \left(\frac{8}{3}u_1 - 16u_2 + \frac{64}{3}u_3\right)\left(\frac{s}{d}\right)^3 \quad (\text{B.17})$$

The mapped infinite element for the 2-D element is an extension of the method described above. The mapping function is derived from those for 1-D conditions in the ξ direction, taken to be the infinite direction, and the standard

Lagrange shape function in the η direction (Zienkiewicz et al., 1983). Figure B.2 shows the mapped infinite element for 2-D element. The infinite direction maps to the local ξ direction. In the figure, x is expressed as

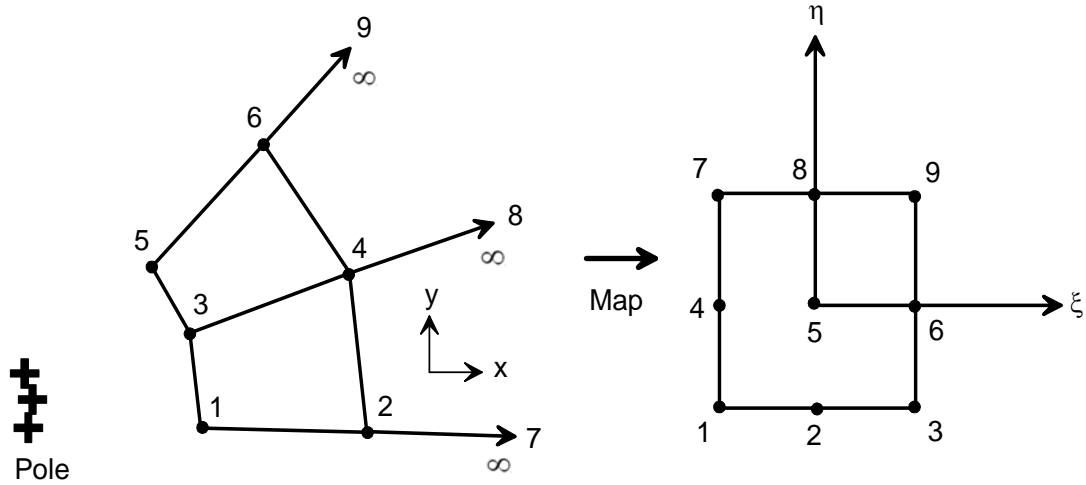


Figure B.2 Mapped Infinite Element for 2-D Element (Zienkiewicz et al., 1983)

$$\begin{aligned}
 x = & N_1(\eta)[(2x_1 - x_2)N_0(\xi) + x_2N_2(\xi)] \\
 & + N_2(\eta)[(2x_3 - x_4)N_0(\xi) + x_4N_2(\xi)] \\
 & + N_3(\eta)[(2x_5 - x_6)N_0(\xi) + x_6N_2(\xi)]
 \end{aligned} \tag{B.18}$$

where $N_i(\eta)$ are standard quadratic Lagrange shape function. Similarly, y is expressed as

$$\begin{aligned}
 y = & N_1(\eta)[(2y_1 - y_2)N_0(\xi) + y_2N_2(\xi)] \\
 & + N_2(\eta)[(2y_3 - y_4)N_0(\xi) + y_4N_2(\xi)] \\
 & + N_3(\eta)[(2y_5 - y_6)N_0(\xi) + y_6N_2(\xi)]
 \end{aligned} \tag{B.19}$$

APPENDIX C

CONVENTIONAL BEARING CAPACITY CALCULATIONS

C.1 Introduction

This appendix presents conventional bearing capacity formulations to predict the bearing capacity load associated with deep foundation surfaces for the same dimensions and soil conditions used in the finite element (FE) analyses for vertical downward pipe movement, discussed in Chapter 6. The maximum tip resistance forces from conventional bearing capacity formulations are calculated and summarized for medium, dense, and very dense sand as characterized in Table 3.2 for $H_c/D = 8, 11, 15, 20,$ and 30 .

C.2 Bearing Capacity for Deep Foundations

The maximum tip resistance of a deep foundation, Q_{tc} , is calculated as

$$Q_{tc} = q_{ult} A_{tip} \quad (C.1)$$

in which q_{ult} = the maximum bearing capacity at the tip, and A_{tip} = area of the base of the foundation. Kulhawy et al. (1983) have shown that, for drained conditions with $H_c/D \geq 5$, q_{ult} can be estimated as

$$q_{ult} = q N_q \xi_{qr} \xi_{qs} \xi_{qd} \quad (C.2)$$

in which q = vertical effective stress at H_c , N_q = bearing capacity factor, ξ_{qr} = rigidity factor, ξ_{qs} = shape factor, and ξ_{qd} = depth factor.

The bearing capacity factor, N_q , is calculated as

$$N_q = \exp(\pi \tan \phi') \tan^2 \left(45^\circ + \frac{\phi'}{2} \right) \quad (C.3)$$

in which ϕ' = effective angle of friction for the soil.

The rigidity factor, ξ_{qr} , is calculated as

$$\xi_{qr} = \exp \left\{ \left[\left(-4.4 + 0.6 \frac{B}{L} \right) \tan \phi' \right] + \left[(3.07 \sin \phi') \frac{(\log_{10} 2I_r)}{(1 + \sin \phi')} \right] \right\} \quad (C.4)$$

in which B = foundation width, L = foundation length, and I_r = rigidity index, which is defined as

$$I_r = \frac{G}{c + q \tan \phi'} \quad (C.5)$$

in which G = shear modulus of soil and q is evaluated at a depth of $\frac{B}{2}$ below the foundation.

The shear modulus is computed from the elastic modulus, E , and Poisson's ratio, ν , by the following:

$$G = \frac{E}{2(1 + \nu)} \quad (\text{C.6})$$

As discussed in Appendix A, the following equation is used to approximate E as

$$\frac{E}{E_i} = (1 - \alpha R_f) \quad (\text{C.7})$$

in which α = fraction of the peak soil strength mobilized at maximum downward force, R_f = reduction factor. Initial tangent modulus, E_i , is approximated by the relationship proposed by Janbu (1963) expressed as

$$E_i = K p_a \left(\frac{\sigma'_3}{p_a} \right)^n \quad (\text{C.8})$$

in which K = constant, σ'_3 = minor principal effective stress, and n = exponent determining the rate of variation of E_i with σ'_3 . The vertical effective stress at the center of the pipe, σ'_{vc} , is used as a proxy for σ'_3 .

The depth factor, ξ_{qd} , is calculated as

$$\xi_{qd} = 1 + 2 \tan \phi' (1 - \sin \phi')^2 \tan^{-1} \left(\frac{H_c}{B} \right) \quad (\text{C.9})$$

in which H_c is a depth from the top of the soil to the center of the pipe and \tan^{-1} terms are expressed in radians.

In this work, $\nu = 0.3$, $c = 0$, and $\xi_{qs} = 1$ were used. To account for uncertainty in the estimation of E , a range of $0.7 < \alpha < 0.9$ was used from the procedure discussed in Appendix A to determine upper and lower bound E_s . Values of N_q , I_r , ξ_{qr} , and ξ_{qd} for $H_c/D = 8, 11, 15, 20,$ and 30 are summarized in Table C.1.

Table C.1 Summarized Bearing Capacity Factors

H _c /D	γ _d (kN/m ³)	φ' _{ps-p} (degrees)	N _q	I _r		ξ _{gr}		ξ _{qd}
				Lower Bound	Upper Bound	Lower Bound	Upper Bound	
8 Medium	16.4	43.6	108.9	66.0	230.5	0.22	0.43	1.27
11 Medium	16.4	43.5	106.8	61.2	200.6	0.21	0.40	1.27
15 Medium	16.4	43.4	104.8	56.7	174.6	0.20	0.38	1.28
20 Medium	16.4	43.3	103.2	52.6	153.0	0.20	0.35	1.28
30 Medium	16.4	43.1	101.0	47.2	126.6	0.19	0.32	1.29
8 Dense	17.1	46.1	161.3	101.8	310.5	0.20	0.37	1.23
11 Dense	17.1	45.9	155.1	91.9	271.4	0.20	0.36	1.24
15 Dense	17.1	45.6	149.6	82.8	236.9	0.19	0.34	1.25
20 Dense	17.1	45.4	144.9	74.9	208.3	0.18	0.33	1.26
30 Dense	17.1	45.2	138.8	64.8	173.1	0.18	0.30	1.26
8 Very Dense	17.7	48.2	229.3	145.7	421.0	0.19	0.34	1.21
11 Very Dense	17.7	47.9	216.6	127.8	357.5	0.18	0.32	1.22
15 Very Dense	17.7	47.5	205.5	111.9	303.5	0.17	0.31	1.23
20 Very Dense	17.7	47.3	196.1	98.6	259.9	0.17	0.29	1.23
30 Very Dense	17.7	46.9	184.4	82.2	208.1	0.16	0.27	1.24

APPENDIX D

DATABASE FOR LOAD TESTS ON DEEP FOUNDATIONS UNDER AXIAL COMPRESSION

D.1 Introduction

This appendix presents information about 14 case histories of field axial compression load tests performed on deep foundations, including piles and drilled shafts. The data show the relationship between vertical force and settlement of the pile and drilled shaft foundation tips. Thus, the data do not include the effects of frictional resistance between the deep foundation and surrounding soil. Table D.1 provides a list of the case number, reference, test location, soil condition, the settlements at the end of the initial linear range, ρ_{L1} , and the settlement at the beginning of final linear range, ρ_{L2} . All the deep foundations were circular in transverse cross-section. The load vs. settlement data for each test was interpreted according to the description in Section 6.2. ρ_{L1} and ρ_{L2} are expressed in the table as a fraction and multiple, respectively, of the diameter, D . Brief description of the test, including soil and ground water condition are provided under the sections that follow. Plots of vertical load vs settlement are presented with ρ_{L1} and ρ_{L2} .

Table D.1 Database for Load Tests on a Deep Foundation under Axial Compression

Case	Reference	Test Location	Soil Condition	ρ_{L1} (%) ¹	ρ_{L2} (%) ²
1	Ismael and Klym, 1979	Walkerton, Ontario, Canada	Sand over clay silt	0.15 D ³	4.4 D
2	Touma and Reese, 1974	Live Oak County, TX	Sand and clay silt	0.22 D	7.85 D
3G1	Reese and Touma, 1972	Houston, TX	Silt and sand	0.16 D	5.99 D
3G2	Reese and Touma, 1972	Houston, TX	Silt and sand	0.15 D	5.79 D
4P1	Aurora and Feese, 1977	Near Austin, TX	Sand and gravel over shale	0.34 D	7.33 D
4P2	Aurora and Feese, 1977	Near Austin, TX	Sand and gravel over shale	0.30 D	6.42 D
4P3	Aurora and Feese, 1977	Near Austin, TX	Sand and gravel over shale	0.23 D	6.56 D
4P4	Aurora and Feese, 1977	Near Austin, TX	Sand and gravel over shale	0.25 D	4.07 D
4P5	Aurora and Feese, 1977	Near Austin, TX	Sand and gravel over shale	0.28 D	5.56 D
5	Bustamante and Gianceselli, 1980	France	Sand and gravel over limestone	0.11 D	4.80 D
6A	Gregersen, Aas, and Dibiagio, 1973	Near Drammen, Norway	Uniform loose normally consolidated sand	0.18 D	5.39 D
6D	Gregersen, Aas, and Dibiagio, 1973	Near Drammen, Norway	Uniform loose normally consolidated sand	0.22 D	6.08 D
7C1	Ackley and Sanders, 1979	Not reported	Gravels over shale	0.20 D	6.75 D
7C4	Ackley and Sanders, 1979	Not reported	Gravels over shale	0.32 D	6.17 D

1. ρ_{L1} : the settlements at the end of the initial linear range; 2. ρ_{L2} : the settlement at the beginning of final linear range; 3. D: diameter

D.2 Case 1

Case 1 pertains to a load test reported by Ismael and Klym (1979). The concrete drilled shaft foundation was 6.4 m (21 ft) in length and 1067 mm (42 in) in width. The test was performed in sand over clay silt in Walkerton, Ontario, Canada. Ground water was encountered at 0.6 m (2 ft) below the surface. From the force vs. settlement plot, a ρ_{L1} value of 0.15 D % and a ρ_{L2} of 4.4 D % were obtained.

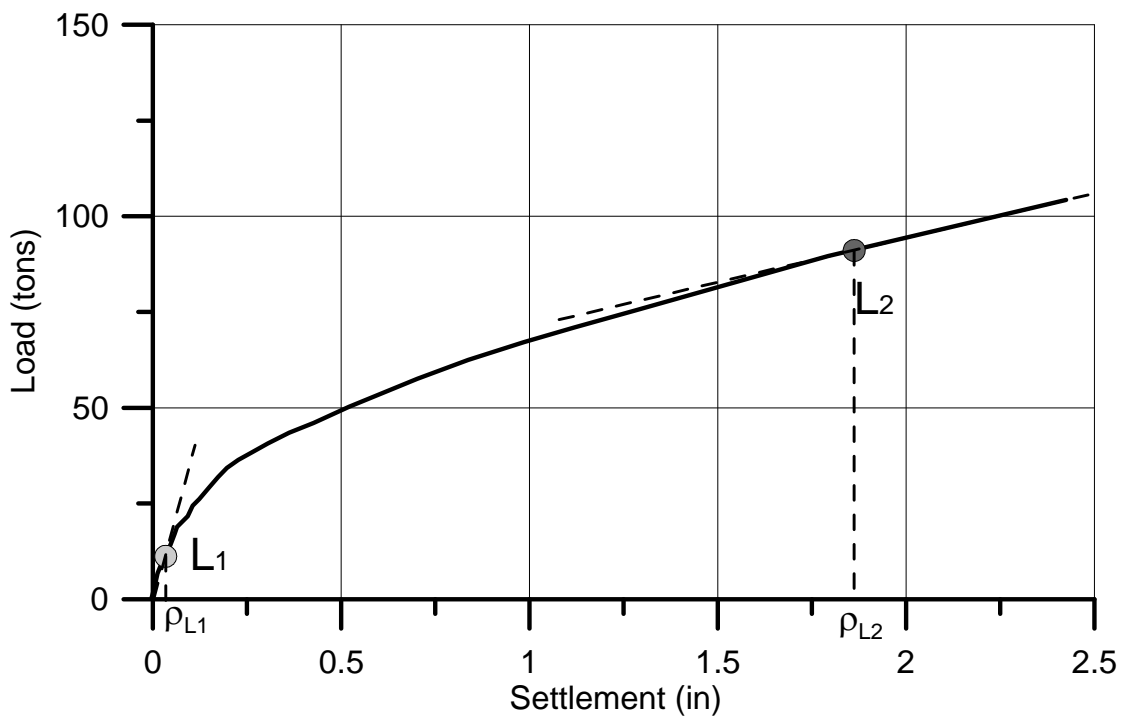


Figure D.1 Case 1

D.3 Case 2

Case 2 pertains to a load test reported by Touma and Reese (1974). The drilled shaft foundation was 10.1 m (33 ft) in length and 762 mm (30 in) in width. The test was performed in sand and clay silt in Live Oak County, Texas. Ground water was not reported. From the force vs. settlement plot, a ρ_{L1} value of 0.22 D % and a ρ_{L2} of 7.85 D % were obtained.

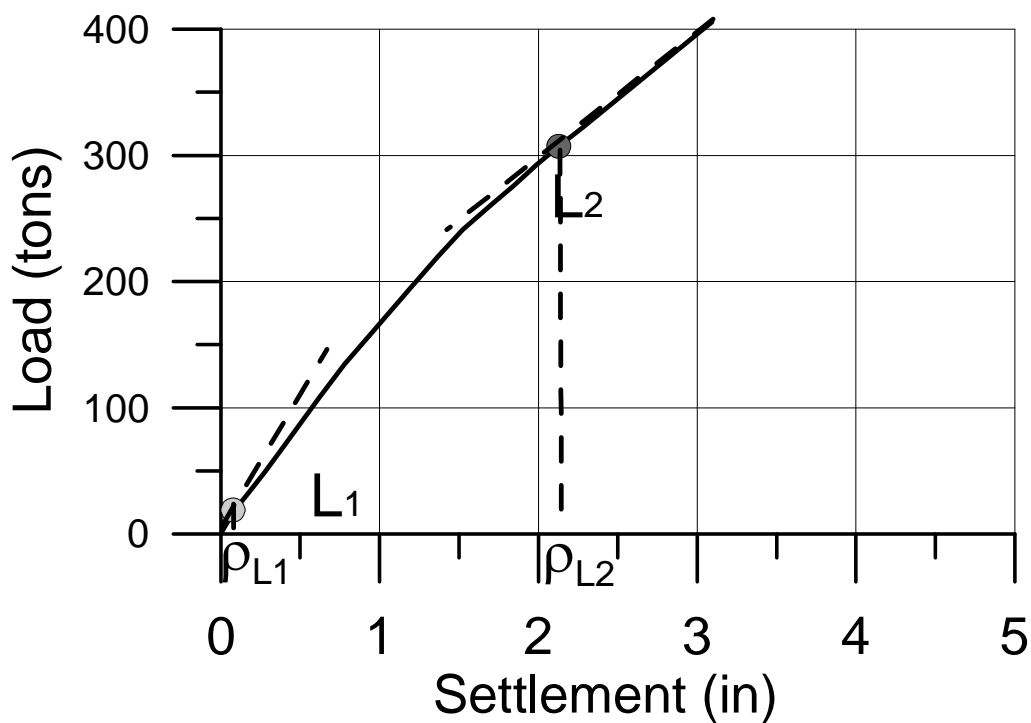


Figure D.2 Case 2

D.4 Case 3G1

Case 3G1 pertains to a load test reported by Reese and Touma (1972). The concrete drilled shaft foundation was 18.7 m (61.5 ft) in length and 935 mm (36.8 in) in width. The test was performed in silt and sand in Houston, Texas. Ground water was encountered at 4.9 m (16 ft) to 9.1 m (30 ft) below the surface. From the force vs. settlement plot, a ρ_{L1} value of 0.16 D % and a ρ_{L2} of 5.99 D % were obtained.

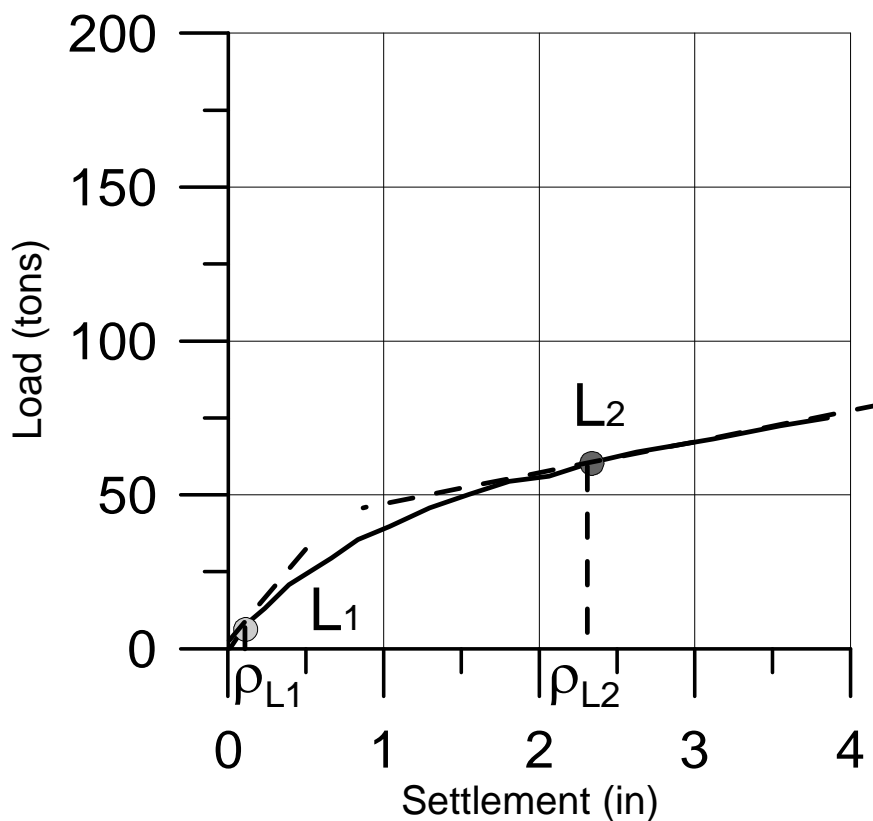


Figure D.3 Case 3G1

D.5 Case 3G2

Case 3G2 pertains to a load test reported by Reese and Touma (1972). The concrete drilled shaft foundation was 24.0 m (78.8 ft) in length and 790 mm (31.1 in) in width. The test was performed in silt and sand in Houston, Texas. Ground water was encountered at 4.9 m (16 ft) to 9.1 m (30 ft) below the surface. From the force vs. settlement plot, a ρ_{L1} value of 0.15 D % and a ρ_{L2} of 5.79 D % were obtained.

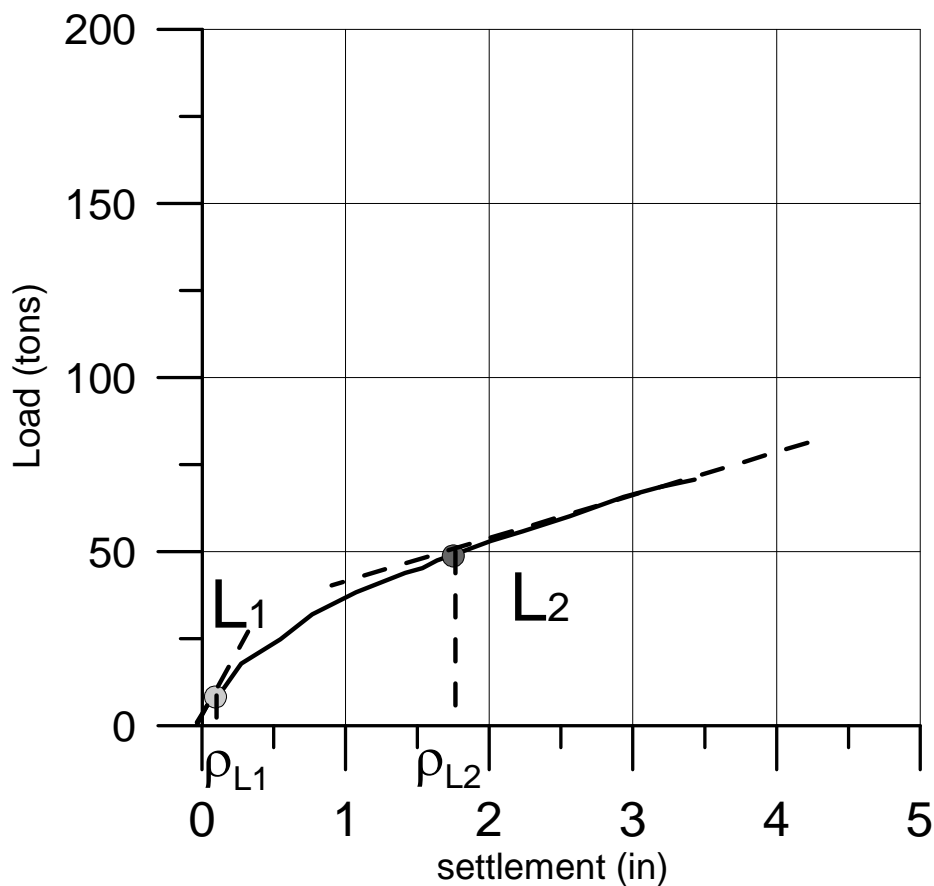


Figure D.4 Case 3G2

D.6 Case 4P1

Case 4P1 pertains to a load test reported by Aurora and Feese (1977). The drilled shaft foundation was 10.2 m in length and 880 mm in width. The test was performed in sand and gravel over shale near Austin, Texas. Ground water was encountered at 2 m below the surface. From the force vs. settlement plot, a ρ_{L1} value of 0.34 D % and a ρ_{L2} of 7.33 D % were obtained.

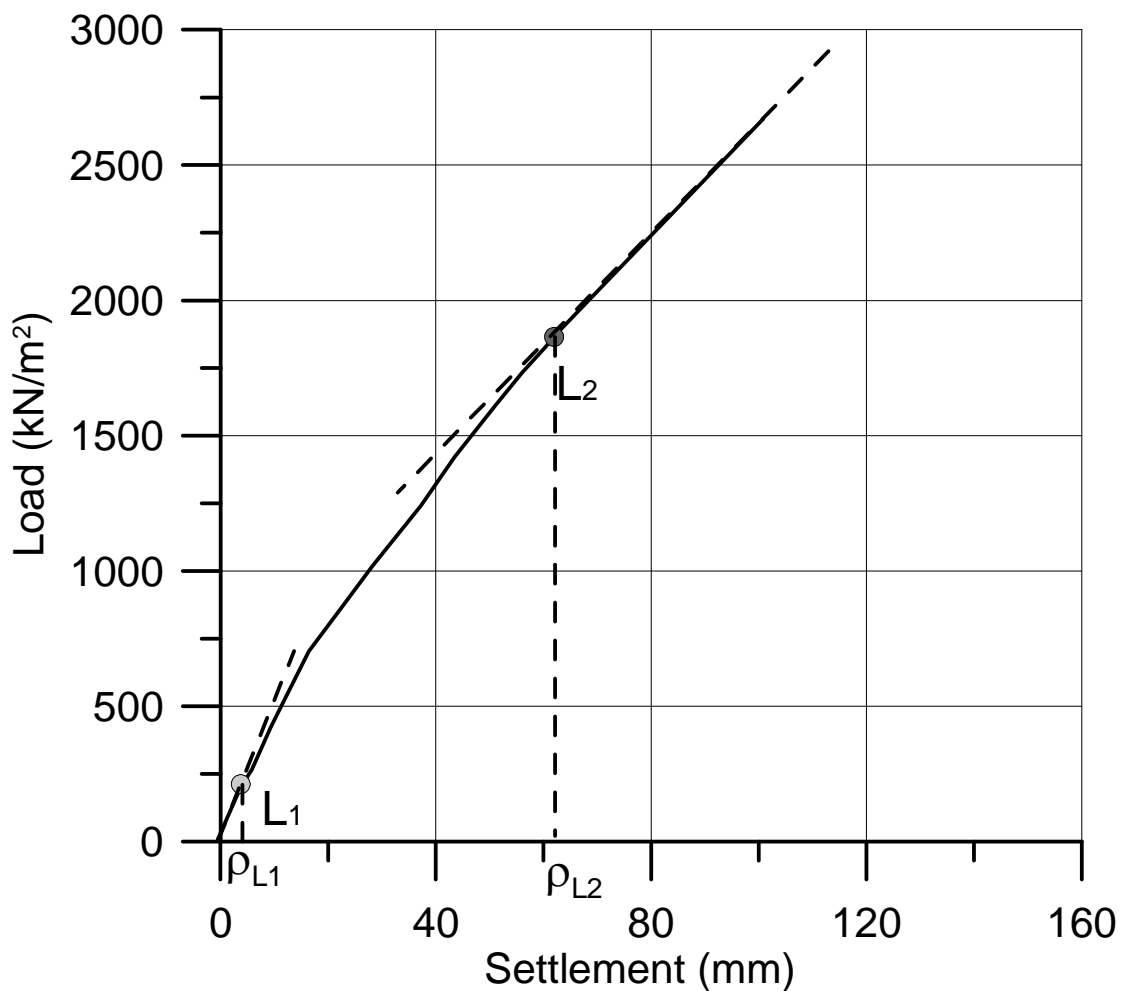


Figure D.5 Case 4P1

D.7 Case 4P2

Case 4P2 pertains to a load test reported by Aurora and Feese (1977). The drilled shaft foundation was 12.9 m in length and 1290 mm in width. The test was performed in sand and gravel over shale near Austin, Texas. Ground water was encountered at 2 m below the surface. From the force vs. settlement plot, a ρ_{L1} value of 0.30 D % and a ρ_{L2} of 6.42 D % were obtained.

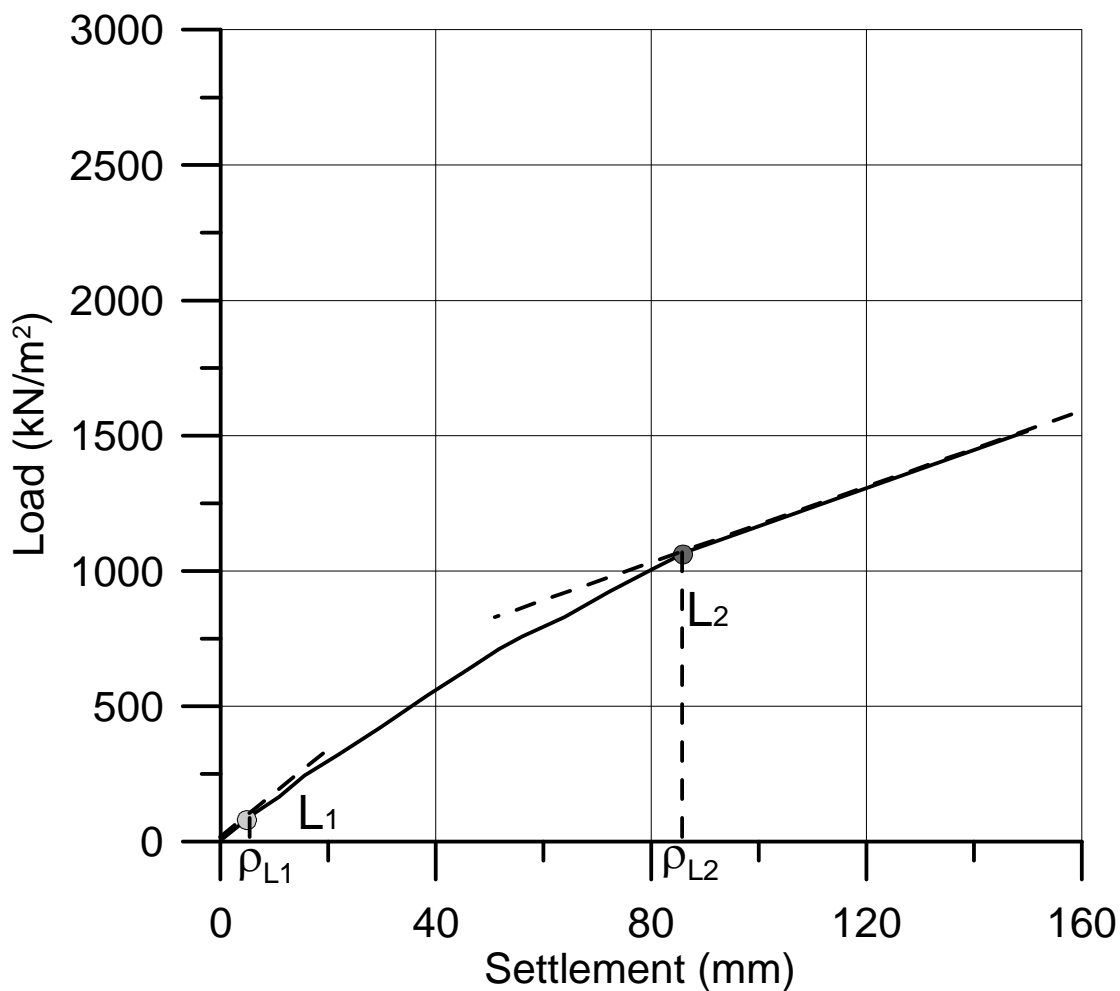


Figure D.6 Case 4P2

D.8 Case 4P3

Case 4P3 pertains to a load test reported by Aurora and Feese (1977). The drilled shaft foundation was 13.0 m in length and 1300 mm in width. The test was performed in sand and gravel over shale near Austin, Texas. Ground water was encountered at 2 m below the surface. From the force vs. settlement plot, a ρ_{L1} value of 0.23 D % and a ρ_{L2} of 6.56 D % were obtained.

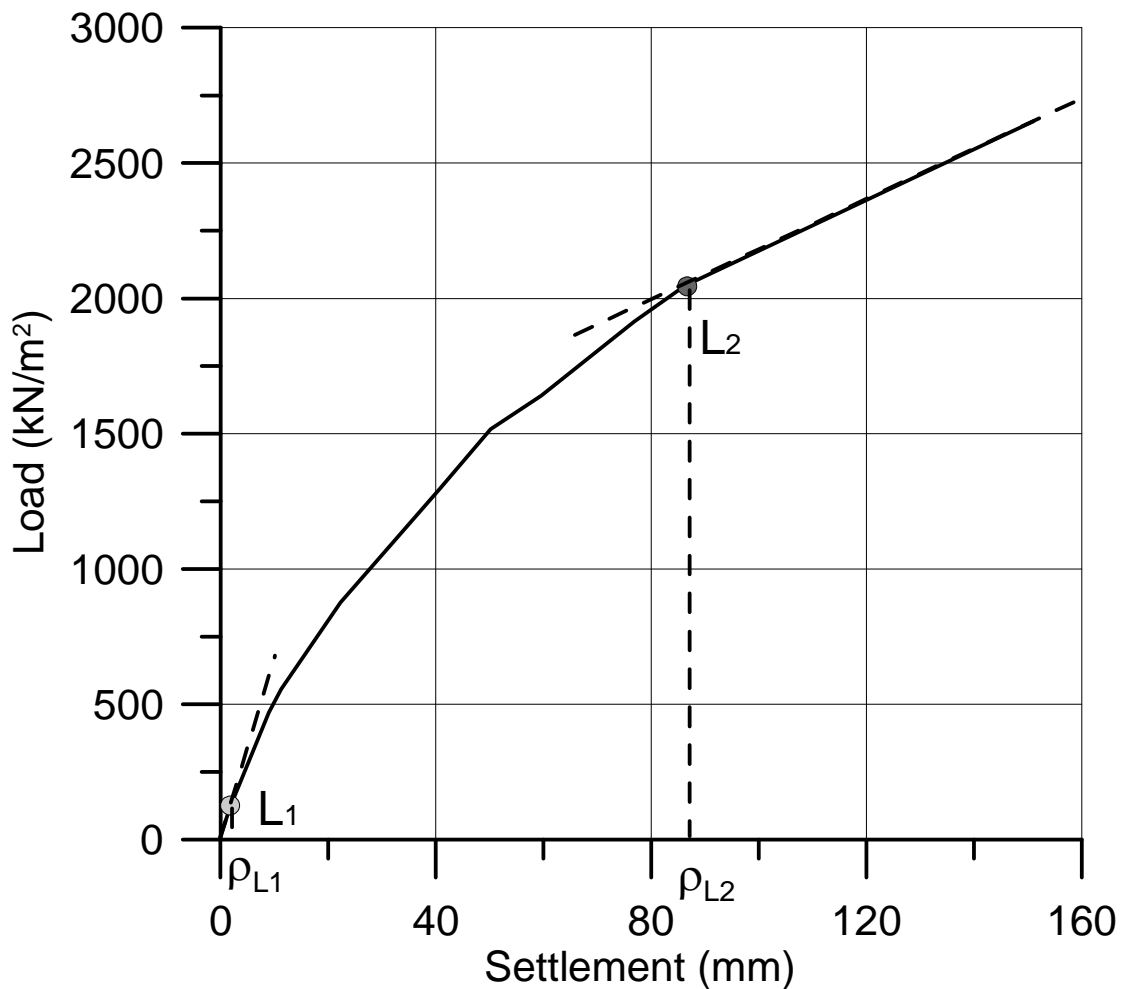


Figure D.7 Case 4P3

D.9 Case 4P4

Case 4P4 pertains to a load test reported by Aurora and Feese (1977). The drilled shaft foundation was 9.95 m in length and 1810 mm in width. The test was performed in sand and gravel over shale near Austin, Texas. Ground water was encountered at 2 m below the surface. From the force vs. settlement plot, a ρ_{L1} value of 0.25 D % and a ρ_{L2} of 4.07 D % were obtained.

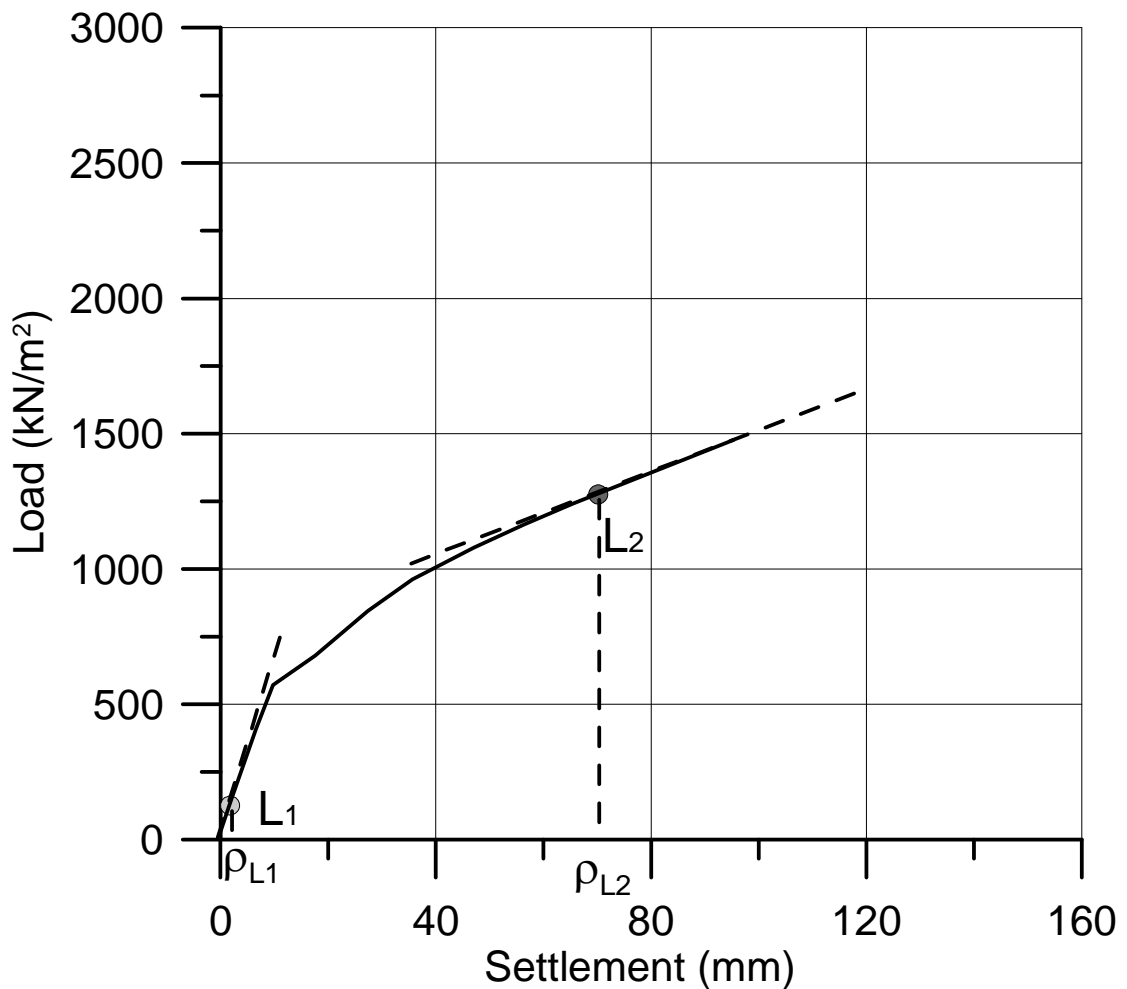


Figure D.8 Case 4P4

D.10 Case 4P5

Case 4P5 pertains to a load test reported by Aurora and Feese (1977). The drilled shaft foundation was 10.0 m in length and 1800 mm in width. The test was performed in sand and gravel over shale near Austin, Texas. Ground water was encountered at 2 m below the surface. From the force vs. settlement plot, a ρ_{L1} value of 0.28 D % and a ρ_{L2} of 5.56 D % were obtained.

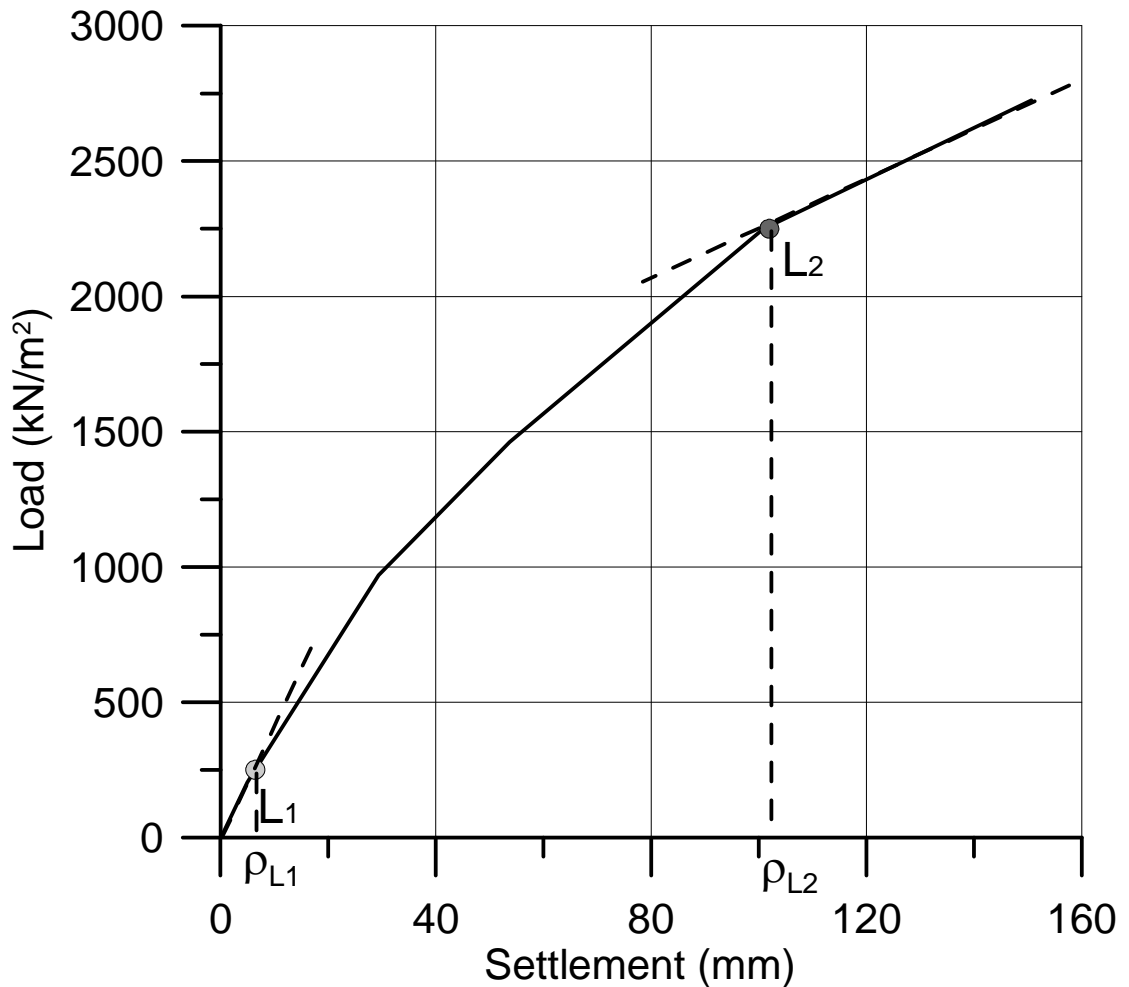


Figure D.9 Case 4P5

D.11 Case 5

Case 5 pertains to a load test reported by Bustamante and Gianceselli (1980). The drilled shaft foundation was 9.8 m in length and 600 mm in width. The test was performed in sand and gravel over limestone in France. Ground water was encountered at 7.5 m below the surface. From the force vs. settlement plot, a ρ_{L1} value of 0.11 D % and a ρ_{L2} of 4.80 D % were obtained.

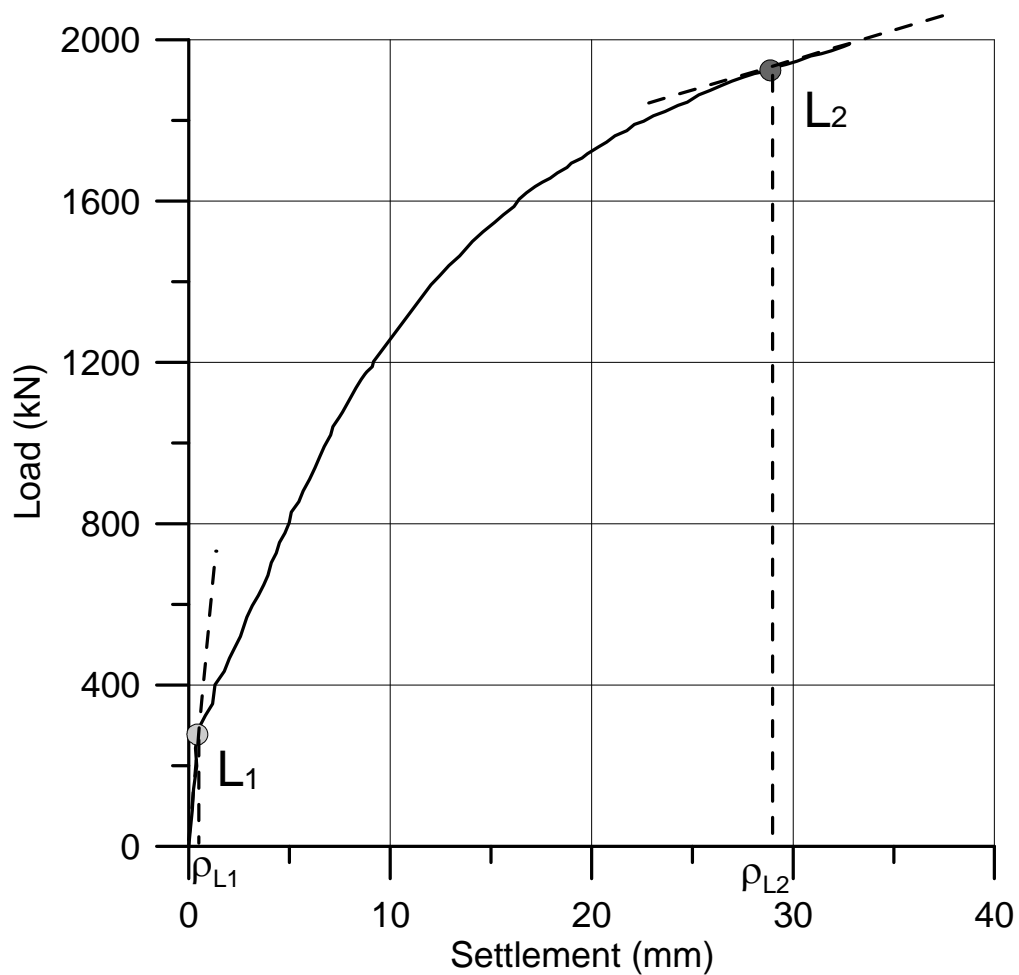


Figure D.10 Case 5

D.12 Case 6A

Case 6A pertains to a load test reported by Gregersen, Aas, and Dibiagio (1973). The driven precast concrete pile was 8 m in length and 280 mm in width. The test was performed in uniform loose normally consolidated sand near Drammen, Norway. Ground water was encountered at 1.7 m below the surface. From the force vs. settlement plot, a ρ_{L1} value of 0.18 D % and a ρ_{L2} of 5.39 D % were obtained.

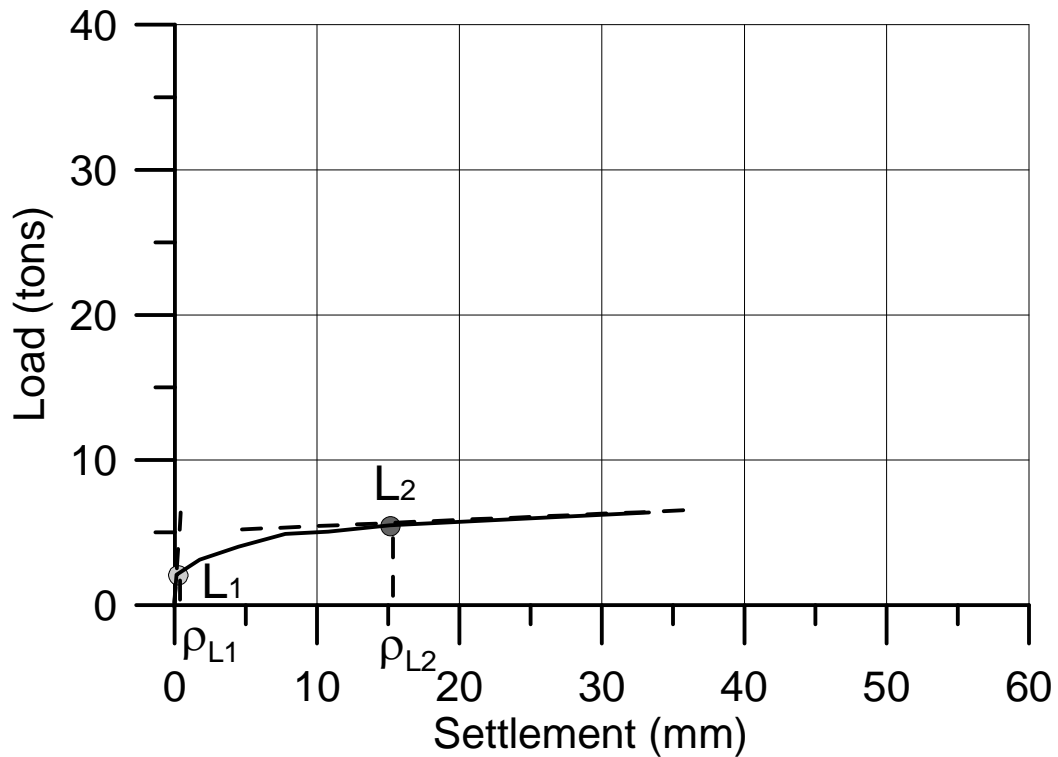


Figure D.11 Case 6A

D.13 Case 6D

Case 6D pertains to a load test reported by Gregersen, Aas, and Dibiagio (1973). The driven precast concrete pile was 8 m in length and 280 mm in width. The test was performed in uniform loose normally consolidated sand near Drammen, Norway. Ground water was encountered at 1.7 m below the surface. From the force vs. settlement plot, a ρ_{L1} value of 0.22 D % and a ρ_{L2} of 6.08 D % were obtained.

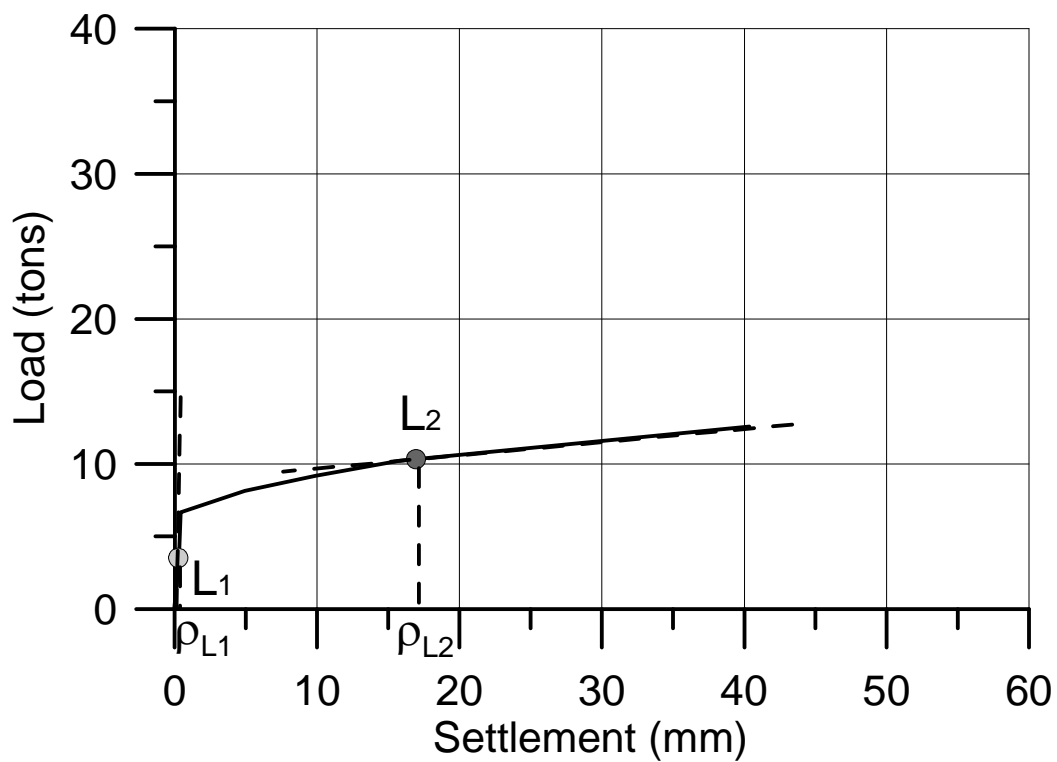


Figure D.12 Case 6D

D.14 Case 7C1

Case 7C1 pertains to a load test reported by Ackley and Sanders (1979). The driven pile was 10.7 m (35 ft) in length and 340 mm (13.38 in) in width. The test was performed in gravels over shale. Ground water was not reported. From the force vs. settlement plot, a ρ_{L1} value of 0.20 D % and a ρ_{L2} of 6.75 D % were obtained.

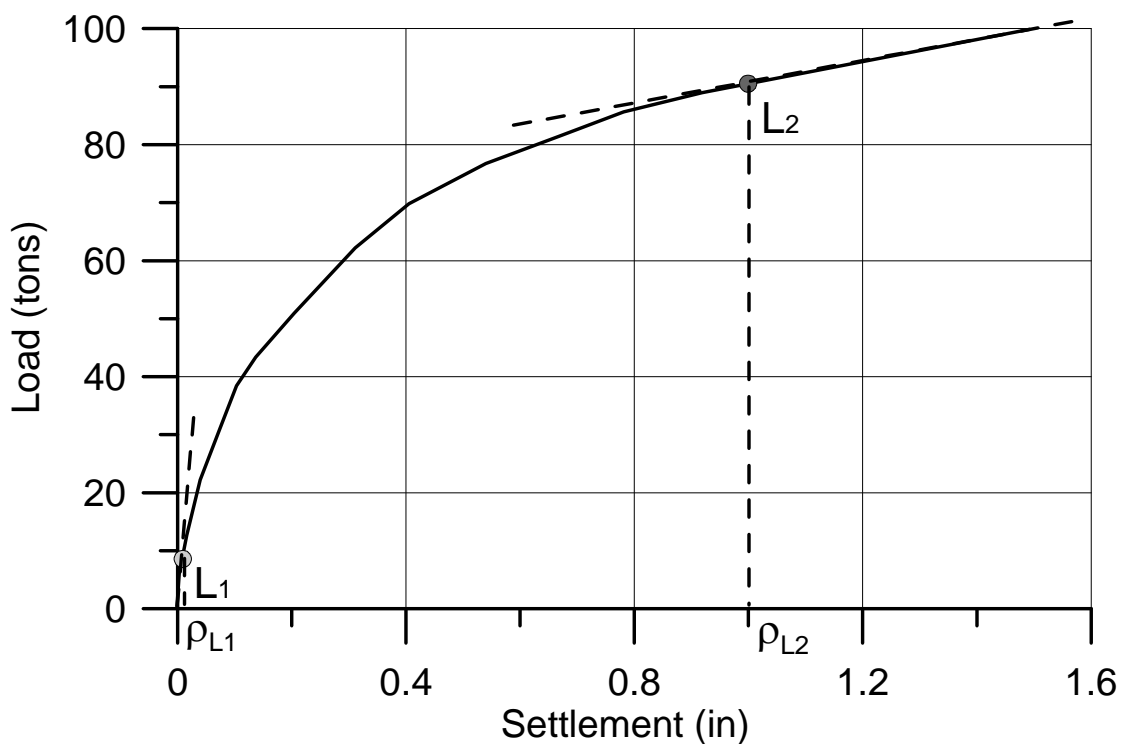


Figure D.13 Case 7C1

D.15 Case 7C4

Case 7C4 pertains to a load test reported by Ackley and Sanders (1979). The driven pile was 22.3 m (73 ft) in length and 340 mm (13.38 in) in width. The test was performed on gravels over shale. Ground water was not reported. From the force vs. settlement plot, a ρ_{L1} value of 0.32 D % and a ρ_{L2} of 6.17 D % were obtained.

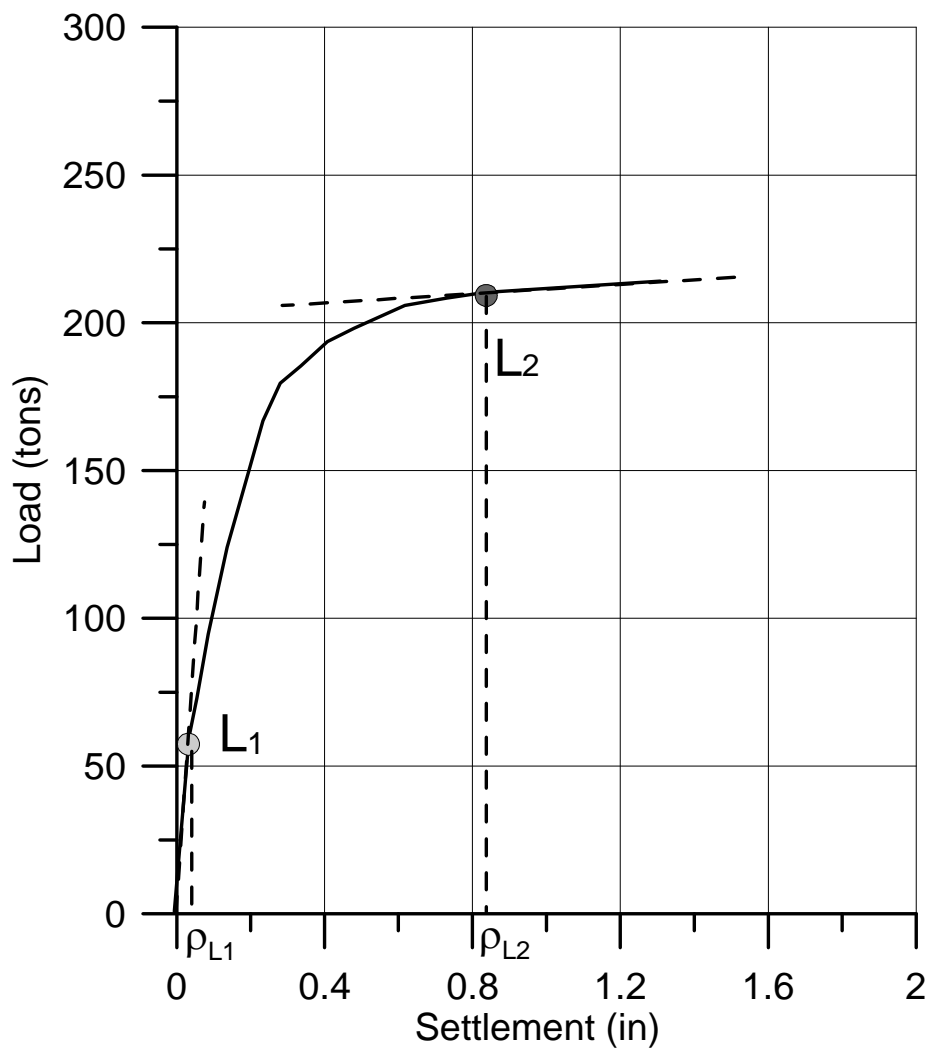


Figure D.14 Case 7C4

D.16 Summary

The vertical force vs. settlement plot for pile foundation tips from the 14 case histories were collected and investigated to determine ρ_{L1} and ρ_{L2} . Figure D.1 shows the histogram of ρ_{L1} and an inferred normal probability density function. The mean value of ρ_{L1} is 0.22 % D and the upper limit is 0.34 % D. This mean value is relatively close to the ρ_{L1} of 0.23 % D reported by Akbas and Kulhawy (2009) for 205 load tests on shallow foundations.

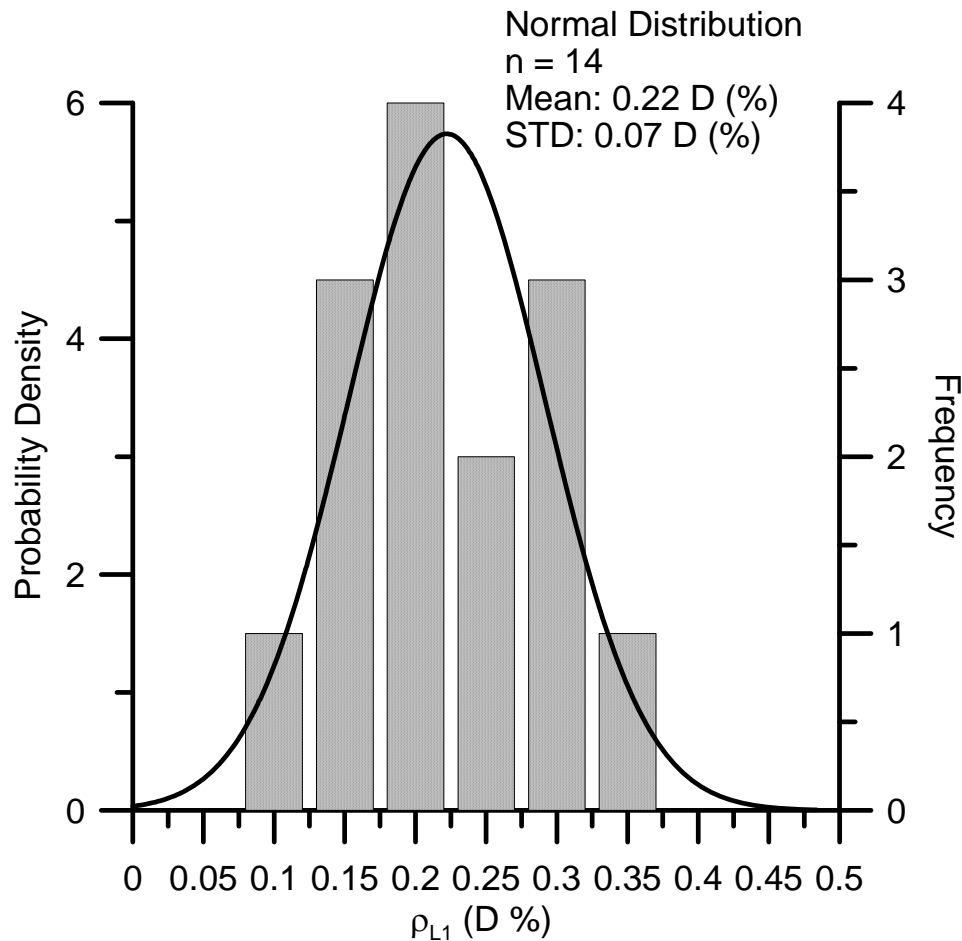


Figure D.15 Histogram of ρ_{L1} from Field Tests

Figure D.2 shows the histogram of ρ_{L2} and its inferred normal probability density function. The mean value of ρ_{L2} is 5.94 % D and the upper limit is 7.85 % D. This mean value is relatively close to the ρ_{L2} of 5.78 % D reported by Akbas and Kulhawy (2009) for 205 load tests on shallow foundations.

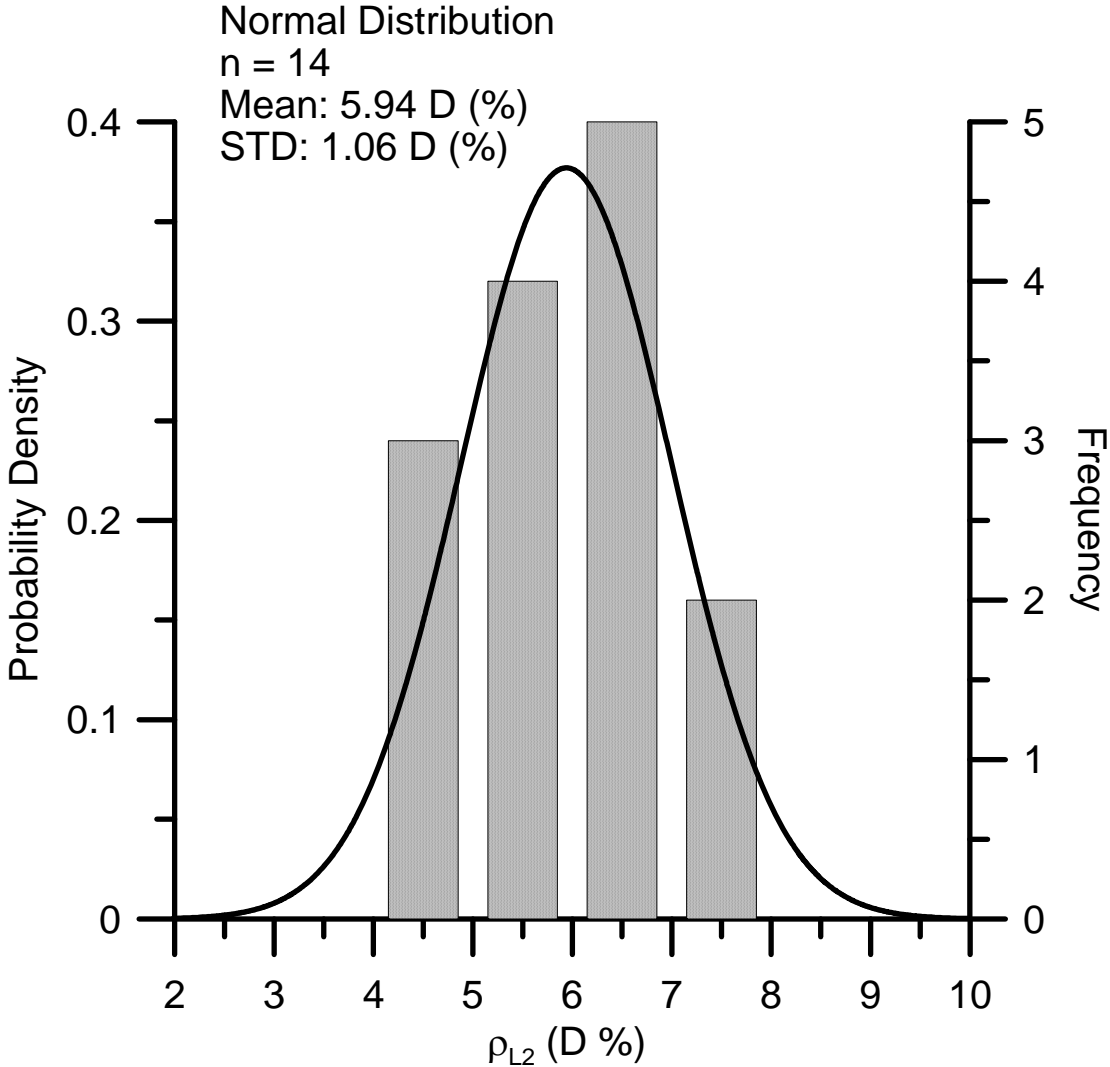


Figure D.16 Histogram of ρ_{L2} from Field Tests

REFERENCES

- ABAQUS. (2009). User Manual and Theory Manual (6.9), Simulia, Dassault Systems, Providence, RI.
- Abbo, A.J., and Sloan, S.W. (1995). "A Smooth Hyperbolic Approximation to the Mohr-Coulomb Yield Criterion." *Computers & Structures*, Vol. 54, No. 3, pp. 427-441.
- Abdoun, T., D. Ha, M.J. O'Rourke, M.D. Symans, T.D. O'Rourke, M.C. Palmer and H.E. Stewart. (2008). "Buried HDPE Pipelines Subjected to Normal Faulting-A Centrifuge Investigation," *Canadian Geotechnical Journal*, Vol. 45, No. 12, pp 1733-1742.
- Ackley, R.E., and Sanders, R.L. (1979). "Load Tests on Piles Driven into Cretaceous Sand." *Proceedings*, ASCE Symposium on Deep Foundations, Atlanta, pp. 1-37.
- Akbas, S.O., and Kulhawy, F.H. (2009). "Axial Compression of Footings in Cohesionless Soils. I: Load-Settlement Behavior." *Journal of the Geotechnical and Geoenvironmental Engineering*, ASCE, Vol. 135, No. 11, Nov., pp. 1562-1574.
- Alsaleh, H., and Shahrour, I. (2009). "Influence of Plasticity on the Seismic Soil-Micropiles-Structure Interaction." *Soil Dynamics and Earthquake Engineering*, Vol. 29, No. 3, pp. 574-578.
- American Lifelines Alliance. (2005) "Seismic Design Guidelines for Water Pipelines" American Lifelines Alliance in partnership with the Federal Emergency Management Agency, Washington, D.C. www.americanlifelinesalliance.org
- ASCE. (1984). "Guidelines for the Seismic Design of Oil and Gas Pipeline Systems.", Committee on Gas and Liquid Fuel Lifelines, American Society of Civil Engineers, Reston, Virginia.
- Anastasopoulos, I., Gazetas, G. Bransby, M.F., Davies, M.C.R. A.El Nahas. (2007). "Fault Rupture Propagation through Sand: Finite-Element Analysis and Validation through Centrifuge Experiments." *Journal of the Geotechnical and Geoenvironmental Engineering*, ASCE, Vol. 133, No. 8, Aug., pp. 943-958.
- Anastasopoulos, I. (2005). "Fault Rupture-Soil-Foundation-Structure Interaction." Ph.D. Dissertation, School of Civil Engineering, National Technical University, Athens, Greece.

- Anderson, C., Wijewickreme, D., Ventura, C., and Mitchell, A. (2004). "Full-Scale Laboratory Testing of Soil-Pipe Interaction in Branched Polyethylene Pipelines." *Experimental Techniques*, Vol. 29, No. 2, pp.33-37.
- Arslan, H., and Sture, S. (2008). "Finite Element Simulation of Localization in Granular Materials by Micropolar Continuum Approach." *Computers and Geotechnics*, Vol. 35, No. 4, pp. 548-562.
- Audibert, J.M.E., and Nyman, K.J. (1977). "Soil Restraint Against Horizontal Motion of Pipes." *Journal of the Geotechnical Engineering Division, ASCE*, Vol. 103, No. GT10, Oct., pp. 1119-1142.
- Aurora, R.P. and Reese, L.C. (1977). "Field Tests of Drilled Shafts in Clay-Shales." *Proceedings, 9th International Conference on Soil Mechanics and Foundation Engineering*, Vol. 1, Tokyo, pp. 371-376.
- Bauer, E. (1996). "Calibration of a Comprehensive Hypoplastic Model for Granular Materials." *Soils and Foundations*, Vol. 36, No. 1, pp. 13-26.
- Bernat, S., and Cambou, B. (1998). "Soil-Structure Interaction in Shield Tunnelling in Soft Soil." *Computers and Geotechnics*, Vol. 22, No. 3-4, pp. 221-242.
- Bettess, P. (1977). "Infinite Elements." *International Journal for Numerical Methods in Engineering*, Vol. 11, pp. 53-64.
- Bird, J., O'Rourke, T.D., Bracegirdle, T., Bommer, J., and Tromans, I. (2004). "A Framework for Assessing Earthquake Hazards for Major Pipelines." *International Conference on Terrain and Geohazard Challenges Facing Onshore Oil and Gas Pipelines*, June 2-4, 2004, London, United Kingdom.
- Bolton, M.D. (1986). "The Strength and Dilatancy of Sands." *Geotechnique*, Vol. 36, No. 1, pp. 65-78.
- Bray, J.D. (1990). "The Effects of Tectonic Movements on Stresses and Deformations in Earth Embankments." Ph.D. Dissertation, University of California at Berkeley, Berkeley, CA.
- Bray, J.D., Seed, R.B., and Seed, H.B. (1994a). "Earthquake Fault Rupture Propagation through Cohesive Soil." *Journal of Geotechnical Engineering*, Vol. 120, No. 3, pp. 543-561.
- Bray, J.D., Seed, R.B., and Seed, H.B. (1994b). "Analysis of Earthquake Fault Rupture Propagation through Cohesive Soil." *Journal of Geotechnical Engineering*, Vol. 120, No. 3, pp. 562-580.

- Budhu, M. (1984). "Nonuniformities Imposed by Simple Shear Apparatus." *Canadian Geotechnical Journal*, Vol. 21, No. 1, pp.125-137.
- Bustamante, M., and Gianceselli, L. (1980). "Portance d'Un Pieux Fore – Tube dans de Calcaire de Saint-Oven." *Bulletin 107*, Liaison de Laboratoires des Ponts et Chaussees, pp. 9-16.
- Chambon, R., Desrues, J., Hammad, W., and Charlier, R. (2005). "CLOe, A New Rate-Type Constitutive Model for Geomaterials Theoretical Basis and Implementation." *International Journal for Numerical and Analytical Methods in Geomechanics*, Vol. 18, No. 4, pp. 253-278.
- Chen, W.F., and Han, D.J. (1987). *Plasticity for Structural Engineers*. Springer-Verlag, New York, New York
- Chen, C.Y., and Martin, G.R. (2002). "Soil–Structure Interaction for Landslide Stabilizing Piles." *Computers and Geotechnics*, Vol. 29, No. 5, pp. 363-386.
- Conte, J.P., Elgamal, A., Yang, Z., Zhang, Y., Acero, G., and Seible, F. (2002). "Nonlinear Seismic Analysis of a Bridge Ground System." *Proceedings*, 15th ASCE Engineering Mechanics Conference, Columbia University, New York, NY
- Cubrinovski, M., Ishihara, K., and Furukawazono, K. (1999). "Analysis of Full-Scale Tests on Piles in Deposits Subjected to Liquefaction." *Proceedings*, 2nd International Conference on Earthquake Geotechnical Engineering, Lisbon, Portugal
- Davis, E.H. (1968). "Theories of Plasticity and the Failure of Soil Masses." *Soil Mechanics, Selected Topics*, I. K. Lee, ed., Butterworth, London.
- Desai, C.S., Somasundaram, S., Frantziskois, G.N. (1986). "A Hierarchical Approach for Constitutive Modelling of Geologic Materials." *International Journal for Numerical and Analytical Methods in Geomechanics*, Vol. 10, No. 3, pp. 225-257.
- Duncan, J.M. (1980). "Hyperbolic stress-strain relationships." *Proceedings*, Symposium on Limit Equilibrium, Plasticity and Generalized Stress-Strain Applications in Geotechnical Engineering, held in conjunction with the 1980 ASCE Annual Convention and Exposition, Hollywood, FL, Oct. 27-31, 1980, pp.443–460
- Duncan, J.M., and Chang, C.Y. (1970). "Nonlinear Analysis of Stress and Strain in Soils." *Journal of Soil Mechanics and Foundations*, ASCE, Vol. 96, No. 5, Sep/Oct., pp. 1629-1653.

- Ellis, E.A., and Springman, S.M. (2001). "Modelling of Soil-Structure Interaction for Piled Bridge Abutment in Plane Strain FEM Analyses." *Computers and Geotechnics*, Vol. 28, No. 2, pp. 79-98.
- Eidinger, J., M. O'Rourke, and J. Bachhuber, (2002). "Performance of Pipelines at Fault Crossings," *Proceedings, 7th U.S. National Conference on Earthquake Engineering*, EERI, Boston, MA, July.
- Erickson, S.G., Staryer, L.M., and Suppe, J. (2001). "Initiation and Reactivation of Faults During Movement over a Thrust-Fault Ramp: Numerical Mechanical Models." *Journal of Structural Geology*, 23, pp. 11-23.
- Fellenius, B.H. (1980). "The Analysis of Results from Routine Pile Load Tests.", *Ground Engineering*, London, Vol. 13, No. 6, pp. 19-31.
- Fleming, W.G.K. (1992). "A New Method for Single Pile Settlement Prediction and Analysis.", *Geotechnique*, Vol. 42, No. 3, pp. 411-425.
- Gartling, D. and Becker, E.B. (1974). "Computationally Efficient Finite Element Analysis of Viscous Flow Problems." *Proceedings, International Conference on Computational Methods in Non-Linear Mechanics*, University of Texas, Austin, Texas
- Gerolymos, N., Vardoulakis, I., and Gazetas, G. (2007). "A Thermo-Porovisco-Plastic Shear Band Model for Seismic Triggering and Evolution of Catastrophic Landslides." *Soils and Foundations*, Vol. 47, No. 1, pp. 11-26.
- Giovanazi, S., and Cubrinovski, M. (2007). "Liquefaction Hazards for Seismic Risk Analysis." *New Zealand Society of Earthquake Engineering 2007 Conference (NZSEE 2007). Proceedings. 2007 Annual NZSEE Technical Conference*, Paper 06. Palmerston North, New Zealand, Apr 2007.
- Gregersen, O.S., Aas, G., and Dibiagio, E. (1973). "Load Tests on Friction Piles in Loose Sand." *Proceedings, 8th International Conference on Soil Mechanics and Foundation Engineering*, Vol. 2, Moscow, pp. 39-45.
- Ha, D., Abdoun, T.H., and O'Rourke, M.J. (2008a). "Soil-Pipeline Interaction Behavior under Strike-Slip Faulting." *Proceedings, Geotechnical Earthquake Engineering and Soil Dynamics IV*, ASCE, Sacramento, CA, May 2008.
- Ha, D., Abdoun, T.H., O'Rourke, M.J., Symans, M.D., O'Rourke, T.D., Palmer M.C., and Stewart H.E. (2008b). "Centrifuge Modeling of Earthquake Effects on Buried High-Density Polyethylene (HDPE) Pipelines Crossing Fault Zones." *Journal of Geotechnical and Geoenvironmental Engineering*, Vol. 134, No. 10, pp. 1501-1515.

- Ha, D., Abdoun, T.H., O'Rourke, M.J., Symans, M.D., O'Rourke, T.D., Palmer M.C., and Stewart H.E. (2010). "Earthquake Faulting Effects on Buried Pipelines - Case History and Centrifuge Study." *Journal of Earthquake Engineering*, Vol. 14, No. 5, pp. 646-669.
- Hamada, M., Isoyama, R., and Wakamatsu, K. (1996). "Liquefaction-Induced Ground Displacement and Its Related Damage to Lifeline Facilities." *Soils and Foundations*, Special No., January 1996, pp. 81-98.
- Hamada, M. and O'Rourke, T.D. Eds. (1992). "Case Studies of Liquefaction and Lifeline Performance During Past Earthquakes." *NCEER-92-0001*, Vol.1, National Center for Earthquake Engineering Research, Buffalo, NY, April
- Hamada, M. and Wakamatsu, K. (1996). "Liquefaction, Ground Deformation and Their Caused Damage to Structures." *The 1995 Hyogoken-Nanbu Earthquake Investigation Into Damage to Civil Engineering Structures*, Committee of Earthquake Engineering, Japan Society of Civil Engineering, June.
- Hansen, J.B. (1961). "The Ultimate Resistance of Rigid Piles Against Transversal Forces." *Bulletin 12*, Danish Geotechnical Institute, Copenhagen, pp.1-9.
- Hirany, A., and Kulhawy, F. H. (1988). "Conduct and Interpretation of Load Tests on Drilled Shaft Foundations: Detailed Guidelines." *Rep. No. EL-5915*, Electric Power Research Institute, Palo Alto, Calif.
- Hirany, A., and Kulhawy, F. H. (1989). "Interpretation of Load Tests on Drilled Shafts. I: Axial compression." *Proceedings*, Foundation Engineering: Current Principles and Practices, GSP 22, F. H. Kulhawy, ed., ASCE, New York, pp. 1132-1149.
- Hirany, A., and Kulhawy, F. H. (2002). "On the Interpretation of Drilled Foundation Load Test Results." *Proceedings*, Deep Foundations 2002, GSP 116, M. W. O'Neill and F. C. Townsend, eds., ASCE, Reston, Va., pp. 1018-1028.
- Honegger, D. and D.J. Nyman, (2004). "Guidelines for the Seismic Design and Assessment of Natural Gas and Liquid Hydrocarbon Pipelines," Pipeline Research Council International, *Catalog No. L51927*, October.
- Horn, R., Taubner, H., Wuttke, M., and Baumgartl, T. (1994). "Soil Physical Properties Related to Soil Structure." *Soil and Tillage Research*, Vol. 30, No. 2-4, pp. 187-216.
- Horsefield, W.T. (1977). "An Experimental Approach to Basement-Controlled Faulting." *Geologie en Mijnbouw*, Vol. 56, No. 4, pp. 363-370.

- Hsu, T-W., Chen, Y-J., and Hung W-C. (2006). "Soil Restraint to Oblique Movement of Buried Pipes in Dense Sand." *Journal of Transportation Engineering*, Vol. 132, No. 2, pp. 175-181.
- Hu, L., and Pu, J.L. (2003). "Application of Damage Model for Soil–Structure Interface." *Computers and Geotechnics*, Vol. 30, No. 2, pp. 165-183.
- Huang, W., Nubel, K., and Bauer, E. (2002). "Polar Extension of a Hypoplastic Model for Granular Materials with Shear Localization", *Mechanics of Materials*, Vol. 34, No. 9, pp. 563-576.
- Ismael, N.F., and Klym, T.W. (1979). "Uplift and Bearing Capacity of Short Piers in Sand.", *Journal of the Geotechnical Engineering Division*, ASCE, Vol. 104, No. GT8, pp. 1061-1074.
- Janbu, N. (1963). "Soil Compressibility as Determined by Oedometer and Triaxial Tests." *Proceedings, European Conference on Soil Mechanics & Foundations Engineering*, Wiesbaden, Germany, Vol. 1, pp.19-25.
- Jefferies, M.G. (1993). "Nor-Sand: A Simple Critical State Model for Sand." *Geotechnique*, Vol. 43, No. 1, pp. 91-103.
- Jeon, S.S., and O'Rourke, T.D. (2005). "Northridge Earthquake Effects on Pipelines and Residential Buildings." *Bulletin of the Seismological Society of America*, Vol. 95, No. 1, Feb., pp.294-318.
- Jewell, R.A., and Roth, C.P. (1987). "Direct Shear Tests on Reinforced Sand." *Geotechnique*, Vol. 37, No. 1, pp. 53-68.
- Jones, S.L., Kesner, K.E., O'Rourke, T.D., Stewart, H.E., Abdoun, T., and O'Rourke, M.J., (2004). "Soil-Structure Interaction Facility for Lifeline Systems." *Proceedings, 13th World Conference on Earthquake Engineering*, Vancouver, BC, Canada, Aug., 2004, Paper No.1621.
- Kananyan, A.S. (1966). "Experimental Investigation of the Stability of Bases of Anchor Foundations." *Soil Mechanics and Foundation Engineering*, Vol. 3, No. 6, pp. 387-392.
- Karimian, H., Wijewickreme, D., and Honegger, D. (2006) "Full-Scale Laboratory Testing to Assess Methods for Reduction of Soil Loads on Buried Pipes Subject to Transverse Ground Movement." *Proceedings, ASME 6th International Pipeline Conference*, Calgary, Alberta, Canada, September, 2006.

- Kennedy, R.P., Chow, A.W., and Williamson, R. A. (1977). "Fault Movement Effects on Buried Oil Pipeline." *Journal of the Transportation Engineering Division*, ASCE, Vol. 103, No. TE5, Sept., pp. 617-633.
- Kennedy, R.P., Darrow, A.C., and Short, S.A. (1979). "Seismic Design of Oil Pipeline Systems." *Journal of the Technical Councils*, ASCE, Vol. 105, No. TC1, Apr., pp. 119-134.
- Klisinski, M., and Mroz, Z. (1988). "Description of Inelastic Deformation and Degradation of Concrete." *International Journal of Solids and Structures*, Vol. 24, No. 4, pp. 391-416.
- Kulhawy, F.H., Trautmann, C.H., Beech, J. F., O'Rourke, T. D., McGuire, W., and Wood, W.A. (1983). "Transmission Line Structure Foundations for Uplift-Compression Loading." *EPRI Report EL-2870*, Electric Power Research Institute, February.
- Ledezma, C., and Bray, J.D. (2010). "Probabilistic Performance-Based Procedure to Evaluate Pile Foundations at Sites with Liquefaction-Induced Lateral Displacement." *Journal of Geotechnical and Geoenvironmental Engineering*, Vol. 136, No. 3, pp. 464-476.
- Li, S., Lai, Y., Zhang, S., and Liu, D. (2009). "An Improved Statistical Damage Constitutive Model for Warm Frozen Clay Based on Mohr-Coulomb Criterion." *Cold Regions Science and Technology*, Vol. 57, No. 2-3, pp. 154-159.
- Lings, M. L., and Dietz, M. S. (2004). "An Improved Direct Shear Apparatus for Sand." *Geotechnique*, Vol. 54, No. 4, pp. 245-256.
- Loukidis, D. (1999). "Active Fault Propagation through Soil." Ph.D Thesis, School of Civil Engineering, National Technical University, Athens, Greece
- Mason, J. A., T. D. O'Rourke, S. Jones, and I. Tutuncu, (2010). "Compression Performance of Steel Pipelines with Welded Slip Joints", *Journal of Pipeline Systems Engineering and Practice*, ASCE, Vol. 1. No. 1, p. 2-10.
- Massoudi, M., Mehrabadi, M.M. (2001). "A Continuum Model for Granular Materials: Considering Dilatancy and the Mohr-Coulomb Criterion." *Acta Mechanica*, Vol. 152, No. 1-4, pp. 121-138.
- McCaffrey, M.A., and O'Rourke, T.D. (1983). "Buried Pipeline Response to Reverse Faulting During the 1971 San Fernando Earthquake." *Proceedings*, ASME 4th national Congress on Pressure Vessels and Piping, Portland, OR, June, 1983.

- Menetrey, P., and Willam, K.J. (1995). "Triaxial Failure Criterion for Concrete and Its Generalization." *ACI Structural Journal*, Vol. 92, No. 3, pp. 311-318.
- Meyerhof, G.G. (1973). "Uplift Resistance of Inclined Anchors and Piles." *Proceedings, 8th International Conference on Soil Mechanics and Foundation Engineering*, Moscow, USSR, Vol. 2, pp. 167-172.
- Morgenstern, N.R., and Tchalenko, J.S. (1967). "Microscopic Structures in Kaolin Subjected to Direct Shear." *Geotechnique*, Vol. 17, No. 4, pp. 309-328.
- Mroueh, H., and Shabrouh, I. (1999). "Use of Sparse Iterative Methods for the Resolution of Three-Dimensional Soil/Structure Interaction Problems." *International Journal for Numerical and Analytical Methods in Geomechanics*, Vol. 23, No. 15, pp. 1961-1975.
- Mroueh, H., and Shabrouh, I. (2003). "A Full 3-D Finite Element Analysis of Tunneling-Adjacent Structures Interaction." *Computers and Geotechnics*, Vol. 30, No. 3, pp. 245-253.
- Muhlhaus, H.B., and Vardoulakis, I. (1987). "The Thickness of Shear Bands in Granular Materials." *Geotechnique*, Vol. 37, No. 3, pp. 271-283.
- Muir Wood, D., (2002). "Some Observations of Volumetric Instabilities in Soils." *International Journal of Solids Structures*, Vol. 39, No. 13-14, pp.3429-3449.
- Muir Wood, D., and Stone, K.J.L. (1994). "Some Observations of Zones of Localization in Model Tests on Dry Sand." *Localization and Bifurcation Theory for Soils and Rocks*, Chambon, R., Desrues, J., and Vardoulakis, I. eds., Balkema, Rotterdam, Netherlands, pp.155-164.
- Naggar, M.H. El. (2002). "The 2002 Canadian Geotechnical Colloquium: The Role of Soil-Pile Interaction in Foundation Engineering." *Canadian Geotechnical Journal*, Vol.41, No. 3, pp. 485-509.
- Nakai, T., Muir Wood, D., and Stone, K.J.L. (1995). "Numerical Calculations of Soil Response over a Displacing Basement." *Soils and Foundation*, Vol. 35, No. 2, pp. 25-35.
- Nath, B. (1980). "The W-Plane Finite Element Method for the Solution of Scalar Field Problems in Two Dimensions." *International Journal for Numerical Methods in Engineering*, Vol. 15, No. 3, pp. 361-379.
- Newmark, N. and W. Hall. (1975). "Pipeline Design to Resist Large Fault Displacement.", *Proceedings, U.S. Conference on Earthquake Engineering*, Ann Arbor, Michigan, pp. 416-425.

- Nobahar, A., Kenny, S., and Phillips, R. (2007). "Buried Pipelines Subject to Subgouge Deformations.", *International Journal of Geomechanics*, Vol. 7, No. 3, pp. 206-216.
- Nyman, K.J. (1982). "Soil Response Against the Horizontal-Vertical Motion of Pipes." Preprint 82-534, presented at ASCE National Convention, New Orleans, Louisiana.
- Oliveira, J.R.M.S., Almeida, M.S.S., Almeida, M.C.F., and Borges, R.G. (2010). "Physical Modeling of Lateral Clay-Pipe Interaction." *Journal of Geotechnical and Geoenvironmental Engineering*, Vol. 136, No. 7, pp. 950-956.
- Olson, N.A. (2009). "Soil Performance for Large Scale Soil-Pipeline Tests." Ph.D. Thesis, Cornell University, Ithaca, New York.
- O'Rourke, M.J., and Deyoe, E. (2004). "Seismic Damage to Segmented Buried Pipe." *Earthquake Spectra*, Vol. 20, No. 4, pp. 1167-1183.
- O'Rourke, M.J., Symans, M.D., Masek, J.P. (2008). "Wave Propagation Effects on Buried Pipe at Treatment Plants." *Earthquake Spectra*, Vol. 24, No. 3, pp. 725-749.
- O'Rourke, M.J., and Nordberg, C. (1992). "Longitudinal Permanent Ground Deformation Effects on Buried Continuous Pipelines." Technical Report NCEER-92-0014, Rensselaer Polytechnic Institute, Troy, NY
- O'Rourke, T.D. (1998). "An Overview of Geotechnical and Lifeline Earthquake Engineering.", *Geotechnical Special Publication No. 75*, ASCE, Reston, VA, Proceedings of Geotechnical Earthquake Engineering and Soil Dynamics Conference, Seattle, WA, August 1998, Vol. 2, pp. 1392-1426.
- O'Rourke, T.D. (2010). "Geohazards and Large, Geographically Distributed Systems.", Rankine Lecture, *Geotechnique*, 60(7), pp. 505-543.
- O'Rourke, T.D., and Bonneau, A.L. (2007). "Lifeline Performance Under Extreme Loading During Earthquakes." *Earthquake Geotechnical Engineering*, Pitilakis, K.D. Eds., Springer, Dordrecht, Netherlands, June, pp. 407-432.
- O'Rourke, T.D., Bonneau, A.L., Pease, J.W., Shi, P., and Wang, Y. (2006). "Liquefaction and Ground Failures in San Francisco." *Earthquake Spectra*, Vol. 22, No. S2, pp. S91-S112.

- O'Rourke, T.D., and Hamada, M. Eds. (1992). "Case Studies of Liquefaction and Lifeline Performance During Past Earthquakes." Vol. 2, *NCEER-92-0002*, NCEER, Buffalo, NY, April 1992.
- O'Rourke T.D., Jeon S-S. (2000). "Seismic Zonation for Lifelines and Utilities." *Proceedings*, 6th International Conference on Seismic Zonation, Palm Springs, CA, November 2000 [EERI CD-ROM].
- O'Rourke, T.D., Jezerski, J.M., Olson, N.A., Bonneau, A.L., Palmer, M.C., Stewart, H.E., O'Rourke, M.J., and Abdoun, T. (2008). "Geotechnics of Pipeline System Response to Earthquakes." *Proceedings*, eotechnical Earthquake Engineering and Soil Dynamics IV, ASCE, Sacramento, CA, May 2008.
- O'Rourke T.D., and Liu, X. (1999). "Response of Buried Pipelines Subject to Earthquake Effects." Multidisciplinary Center for Earthquake Engineering Research, *Monograph Series* No. 3, MECCR, Buffalo, New York.
- O'Rourke, T.D., and Trautmann, C. H. (1980). "Analytical Modeling of Buried Pipeline Response to Permanent Earthquake Displacements." Geotechnical Engineering Report 80-4, Cornell University, Ithaca, New York.
- O'Rourke, T.D. and C. Trautmann, (1981). "Earthquake Ground Rupture Effects on Jointed Pipe," *Proceedings*, Second Specialty Conference of the Technical Council on Lifeline Earthquake Engineering, ASCE, Aug., p. 65-80.
- O'Rourke, T.D., Turner, J.E., Jeon, S-S., Stewart, H.E., Yang, Y., and Shi, P., (2005). "Soil-Structure Interaction Under Extreme Loading Conditions." *13th Spencer J. Buchanan Lecture*, Texas A&M University, College Station, Texas.
- O'Rourke, T.D., Y. Wang, and P. Shi, (2004). "Advances in Lifeline Earthquake Engineering", Keynote Paper, *Proceedings*, 13th World Conference on Earthquake Engineering, Vancouver, B.C., Canada, Aug., Paper No. 5003.
- Oversen, N.K., and Stromann, H. (1972). "Design Method for Vertical Anchor Slabs in Sand." *Proceedings*, *Specialty Conference on Performance of Earth and Earth-Supported Structures*, ASCE, New York, Vol. 1, pp. 1481-1500.
- Palmer, M.C., O'Rourke, T.D. Stewart, H.E., O'Rourke, M.J., and Symans, M (2006). "Large Displacement Soil-Structure Interaction Test Facility for Lifelines." *Proceedings*. 8th US National Conference on Earthquake Engineering and 100th Anniversary Earthquake Conference Commemorating the 1906 San Francisco Earthquake, EERI, San Francisco, CA. April, Paper 1257.

- Paulin, M.J., Philips, R., Clark, J.I., Trigg, A., and Konuk, I. (1998). "A Full-Scale Investigation into Pipeline-Soil Interaction." *Proceedings, International Pipeline Conference*, Calgary, Alberta, ASME, pp. 779-788.
- Pimentel, M., Costa, P., Felix, C., and Figueiras, J. (2009). "Behavior of Reinforced Concrete Box Culverts Under High Embankments." *Journal of Structure Engineering*, Vol. 135, No. 4, pp. 366-375.
- Pietruszezak, S.T., and Mroz, Z. (1981). "Finite-Element Analysis of Deformation of Strain Softening Materials." *International Journal of Numerical Methods in Engineering*, Vol. 17, No. 3, pp. 327-334.
- Potts, D.M., Dounias, G. T., and Vaughan, P. R. (1987). "Finite Element Analysis of the Direct Shear Box Test." *Geotechnique*, Vol. 37, No. 1, pp. 11-23.
- Potts, D.M., Dounias, G. T., and Vaughan, P. R. (1990). "Finite Element Analysis of Progressive Failure of Carsington Embankment." *Geotechnique*, Vol. 40, No. 1, pp. 79-101.
- Potts, D.M., Kovacevic, N., and Vaughan, P. R. (1997). "Delayed Collapse of Cut Slopes in Stiff Clay." *Geotechnique*, Vol. 47, No. 5, pp. 953-982.
- Reese, L.C., and Touma, F.T. "Load Tests of Instrumented Drilled Shafts Constructed by the Slurry Displacement Method." *Research Report 108*, Department of Civil Engineering, University of Texas, Austin, TX, 79 p.
- Rha, C., and Taciroglu, E. (2007). "Coupled Macroelement Model of Soil-Structure Interaction in Deep Foundations." *Journal of Engineering Mechanics*, Vol. 133, No. 12, pp. 1326-1340.
- Robert, D.J. and Soga, K. (2007). "Evaluation of pipeline-soil interaction in unsaturated soils by lateral permanent ground deformation." *Report to Tokyo Gas Co. Ltd.*, Cambridge University, Cambridge, UK.
- Robert, D.J. and Soga, K. (2009). "Simulations of Soil-Pipeline Interactions in Unsaturated Soils." *Report to Tokyo Gas Co. Ltd.*, Cambridge University.
- Roth, W. H., Sweet, J., and Goodman, R.E. (1982). "Numerical and Physical Modeling of Flexural Slip Phenomena and Potential for Fault Movement." *Rock Mechanics Supplement*, 12, pp. 27-46.
- Rowe, P.W. (1962). "The Stress Dilatancy Relation for Static Equilibrium of an Assembly of Particles in Contact." *Proceedings, Royal Society of London*, Vol.269, No. 1339, pp. 500-527.

- Rowe, P.W. (1969). "The Relation between the Shear Strength of Sands in Triaxial Compression, Plane Strain and Direct Shear." *Geotechnique*, Vol. 19, No. 1, pp. 75-86.
- Roscoe, K.H. (1970). "The Influence of Strains in Soil Mechanics." 10th Rankine Lecture. *Geotechnique*, Vol. 20, No. 2, pp. 129-170.
- Saada, A.S., and Townsend, F.C. (1981). "State of the Art: Laboratory Strength Testing of Soils." *ASTM Special Technical Publication 740*, ASTM, West Conshohocken, PA., pp. 7-77.
- Schuster, R.L. Eds. (1991). "The March 5, 1987 Ecuador Earthquakes: Mass Wasting and Socioeconomic Effects." *Natural Disaster Studies*, Vol. 5, National Academy Press, Washington, D.C.
- Schweiger, H.F. (1994). "On the Use of Drucker-Prager Failure Criteria for Earth Pressure Problems." *Computers and Geotechnics*, Vol. 16, No. 3, pp. 223-246.
- Schweiger, H.F. (2008). "The Role of Advanced Constitutive Models in Geotechnical Engineering." *Geomechanics and Tunnelling*, Vol. 1, No. 5, pp. 336-344.
- Scott, R.F., and Schoustra, J.J. (1974). "Nuclear Power Plant Sitting on Deep Alluvium." *Journal of the Geotechnical Engineering Division*, ASCE, Vol. 100, No.4., pp. 449-459.
- Shibuya, S., Mitachi, T., and Tamate, S. (1997). "Interpretation of Direct Shear Box Testing of Sands as Quasisimple Shear." *Geotechnique*, Vol. 47, No. 4, pp. 769-790.
- Smith, I.M., and Su, N. (1997). "Three-Dimensional FE Analysis of a Nailed Soil Wall Curved in Plan." *International Journal for Numerical and Analytical Methods in Geomechanics*, Vol. 21, No. 9, pp. 583-897.
- Stone, K.J.L., and Muir Wood, D. (1992). "Effects of Dilatancy and Particle Size Observed in Model Tests on Sand." *Soils and Foundations*, Vol. 32, No. 4, pp.43-57.
- Sun, De'An, Yao, Y-P., and Matsuoka, H. (2006). "Modification of Critical State Models by Mohr-Coulomb Criterion." *Mechanics Research Communications*, Vol. 33, No. 2, pp. 217-232.
- Taylor, D. W. (1948). *Fundamentals of Soil Mechanics*. John Wiley and Sons, New York, New York.

- Terzaghi, K., and Peck, R. B. (1948). *Soil Mechanics in Engineering Practice*, John Wiley and Sons, New York, New York.
- Thomas, H.G. (1978). Discussion of “Soil Restraint Against Horizontal Motion of Pipes.” By J.M.E. Audibert and K.J. Nyman, *Journal of the Geotechnical Engineering Division*, ASCE, Vol. 104, No. GT9, Sept., pp. 1214-1216.
- Tokimatsu, K. and Suzuki, H. (2004). “Pore Water Pressure Response around Piles and its Effects on p-y Behavior during Soil Liquefaction.” *Soils and Foundations*, JGS, Vol. 44, No. 6, pp. 101-110.
- Toprak, S., and Taskin, F. (2006). “Estimation of Earthquake Damage to Buried Pipelines Caused by Ground Shaking.” *Natural Hazards*, Springer Netherlands, Vol. 40, No. 1, pp. 1-24.
- Toprak, S., Taskin, F., and Cem Koc, A. (2009). “Prediction of Earthquake Damage to Urban Water Distribution Systems: A Case Study for Denizli, Turkey.” *Bulletin of Engineering Geology and the Environment*, Springer, Berlin, Vol. 68, No. 4, pp. 499-510.
- Touma, F.T., and Reese, L.C. (1974). “Behavior of Bored Piles in Sand.” *Journal of the Geotechnical Engineering Division*, ASCE, Vol. 100, No. GT7, pp. 749-761.
- Trautmann, C.H. (1983). “Behavior of Pipe in Dry Sand Under Lateral and Uplift Loading.” Ph.D. Thesis, Cornell University, Ithaca, New York.
- Trautmann, C.H., and O’Rourke, T.D. (1983). “Behavior of Pipe in Dry Sand Under Lateral and Uplift Loading.” *Geotechnical Engineering Report 83-7*, Cornell University, Ithaca, New York.
- Trautmann, C.H., and O’Rourke, T.D. (1985). “Lateral Force-displacement Response of Buried Pipe.” *Journal of Geotechnical Engineering*, Vol. 111, No. 9, pp. 1077-1092.
- Trautmann, C.H., O’Rourke, T.D., and Kulhawy, F.H. (1985). “Uplift Force-displacement Response of Buried Pipe.” *Journal of Geotechnical Engineering*, Vol. 111, No. 9, pp. 1061-1076.
- Turner, J.E., (2004). “Lateral Force – Displacement Behavior of Pipes in Partially Saturated Sand.” M.S. Thesis, Cornell University, Ithaca, New York.
- Tutuncu, I. and T.D. O’Rourke, (2006). “Compression Behavior of Nonslender Cylindrical Steel Members with Large-Scale Geometric Imperfections” *Journal of Structural Engineering*, ASCE, Vol. 132, No. 8, pp. 1234-1241.

- Ungless, R.L. (1973). "An Infinite Finite Element." M.A.Sc. Thesis, University of British Columbia, Vancouver, BC, Canada
- Vardoulakis, I., and Graf, B. (1985). "Calibration of Constitutive Models for Granular Materials Using Data from Biaxial Experiments." *Geotechnique*, Vol. 35, No. 3, pp. 299-317.
- Walters, J.V., and Thomas, J.N. (1982). "Shear Zone Development in Granular Materials." *Proceedings*, 4th International Conference on Numerical Methods in Geomechanics, Vol. I, Edmonton, Canada, pp. 263-274.
- White, R.J., Stone, K.J.L., and Jewel, R.J. (1994). "Effect of Partical Size on Localization Development in Model Tests on Sand." *Proceedings*, International Centrifuge Conference, Leung, C. F., Lee, F. H., and Tan T. S. eds., Balkema, Rotterdam, Netherlands, pp. 817-822.
- Willam, K.J., and Warnke, E.P. (1974). "Constitutive Model for Triaxial Behavior of Concrete." *Concrete Structures Subjected to Triaxial Stresses*, International Association for Bridges and Structural Engineering, Bergamo, Italy, May.
- Wong, K.S., and Duncan, J.M. (1974). "Hyperbolic Stress-Strain Parameters for Nonlinear Finite Element Analyses of Stresses of Stresses and Movements in Soil Masses." *Report No. TE-74-3*, University of California, Department of Civil Engineering, Berkeley, California.
- Wu, W., and Thomson, R. (2007). "A Study of the Interaction Between a Guardrail Post and Soil During Quasi-Static and Dynamic Loading." *International Journal of Impact Engineering*, Vol. 34, No. 5, pp. 883-898.
- Xu, J., Abadalla, B., Eltaher, A., and Jukes, P. (2009). "Permafrost Thawing-Pipeline Interaction Advanced Finite Element Model." *Proceedings*, ASME 28th International Conference on Ocean, Offshore and Arctic Engineering, Honolulu, Hawaii, May, 2009.
- Yargici, V. (2003). "Assessment of Buried Pipeline Performance During the 1999 Duzce Earthquake." Ph.D. Thesis, The Middle East Technical University, Ankara, Turkey.
- Yimsiri, S., Soga, K., Yosizaki, K., Dasari, G.R., and O'Rourke, T. D. (2004). "Lateral and Upward Soil-Pipeline Interaction in Sand for Deep Embedment Conditions." *Journal of Geotechnical and Geoenvironmental Engineering*, ASCE, Vol. 130, No. 8, pp. 830-842.
- Yeh, C-H., Shih, B-J., Chang, C-H., Walter Chen, W.Y., Liu, G-Y., and Hung H-Y. (2006). "Seismic Damage Assessment of Potable Water Pipelines."

Proceedings, 4th International Conference on Earthquake Engineering, Taipei, Taiwan, Oct., 2006.

Yoshishaki, K., T.D. O'Rourke, and M. Hamada (2001), "Large Deformation Behavior of Buried Pipelines with Low-Angle Elbows Subjected to Permanent Ground Deformation," *Journal of Structural Mechanics and Earthquake Engineering*, JSME, Vol. 4, No. 50, pp. 215-228.

Yoshizaki, K., O'Rourke, T.D., and Hamada, M. (2003). "Large-Scale Experiments of Buried Steel Pipelines with Elbows Subjected to Permanent Ground Deformation." *Structural Engineering/Earthquake Engineering*, JSCE, Vol. 20, No. 1, pp. 1s-11s.

Youd, T.L. (1973). "Ground Movements in the Van Norman Lake Vicinity During San Fernando Earthquake." *San Fernando, California, Earthquake of February 9, 1971*, U.S. Department of Commerce, Washington, D.C., Vol. 3, pp. 197-206.

Zienkiewicz, O.C., Emson, C., and Bettess, P. (1983). "A Novel Boundary Infinite Element" *International Journal for Numerical Methods in Engineering*, Vol. 19, No. 3, pp. 393-404.